Impact of water activity on the mineralogy of hydrated cement

THÈSE N^{O} 6487 (2015)

PRÉSENTÉE LE 27 FÉVRIER 2015
À LA FACULTÉ DES SCIENCES ET TECHNIQUES DE L'INGÉNIEUR
LABORATOIRE DES MATÉRIAUX DE CONSTRUCTION
PROGRAMME DOCTORAL EN SCIENCE ET GÉNIE DES MATÉRIAUX

ÉCOLE POLYTECHNIQUE FÉDÉRALE DE LAUSANNE

POUR L'OBTENTION DU GRADE DE DOCTEUR ÈS SCIENCES

PAR

Luis Guillermo BAQUERIZO IBARRA

acceptée sur proposition du jury:

Prof. D. Damjanovic, président du jury
Prof. K. Scrivener, Dr T. Matschei, directeurs de thèse
Dr D. Kulik, rapporteur
Prof. H. Pöllmann, rapporteur
Prof. G. Renaudin, rapporteur

ÉCOLE POLYTECHNIQUE
FÉDÉRALE DE LAUSANNE

Suisse
2015

A mind is like a parachute,

it doesn't work unless it's open.

— Frank Zappa

A mi familia.

Acknowledgement

Now that I have finally reached the end of this 4-year adventure, called PhD studies, it is time to thank everyone who made this dream come true.

First of all I would like to thank the European Union and the Marie Curie initiative* for their financial contribution to this project. I would also like to thank the Nanocem Consortium and the fantastic program called TRANSCEND, of which I was part. This program gave me the opportunity to attend courses, conferences, workshops, seminars, and to visit several wonderful locations across Europe, and most importantly, to meet a fantastic group of people: my fellow Transcend students, scientist and researchers who are part of this "cement world". I feel very lucky to have been part of this program, and to have been able to share exciting moments with the Nanocem people.

I would like to thank my thesis director, Prof. Karen Scrivener, not only for building the "Nanocem family", but also for her guidance during the development of this project. Her support and trust were very important to me. Thanks a lot to Marie-Alix, for all the great work she did for the TRANSCEND project and for Nanocem. A big thanks to the EPFL, especially the LMC, because although my research was not carried out in their facilities, its doors were always open to me.

My PhD was not conventional, because I had the great privilege of doing it at Holcim Technology Ltd. I have no words to thank this great company for the huge opportunity they gave me when they allowed me to pursue my degree in their facilities. I consider this opportunity as "unique", because I could learn and experience so many things that I believe students usually do not. During my stay at Holcim I could grow, as a professional and as a person, and for this I will always be grateful to this great company.

I immensely thank the Innovation Function @Holcim, and all its members and departments. I had the opportunity to learn not only scientific/technical stuff, but also management and innovation-related topics, which are extremely important for my personal development. Thanks a lot to the management team for teaching me that communication, collaboration and innovation management are extremely important to succeed.

A very special thanks to my "Product Technology family", with whom I spent probably the best 4 years of my life in the beton labor. I thank Moussa for his directness and frankness, Michael for his trust (also for his bicycle, pity it got robbed), Lesley because with her smile she illuminated the whole lab, Fabrizio for his openness in the lab, Dr. Manuel Rudolf for letting me call him Dr. Manuel Rudolf, my apple-fellow and former officemate David for all the cool discussions and family times we spent together, and everybody who is or was part of the team, my new officemate Mathieu, Mercedes, Winnie, Tianhe, Guanshu, Roger and the lab guys, etc, etc. The time we spent together will stay with me forever.

---

*This project is part of a Marie Curie ITN funded by the European Union Seventh Framework Programme (FP7 /2007–2013) under grant agreement n°264448.

The great work we did in this project would not have been possible without the support of the Analytical Lab and its members, Willi, Helmut, Andrea and Daniele. I thank them all immensely.

I would like to thank all the non-Holcim people for their support during my studies. I thank Lund University, especially Prof. Lars Wadsö, Mahsa and Alva for the fantastic collaboration, joint work and very fruitful discussions. This is a team I could always work with. Thanks to Wilson for showing me the importance of multidisciplinary work. Thanks to my friends at the LMC, Elise, Berta, Mo, Arnaud, Julien, Pawel, John, and Ruben for the fun moments and the cool times we spent together.

I want to thank the person who made all this possible, my dear boss and thesis co-director, Dr. Thomas Matschei. I still remember the first skype meeting we had on August 24th 2010. And I remember this day very well because this was the day my life changed, and not only for me, but for my family as well. Thomas gave me the opportunity to "change my stars" and to make my dreams come true. He has been a fantastic supervisor, a person I could always talk to. We had a lot of fun working on this project due to the mutual "fascination" we share for "this stuff". I thank Thomas infinitely, not only for being my boss, but also for being my friend.

Everything I have accomplished in my life, I owe to my family. I thank my beautiful wife Silvia for being with me in this adventure. Her support, dedication and love were my fuel throughout these years, and this would have not been possible without her. I thank my little son Guillermo, for being my inspiration, because seeing him grow up was all I needed to keep myself motivated. I thank my mom Dionnes, my dad at earth Raúl, my dad at heaven Guillermo, my sister Dionnes María, my grandma Liduina and all my relatives in Ecuador, who were always "pushing" me towards new challenges and experiences. The support of my parents, first during my Master and then during my PhD was crucial to achieve this. Thanks a lot to my cousin Paolo and his family for all the great moments we spent together in Spain.

Todo lo que he conseguido en mi vida se lo debo a mi familia. Agradezco mucho a mi esposa Silvia por estar conmigo durante esta aventura. Su apoyo, dedicación y amor fueron mi combustible a lo largo de estos años, y este logro no habría sido posible sin ella. A mi querido hijo Guillermo, por ser mi fuente de inspiración, porque el verlo crecer fue lo único que necesité para sentirme motivado. Agradezco a mi madre Dionnes, a mi padre Raúl y a mi hermana Dionnes María, ya que su apoyo primero durante mi masterado y luego durante mi doctorado, fue crucial para alcanzar esta meta. También a mi abuelita Liduina y a mi padre Guillermo que desde el cielo siempre estuvieron a mi lado, y a toda mi familia en Ecuador que siempre me "empujaron" hacia nuevos desafíos y experiencias. Muchas gracias a mi primo Paolo y a su familia por todos los grandes momentos que pasamos juntos en España.

I would also like to thank all the new friends we made in these "strange lands", for their friendship and for the great experiences we share together.

And finally I would like to thank my examiners, Dr. Dmitri Kulik, Prof. Herbert Pöllmann, and Prof. Guillaume Renaudin, for critically reviewing this work.

I dedicate this work to my family, to my colleagues and to my friends.

Holderbank, January 27, 2015 Luis G. Baquerizo Ibarra

Abstract

Cement hydrates and their chemically bound water content are sensitive to changes in relative humidity (RH) and temperature. This may cause specific solid volume changes affecting dimensional properties of hydrated cement paste such as shrinkage, swelling and expansion, and therefore impact the performance and the transport properties of cementitious materials.

The present thesis studies the impact of drying conditions on the structure and thermodynamic properties of crystalline cement hydrates in different hydration states (i.e. varying molar water contents). The cement hydrates studied include the most important AFm and AFt phases present in different types of cements.

A novel multi method approach, including XRD, TGA, DSC, sorption balance measurements, sorption calorimetry and the hydrate pair – humidity buffer method, was used to derive physico-chemical boundary conditions and the thermodynamic properties of the studied hydrated phases. The stability and hydration states of AFm phases depend on the anion content and the exposure conditions. Some phases such as monosulfoaluminate and hydroxy-AFm are very sensitive to different relative humidities. On the other hand monocarboaluminate and strätlingite present very good volume stability with varying RH. Ettringite shows a strong hysteresis during desorption/adsorption, and the thermodynamic properties associated with its decomposition and reformation were determined.

The experimental results were included into a thermodynamic model capable of predicting the response of cementitious systems considering the “true” crystal water content on the final phase assemblage in two different scenarios: i) during hydration, even at conditions where the amount of water added was insufficient for complete hydration, and ii) during drying and re-wetting processes in already hydrated systems.

Our work hence opens the possibility to model the response of various cement materials exposed to different climatic conditions and to engineer cementitious systems with respect to minimizing volume changes in the course of drying, which may positively impact properties like drying shrinkage and total porosity.

Keywords

Cement hydrates, AFm phases, AFt phases, hydration states, thermodynamic modelling, relative humidity, characterization techniques.

Résumé

Les produits de l'hydratation du ciment ont un contenu en eau chimiquement liée qui est fonction de l'humidité relative et de la température ambiante. En conséquence, leur volume massique varie et cela affecte les propriétés dimensionnelles des pâtes de ciment. Des phénomènes de retrait, gonflement et expansion peuvent ainsi altérer les performances et les propriétés de transport des matériaux cimentaires.

Cette thèse étudie l'impact des conditions de séchage sur la structure et les propriétés thermodynamiques des hydrates cimentaires cristallins à différents d'état d'hydratation, ou en d'autres termes pour des contenus molaires en eau différents. La majorité des hydrates cimentaires issus de l'hydratation des ciments, notamment les phases AFt et AFm, ont ainsi été étudiés.

Une approche holistique novatrice incluant la diffraction des rayons X, la thermogravimétrie, la calorimétrie différentielle à balayage, les isothermes de sorption-désorption, la calorimétrie de sorption et une méthode novatrice d'étude des pairs d'hydrates et de leur humidité relative à l'équilibre, a été utilisée afin de dériver les conditions aux limites physico-chimiques ainsi que les constantes thermodynamiques de chaque hydrate cimentaire étudié. La stabilité et l'état d'hydratation des phases AFm dépend de leur teneur anionique ainsi qu'aux conditions d'exposition. Certaines phases telles que le monosulfoaluminate ou hydroxy-AFm sont très sensibles aux conditions de séchage. Au contraire, le monocarboaluminate ou la strätlingite ont une bonne stabilité volumique. La phase ettringite présente un comportement hystérétique entre la sorption et la désorption et les propriétés thermodynamiques associées à sa décomposition et à a sa reformation ont été déterminées.

Les résultats expérimentaux ont été inclus dans un model thermodynamique capable de prédire le comportement de systèmes cimentaires en considérant leur teneur "réelle" en eau chimiquement liée sur l'assemblage final de phases pour deux scénarios distincts: i) pendant l'hydratation, en considérant aussi des conditions pour lesquelles l'hydratation complète n'est pas réalisée, et ii) lors des phases de séchage et de réhumidification pour des systèmes initialement hydratés.

Ce travail ouvre la possibilité de modéliser le comportement de nombreux matériaux cimentaires exposés sous différentes compositions atmosphériques et ainsi de concevoir des matériaux cimentaires dont les variations dimensionnelles au cours du séchage sont optimisées et en optimisant des propriétés telles que le retrait de séchage ou la porosité totale.

Mots-clés

Hydrates cimentaires, phases AFm, phases AFt, état d'hydratation, modélisation thermodynamique, humidité relative, méthode de caractérisation.

Resumen

Los hidratos de cemento y su contenido de agua son sensibles a cambios en la humedad relativa y temperatura. Esto puede causar cambios de volumen que afectan a las propiedades dimensionales del cemento hidratado, tales como la contracción y la expansión, y por lo tanto afectar el rendimiento y la movilidad de agua en materiales cementicios.

La presente tesis estudia el impacto de las condiciones de secado sobre la estructura y las propiedades termodinámicas de hidratos de cemento cristalinos en diferentes estados de hidratación (es decir, diferentes contenidos molares de agua). Los hidratos de cemento estudiados en este trabajo incluyen a las fases del tipo AFm y AFt más importantes presentes en diferentes tipos de cementos.

Una nueva metodología, la cual incluye XRD, TGA, DSC, balanza de sorción, calorimetría de sorción y el método de pares de hidratos – regulador de humedad, fue utilizada para derivar las condiciones físico-químicas de equilibrio y las propiedades termodinámicas de las fases hidratadas estudiadas. La estabilidad y los estados de hidratación en las fases AFm dependen del contenido de aniones y de las condiciones de exposición. Algunas fases tales como el monosulfoaluminato y el hidroxi-AFm son muy sensibles a cambios en la humedad relativa. Por otro lado, el monocarboaluminato y la estratlingita presentan muy buena estabilidad volumétrica en función de la humedad relativa. Etringita muestra una fuerte histéresis durante la desorción/adsorción, y las propiedades termodinámicas asociadas con su descomposición y reformación se determinaron en esta tesis.

Los resultados experimentales se incluyeron en un modelo termodinámico capaz de predecir la respuesta de diferentes sistemas cementicios considerando el "verdadero" contenido de agua cristalina en el sistema hidratado en dos escenarios diferentes: i) durante la hidratación, incluso en condiciones en las que el agua añadida era insuficiente para hidratar completamente la muestra, y ii) durante el secado y re-hidratación en sistemas previamente hidratados.

Nuestro trabajo abre la posibilidad de modelar la respuesta de diversos materiales cementicios expuestos a diferentes condiciones climáticas y de diseñar sistemas volumétricamente más estables durante condiciones de secado, lo cual puede afectar positivamente las propiedades como la contracción por secado y la porosidad total.

Palabras clave

Hidratos de cemento, fases AFm, fases AFt, estados de hidratación, modelización termodinámica, humedad relativa, métodos de caracterización.

Contents

Acknowledgement iii

Abstract v

Résumé vii

Resumen ix

Glossary xv

List of Figures xix

List of Tables xxiii

1 Introduction 1

1.1 Objectives of the thesis 2

1.2 Layout of the thesis 2

2 Thermodynamic approach 5

2.1 Thermodynamic equations 5

2.2 Estimation of heat capacity 6

2.3 Software and standard database 7

2.4 Solid solutions 7

2.5 References 8

3 Methods to determine hydration states of minerals and cement hydrates 11

3.1 Introduction 11

3.1.1 General 11

3.1.2 Hydration states of crystalline cement hydrates 12

3.1.3 Scope of this chapter 12

3.2 Materials and sample preparation 13

3.3 Experimental methods and analysis 14
3.3.1 X-Ray Diffraction (XRD) 14
3.3.2 Thermogravimetric analysis (TGA) 15
3.3.3 Hydrate pair - humidity buffer method 15
3.3.4 Sorption balance 16
3.3.5 Sorption calorimetry 17
3.4 Results 18
3.4.1 Validation 18
3.4.2 Results of monosulfoaluminate measurements 23
3.5 Discussion 30
3.5.1 Correlation between the methods and accuracy 30
3.5.2 Interactions between Na_2SO_4 and water vapor 31
3.5.3 Interactions between LDH-type cement hydrates and water vapor 31
3.6 References 32

4 Hydration states of AFm phases 37
4.1 Introduction 37
4.1.1 Monosulfoaluminate (Ms) 38
4.1.2 Hydroxy–AFm (OH-AFm) 38
4.1.3 Monocarboaluminate (Mc) 38
4.1.4 Hemicarboaluminate (Hc) 39
4.1.5 Strätlingite (Str) 39
4.1.6 Relevance of this study 40
4.2 Experimental methods 40
4.3 Results and discussion 40
4.3.1 Monocarboaluminate 41
4.3.2 Hemicarboaluminate 43
4.3.3 Strätlingite 48
4.3.4 Hydroxy-AFm 51
4.3.5 Monosulfoaluminate 55
4.3.6 Summary of results 57
4.4 Discussion and implications on volume stability of cement paste 59
4.5 References 62

5 Impact of water activity on the stability of ettringite 65

5.1 Introduction 65

5.2 Experimental procedure 67

5.2.1 Preparation of ettringite 67

5.2.2 Experimental methods 67

5.3 Results 67

5.3.1 XRD and TGA 67

5.3.2 Sorption balance 71

5.3.3 Calorimetry tests 72

5.3.4 Density measurements 77

5.4 Thermodynamic modelling 78

5.4.1 Thermodynamic modelling of hysteresis loops 78

5.4.2 Decomposition and reformation modelling of ettringite vs metaettringite 79

5.4.3 Determination of the theoretical decomposition/reformation behaviour with no hysteresis 82

5.4.4 The impact of water activity on the stability of ettringite 83

5.5 Discussion 85

5.6 References 86

6 Thermodynamic modelling of the water content of cementitious systems 89

6.1 Introduction 89

6.2 Materials and methods 90

6.3 Experimental results on C_3A and CA 90

6.4 Stability of AFm phases as function of RH and temperature 94

6.4.1 Monosulfoaluminate 94

6.4.2 Monocarboaluminate 96

6.4.3 Hemicarboaluminate 96

6.4.4 Hydroxy-AFm 97

6.4.5 Strätlingite 98

6.4.6 Remarks on AFm phases 99

6.5 Thermodynamic modelling of the hydration of C_3A and CA in the presence of calcium hydroxide, calcium carbonate and calcium sulfate 99

6.5.1 The C_3A subsystem 100

6.5.2 The CA subsystem 107

6.6 Applied thermodynamic modelling to assess the drying behaviour of hydrated cementitious systems 112

6.6.1 Subsystem relevant to OPC and limestone blended cements 112

6.6.2 Subsystem relevant to calcium aluminate cements 114

6.6.3 Remarks on the drying behaviour of hydrated systems 115

6.7 Discussions 115

6.8 References 116

7 Conclusions 121

7.1 Main results obtained 121

7.2 Remarks and future development 122

Annexes 125

A. TGA measurements 126

B. N_2 – sorption isotherms 130

C. Thermodynamic properties 131

D. References Annexes 133

Curriculum Vitae 135

Glossary

Oxide notation

- A: Al_2O_3
- C: CaO
- S: SiO_2
- Ŝ: SO_3
- Ĉ: CO_2
- F: Fe_2O_3
- H: H_2O

Clinker and cement phases

- C_3A: tricalcium aluminate
- CA: monocalcium aluminate
- C_3S: tricalcium silicate
- C_2S: dicalcium silicate
- C_4AF: ferrite
- CĈ : calcite
- CŜ : anhydrite
- $C\hat{S}H_2$: gypsum
- CH : Portlandite

Cements and additions

- CAC : calcium aluminate cement
- CSA : calcium sulfoaluminate cement
- PC : Portland Cement
- SCMs : Supplementary Cementitious Materials

Cement hydrates

Numeric index can be added to the abbreviation to denote the water content of the phase.

- Ms : monosulfoaluminate
- Mc : monocarboaluminate

- Hc : hemicarboaluminate
- Str : strätlingite
- OH-AFm : hydroxy-AFm
- Ett : ettringite

Techniques

- XRD : X-ray diffraction
- TGA : thermogravimetry analysis
- DSC : differential scanning calorimetry
- DVS : dynamic vapour sorption
- DTG : derivative thermogravimetry
- SEM : scanning electron microscopy
- NMR Nuclear Magnetic Resonance
- BET: Brunauer Emmet Teller (theory for specific surface measurements)

Thermodynamic terms

- GEMS: Gibbs energy minimization software
- C_p° standard molar heat capacity of species at T, P (J/K mol)
- ΔC_p° standard molar heat capacity change of reaction (J/K mol)
- $\Delta G_r°$: standard molar Gibbs free energy of reaction (kJ/mol)
- $\Delta H_r°$: standard molar enthalpy of reaction (kJ/mol)
- $\Delta S_r°$: standard molar entropy of reaction (J/K mol)
- $\Delta G_f°$: standard molar Gibbs free energy of formation (kJ/mol)
- $\Delta H_f°$: standard molar enthalpy of formation (kJ/mol)
- $S°$: standard molar entropy (J/K mol)
- $\Delta H_{sorp}°$: standard molar enthalpy of sorption (kJ/mol)
- $\Delta H_{cond}°$: standard molar enthalpy of condensation of water at 25 °C and 1 bar (-44 kJ/mol)
- $\Delta H_{vap}°$: standard molar enthalpy of evaporation of water at 25 °C and 1 bar (44 kJ/mol)
- $\Delta H_{mix}°$: standard molar enthalpy of mixing (kJ/mol)
- R: universal gas constant (8.31451 J/K mol)

- P_{vap}: thermal power of evaporation.
- P_{sorp}: thermal power of sorption.
- $V°$: standard molar volume.
- °: standard thermodynamic property at 298 K and 1 bar.

Others

- Eq.: equation
- wt.%: weight percent
- vol.%: volume percent
- t.s. : this study
- w/s : water to solid weight-ratio
- DOH: degree of hydration
- PSI : Paul Scherrer Institute

List of Figures

Figure 1:1 Relative volumes of the cement phases and hydration products in the microstructure of a Portland cement type I 1

Figure 3:1 Anton Paar Cryo & Humidity Chamber: CHC plus+. 15

Figure 3:2 a) RH/T phase diagram of the system A - H_2O. b) Set-up of the hydrate pair – humidity buffer method. 16

Figure 3:3 a) Photo of the DVS Advantage machine used in this study. b) Schematic picture of the sorption balance operation. 17

Figure 3:4 a) Photo of the twin isothermal calorimetry used (Lund University). b) Schematic graphic of the sorption ampoule. 18

Figure 3:5 RH/T phase diagram of the system Na_2SO_4 + H_2O at 1 bar 19

Figure 3:6 Van't Hoff plot of our experimental results at different temperatures for reaction 20

Figure 3:7 a) RH step-wised program for the sorption balance. b) Mass change of sample. (c) dm/dt of sample. 21

Figure 3:8 Calculated RH of deliquescence of Na_2SO_4 21

Figure 3:9 The results of two measurements on thenardite with sorption calorimetry. 22

Figure 3:10 SEM picture of monosulfoaluminate. 23

Figure 3:11 a) XRD patterns and b) refined lattice parameter and volume of the lattice of monosulfoaluminate 24

Figure 3:12 TGA of monosulfoaluminate dried at different conditions at 25°C. 24

Figure 3:13 a) Ms10.5-Ms12 equilibria at 1 bar. b) Van't Hoff plot for Ms10.5-Ms12 equilibria. 26

Figure 3:14 Sorption isotherm of monosulfoaluminate at 25 °C. 27

Figure 3:15 Sorption calorimetry results on initially vacuum dried monosulfoaluminate at 25 °C. 27

Figure 3:16 a) Volume changes of monosulfoaluminate vs RH and related enthalpies of reaction at 25°C. b) Swelling of a compacted monosulfoaluminate sample 29

Figure 4:1 Schematic figure of the lamellar structure of an AFm phase. 37

Figure 4:2 SEM pictures of monocarboaluminate. 41

Figure 4:3 XRD patterns of some Mc samples dried at different conditions. 41

Figure 4:4 Refined lattice parameters of Mc dried at 5, 25 and 50 °C and different RHs during 12-24 months. 42

Figure 4:5 Water content of monocarboaluminate as function of RH at 25 °C measured by sorption balance. 42

Figure 4:6 Sorption calorimetry results showing the calculated sorption isotherm (left) and mixing enthalpy (right) of dry monocarboaluminate at 25°C 43

Figure 4:7 SEM pictures of hemicarboaluminate 44

Figure 4:8 XRD patterns of hemicarboaluminate 44

Figure 4:9 Refined lattice parameters of Hc dried at 5, 25 and 50 °C. 45

Figure 4:10 XRD patterns of a sample initially containing cHc, hydrogarnet (C_3AH_6) and portlandite (CH), and subsequently exposed to high RH at 5 and 50 °C. 46

Figure 4:11 Sorption isotherm of hemicarboaluminate at 25 °C measured by the sorption balance method. 46

Figure 4:12 Calculated sorption isotherm (left) and mixing enthalpy (right) of initially dry hemicarboaluminate at 25°C from sorption calorimetry testing. 47

Figure 4:13 a) SEM pictures of strätlingite. b) XRD pattern of a strätlingite sample 48

Figure 4:14 XRD patterns of strätlingite dried at 25 °C and different RHs 49

Figure 4:15 Refined lattice parameters at 5 °C, 25 °C and 50 °C 49

Figure 4:16 Sorption isotherm of strätlingite at 25 °C measured by sorption balance. 49

Figure 4:17 Calculated sorption isotherm (left) and measured mixing enthalpy (right) of initially dry strätlingite at 25 °C by sorption calorimetry. 50

Figure 4:18 Summary graph showing water content and volume of the lattice of strätlingite as a function of RH at different temperatures. 51

Figure 4:19 SEM pictures of hydroxy-AFm. 51

Figure 4:20 XRD patterns of OH-AFm dried at a) 5 °C and b) 25 °C. c) Refined lattice parameter a and c and volume V of samples dried at 5 and 25 °C. 52

Figure 4:21 Sorption isotherm measured on OH-AFm by sorption balance at 25 °C. 53

Figure 4:22 Calculated sorption isotherm (left) and mixing enthalpy (right) of initially dry OH-AFm at 25 °C by sorption calorimetry. 54

Figure 4:23 OH-AFm10 – OH-AFm13 and OH-AFm13 – OH-AFm11 equilibria at 1 bar measured with the hydrate pair – humidity buffer method. 54

Figure 4:24 XRD patterns of monosulfoaluminate tested in situ using a humidity chamber at 5 °C. ... 56

Figure 4:25 XRD patterns of monosulfoaluminate tested in situ using a humidity chamber at 92% RH from 5 °C to 18 °C. 56

Figure 4:26 Approximate stability regions of Ms16 and Ms12 < 20 °C. 57

Figure 4:27 Summary graph showing the different hydration states as function of RH at 25 °C. 58

Figure 4:28 Volume changes of the AFm phases studied as function of RH at 25 °C. 61

Figure 5:1 XRD patterns of ettringite samples dried at a) 25 °C, b) 50 °C and b) 80 °C. 69

Figure 5:2 Refined lattice parameters of samples aged at all temperatures studied. 69

Figure 5:3 TGA water content of samples aged at different temperatures and RHs inside hermetic glass bottles....... 70

Figure 5:4 XRD patterns of ettringite tested in situ using a humidity chamber in absorption....... 70

Figure 5:5 Sorption balance test carried out on two ettringite samples....... 71

Figure 5:6 Calculated sorption isotherm at 25°C (left) and enthalpy of mixing (right) of vacuum dry ettringite at 25°C during sorption calorimetry testing 73

Figure 5:7 Isothermal calorimetry measurements of initially vacuum dried ettringite samples....... 74

Figure 5:8 DSC measurements on Ett31 at a) 60 °C and b) 65 °C. 75

Figure 5:9 Density of the different hydration states of ettringite as function of water content n. 78

Figure 5:10 Decomposition a) RH and b) PH2O as function of temperature....... 81

Figure 5:11 Reformation a) RH and b) PH2O as function of temperature....... 81

Figure 5:12 Van't Hoff plots of the decomposition and reformation processes 83

Figure 5:13 a) RH and b) PH_2O as function of temperature showing the zones of reformation and decomposition of ettringite. 84

Figure 5:14 Predicted RH vs temperature phase diagram during drying of ettringite in equilibrium with other cement hydrates. 85

Figure 6:1 Measured RH using the hydrate pair-humidity buffer method on C_3A mixed with small amounts of water (w/s ~ 0.05)....... 92

Figure 6:2 Test4: Measured RH using the hydrate pair-humidity buffer method on CA mixed with small amounts of water (w/s ~ 0.05)....... 92

Figure 6:3 TGA patterns of the C_3A and CA experiments (test 1 and 4 from Figure 6:1 and Figure 6:2). 93

Figure 6:4 Experimental points (filled dots) used to calculate the thermodynamic properties of C_3A_hyd and CA_hyd shown in Table 6:1. 93

Figure 6:5 Predicted stability of monosulfoaluminate as function of RH and temperature at 1 bar....... 95

Figure 6:6 Predicted stability of monocarboaluminate as function of RH and temperature at 1 bar....... 96

Figure 6:7 Predicted stability of hemicarboaluminate as function of RH and temperature at 1 bar....... 97

Figure 6:8 Predicted stability of hydroxy-AFm as function of RH and temperature at 1 bar 98

Figure 6:9 Predicted stability of strätlingite as function of RH and temperature at 1 bar. 99

Figure 6:10 Calculated ternary phase diagram C_3A-CH-H_2O at a) 25 °C and b) 5 °C....... 101

Figure 6:11 Calculated ternary phase diagram C_3A-$CaCO_3$-H_2O at 25 °C and 1 bar. 102

Figure 6:12 Calculated ternary phase diagram C_3A-$CaCO_3$-H_2O at 25 °C and 1 bar in portlandite (CH) saturated conditions. 103

Figure 6:13 Calculated ternary phase diagram C_3A-$CaSO_4$-H_2O at 25 °C and 1 bar. Points V1 and V2 are two validation tests 105

Figure 6:14 Measured RH using the hydrate pair – humidity buffer method on two validation tests, denoted as V1 and V2 in Figure 6:13 (the former was done twice) 105

Figure 6:15 Predicted and measured phase assemblage and RH of the validation points a) V1 and b) V2 shown in Figure 6:13. 106

Figure 6:16 Calculated ternary phase diagram C_3A-$CaSO_4$-H_2O, saturated with respect to $CaCO_3$, at 25 °C and 1 bar. 107

Figure 6:17 Calculated ternary phase diagram CA-CH-H_2O at a) 25 °C and b) 5 °C. 108

Figure 6:18 Calculated ternary phase diagram CA-CH-H_2O at 5 °C and 1 bar, suppressing the formation of C_3AH_6. 109

Figure 6:19 Calculated ternary phase diagram CA-$CaCO_3$-H_2O at 25 °C and 1 bar. 110

Figure 6:20 Calculated ternary phase diagram CA-$CaSO_4$-H_2O at 25 °C and 1 bar. 111

Figure 6:21 Calculated ternary phase diagram CA-$CaSO_4$-H_2O, saturated with respect to $CaCO_3$, at 25 °C and 1 bar. 112

Figure 6:22 Calculated specific volume changes of a hydrated model mixture 113

Figure 6:23 Calculated volume phase assemblages with respect to changes in RH at 25°C 113

Figure 6:24 Calculated specific volume changes of a hydrated model mixture 114

Figure 6:25 Calculated volume phase assemblages with respect to changes in RH at 25°C 114

Figure A:1 TGA and DTG patters of monocarboaluminate dried at different conditions at 25 °C 126

Figure A:2 TGA and DTG patters of hemicarboaluminate dried at different conditions. 127

Figure A:3 TGA and DTG patters of strätlingite dried at 25 °C. 127

Figure A:4 TGA and DTG patters of hydroxy- AFm dried at different conditions. 128

Figure A:5 TGA and DTG patters of ettringite dried at 25 °C. 128

Figure A:6 TGA and DTG patters of ettringite dried at 50 °C. 129

Figure A:7 TGA and DTG patters of ettringite stored at 80 °C under drying and rewetting conditions. 129

Figure B:1 N_2 – isotherm measured using ASAP™ 2020 (Micromeritics) on Ms, Mc, Hc and Ett 130

Figure B:2 N_2 – isotherm measured using ASAP™ 2020 (Micromeritics) on Str and synthetic C-S-H (Ca/Si = 0.66). 130

List of Tables

Table 2:1 Reference phases and reactions used to calculate the heat capacities of Ms14 and Ms16. ... 6

Table 3:1 Most important AFm and AFt phases and reported water content. ... 12

Table 3:2 Equilibrium RH of selected saturated salt solutions at different temperatures. ... 14

Table 3:3 Derived Thermodynamic data for reaction (3.1) at 25 °C and 1 bar ... 20

Table 3:4 Derived thermodynamic data for the changes of hydration states of monosulfoaluminate at 25 °C and 1 bar. ... 30

Table 3:5 Molar volume and density of monosulfoaluminate hydration states. ... 30

Table 4:1 Derived thermodynamic data for the changes of hydration states of AFm phases at 25 °C and 1 bar. ... 59

Table 4:2 Standard molar thermodynamic properties of the studied cement hydrates at 25 °C and 1 bar. ... 60

Table 5:1 Molar volume and density of monosulfoaluminate hydration states. ... 73

Table 5:2 Enthalpy of mixing values during absorption. ... 76

Table 5:3 Enthalpy of dehydration and rehydration reported by Struble and Brown. ... 77

Table 5:4 Standard molar thermodynamic properties of the ettringite and metaettringite hydrates at 25 °C and 1 bar ... 82

Table 6:1 Empirical standard molar thermodynamic properties of bulk and hydroxylated C_3A and CA at 25 °C and 1 bar. ... 94

Table C:1 Standard molar thermodynamic properties of clinker phases and other cement phases at 25 °C and 1 bar. ... 131

Table C:2 Standard molar thermodynamic properties of the studied cement hydrates at 25 °C and 1 bar. ... 132

1 Introduction

It is generally accepted that concrete deformations due to shrinkage, swelling, expansion and/or creep strongly depend on the constitution of the internal microstructure, the related porosity and the exposure conditions. On the other hand, an often neglected phenomenon is the sensitivity of individual cement hydrates and their water content to changes in relative humidity (RH) and temperature, which may cause specific solid volume changes that in turn may also impact microstructural features.

Varying hydration states, i.e. water content of C-S-H, AFm and AFt phases may have a direct impact on the specific density/volume of cement paste, e.g. the volume of some hydrates can change as much as 20% during drying and strongly affect the porosity and performance of a cementitious system.

As shown in Figure 1:1, a PC paste is composed of different hydrate phases, each of which contributes differently to the total specific solid volume. C-S-H is the most abundant hydrate as it fills about 50% to 60% of the total solid volume. On the other hand, hydrated calcium aluminate and –ferrite phases, i.e. AFm and AFt containing significant amounts of sulfate and/or carbonate, also occupy a significant fraction of the solid volume. It is well known that C-S-H, AFm and AFt phases are sensitive to drying, as their specific chemical or structural bound water fraction is relatively high. Due to thermodynamic driving forces, the above mentioned phases tend to lose water if dried, i.e. they change their chemically bound water fraction, or if re-wetted, they will uptake water until in equilibrium with the surrounding water vapor pressure of the considered chemical system.

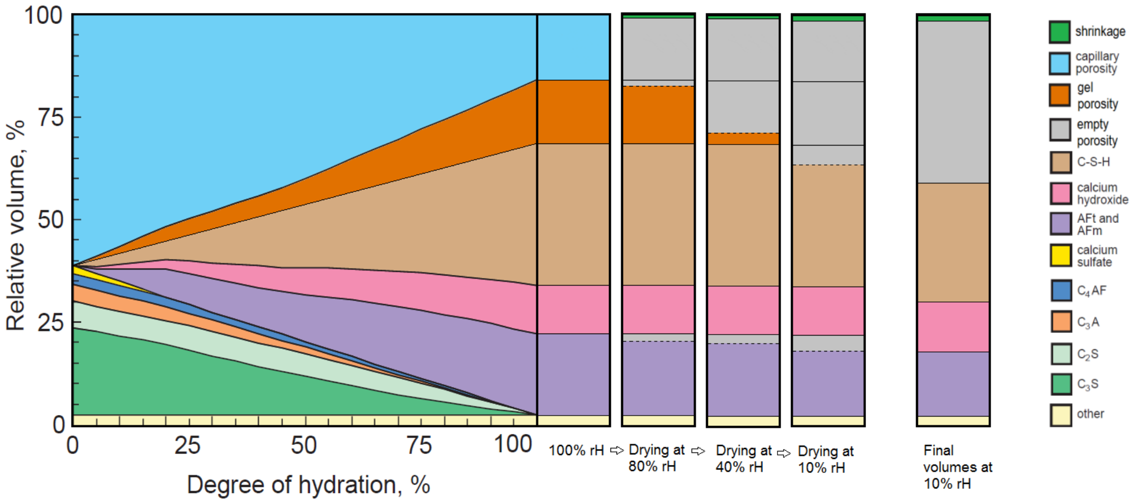

Figure 1:1 Relative volumes of the cement phases and hydration products in the microstructure of a Portland cement type I with a w/s of 0.5 according to Tennis and Jennings [1] (adapted from [2]) and changes of solid volumes and porosity after drying at 80%, 40% and 10% RH (the volume changes are just an approximation).

Although C-S-H is the main hydration product of PC based systems, in alternative cementitious binders such as calcium sulfoaluminate cements and calcium aluminate cement blended systems, the proportion of AFm and AFt phases is rather large, reaching up to 80 vol.% of the hydrated paste.

There are numerous studies on the shrinkage behaviour, changes of mechanical properties, volume and mass variations in cement pastes as function of RH and temperature, but a systematic study summarizing the hydration states of individual hydrates and the related exposure conditions is still not available.

1.1 Objectives of the thesis

The purpose of this work is to develop a thermodynamic model capable of assessing the impact of water activity and temperature on the stability of cementitious systems. The objectives are summarized as follows:

- Experimental investigation of the hydration states of cement hydrates as function of RH and temperature) and determination of their thermodynamic properties.
  - Study limited to AFm and AFt phases

- Derivation of a thermodynamic model to predict:
  - the hydrate phase assemblage of cementitious systems hydrated with less water than required to achieve 100% degree of hydration (DOH), i.e. in equilibrium with unreacted clinker phases.
  - the drying behaviour of cementitious systems at RH < 100% as function of temperature.

The model developed in this work can be used as a tool to potentially optimize cementitious systems with respect to minimizing relative volume changes in the course of drying, which may positively impact properties like drying shrinkage and total porosity.

1.2 Layout of the thesis

The chapters shown in this thesis contain results presented in peer reviewed papers published or already submitted.

In Chapter 2, the thermodynamic equations used in this thesis are presented.

Chapter 3 presents the multi-method approach developed to investigate the impact of varying relative humidity (RH) and temperature on the structure and thermodynamic properties of salts and crystalline cement hydrates in different hydration states (i.e. varying molar water contents). With this methodology the physico-chemical boundary conditions and the thermodynamic properties of hydrated phases can be determined. The materials and sample preparation of clinker and hydrated phases are also presented in this chapter.

Chapter 4 reports the experimental results on the different hydration states of the most important AFm phases: monocarboaluminate, hemicarboaluminate, strätlingite, hydroxy-AFm and monosulfoaluminate, and the thermodynamic properties associated with changes in their water content during absorption/desorption.

In **Chapter 5** the stability of ettringite as function of temperature and water vapour pressure was studied on synthetic samples. Thermodynamic modelling of the drying/rewetting behaviour is also given in this chapter.

Chapter 6 presents the thermodynamic model developed in this work. The model was used to study the stability of AFm and AFt phases, and more complex cementitious systems.

Chapter 7 summarizes the most important findings, the novelty and the limitations of this work. Also recommendations and perspectives for future work are given.

References

[1]. P.D. Tennis, H.M. Jennings, A model for two types of calcium silicate hydrate in the microstructure of Portland cement pastes, Cem. Concr. Res. 30, 2000, 855-863.

[2]. Design and Control of Concrete Mixtures, 15th Edition, Portland Cement Association, 2011.

2 Thermodynamic approach

2.1 Thermodynamic equations

Changes of hydration states considered in this study follow the reference reaction (2.1):

$$\mathrm{A \cdot xH_2O(s)} \; + (\mathrm{y} - \mathrm{x})\mathrm{H_2O(g)} \leftrightarrow \mathrm{A \cdot y\, H_2O(s)} \qquad (2.1)$$

where s and g are solid and gas, respectively, A is a hydrate containing x or y water molecules, where x ≥ 0 and y > x. The Gibbs free energy of reaction (2.1) is given by:

$$\Delta G_r^o = -RT\ln K = -RT\ln\frac{a(\mathrm{A{\cdot}yH_2O})}{a(\mathrm{A{\cdot}xH_2O})\;a(\mathrm{H_2O})^{\mathrm{y-x}}}$$

By assuming that the activity of all solids equals 1.0,

$$\Delta G_\mathrm{r}^o = -RT\ln[a(\mathrm{H_2O})^{\mathrm{x-y}}] = (\mathrm{y-x})RT\ln[f(\mathrm{H_2O})] = (\mathrm{y-x})RT\ln\frac{f^*(\mathrm{H_2O})RH}{100} \qquad (2.2)$$

where ΔG_r° is the standard Gibbs free energy of the reaction (2.1), T is the absolute temperature, K is the equilibrium constant, R is the gas constant (8.31451 J/K mol), $a(H_2O)$ is the activity of H_2O vapour, $f(H_2O)$ is the equilibrium fugacity, $f^*(H_2O)$ is the fugacity of pure H_2O at T and RH is the equilibrium relative humidity in percent [1]-[3]. The standard enthalpy of reaction ΔH_r° can be calculated with the van't Hoff equation:

$$\frac{\partial(\ln K)}{\partial(1/T)} = -\frac{\Delta H_\mathrm{r}^o}{R} \qquad (2.3)$$

The standard entropy of reaction ΔS_r° can be calculated from the following equation:

$$\Delta G_\mathrm{r}^o = \Delta H_\mathrm{r}^o - T\Delta S_\mathrm{r}^o \qquad (2.4)$$

The aforementioned equations refer to a specific reaction, which can be either dehydration/decomposition or rehydration/reformation.

The enthalpy of reaction ΔH_r° can also be determined from sorption calorimetry with the following relations:

$$\Delta H_\mathrm{sorp} = \Delta H_\mathrm{cond} + \Delta H_\mathrm{mix} \qquad (2.5)$$

$$\Delta H_\mathrm{r}^o = \Delta H_\mathrm{sorp} \cdot n \qquad (2.6)$$

where ΔH_sorp is the enthalpy of sorption (enthalpy value per g or mol of H_2O absorbed), ΔH_cond is the enthalpy of condensation of water at 25 °C (-2440 J/g H_2O or -44 kJ/mol H_2O), ΔH_mix is the mixing enthalpy (output of the sorption calorimetry test), and n is the number of ad/ab-sorbed water molecules during a change of hydration state (equal to y-x from reaction (2.1)). In this work the mixing enthalpy represents an “excess enthalpy” indicating how much additional heat is obtained from a sorption process compared to condensation of water and it is not related to the formation of solid solutions.

2.2 Estimation of heat capacity

The heat capacity of solids was calculated according to Eq. (2.7):

$$C_p^o = a_0 + a_1 T + a_2 T^{-2} + a_3 T^{-0.5} \tag{2.7}$$

where a_0, a_1, a_2 and a_3 are empirical coefficients characteristic of each solid phase. For the reference reaction (2.8), these coefficients were calculated according to Eq. (2.9):

$$\mathrm{A} \rightarrow \mathrm{yB} + \mathrm{zC} \tag{2.8}$$

$$a_{n,A} = y \cdot a_{n,B} + z \cdot a_{n,C} \tag{2.9}$$

The reactions shown in Table 2:1, involving solids having a known heat capacity and similar structure [4]-[5], were used to calculate the coefficients and the heat capacities of Ms16 and Ms14.

Table 2:1 Reference phases and reactions used to calculate the heat capacities of Ms14 and Ms16.

Phase	Reference reaction	a_0	a_1	a_2	a_3	C_p (J/mol K)	Ref.
$C\hat{S}$		70	0.099	0	0	99.6	[6]
$C\hat{S}H_2$		91	0.318	0	0	186.2	[6]
$C_4A\hat{S}H_{12}$ (Ms12)		594	1.168	0	0	942.2	[7]
$C_4A\hat{S}H_{14}$ (Ms14)	$C_4A\hat{S}H_{14} + C\hat{S} \rightarrow C_4A\hat{S}H_{12} + C\hat{S}H_2$	615	1.387	0	0	1028.5	t.s.
$C_4A\hat{S}H_{16}$ (Ms16)	$C_4A\hat{S}H_{16} + 2C\hat{S} \rightarrow C_4A\hat{S}H_{12} + 2C\hat{S}H_2$	636	1.606	0	0	1114.8	t.s.

t.s.: this study

For the calculation of heat capacities of the lower hydration states, it was assumed that the change of heat capacity ($\Delta C_p°$) was zero within the range of temperatures studied (0 to 100 °C) at 1 bar. Then, Eq. (2.11) can be used to calculate the C_p of any hydration state, knowing the heat capacities of the higher hydration state and of H_2O (gas) involved in the reaction. Although this assumption is not completely correct, the heat capacity effects of a particular desorption/absorption process is relatively small within the range of temperatures studied and do not affect considerably the modelled behaviour shown in Chapters 5 and 6.

$$\Delta C_{\mathrm{p}}^{o} = \Sigma C_{\mathrm{p\,products}}^{o} - \Sigma C_{\mathrm{p\,reactants}}^{o} \tag{2.10}$$

$$\Sigma C_{\mathrm{p\,products}}^{\mathrm{o}} = \Sigma C_{\mathrm{p\,reactants}}^{\mathrm{o}} \tag{2.11}$$

2.3 Software and standard database

The thermodynamic properties of the different hydration states were calculated as follow: the Gibbs free energy of reaction ($\Delta G_{\mathrm{r}}°$) from Eq. (2.2), the enthalpy of reaction ($\Delta H_{\mathrm{r}}°$) directly measured by the sorption calorimetry (see Chapter 3), and finally the entropy of reaction ($\Delta S_{\mathrm{r}}°$) from Eq. (2.4). If calorimetry data was not available, ΔHr° was calculated with Eq. (2.3) (van't Hoff equation) using the hydrate pair – humidity buffer method (see Chapter 3).

The thermodynamic properties were introduced into the project database in GEM-Selektor [8]-[9], a software package including a GEM (Gibbs free energy minimisation) solver [9], a built-in thermodynamic database [6] complemented with a cement database (cemdata14) [10]-[13] and a graphical user interface. This software was used to model the drying and hydration behaviour of pure phases and different cementitious systems.

In order to model the behaviour of cementitious systems in water-unsaturated conditions, a steam component must be introduced in the project database. During modelling the steam component will be incorporated into the gaseous phase and its fugacity in equilibrium conditions will be calculated. Since the fugacity at water-saturated conditions is known, the predicted equilibrium RH can be calculated as follows:

$$RH = \frac{f(\mathrm{H_2O})100}{f^{*}(\mathrm{H_2O})} \tag{2.12}$$

GEM-Selektor has been widely used to model the hydration behaviour of different cementitious systems [11]-[20]. In this work the mentioned software was used for the first time to model the phase assemblages of systems in water unsaturated conditions, i.e. in the absence of liquid water or aqueous electrolyte.

2.4 Solid solutions

In this work the occurrence of solid solutions between different phases, e.g. monosulfoaluminate and hydroxy-AFm, was not studied. Nevertheless, when a transition between higher and lower hydration states of the same phase, e.g. between Ett32 and Ett30, did not take place stepwise, an ideal binary solid solution was used to model the water content of the resulting phase. The ideal solid solution phases were directly introduced in GEM-Selektor using the in-built model for ideal mixtures. For more information about the calculation of speciation and mixing in ideal and non-ideal solid solutions, gaseous fluids and aqueous electrolytes please refer to [5],[8],[9] and the GEM-Selektor pdf documentation.

2.5 References

[1]. I.M. Chou, R.R. Seal II, B.S. Hemingway, Humidity buffers and their application to the studies of dehydration reactions of sulfate salts at 0.1 Mpa, Am. Geophys., Union Trans. 79 (1998) S364.

[2]. I.M. Chou, R.R. Seal II, B.S. Hemingway, Determination of melanterite-rozenite and chalcanthite-bonattite equilibria by humidity measurements at 0.1MPa, Am. Mineral. 87 (2002) 108-114.

[3]. I.M. Chou, R.R. Seal II, Determination of epsomite-hexahydrite equilibria by the humidity-buffer technique at 0.1MPa with implications for phase equilibria in the system $MgSO_4$-H_2O, Astrobiology 3 (2003) 619-630.

[4]. H.C. Helgeson, J.M. Delany, H.W. Nesbitt, D.K. Bird, Summary and critique of the thermodynamic properties of rock-forming minerals, American Journal of Science 278-A (1978), 229.

[5]. T. Matschei, Thermodynamics of Cement Hydration. PhD Dissertation, University of Aberdeen, 2007.

[6]. W. Hummel, U. Berner, E. Curti, F.J. Pearson, T. Thönen, Nagra/PSI Chemical Thermodynamic Data Base 01/01.Universal Publishers, Parkland, Florida, USA, 2002.

[7]. J. Ederova, V. Satava, Heat capacities of C_3AH_6, C_4ASH_{12} and $C_6A\hat{S}_3H_{32}$, Thermochimica Acta 31 (1979) 126-128.

[8]. D.A Kulik, T. Wagner, S.V Dmytrieva, G. Kosakowski, F.F. Hingerl, K.V. Chudnenko, U. Berner, (2013): GEM-Selektor geochemical modeling package: revised algorithm and GEMS3K numerical kernel for coupled simulation codes, Comput. Geosci. 17 (2013) 1-24 http://gems.web.psi.ch

[9]. T. Wagner, D.A. Kulik, F.F. Hingerl, S.V. Dmytrieva, GEM-Selektor geochemical modeling package: TSolMod library and data interface for multicomponent phase models, Canadian Mineralogist 50 (2012) 1173-1195.

[10]. Cemdata14, release date 07.05.2014 during the 4th GEMS Workshop, EMPA, Switzerland.

[11]. T. Matschei, B. Lothenbach, F. Glasser, Thermodynamic properties of Portland cement hydrates in the system CaO-Al_2O_3-SiO_2-$CaSO_4$-$CaCO_3$-H_2O, Cem. Concr. Res. 37 (2007) 1379-1410.

[12]. B. Lothenbach, T. Matschei, G. Möschner, F. Glasser, Thermodynamic modelling of the effect of temperature on the hydration and porosity of Portland cement, Cem. Concr. Res. 38 (2008) 1-18.

[13]. B. Lothenbach, L. Pelletier-Chaignat, F. Winnefeld, Stability in the system CaO–Al_2O_3–H_2O, Cem. Concr. Res. 42 (2012) 1621 – 1634.

[14]. B. Lothenbach, D. Rentsch, E. Wieland, Hydration of a silica fume blended low-alkali shotcrete cement, Physics and Chemistry of the Earth, Parts A/B/C, Volumes 70–71 (2014) 3-16.

[15]. F. Deschner, B. Lothenbach, F. Winnefeld, J. Neubauer, Effect of temperature on the hydration of Portland cement blended with siliceous fly ash, Cem. Concr. Res. 52 (2013) 169-181.

[16]. G. Le Saoût, B. Lothenbach, A. Hori, T. Higuchi, F. Winnefeld, Hydration of Portland cement with additions of calcium sulfoaluminates, Cem. Concr. Res. 43 (2013) 81-94.

[17]. L. Pelletier, F. Winnefeld, B. Lothenbach, The ternary system Portland cement–calcium sulphoaluminate clinker–anhydrite: Hydration mechanism and mortar properties, Cem. Concr. Comp. 32 (2010) 497-507.

[18]. F. Winnefeld, B. Lothenbach, Hydration of calcium sulfoaluminate cements — Experimental findings and thermodynamic modelling, Cem. Concr. Res. 40 (2010) 1239-1247.

[19]. J. Bizzozero, C. Gosselin, K.L. Scrivener, Expansion mechanisms in calcium aluminate and sulfoaluminate systems with calcium sulfate, Cem. Concr. Res. 56 (2014) 190-202.

[20]. L. Baquerizo, T. Matschei and K. Scrivener, Volume stability of CAC-$CaSO_4$-$CaCO_3$-H_2O systems during drying, International Conference on Calcium Aluminates, Avignon - France, May. 18 – 21, 2014, pp. 274-283.

3 Methods to determine hydration states of minerals and cement hydrates

The results presented in this chapter have been published in reference [1].

3.1 Introduction

3.1.1 General

Varying hydration states of minerals and hydrated phases and their associated changes in molar volume (i.e. density) is a common cause of failure in porous materials. Two mechanisms can be distinguished: i) crystals that can precipitate from a saturated solution and grow in confined spaces such as porous media due to changes in temperature and relative humidity (RH) and ii) hydrated minerals such as clays that can absorb or release water from their structure depending on the external conditions producing swelling or shrinkage directly without dissolution and recrystallization.

The first mechanism, commonly called salt damage, is one of the main reported causes of failure in stones, cultural heritage buildings, and any porous building material [2]-[4]. The growth of salts produces a crystallization pressure which can exceed the tensile strength of a porous material causing its rupture. Most cases of the damage are the consequence of unfavourable conditions of temperature and RH that result in repeated cycles of dissolution and crystallization, or hydration and dehydration [4]. Sodium sulfate is very well known for its ability to cause damage to porous media such as building stone. This is usually attributed to the growth of $Na_2SO_4\cdot10H_2O$ (mirabilite) from a supersaturated solution [2]. In relation to Portland cement-based concretes, the crystallization of ettringite due to external sulfate attack or autogenous delayed ettringite formation can cause complete failure of structures [5]-[6].

The second mechanism is related to the ability of layered minerals such as smectite clays and layered double hydroxides (LDH) to absorb or release water from the interlayer space depending on the external conditions, especially varying temperature and RH [7]-[8]. Ca^{2+}-montmorillonite, for instance, shows an increase of basal space d(001) from ~0.97 nm in the anhydrous state up to ~1.8 nm in the three-layer hydrate, which is associated with considerable changes in molar volume [9]. LDH are lamellar materials with positively charged layers and charge-balancing anions in the interlayer and they have many physical and chemical properties in common with those of clay minerals such as ion-exchange properties and swelling in water [8]. Several phases formed during hydration of cement belong to this family and each of these can exist in several different well-defined hydration states.

3.1.2 Hydration states of crystalline cement hydrates

Cement clinker phases react chemically with water to form cement hydrates. Some of these hydrates are crystalline phases with LDH- or ettringite-type structures. These so called Alumino-Ferrite mono- and tri-phases (AFm and AFt) show different hydration states depending on the temperature and relative humidity (RH) to which they are exposed, similar to what is observed in many clay minerals. Varying the hydration states of these phases can have a significant impact on the density of cement paste. The molar volume of some AFm phases can decrease by as much as 20% during drying [10], strongly influencing the porosity and performance of cementitious systems.

The most important AFm and AFt phases and their reported water contents are presented in Table 3:1. Water molecules can be incorporated in the interlayer in AFm phases (LDH-type) or in the interchannel in AFt phases (ettringite type). In the case of AFm phases different types of interlayer water can be identified: water molecules strongly bound to the calcium cations of the main layer, and space filling water molecules which are lost first during an increase in temperature or a decrease in RH [11].

Table 3:1 Most important AFm and AFt phases and reported water content.

	Phase name	Chemical formula	Cement notation	Ref.
AFm	Monosulfoaluminate	$[Ca_4(Al)_2(OH)_{12}]^{2+}$ $[SO_4{\cdot}nH_2O]^{2-}$ n=4-10	$C_4A\hat{S}H_{6+n}$	[12]-[20]
	Hydroxy-AFm	$[Ca_4(Al)_2(OH)_{12}]^{2+}$ $[(OH)_2{\cdot}nH_2O]^{2-}$ n=4-12	C_4AH_{7+n}	[12]-[13],[15],[19]-[21]
	Monocarboaluminate	$[Ca_4(Al)_2(OH)_{12}]^{2+}$ $[CO_3{\cdot}nH_2O]^{2-}$ n=5	$C_4A\hat{C}H_{6+n}$	[12]-[13],[15],[19]-[22]
	Hemicarboaluminate	$[Ca_4(Al)_2(OH)_{12}]^{2+}$ $[1/2CO_3\,(OH){\cdot}nH_2O]^{2-}$ n=0-5.5	$C_4A\hat{C}_{0.5}H_{6.5+n}$	[12]-[13],[15],[19]-[21],[23]
AFt	Ettringite	$[Ca_6(Al)_2(OH)_{12}{\cdot}24H_2O]^{3+}$ $[3SO_4{\cdot}nH_2O]^{3-}$ n=0-6	$C_6A\hat{S}_3H_{30+n}$	[12]-[14],[24]

There is presently no systematic approach to assessing the stability range (as a function of temperature and RH) of cement hydrates which takes into account the impact of different hydration states. Moreover, a complete database of thermodynamic properties related to the absorption/desorption of water from the crystal structures of such hydrates is not yet available.

3.1.3 Scope of this chapter

The aim of this chapter is to examine a set of characterization techniques intended for to the determination of the hydration states of minerals such as cement hydrates and see how these methods correlate with or complement each other. Some of the techniques studied have already been widely used, such as X-ray diffraction (XRD) and thermogravimetric analysis (TGA), but others, for instance the sorption balance technique and sorption calorimetry, are less well known. Subsequently, measurements and calculations of enthalpies related to the absorption/desorption processes are described using results from sorption calorimetry and from a novel hydrate pair - humidity buffer method that makes use of phase rule constraints [25]-[26]. A similar approach was used by Chou et al. to study the stability of hydrated sulfate salts [27]-[31]. The experimental results from sorption balance, sorption calorimetry and the hydrate pair - humidity buffer method were validated on the relatively well described system Na_2SO_4–H_2O, including the salts thenardite and mirabilite.

At the end of the chapter, the stability ranges of the different hydration states of monosulfoaluminate (Ms) are presented, as well as the thermodynamic properties associated with these changes. Monosulfoaluminate was chosen to test the methodology as it is one of the most common AFm cement hydrates, which can make up to 10% by volume of a hydrated cement paste. This hydrate contains a sulfate anion (SO_4^{2-}) in its interlayer and exists in different hydration states. The study of other AFm phases and ettringite is shown in Chapter 4 and 5, respectively.

3.2 Materials and sample preparation

The synthesis of each cement phase used in this study is described in this section. All syntheses were done from analytical grade reagents. C_3A ($3CaO{\cdot}Al_2O_3$) and CA ($CaO{\cdot}Al_2O_3$) were prepared from stoichiometric mixes of $CaCO_3$ and Al_2O_3 at 1400 °C, based on the procedure given by Matschei et al. for C_3A [32]. Anhydrite $CaSO_4$ was prepared by dehydration of gypsum in a muffle furnace at 550 °C overnight. CaO was prepared from $CaCO_3$ calcined at 900 °C overnight.

The main precursor in the synthesis of the AFm phases (excluding strätlingite) and ettringite studied was tricalcium aluminate, C_3A ($3CaO{\cdot}Al_2O_3$). Double distilled CO_2 free water with a water to solid ratio (w/s) of 20 was used in the synthesis of all hydrates. Monosulfoaluminate ($C_4A\hat{S}H_{14}$), monocarboaluminate ($C_4A\hat{C}H_{11}$) and hydroxy-AFm (C_4AH_{19}) were prepared by suspending a 1:1 molar mixture of C_3A and either $CaSO_4$, $CaCO_3$ or CaO, respectively. In the case of hemicarboaluminate ($C_4A\hat{C}_{0.5}H_{12}$), C_3A, $CaCO_3$ and CaO were used with molar ratios 2:1:1. For the synthesis of strätlingite a stoichiometric mix of CaO, $Na_2SiO_3{\cdot}5H_2O$ and $NaAlO_2$ was used. Since the water content of the sodium silicate and sodium aluminate precursors might vary, the water content was measured by TGA to correct the initial mix composition prior to synthesis. Ettringite was prepared from a suspension of a 1:3 molar mixture of C_3A and $CaSO_4$. Monosulfoaluminate was prepared at 5 and 80°C, while hydroxy-AFm was made at 5°C. The other phases were kept at room temperature. The different mixtures were stirred using a magnetic stirrer for 3 days and then periodically agitated during 2 weeks.

Once purity has been confirmed by XRD, the solids were vacuum filtered under N_2 atmosphere in a glove box and then placed inside small (open) plastic bottles, which were subsequently introduced inside hermetically sealed glass bottles containing salt solutions at the bottom in order to equilibrate the samples at different RHs [33] (see Table 3:2). Finally the glass bottles were conditioned at 5, 25 and 50 °C during different periods of time (from 6 to 30 months). Ettringite was also dried at 80 °C. The RH was periodically checked using a Testo 174H humidity probe, except in the case of aging at 80 °C, which exceeds the operation temperature of the probe.

Reagent grade thenardite (Na_2SO_4) was obtained from Sigma Aldrich, > 99% pure, and mirabilite $Na_2SO_4{\cdot}10H_2O$ was prepared by wetting thenardite with degassed and deionized water. These samples were used to validate some of the techniques studied.

Table 3:2 Equilibrium RH of selected saturated salt solutions at different temperatures [33].

Salt solution	RH (%)			
	5°C	25°C	50°C	80°C
LiBr	---	---	---	5.2
Na(OH)	10.5[a]	8.2	4.9	---
CH_3CO_2K	26[a]	22.5	19[a]	---
$MgCl_2$	33.6	32.8	30.5	26.1
NaBr	---	---	---	51.4
$Mg(NO_3)_2$	58.9	52.9	45.4	---
NaCl	75.7	75.3	74.4	---
KCl	87.7	84.3	81.2	78.9
K_2SO_4	98.5	97.3	95.8	---

[a] Measured

3.3 Experimental methods and analysis

3.3.1 X-Ray Diffraction (XRD)

This characterization technique was used to analyse the crystal structure, e.g. space group and lattice parameters of synthetic cement hydrates, as well as to identify possible impurities precipitated during the synthesis. Then, changes of the unit cell volume can be calculated when samples are exposed to different temperatures and RHs.

X-ray analyses of monosulfoaluminate wet and dried to different RHs were carried out at room temperature (unless otherwise stated) with a Bruker D8 Advance diffractometer (CuKα radiation, 45 mA, 35 kV) equipped with a Super Speed detector, in the 2θ range 5-70°, with a step size and time per step of 0.02° and 0.5 s, respectively. Samples were prepared inside a glove box filled with N_2. A low background- airtight specimen holder (Bruker AXS) was used to avoid carbonation and drying during testing. Samples were mixed with small amounts of rutile in order to correct for pattern displacement due to variations in sample height. The peak profile and lattice parameters were determined by a LeBail fit [34] using TOPAS 4.2 (Bruker AXS). When the crystal structure of a specific hydration state was not known, assumptions such as space group and initial lattice parameters were made in order to obtain relevant data. In the case of monosulfoaluminate, the crystal structure of kuzelite was used as starting model [35]. Phase quantification was carried out using Rietveld analysis implemented in TOPAS 4.2.

In addition to conventional XRD, a humidity chamber CHC plus$^+$ from Anton Paar (see Figure 3:1) coupled to a Bruker D8 Advance diffractometer (CuKα radiation, 45 mA, 35 kV) was used to determine lattice parameters of the lowest hydration state of monosulfoaluminate under dry N_2 flow at 90 °C.

In this work, when several XRDs are shown in one graph, their intensities axes are not the same (unless otherwise stated) because the samples tested were different and no spinning was possible during characterization due to the use of the airtight sample holder, which highly impact the preferred orientation.

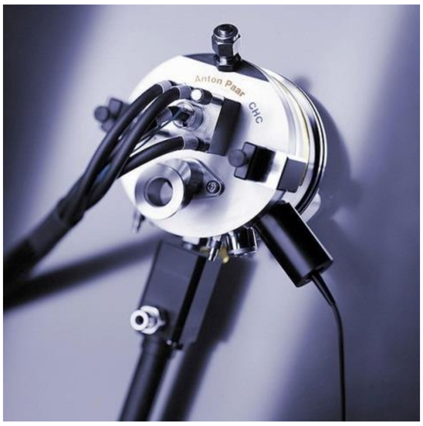

Figure 3:1 Anton Paar Cryo & Humidity Chamber: CHC plus+. (Picture taken from http://www.anton-paar.com/corp-en/products/details/cryo-humidity-chamber-chc-plus/).

3.3.2 Thermogravimetric analysis (TGA)

Thermogravimetry measurements were carried out with a Mettler Toledo TGA/SDTA 851^e under N_2 flux, over the temperature range 25-1200 °C with a heating rate of 20 K/min. Measurements were done on samples dried at different RH once the presence of a single hydration state was confirmed by XRD. This data enabled us to measure the water content of pure hydrates. Together with the volume information obtained by XRD, the density of a cement hydrate dried at a specific temperature and RH can be calculated.

3.3.3 Hydrate pair - humidity buffer method

This method was developed to determine the RH at which a change in hydration state occurs. It applies the salt-hydrate pair principle which considers a thermodynamic equilibrium between hydrate pairs, i.e. two hydration states of the same salt, and the water vapor pressure of the surrounding gas. Similar methods have been used before mainly as humidity calibrators [25] and to control RH in confined environments [26],[36].

The technique is based on simple phase rule restrictions. Consider a chemical system with 2 components (C), a solid of chemical composition **A** and water H_2O. As shown in the imaginary RH/T phase diagram in Figure 3:2a, component **A** may take up water and exist with different hydration states x and y hence forming the phases $\mathbf{A}\cdot xH_2O$ and $\mathbf{A}\cdot yH_2O$ (consider that $x \geq 0$ and $y > x$) or dissolve to form a solution. If we consider the line *b,* there are 3 phases (P) coexisting: $\mathbf{A}\cdot xH_2O$, $\mathbf{A}\cdot yH_2O$ and water vapor. Using the phase rule the number of degrees of freedom (F) of the system is then 1 (F = C – P + 2; C=2; P=3 therefore F=1). Hence, at each temperature the system will have a fixed vapor pressure (or RH). Under these conditions the system is buffered, which means that under isothermal conditions the RH of the system will not change as long as the 3 phases are present.

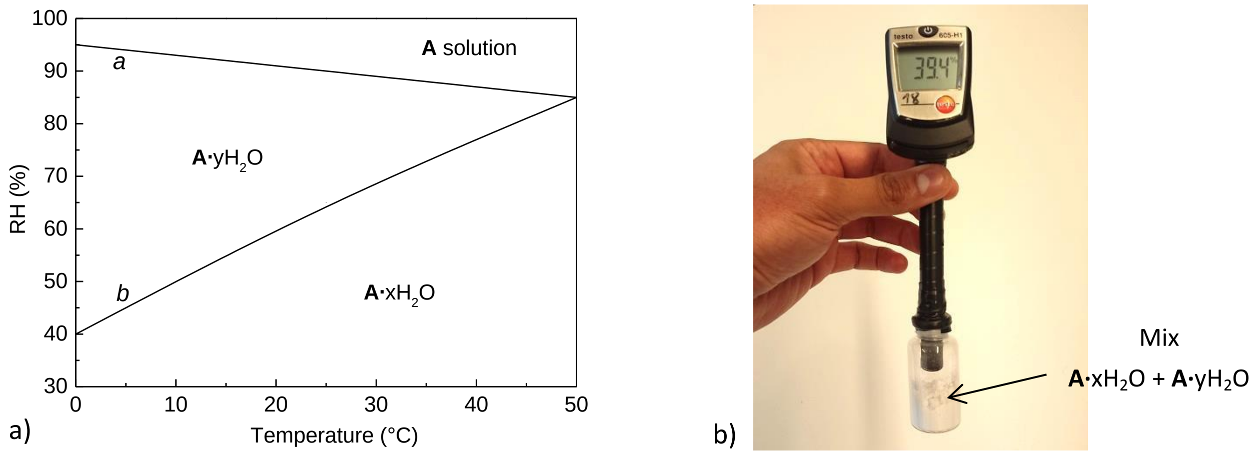

Figure 3:2 a) RH/T phase diagram of the system A - H_2O. b) Set-up of the hydrate pair – humidity buffer method.

The thermodynamic properties of the de/rehydration process **A**·yH_2O↔**A**·xH_2O shown in reaction (2.1) can be calculated with Eq. (2.2), Eq. (2.3) and Eq. (2.4) as shown in Chapter 2.

Experimentally, a mixture of two phases with different hydration states was placed inside a small container (20 ml glass bottles) and the RH at which the combined system reached equilibrium was recorded with a tightly fitted pen hygrometer (Testo 605-H1, accuracy ± 3% RH) as shown in Figure 3:2b. The hygrometer was tightened to the container with Parafilm and with insulating tape on top of it to avoid any leakage. Since the system is closed and there is no exchange of water with the exterior, the RH inside will be forced to be at equilibrium with the two hydrate phases at the given temperature. The same type of measurement can be made for a phase in equilibrium with its saturated aqueous solution (see line *a* Figure 3:2a). By varying the temperature during the experiments it is possible to assess phase boundary curves, which can then be used to construct RH-T phase diagrams. With Eqs. (2.2) – (2.4) the thermodynamic properties of the studied phases can be assessed.

3.3.4 Sorption balance

The sorption balance is commonly used in the pharmaceutical industry to study sorption behaviour. In the present study a DVS Advantage (Surface Measurement Systems, London, UK) was used [38]. A photo and a schematic picture of the sorption balance operation are shown in Figure 3:3. The mass of the small (5-100 mg) sample is continuously measured with an analytical balance while it is exposed to a program which varies RH. The desired RH is reached by mixing different proportions of dry and water vapor saturated nitrogen gas streams. The accuracy of the generated RH is better than 1.5%.

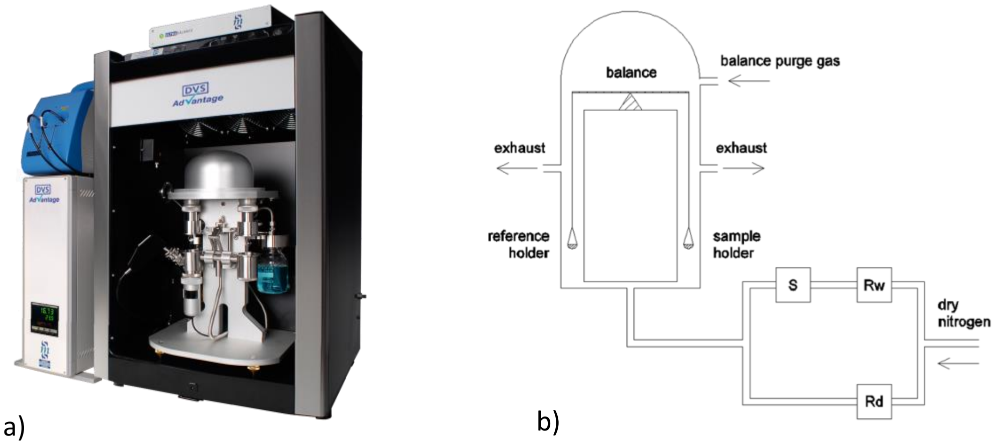

Figure 3:3 a) Photo of the DVS Advantage machine used in this study. b) Schematic picture of the sorption balance operation. Rw and Rd are mass flow controllers for the saturated and dry gas; S is the saturator. (Photo taken from http://surfacemeasurementsystems.com/products/dvs-instruments/dvs-advantage/)

With the sorption balance the mass of water taken up or released during a hydration/dehydration phase transformation or deliquescence and the water activity at which the process takes place can both be quantified. The mass is directly measured by the balance. To determine the water activity (RH/100) of a specific transformation one has to run either a ramp or a step method [39]-[40]. The step method is less sensitive to disturbances and less time consuming than the ramp method and therefore this regime was chosen for testing the samples. If the (constant) mass change rate $\mathrm{d}m/\mathrm{d}t$ at each RH level is plotted as a function of the RH of the gas stream, a linear curve fit intersects $\mathrm{d}m/\mathrm{d}t = 0$ at the water activity at which an absorption/ desorption process takes place.

3.3.5 Sorption calorimetry

This technique provides the means to continuously scan water activity of a small sample, while simultaneously measuring water activity, moisture content and sorption enthalpy during an ad/absorption process.

The double twin isothermal sorption calorimeter used in this study (see Figure 3:4a) is described in detail elsewhere [41]. It has two measuring positions placed 90 mm apart. The ampoule where the diffusion-sorption process takes place is schematically shown in Figure 3:4b. When introduced into the calorimeter, thermal power of evaporation (P_{vap}) and thermal power of sorption (P_{sorp}) are continuously measured by two twin microcalorimeters at the top and bottom chambers of the ampoule, respectively. The dry sample is loaded in the bottom chamber, after which water is injected in the top and is transported by diffusion to the sample during the measurement. The diffusion rate depends on the geometry of the connecting tube and the water activity over the sample. The water diffusion rate, and thus the rate of change of moisture content of the sample, is proportional to P_{vap}. The water activity is calculated from the evaporation rate, and the mixing enthalpy is calculated by comparing the thermal powers of sorption and vaporization (more details about the method can be found in [42]).

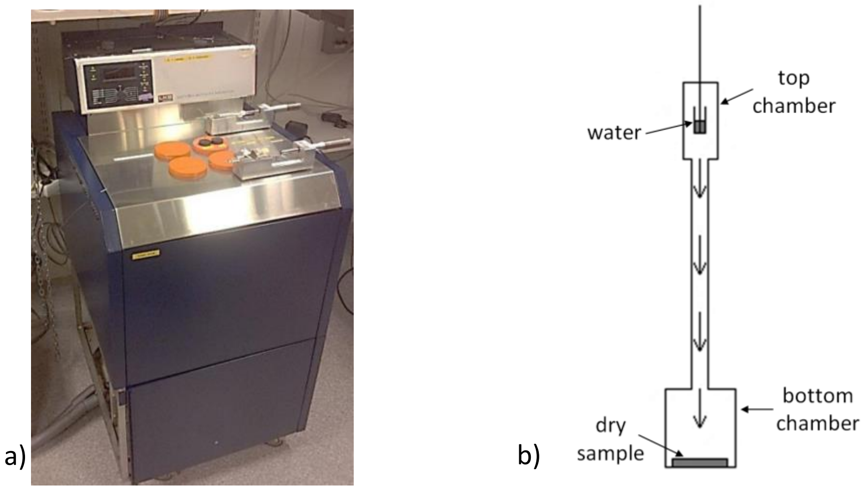

Figure 3:4 a) Photo of the twin isothermal calorimetry used (Lund University). b) Schematic graphic of the sorption ampoule. A dry sample is loaded in the bottom chamber and water is injected in the top chamber, where thermal power of sorption (P_{sorp}) and thermal power of evaporation (P_{vap}) are continuously measured by two twin microcalorimeters, respectively.

The enthalpy measured from the sorption microcalorimeter is normally presented as a mixing enthalpy, i.e., the difference between the enthalpy of the sorption process and that of condensation of liquid water. The mixing enthalpy can be seen as an “excess enthalpy” indicating how much additional heat is obtained from a sorption process compared to condensation of water. Sorption enthalpy, condensation enthalpy and the mixing enthalpy are related according to Eq. (2.5).

Note, that the sorption enthalpy and the mixing enthalpy are properties of the moisture state at which the sorption/mixing takes place, while the condensation enthalpy of water is constant under isothermal conditions with a value of -2440 J/g H_2O (or -44 kJ/mol H_2O) at 25 °C. The thermodynamic sign convention used in this work states that processes are considered from the system viewpoint, i.e., if heat is lost by the system to the surroundings (heat is produced) the enthalpy change is negative. Enthalpies of sorption, condensation and mixing are therefore all negative.

3.4 Results

3.4.1 Validation

Before testing cement hydrates, the hydrate pair - humidity buffer method, sorption balance and sorption calorimetry were validated with the system Na_2SO_4-H_2O which is relatively well described in the literature.

3.4.1.1 *Hydrate pair – humidity buffer method*

Consider the RH/T phase diagram of the system Na_2SO_4-H_2O as shown in Figure 3:5 taken from Linnow [37]. Phase boundaries are shown with the lines *a, b* and *c*. Line *b* is the boundary between thenardite (Na_2SO_4) and mirabilite ($Na_2SO_4 \cdot 10H_2O$), both of them in the solid state. Above and below this line $Na_2SO_4 \cdot 10H_2O$ and Na_2SO_4 are the stable phases, respectively, but both phases can coexist on the line. The dotted line corresponds to a solution in metastable equilibrium with respect to thenardite and supersaturated with respect to mirabilite [2]. To validate the method, three different mixes were prepared: one mix of 80%-20% thenardite - mirabilite and two mixes of 50%-50%. A few measurements were done using saturated solutions in order to measure the solid-liquid lines *a* and *c*. The measured RH for the thenardite-mirabilite equilibrium (filled dots) as well as the mirabilite or thenardite - saturated solution phase boundaries (open dots) are shown in Figure 3:5, respectively. As can be seen there is good agreement with the phase diagram published by Linnow [37], which is based on thermodynamic data of aqueous Na_2SO_4 and the crystalline phases. Measurements done at around 5 °C on the thenardite-mirabilite boundary were rather scattered which might be due to low accuracy of the hygrometers at low temperature or the occurrence of other metastable equilibria including Na_2SO_4(III) and $Na_2SO_4 \cdot 7H_2O$ [4]. Since the purpose of this work was not to study in the detail the equilibrium of the system Na_2SO_4-H_2O no further analysis was carried out in these samples.

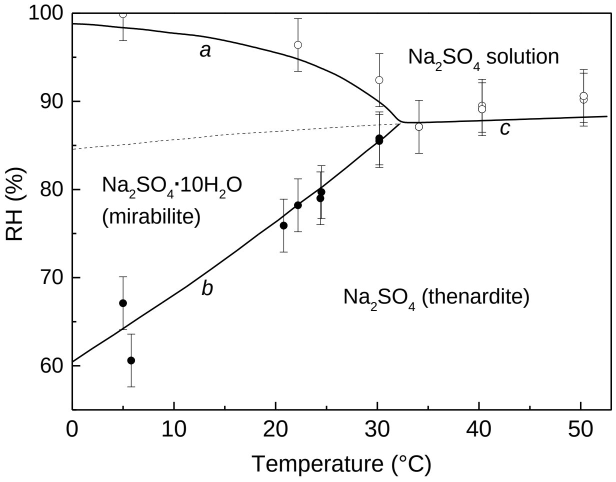

Figure 3:5 RH/T phase diagram of the system Na_2SO_4 + H_2O at 1 bar (taken from Linnow [37]). The filled and open dots are our experimental results using the hydrate pair - humidity buffer method.

In a next step the related thermodynamic relations are cross-checked. For the reaction:

$$Na_2SO_4 \cdot 10H_2O(s) \rightarrow Na_2SO_4(s) + 10H_2O(g) \tag{3.1}$$

mirabilite thenardite

The Gibbs free energy of reaction was calculated according to Eq. (3.2):

$$\Delta G_r^o = -RT\ln[a(\mathrm{H_2O})^{10}] = -10RT\ln\frac{f^*(\mathrm{H_2O})RH}{100} \tag{3.2}$$

Figure 3:6 shows the relation between $\ln K$ and $1/T$. The error considered in the graph is due to the accuracy of the hygrometer (± 3%) and the plotted 95% prediction bands were calculated using Origin Pro 8.5. Finally, $\ln K$ can be obtained at any temperature according to the following equation:

$$\ln K(\pm 0.8) = 174.2 - \frac{62797.0}{T} \tag{3.3}$$

The standard enthalpy of reaction $\Delta H_r°$ was calculated with help of the van't Hoff equation (Eq. (2.3)) using the slope value $\partial(\ln K)/\partial(1/T)$ obtained from Figure 3:6. The standard entropy of reaction $\Delta S_r°$ was calculated from Eq. (2.4). Finally the calculated values of $\Delta G_r°$, $\Delta H_r°$ and $\Delta S_r°$ for reaction (3.1) are summarized in Table 3:3. The results are in very good agreement with previously reported values, although the uncertainty in our data is probably larger in comparison to other techniques when we take the accuracy of the hygrometer as given by the manufacturer (+/-3% RH) into account. Nevertheless the results underline that even with the use of a simple experimental setup, as used here, it is possible to derive relatively complex phase diagrams and related thermodynamic data.

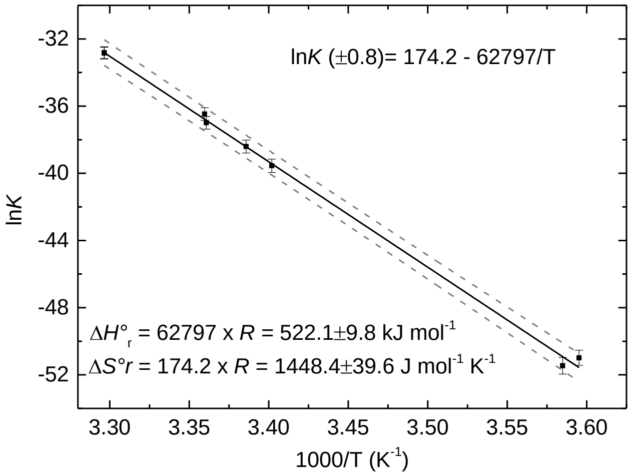

Figure 3:6 Van't Hoff plot of our experimental results at different temperatures for reaction (3.1). Dashed line represents the 95% prediction band calculated with Origin Pro 8.5.

Table 3:3 Derived Thermodynamic data for reaction (3.1) at 25 °C and 1 bar [a]

$\Delta G_r°$ [kJ/mol]	$\Delta H_r°$ [kJ mol^{-1}] [b]	$\Delta H_{mix}°$ [kJ mol^{-1}] [c]	$\Delta S_r°$ [J mol^{-1} K^{-1}]	Ref.
90.3 ± 1.9	522.1± 9.8	82.1	1448.4± 39.6	This study
90.6	521.8	81.8	1444.7	[43]
	521.6	81.6		[44]

[a] Errors were calculated considering the accuracy of the hygrometers, the calculated 95% prediction band and the error in the calculated slope of the curve in Figure 3:6.

[b] Calculated considering H_2O as a gas.

[c] Calculated considering H_2O as a liquid (for reaction (3.1) subtract the heat of evaporation of 10 moles of H_2O, $\Delta H°_{evap}$ = 44 kJ/mol).

3.4.1.2 Sorption balance

To validate the operation of the sorption balance, Na_2SO_4 powder vacuum dried at 100 °C for 24 hours was used. The measurements were carried out at 25°C. Figure 3:7a and b show the applied RH ramp program and the related evolution of sample mass, respectively. From 0% to 85% RH no water was absorbed by the sample. At RH >85% we observed a linear mass increase, corresponding to a constant water uptake rate. During drying a linear mass decrease was observed at RH< 85%. In Figure 3:7c the mass change rate versus time is plotted and $\mathrm{d}m/\mathrm{d}t$ at the final 10 min of each step was used to derive Figure 3:8. The line fitted to these points passes $\mathrm{d}m/\mathrm{d}t = 0$ at a RH of 88.3%, which means that Na_2SO_4 absorbs water vapor until the sample reaches a metastable equilibrium with its saturated solution at a water activity of about 0.88 or 88% RH rather than precipitating as mirabilite, despite an obvious supersaturation with respect to this phase. This value is in agreement with the 87% RH shown in Figure 3:5 (metastability line). Since no equilibrium was reached in any of the set RH, the sorption isotherm could not be plotted.

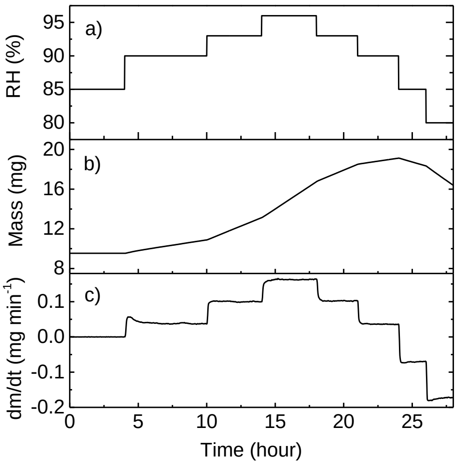

Figure 3:7 a) RH step-wised program for the sorption balance. b) Mass change of sample. (c) dm/dt of sample.

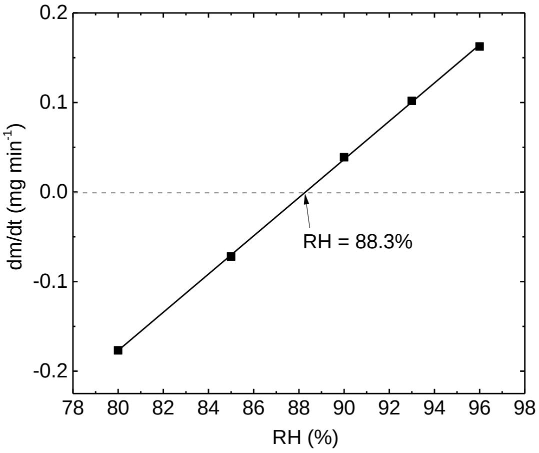

Figure 3:8 Calculated RH of deliquescence of Na_2SO_4

3.4.1.3 Sorption calorimetry

The validation experiments were conducted at 25 °C on sodium sulfate dried as described in the previous section. Two measurements were carried out using different sample sizes.

Figure 3:9 shows that both the sorption isotherm and the mixing enthalpy plot can be divided into two parts. First there is a constant water activity that ends at a moisture content of about 2.0 g H_2O/g Na_2SO_4; secondly a process with gradually increasing water activity. Note that the water activity only changes a few tenths of a percent during the period of constant water activity. Figure 3:9 can be interpreted as follows:

- The initial water activity is ~0.87 (or 87% RH) in both measurements and this is in agreement with both the literature [4],[37] and the sorption balance measurement done in this study for a solution in metastable equilibrium with respect to thenardite (supersaturated with respect to mirabilite) (the dotted line in Figure 3:5). Thenardite is thus dissolved to form a (metastable) saturated solution, similar to what happens at equilibrium above 32 °C where mirabilite is not stable.

- The moisture content increases at constant water activity up to a value of about 2.0 g H_2O/g Na_2SO_4 or 3.52 mol Na_2SO_4/kg H_2O, which agrees with the reported solubility of thenardite [4],[44].
- The mixing enthalpy for a dissolution process should be constant and the measurement on the larger sample indicates that the value is about -125 J/g H_2O. The measurement on the smaller sample shows a drifting value, possibly because as the dissolution of the thenardite particles proceeds, a thicker and ticker layer of saturated solution is formed, the outer parts of which are more dilute (also seen in the slight increase in the water activity during the measurement). We have not found any values in literature to validate this metastable dissolution enthalpy.
- At moisture contents above about 2.0 g H_2O/g Na_2SO_4 the water activity starts to shift to higher values. At this point the last thenardite crystals have dissolved and as the measurement continues, the solution gets increasingly more and more diluted by the absorption of water. This is substantiated by the fact that the sample is a transparent liquid after the measurement. At a moisture content of 3.0 g H_2O/g Na_2SO_4, where the measurement on the smaller sample ends, the system is still within the supersaturated region of the phase diagram with respect to mirabilite. However, there is no indication that any mirabilite forms during our measurements.
- Above a moisture content of 2.0 g H_2O/g Na_2SO_4 the measured enthalpy is due to the dilution of the aqueous solution. At increased moisture contents this will approach zero (pure water). Note the step in the mixing enthalpy from about -120 to -60 J/g H_2O when the last thenardite crystal is dissolved.

The three measured parameters have quite different errors. The moisture content is the most robust result, while the measurement of water activity can be disturbed by slow kinetics of absorption in some systems – even if this does not seem to be the case for the present measurements. The mixing enthalpy results become increasingly more uncertain at high RHs. Although we cannot at present make confident uncertainty calculations, a tentative estimate is that the error of the mixing enthalpies is at least ±10, ±20, and ±30 J/g H_2O at 80, 90 and 95% RH, respectively.

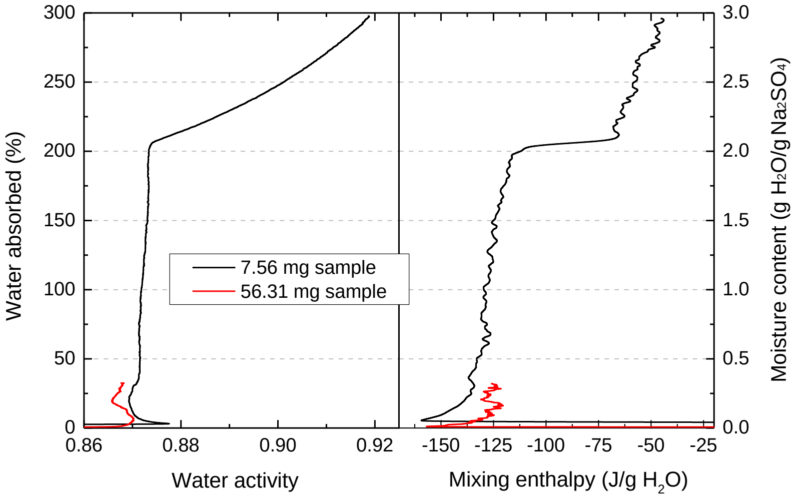

Figure 3:9 The results of two measurements on thenardite with sorption calorimetry. The left diagram shows the sorption isotherm and the right one the mixing enthalpy as function of the moisture content (note that this graph is plotted with the mixing enthalpy on the x axis in order to compare it with the sorption isotherm graph). The y axes water absorbed and moisture content are proportional.

3.4.2 Results of monosulfoaluminate measurements

During cement hydration, C_3A reacts with calcium sulfate (gypsum, hemihydrate or anhydrite) to produce ettringite, which subsequently reacts with the remaining C_3A to form monosulfoaluminate, an LDH-type AFm phase. This cement hydrate is known to present different hydration states and have a characteristic hexagonal morphology as shown in Figure 3:10. In this section the results obtained on synthetic monosulfoaluminate (Ms) using the aforementioned characterization techniques are presented.

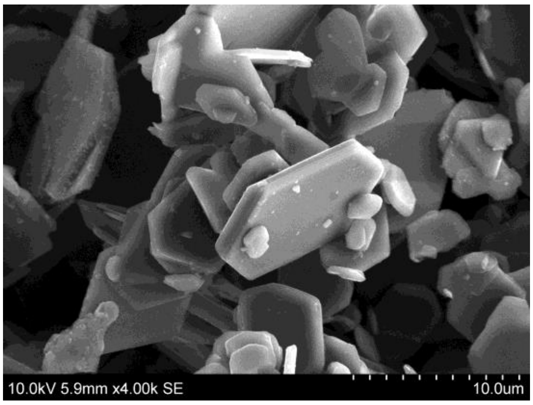

Figure 3:10 SEM picture of monosulfoaluminate.

3.4.2.1 XRD and TGA

As shown in the X-ray diffractograms in Figure 3:11a at 25 °C, Ms14 (the index 14 gives the water content of the phase in moles) is the hydration state observed under saturated conditions (100% RH) but it dehydrates at 97% RH to Ms12 which is found until 23% RH (the water content of Ms12 was verified by TGA). At 8% RH an even lower hydration state appears, which according to Dosch et al. [15] corresponds to Ms10, but according to our TGA results it is more likely to be Ms10.5, which agrees with results presented by Pöllmann [14]. An additional lower hydration state was obtained by vacuum drying the sample. According to TGA measurements this corresponds to Ms9. Since this hydration state tends to rehydrate fast at RH > 2%, XRD measurements were done using a sample dried in situ at 90 °C under N_2 flux in the humidity chamber. As no other hydration state was observed from 25 °C to 90 °C during the in-situ drying we assumed that this hydration state is the same one observed close to 0% RH at room temperature during vacuum drying. The exact RHs at which changes of hydration states take place were determined using sorption balance, sorption calorimetry and the hydrate pair - humidity buffer method, which gave comparable results.

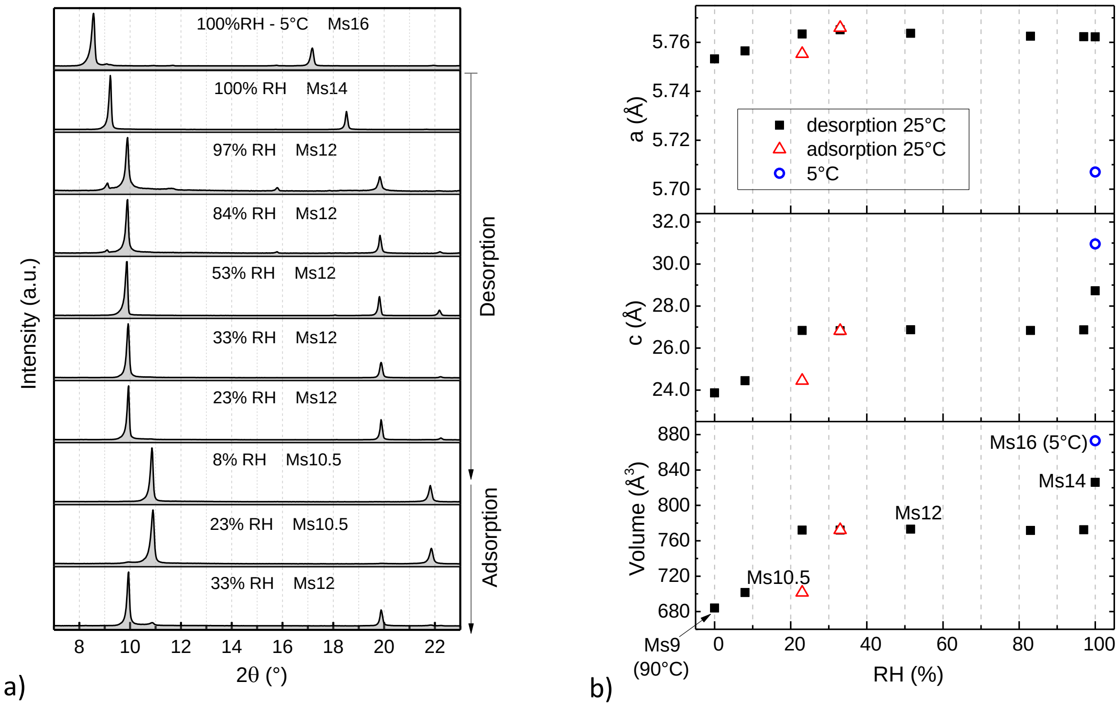

Figure 3:11 a) XRD patterns and b) refined lattice parameter and volume of the lattice of monosulfoaluminate dried at different RH at 25°C (unless otherwise stated).

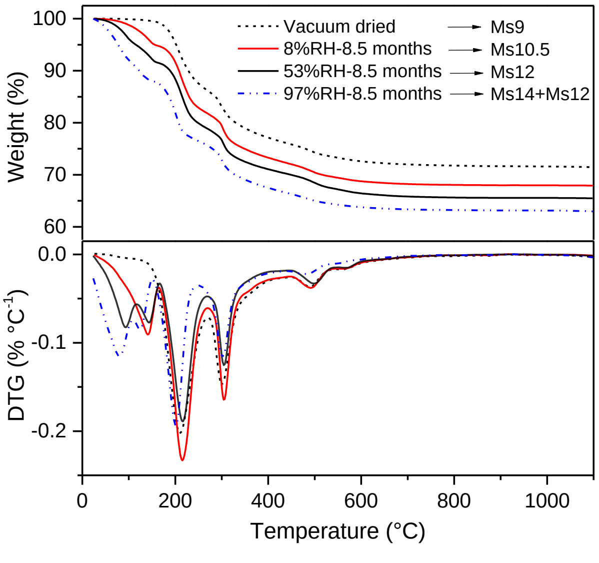

Figure 3:12 TGA of monosulfoaluminate dried at different conditions at 25°C.

An adsorption experiment was carried out after the desorption experiment, as shown in Figure 3:11a. After 1 year exposure of Ms10.5 to 23% and 33% RH, respectively, rehydration to Ms12 is only observed at 33% RH. Also when Ms12 is rewetted (immersed in water) it does not rehydrate to Ms14 at 25 °C. This hysteretic behaviour will be further discussed in the coming sections.

In order to study the stability of Ms14, a series of in situ tests using the humidity chamber were carried out at temperatures >50 °C and high RHs. Rehydration Ms12→Ms14 takes place at around 90, 85 and 78% RH at 50, 65 and 75 °C.

A water-rich hydration state was obtained by wet synthesis at 5 °C. According to several references it corresponds to Ms16 [14]-[15]. Nevertheless, most of the time the sample contained traces of Ms14, making the study of its stability difficult. For this reason, and because Ms16 was never observed from 25 °C to 85 °C in wet conditions, this hydration state was not considered during our stability and thermodynamic properties derivation analysis in this chapter.

Attempts to index the diffraction patterns of the different hydration states were unsuccessful due to impurities, mainly small traces of ettringite and carbonates. For this reason, the structure used for the refinement of the different hydration states of monosulfoaluminate was the kuzelite refined crystal structure published by Allmann [35] (ICSD# 100138, PDF# 41-0477) using the LeBail method [34]. The refined lattice parameters and volume of the different hydration states of monosulfoaluminate are given in Figure 3:11b. Ms16 refined lattice parameters are also included in this graph. It is worth noting that a decrease of RH can often lead to a very significant reduction in molar volume, in this case (i.e. for Ms14→Ms9) approximately 17% as shown in Figure 3:11b.

Figure 3:12 shows the TGA curves of four different hydration states of monosulfoaluminate. The derivative plot shows similar weight losses at temperatures > 175 °C. The main differences are observed below this temperature. Ms12 shows two well defined water losses at 90 °C and 140 °C and Ms10.5 only a single water loss at 140 °C. In order to verify the water content of Ms14, a TGA test was carried out on a sample dried at 97% RH for two months. Unfortunately the sample was composed of Ms14+Ms12, so, for this reason, and because a considerable amount of condensed water is also present in the sample at this RH, it was not possible to determine the precise water content of this hydration state. A similar problem occurred for Ms16. It was therefore simply assumed that the widely reported water contents of Ms14 and Ms16 were correct.

3.4.2.2 *Hydrate pair - humidity buffer method*

This method was used to determine the equilibrium Ms10.5-Ms12 according to the reaction:

$C_4A\hat{S}H_{12}(s) \rightarrow C_4A\hat{S}H_{10.5}(s) + 1.5H_2O(g)$ or

$$Ms12(s) \rightarrow Ms10.5(s) + 1.5H_2O(g) \tag{3.4}$$

Experimentally a mixture of Ms10.5 and Ms12 was placed inside a small container and the equilibrium RH at different temperatures was recorded. The measurements were repeated 3 times for each RH point at the same temperatures from 19 °C to 50 °C in order to obtain representative results. One of the mixes was rejected due to large differences in recorded RH, probably due to leakage during the testing. The accuracy of the hygrometers (± 3% RH) was considered in the graphs and in the calculations. A diagram presenting the measured critical RH of phase transition between Ms10.5 and Ms12 as function of temperature is shown in Figure 3:13a.

For reaction (3.4) we can write:

$$\Delta G_r^o = -RT\ln K = -RT\ln[f(\mathrm{H_2O})^{1.5}] = -1.5RT\ln\frac{f^*(\mathrm{H_2O})RH}{100} \tag{3.5}$$

From Eq. (3.5) and the data presented in Figure 3:13a, a linear van't Hoff plot (Figure 3:13b) can be derived. Then $\ln K$ follows Eq. (3.6):

$$\ln K(\pm 0.1) = 26.2 - \frac{9895.8}{T} \tag{3.6}$$

The standard thermodynamic properties $\Delta G_r°$, $\Delta H_r°$ and $\Delta S_r°$ were calculated using Eqs. (2.2), (2.3) and (2.4), respectively and are shown in Figure 3:13b. The values are positive because reaction (3.4) shows a dehydration process; however, assuming a rehydration process these values would be negative.

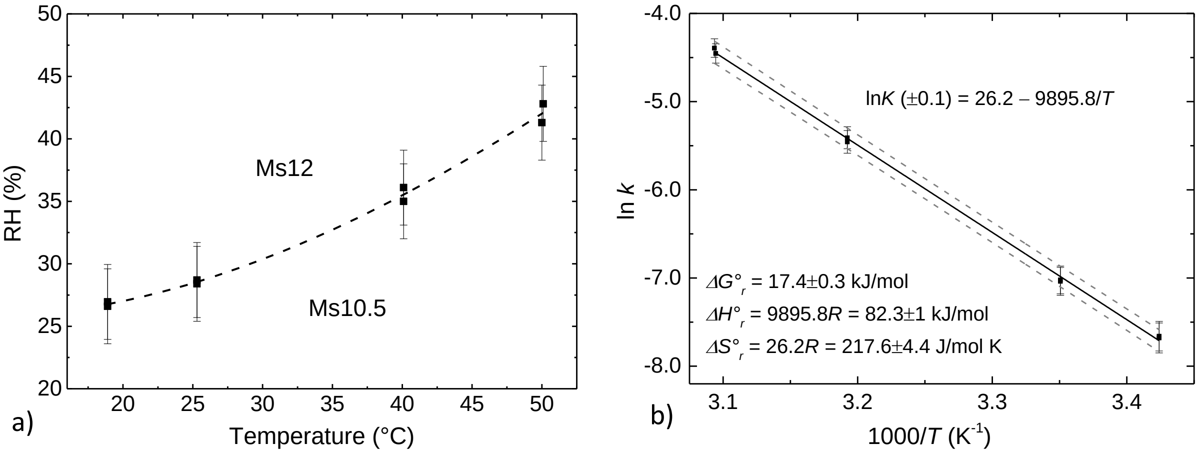

Figure 3:13 a) Ms10.5-Ms12 equilibria at 1 bar. b) Van't Hoff plot for Ms10.5-Ms12 equilibria. The dashed lines represent the 95% prediction band.

3.4.2.3 Sorption balance

A sorption balance measurement was carried out on a monosulfoaluminate sample aged at 33% RH for 12 months, thus the initial hydration state was Ms12. The sample (10.1 mg) was initially equilibrated at 30% RH, followed by a desorption down to 0% RH, absorption up to 97% RH and finally desorption down to the initial state (30% RH). The test lasted about 92 hours and the RH at each step was kept constant during 2 to 3 hours (12 hours in the case of 0% RH). In contrast to the validation test done on Na_2SO_4 a constant mass was achieved in almost all the steps during this experiment and thus the mass change rate could not be used to determine the RH at which a change of hydration state took place. Nevertheless we could determine the complete sorption isotherm (Figure 3:14) which is also useful to determine sudden changes of mass and thus of hydration states.

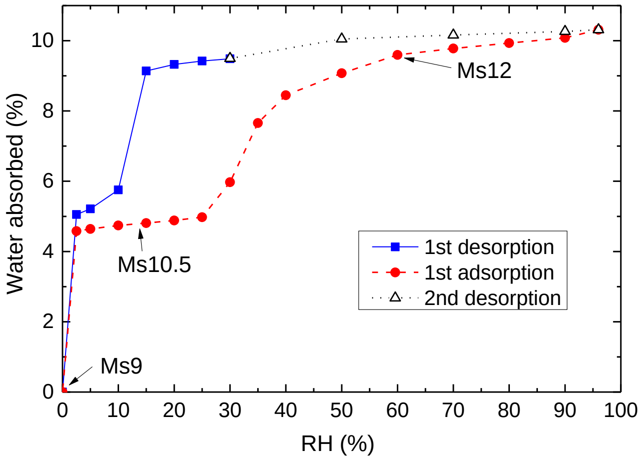

Figure 3:14 Sorption isotherm of monosulfoaluminate at 25 °C.

3.4.2.4 Sorption calorimetry

A sorption calorimetry measurement was done on monosulfoaluminate at 25 °C. The sample was initially vacuum-dried for 24 hours at room temperature, which means that at the beginning of the test the hydration state was Ms9 (as found by TGA). The initial mass of the sample was 89.6 mg.

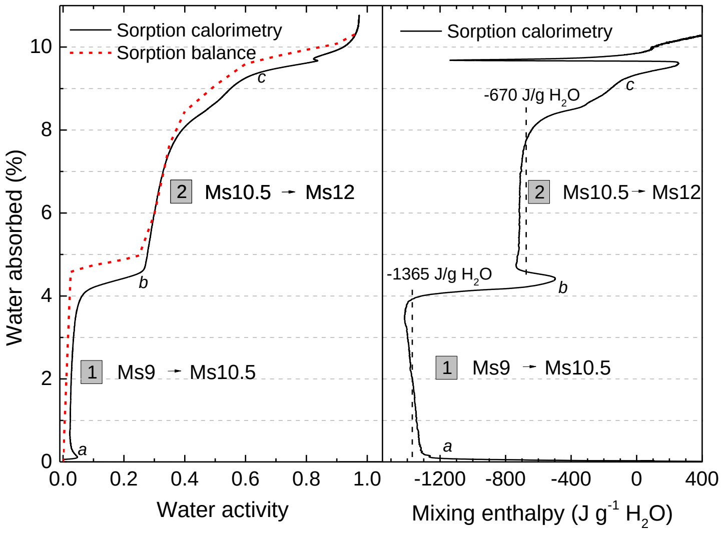

Figure 3:15 Sorption calorimetry results on initially vacuum dried monosulfoaluminate at 25 °C. The left graph shows the calculated sorption isotherm (sorption balance isotherm is superposed for comparison). The right graph presents the mixing enthalpy measured on the sample (the dashed lines represent the mean mixing enthalpies for the two observed processes).

Two hydration processes were observed (labelled 1 and 2 in Figure 3:15). The calculated sorption isotherm is shown in Figure 3:15 and is in good agreement with the isotherm measured by sorption balance.

Process 1 refers to the hydration step of Ms9 to Ms10.5 which is in very good in agreement with the sorption balance measurements. Stoichiometrically this process can be described by the following reaction:

$Ms9(s) + 1.5H_2O(g) \rightarrow Ms10.5(s)$ (3.7)

This process starts and finishes in the points *a* and *b*, respectively (see Figure 3:15). As the hydrate pair – humidity buffer method could not be used to calculate the thermodynamic properties of this reaction/process, the experimental findings of the calorimetry measurements shows that the critical RH for the transformation of Ms9 to Ms10.5 is at around 2%RH. Thus the Gibbs free energy of reaction $\Delta G_r°$ of reaction (3.7) can be calculated according to Eq. (2.2), giving a value of 27.3 kJ/mol. As shown in Figure 3:15, the mixing enthalpy of this process is not completely constant, having an average value of -1365 J/g H_2O. The related sorption enthalpy ΔH_{sorp} for reaction (3.7) can now be calculated according to Eq. (2.5):

$$\Delta H_{sorp} = \Delta H_{cond} + \Delta H_{mix} = -2440\text{ J/g H}_2\text{O} - 1365\text{ J/g H}_2\text{O} = -3805\text{ J/g H}_2\text{O} = -68.6\text{ kJ/mol H}_2\text{O}$$

Since 1.5 moles of H_2O are needed to complete the hydration reaction (3.7), the total standard enthalpy of this reaction can be calculated using Eq. (2.6):

$$\Delta H_r^o = -68.6\text{ kJ/mol H}_2\text{O} \times 1.5 = -102.8\text{ kJ/mol}$$

Process 2 follows the hydration reaction (3.8):

$Ms10.5(s) + 1.5H_2O(g) \rightarrow Ms12(s)$ (3.8)

This reaction was also studied with the invariant point method. As seen in Figure 3:15 this process starts at point *b* and finish approximately at point *c* where the mixing enthalpy is close to zero. The mixing enthalpy of this second process is around -670 J/g H_2O in the constant region. Following the same procedure as shown in Process 1 the corresponding standard enthalpy of reaction (3.8) is:

$$\Delta H_{sorp} = \Delta H_{cond} + \Delta H_{mix} = -2440\text{ J/g H}_2\text{O} - 670\text{ J/g H}_2\text{O} = -3110\text{ J/g H}_2\text{O} = -56.0\text{ kJ/mol H}_2\text{O}$$

$$\Delta H_r^o = -56.0\text{ kJ/mol H}_2\text{O} \times 1.5 = -84.0\text{ kJ/mol}$$

This value is in good agreement to the enthalpy of reaction calculated from the invariant point method, 82.3 kJ/mol. Please note that the enthalpy value calculated with sorption calorimetry is negative because the test measures an absorption process which is exothermic.

In addition to processes 1 and 2, an endothermic process followed by an exothermic peak is observed after point *c*. As there is no significant increase in moisture content corresponding to this event, it seems that it has its origin in, for example, a conformational/ morphological change that may be initiated by the increase in moisture content, but does in itself not involve the uptake of water. It should be noted that although the thermal effect of this event is clearly seen, the uncertainty in the absolute values increases significantly at high RH; thus the increase of the mixing enthalpy to positive values after the sharp exothermal peak is probably an artefact as the RH then approaches 100%.

It is worth noticing the very good agreement between the sorption isotherm measured on monosulfoaluminate by sorption balance and the one calculated one by sorption calorimetry as shown in Figure 3:15. This clearly shows the power and reliability of this technique, which can also be used to study ad/absorption processes in salts, minerals, proteins, pharmaceutical products, etc.

3.4.2.5 Summary of results on monosulfoaluminate

A summary of results obtained for monosulfoaluminate is shown in Figure 3:16a and Table 3:4. The hysteretic behaviour observed in the sorption balance and XRD measurements is represented by a dashed-line. In the experimental studies Ms12 is observed when Ms14 is dried at 97% RH, for this reason the dehydration process Ms14 → Ms12 was assumed to take place at this RH. The rehydration Ms12 → Ms14 at 25 °C was not observed by any of the techniques used in this study.

The density values of the different hydration states of monosulfoaluminate are shown in Table 3:5 and were calculated with Eq. (3.9):

$$D = ZM/N_A V \qquad (3.9)$$

where D is the density, Z is the number of formula units per unit cell (which is 1.5 in our case), M is the molecular weight of the hydration state, V is the unit cell volume obtained from the XRD lattice parameters refinement and N_A is the Avogadro's number.

To show how critical may be the changes of hydration states, a short experiment was carried out on a sample initially dried at 8% RH and 25 ° C. This powder sample was then compacted to form a small disc (Φ: 15 mm and thickness: 3 mm) and subsequently exposed to 97% RH and 25 °C during 5 days. The results can be observed in Figure 3:16b and clearly show the expansion and cracking of the sample due to the rehydration reaction $Ms10.5(s) + 1.5H_2O(g) \rightarrow Ms12(s)$.

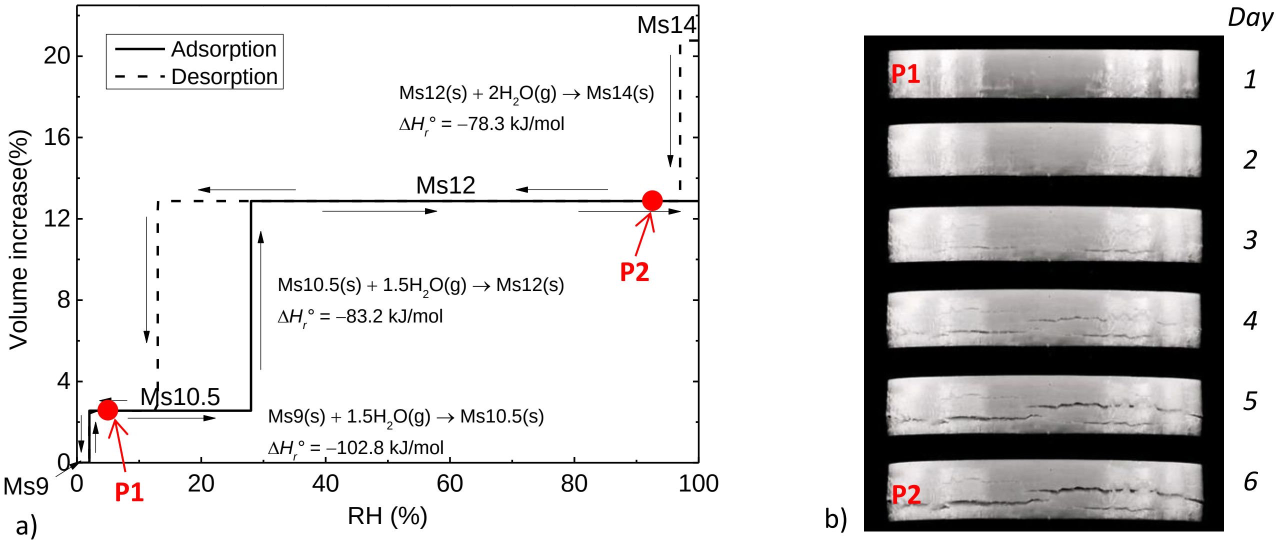

Figure 3:16 a) Volume changes of monosulfoaluminate vs RH and related enthalpies of reaction at 25°C. b) Swelling of a compacted monosulfoaluminate sample due to the change of hydration state Ms10.5 → Ms12. The initial state corresponds to P1 and the final one to P2 from the volume changes graph.

Table 3:4 Derived thermodynamic data for the changes of hydration states of monosulfoaluminate at 25 °C and 1 bar.

Reaction	Change of hyd. state (% RH)	ΔG_r° (kJ/mol)	ΔH_r° (kJ/mol)	ΔS_r° (J/mol K)
$Ms14(s) \rightarrow Ms12(s)+2H_2O(g)$	97	17.2	78.3 [a]	205.2
$Ms12(s) \rightarrow Ms10.5(s)+1.5H_2O(g)$	28.5 [b]	17.4	83.2 [c]	220.5
$Ms10.5(s) \rightarrow Ms9(s)+1.5H_2O(g)$	2 [d]	27.3	102.8 [e]	253.3

[a] Calculated considering a change of hydration state at 97, 90, 85 and 78% RH at 25, 50, 65 and 75 °C, respectively
[b] From hydrate pair - humidity buffer method
[c] Average value from sorption calorimetry and the hydrate pair –humidity buffer method
[d] From sorption balance
[e] From sorption calorimetry

Table 3:5 Molar volume and density of monosulfoaluminate hydration states.

Hydration state	Formula	V° (cm^3/mol)	Density (kg/m^3)
Ms16	$[Ca_4(Al)_2(OH)_{12}]^{2+} [SO_4{\cdot}10H_2O]^{2-}$	350.5	1981.7
Ms14	$[Ca_4(Al)_2(OH)_{12}]^{2+} [SO_4{\cdot}8H_2O]^{2-}$	331.6	1985.9
Ms12	$[Ca_4(Al)_2(OH)_{12}]^{2+} [SO_4{\cdot}6H_2O]^{2-}$	310.1	2007.7
Ms10.5	$[Ca_4(Al)_2(OH)_{12}]^{2+} [SO_4{\cdot}4.5H_2O]^{2-}$	281.6	2114.9
Ms9	$[Ca_4(Al)_2(OH)_{12}]^{2+} [SO_4{\cdot}3H_2O]^{2-}$	274.6	2070.2

3.5 Discussion

3.5.1 Correlation between the methods and accuracy

The complementarity of the different methods shown in this work is evident. While XRD and TGA provide important structural data about the different hydration states, they cannot derive information about critical de/rehydration RH and thermodynamic properties. These were instead obtained by sorption calorimetry, sorption balance and the hydrate pair – humidity buffer method.

Sorption calorimetry was demonstrated to be a powerful tool which can give an almost complete thermodynamic description of a sorption process, although part of a measurement or a whole measurement may take place at metastable conditions. This has to be kept in mind when such experiments are evaluated. When calculating thermodynamic properties with the hydrate pair - humidity buffer method, one has to consider that the accuracy of this method is determined by the hygrometers used to record RH, and thus, it is recommended to crosscheck the results with, for instance, sorption calorimetry measurements. Nevertheless, average values calculated agree well with previously reported data on Na_2SO_4, so despite the accuracy issue, the hydrate pairs – humidity buffer method proved to be a simple, reliable and fast technique to determine stability ranges of different hydration states of minerals and thermodynamic properties of de/rehydration.

3.5.2 Interactions between Na_2SO_4 and water vapor

Na_2SO_4 (thenardite) and $Na_2SO_4 \cdot 10H_2O$ (mirabilite) were used to validate the sorption balance, the sorption calorimetry and the hydrate pair - humidity buffer method. The thenardite - mirabilite equilibrium RH as function of temperature and the enthalpy of reaction (3.1) determined by the humidity buffer method was in agreement with previously published data.

However, during sorption balance and sorption calorimetry tests, the critical RH at which the first absorption process occurred on thenardite was about 87% RH (no water was absorbed below this RH), which corresponds to a solution in metastable equilibrium with respect to thenardite and supersaturated with respect to mirabilite [2],[4],[37]. The presence of a solution at the end of the calorimetry test confirmed the dissolution of thenardite during the measurement. This means that during an absorption process thenardite will tend to dissolve into a metastable solution with no precipitation of mirabilite. This behaviour was also observed by Rodriguez-Navarro et al. [3] with in situ environmental scanning electron microscopy (ESEM) showing no hydration of thenardite into mirabilite but dissolution; during drying they observed crystallization of both thenardite and mirabilite. It has to be considered that our absorption tests took place under unconstrained conditions in a free non-confined space, opposite to what happens in real conditions where the deliquescence and crystallization of salts happen in porous media such as stone and building materials. In those cases a reduction of water activity and different supersaturation levels due to pore size can alter the dissolution behaviour observed in our tests and mirabilite might precipitate upon hydration of thenardite.

At the end of the first absorption process at 87% RH (as measured by sorption calorimetry) the sample has absorbed 2g H_2O/g Na_2SO_4, which agrees perfectly with reported values of thenardite solubility [4],[44]. The second process observed in the sorption calorimetry test, which starts once all the initial salt has been dissolved, is dilution of the initially saturated solution into a more and more dilute solution. This shows a lower mixing enthalpy compared to the dissolution process. Unfortunately, we have not found literature values to compare our enthalpy results because of the metastable nature of the processes.

3.5.3 Interactions between LDH-type cement hydrates and water vapor

Five hydration states of monosulfoaluminate were reported in this chapter: Ms16, Ms14, Ms12, Ms10.5 and Ms9. Ms14 is stable under saturated conditions over 20°C and once it dehydrates to Ms12 it does not rehydrate to Ms14 at room temperature. Ms9 was obtained at a water activity close to zero. A hysteresis in the equilibria Ms10.5-Ms12 and Ms12-Ms14 was observed with XRD and sorption balance measurements, probably due to kinetic constraints or crystal size; it is believed that the larger the crystal size the longer it would take to absorb water within the structure. Another possibility for the hysteretic behaviour is a related activation energy of de/rehydration, which might be needed to remove/introduce water within the hydrate. In minerals such as clays, hysteresis can occur due to a non-reversible ordering due to changes that occur in the structure of the material while water is being absorbed [45]. However, during the hydrate pair – humidity buffer method the equilibrium RH between Ms10.5 and Ms12 agrees with the adsorption regime. Hysteresis will be treated more in detail in the subsequent chapters. Enthalpy of sorption for the reaction Ms9→Ms10.5 was calculated from sorption calorimetry results, while the reaction Ms10.5→Ms12 was evaluated from both sorption calorimetry and the humidity buffer method, resulting in similar values. The sorption isotherms measured with sorption balance and sorption calorimetry were qualitatively and quantitatively similar. A water rich hydration state, Ms16, was found in wet conditions at low temperatures (5 °C) by XRD. Thermodynamic properties of the dehydration for the reaction Ms16→Ms14 were not calculated due to lack of stability even in wet state. The complete stability of Ms16 will be assessed in Chapter 4.

The results clearly show the impact of drying condition on crystalline cement hydrates. At room temperature monosulfoaluminate will decrease about 17% in volume from Ms14 to Ms9. Although in real conditions the dehydration Ms14→Ms12 can occur, it is unlikely for a concrete structure to reach humidities where Ms10.5 and Ms9 are stable, 28.5% and 2% RH, respectively. Nevertheless, these low humidities are easily obtained during sample preparation prior to characterization, which includes vacuum drying, P-drying, solvent exchange and so on, which highlight the importance of our results in connection to the analysis of a hydrated cement paste.

3.6 References

[1]. L.G. Baquerizo, T. Matschei, K.L. Scrivener, M. Saedipour, A. Thorell, L. Wadsö, Methods to determine hydration states of minerals and cement hydrates, Cem. Concr. Res. 65 (2014) 85-95.

[2]. R. Flatt, Salt damage in porous materials: how high supersaturations are generated, J. Cryst. Growth. 242 (2002) 435-454.

[3]. C. Rodriguez-Navarro, E. Doehne, E. Sebastian, How does sodium sulfate crystallize? Implications for the decay and testing of building materials, Cem. Concr. Res. 30 (2000) 1527-1534.

[4]. M. Steiger, S. Asmussen, Crystallization of sodium sulfate phases in porous materials: The phase diagram Na_2SO_4–H_2O and the generation of stress, Geochim. Cosmochim. Acta. 72 (2008) 4291-4306.

[5]. M. Collepardi, A state-of-the-art review on delayed ettringite attack on concrete, Cem. Concr. Compos. 25 (2003) 401-407.

[6]. H.F.W. Taylor, C. Famy, K.L. Scrivener, Delayed ettringite formation, Cem. Concr. Res .31 (2001) 683-693

[7]. F. Bergaya, G. Lagaly, Chapter 1 - General Introduction: Clays, Clay Minerals, and Clay Science, in: F. Bergaya, G. Lagaly (Eds.), Developments in Clay Science, Elsevier, 2013, pp. 1-19.

[8]. C. Forano, U. Costantino, V. Prévot, C. Taviot Gueho, Chapter 14.1 - Layered Double Hydroxides (LDH), in: F. Bergaya, G. Lagaly (Eds.), Developments in Clay Science, Elsevier, 2013, pp. 745-782.

[9]. M.F. Brigatti, E. Galan, B.K.G. Theng, Chapter 2 - Structure and Mineralogy of Clay Minerals. in: F. Bergaya, G. Lagaly (Eds.), Developments in Clay Science, Elsevier, 2013, pp. 21-81.

[10]. L. Baquerizo, T. Matschei, K. Scrivener, The impact of water chemical potential on the hydration states of Monosulfoaluminate, in: Proceedings of the 31th Cem. Concr. Science Conference, London, England, 2011.

[11]. H. Pöllmann, T. Runcevski, R. Dinnebier, Synthesis and characterization of layered carbonated Calcium Aluminate Hydroxi Carbonate Hydrates, in: IV Int. Work Layered Materials, Campinas SP, Brazil, 2012.

[12]. H.F.W. Taylor, Cement Chemistry, second ed., Thomas Telford, London, 1997.

[13]. H.E. Schwiete, U. Ludwig, Crystal structures and properties of cement hydration products (hydrated calcium aluminates and ferrites), in: 5th ISCC, Vol 2, 1968, pp. 37-67.

[14]. H. Pöllmann, Characterization of Different Water Contents of Ettringite and Kuzelite, in: Proceeding of the XII Int. Congress on the Chemistry of Cement, Montreal, Canada, 2007.

[15]. W. Dosch, H. Keller, H. Strassen, 5th ISCC, Vol 2, 1968, pp. 72-77.

[16]. D. Damidot, F.P. Glasser, Thermodynamic investigation of the CaO-Al_2O_3-$CaSO_4$-H_2O at 50°C and 85°C, Cem. Concr. Res. 22 (1992) 1179-1191.

[17]. I. Kaprálik, F. Hanic, Phase relations in the subsystem $C_4A_3\bar{S}$-$C\bar{S}H_2$-CH-H_2O of the system CaO-Al_2O_3-$C\bar{S}$-H_2O referred to hydration of sulphoaluminate cement, Cem Concr Res 19 (1989) 89-102.

[18]. H.J. Kuzel, Initial Hydration Reactions and Mechanisms of Delayed Ettringite Formation in Portland Cements, Cem. Concr. Compos. 18 (1996) 195-203.

[19]. H. Pöllmann, Die Kristallchemie der Neubildungen bei Einwirkung von Schadstoffen auf hydraulische Bindemittel, PhD Dissertation, University of Erlangen-Nuernberg, 1984.

[20]. M.H. Robert, Calcium Aluminate Hydrates and Related Basic Salt Solid Solutions, in: 5th ISCC, Vol 2, 1968, pp. 104-117.

[21]. R. Fischer, H.J. Kuzel, Reinvestigation of the system $C_4A{\cdot}nH_2O$ - $C_4A{\cdot}CO_2{\cdot}nH_2O$, Cem. Concr. Res. 12 (1982) 517-526.

[22]. M. Francois, G. Renaudin, O. Evrard, A Cementitious Compound with Composition $3CaO{\cdot}Al_2O_3{\cdot}CaCO_3{\cdot}11H_2O$, Acta Cryst. C54 (1998) 1214-1217.

[23]. T. Runcevski, R.E. Dinnebier, O.V. Magdysyuk, H. Pöllmann, Crystal structures of calcium hemicarboaluminate and carbonated calcium hemicarboaluminate from synchrotron powder diffraction data, Acta Cryst. B68 (2012) 493-500.

[24]. G. Renaudin, Y. Filinchuk, J. Neubauer, F. Goetz-Neunhoeffer, A comparative structural study of wet and dried ettringite, Cem. Concr. Res. 40 (2010) 370-375.

[25]. K.J. Parkinson, W. Day, Water Vapour Calibration using Salt Hydrate Transitions, J. Exp. Bot. 32 (1981) 411-418.

[26]. G.M. Richardson, R.S. Malthus, Salts for static control of humidity at relatively low levels, J. Appl. Chem. 5 (1955) 557-567,

[27]. I.M. Chou, R.R. Seal II, B.S. Hemingway, Humidity buffers and their application to the studies of dehydration reactions of sulfate salts at 0.1 Mpa, Am. Geophys., Union Trans. 79 (1998) S364.

[28]. I.M. Chou, R.R. Seal II, B.S. Hemingway, Determination of melanterite-rozenite and chalcanthite-bonattite equilibria by humidity measurements at 0.1MPa, Am. Mineral. 87 (2002) 108-114.

[29]. I.M. Chou, R.R. Seal II, Determination of epsomite-hexahydrite equilibria by the humidity-buffer technique at 0.1MPa with implications for phase equilibria in the system $MgSO_4$-H_2O, Astrobiology 3 (2003) 619-630.

[30]. I.M. Chou, R.R. Seal II, Determination of goslarite-bianchite equilibria by the humidity-buffer technique at 0.1MPa, Chem. Geol. 215 (2005) 517-523.

[31]. I.M. Chou, R.R. Seal II, Acquisition and Evaluation of Thermodynamic Data for Morenosite-Retgersite Equilibria at 0.1 MPa, Am. Mineral. 88 (2003) 1943-1948.

[32]. T. Matschei, Thermodynamics of Cement Hydration. PhD Dissertation, University of Aberdeen, 2007.

[33]. L. Greenspan, Humidity fixed points of binary saturated aqueous solutions, J. Res. Nat. Bur. Standards Sect. A 81A (1977) 89–96.

[34]. A. Le Bail, H. Duroy, J.L. Fourquet, Ab-initio structure determination of LiSbWO6 by X-ray powder diffraction, Mat. Res. Bull. 23 (1988) 447-452.

[35]. R. Allmann, Refinement of the hybrid layer structure $[Ca_2Al(OH)_6]^+ \cdot [1/2SO_4 \cdot 3H_2O]^-$, Neues Jb. Miner. Monat. (1977) 136-144.

[36]. J.F. Young, Humidity control in the laboratory using salt solutions – a review, J. Appl. Chem. 17 (1967) 241-245.

[37]. K. Linnow, Salt damage in porous materials: an XRD investigation, PhD dissertation, Universität Hamburg, 2007.

[38]. D.R. Williams, The characterisation of powders by gravimetric water vapor sorption, Int. Labmate. 20 (1995) 40-42.

[39]. L. Wadsö, A. Anderberg, I. Ålund, O. Söderman, An improved method to validate the relative humidity generation in sorption balances, Eur. J. Pharm. Biopharm. 72(1) (2009) 99–104

[40]. L. Wadsö, N. Markova, Comparison of three methods to find the vapor activity of a hydration step, Eur. J. Pharm. Biopharm. 51(1) (2001) 77-81.

[41]. L. Wadsö, N. Markova, A double twin isothermal microcalorimeter, Thermochim. Acta 360 (2000) 101-107.

[42]. L. Wadsö, N. Markova, A method to simultaneously determine sorption isotherms and sorption enthalpies with a double twin microcalorimeter, Rev. Sci. Instrum. 73 (2002) 2743-2754.

[43]. S.E.D. Hamad, A study of the reaction $Na_2SO_4{\cdot}10H_2O \rightarrow Na_2SO_4 + 10\ H_2O$ in the temperature range 0 to 25°C, Thermochim. Acta 17 (1976) 85–96.

[44]. P. Marliacy, R. Solimand, M. Bouroukb, L. Schuffenecker, Thermodynamics of crystallization of sodium sulfate decahydrate in H_2O-NaCl-Na_2SO_4: application to $Na_2SO_4{\cdot}10H_2O$-based latent heat storage materials, Thermochim. Acta 344 (2000) 85-94.

[45]. M.H. Fu, Z. Zhang, P.F. Low, Changes in the properties of a montmorillonite-water system during the adsorption and desorption of water: hysteresis, Clays Clay Miner. 38 (1990) 485-492

4 Hydration states of AFm phases

The results presented in this chapter have been submitted for publication [1].

4.1 Introduction

AFm (Al_2O_3–Fe_2O_3–mono) phases are hydrated tetracalcium aluminate-ferrite compounds belonging to the lamellar double hydroxide family. They are formed during the hydration process of Portland and calcium aluminate cements. AFm phases are composed of positively charged main layers $[Ca_2(Al,Fe)(OH)_6]^+$ and negatively charged interlayers $[X{\bullet}nH_2O]^-$ where X is either one monovalent anion or half a divalent anion. Since Fe substitution for Al is limited in cement paste [2], in this study we focus on the aluminium AFm phases. The general formulae (in cement notation[1]) $C_4AX_2H_n$ for monovalent anions (OH^-, NO_3^-) and C_4AXH_n for divalent anions (SO_4^{2-}, CO_3^{2-}) are generally used in cement chemistry [3]. The substitution of Ca by the smaller Al atoms (one Ca atom in three by one Al) distorts the structure of the principal layer which allows each Ca atom to coordinate the oxygen atom of an interlayer H_2O molecule in addition to its six OH^- groups [3]. A crystal may contain more than one species of X anions. The interlayer thickness depends on the nature of the X anion and the amount of interlayer water n [3]-[4]. Figure 4:1 shows a schematic of the lamellar AFm structure.

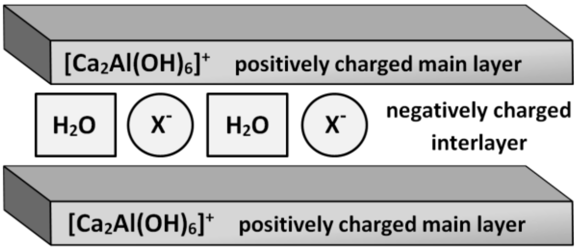
[Ca₂Al(OH)₆]⁺ positively charged main layer
H₂O
X⁻
H₂O
X⁻
negatively charged interlayer
[Ca₂Al(OH)₆]⁺ positively charged main layer

Figure 4:1 Schematic figure of the lamellar structure of an AFm phase.

The anion content depends on the cement composition. Thus in a typical Portland cement (PC) the common anions are hydroxide (OH^-) and sulfate (SO_4^{2-}). If PC is blended with limestone, the anion will be a carbonate (CO_3^{2-}) [19] and in case it is blended with slag or fly ash, the interlayer anion might be an aluminosilicate ($AlSiO_8H_8^-$). The anion also depends on the service environment, e.g., in marine applications, chloride (Cl^-) can displace other anions and form AFm phases such as Friedel's salt and Kuzel's salt [3],[5]. A short summary of the phases studied in this thesis and their different hydration states follows. The phases are denoted by an abbreviation[2] followed by an index which denotes the water content in moles, thus the 14 H_2O hydration state of monosulfoaluminate will be denoted as Ms14.

4.1.1 Monosulfoaluminate (Ms)

Monosulfoaluminate is a common cement hydrate formed during hydration of cements with $CaCO_3$ content <1% [6] by reaction of the initially formed ettringite with the remaining tricalcium aluminate. It is an analogue of the natural occurring mineral kuzelite, whose crystal structure was refined by Allman [6]. Its formula is $C_4A\hat{S}H_{6+x}$ (which we will denote as Ms(6+*x*) in this study), where *x* is the interlayer water content, which according to several references may vary from 2 to 10, depending on the exposure temperature and RH [3],[7]-[14]. However, there is no unified data showing the stability range of this hydrate except a recent study by Baquerizo et al. [15] that reports the hydration states Ms14, Ms12, Ms10.5 and Ms9, and the thermodynamic properties related to their formation (also reported in Chapter 3). In this chapter, the previous results are complemented with low temperature studies investigating the stability of the water-rich hydration state Ms16.

4.1.2 Hydroxy–AFm (OH-AFm)

The first studies related to the structural description of hydroxy-AFm (also called "C_4A hydrates") were published by Ahmed et al. [16] and Buttler et al. [17]. Its formula can be written as C_4AH_{7+x} (or OH-AFm(7+*x*)), where the anions are two $(OH)^-$ groups and the interlayer water content *x* varies from 0 to 12 according to the literature [3]-[4],[10],[13]-[14],[16]-[17], although there are contradictions in terms of water content and the related layer thickness at different conditions. The occurrence of OH-AFm in hydrated Portland cement pastes is not likely, mainly due to the presence of sulfates and carbonates, favouring the precipitation of monosulfoaluminate, OH-SO_4-AFm solid solutions [19] and carboaluminate phases [20], and also because of its metastable nature with respect to hydrogarnet (C_3AH_6) and portlandite (CH) [21] at temperatures >20°C.

4.1.3 Monocarboaluminate (Mc)

The crystal structure of monocarboaluminate $C_4A\hat{C}H_{11}$ was first determined by Fisher and Kuzel [18]. The lamellar structure contains only one type of structural element, with $[Ca_4(Al)_2(OH)_{12}]^{2+}$ as the main layer and $[CO_3^{2-}\bullet 5H_2O]^{2-}$ as the interlayer content. Francois et al. [22] later refined the crystal structure of monocarboaluminate. Their results are well accepted, and basically state that the main difference with respect to other AFm phases is that one oxygen atom of the carbonate (CO_3^{2-}) group occupies the seventh coordination site of one out of four Ca atoms contained in the main layer. Additionally, every oxygen atom of the carbonate groups contributes to the formation of relatively strong hydrogen bonds with water molecules, providing a strong cohesion between the inter- and the main layer. This seems to be a plausible explanation for why monocarboaluminate is comparatively stable over a wide range of exposure conditions. For this reason, Mc11 is the only hydration state reported at 25 °C, although lower water contents have been reported with increasing temperature [13],[18]. In a later work by Renaudin et al. [23], two modifications of monocarboaluminate were reported, an ordered and a disordered structure with different stacking sequences of the layers. Another proof of the high stability of monocarboaluminate has been presented by Moon et al. [24] with synchrotron X-ray diffraction studies under high pressure (4.3 GPa), showing a perfectly reversible pressure-induced dehydration with no critical effect on the bulk modulus due to its strong framework.

4.1.4 Hemicarboaluminate (Hc)

Hemicarboaluminate ($C_4A\hat{C}_{0.5}H_{12}$ or Hc12) is a carbonated AFm phase similar to monocarboaluminate, where half a carbonate group ($0.5CO_3^{2-}$) has been replaced by an $(OH)^-$ group. Fisher and Kuzel [18] indexed the powder diffraction pattern but the crystal structure was not solved. In contrast to other AFm phases, Hc12 shows slight differences in basal spacing probably due to limited solid solutions and/or slight differences in interlayer water [3],[13],[18]. Other hydration states than Hc12 have been reported for higher temperatures [13],[14],[18]. Moon et al. [25] demonstrated that the application of pressures > 0.5 GPa results in a volume contraction due to pressure-induced dehydration and partial removal of the weakly bound interlayer water.

Runcevski et al. [26] solved the crystal structure of synthetic hemicarboaluminate and refined it in the R3c space group of the trigonal crystal system. However, another phase, called carbonated hemicarboaluminate (cHc) was also found together with Hc due to partial carbonation. Its crystal structure was also solved, showing the same space group as Hc but with lower *c* lattice parameter. When Hc was exposed to increasing temperatures in an atmosphere with a reduced amount of CO_2, cHc was formed. It should be mentioned that this cHc has been previously reported as a lower hydration state of Hc rather than as a new phase [18].

4.1.5 Strätlingite (Str)

Strätlingite (C_2ASH_8), also called gehlenite hydrate, is a cement hydrate which can occur as a hydration product in slag-, metakaolin- or fly ash blended cements, as well as in hydrated high-alumina cements [27]-[28]. According to structural data published by Rinaldi et al. [29], strätlingite, with a formula $C_2ASH_{7.25}$, has the same principal layer constitution as other AFm phases, but with an aluminosilicate anion as interlayer, which is a double tetrahedral sheet of composition $[(T,\square)_4(OH,O)_8]^-$, where □ is a vacant tetrahedral site and T can be Si or Al. This phase is more complex than other AFm phases, due to the vacant sites and partial occupancy of some groups, including hydroxyl sites and water molecules, which can alter the water content of this phase. This is the likely reason why strätlingite is usually reported as Str8 although structural data by Rinaldi presents a total water content of 7.25 moles (Str7.25). Similar to hemicarboaluminate, strätlingite shows an abrupt contraction in volume when subjected to high pressures (up to 5 GPa) [25]. These volume changes can be associated with a structural transition or with the removal of weakly bound interlayer water.

4.1.6 Relevance of this study

Presently, there is neither complete experimental data nor thermodynamic properties associated with changes of hydration states in AFm phases. In the present chapter, these missing data are derived using the multi-method approach shown in chapter 3 and in [15], which includes the combined use of X-ray diffraction (XRD), thermogravimetric analysis (TGA), sorption balance measurements, sorption calorimetry, and the hydrate pair - humidity buffer method. The obtained information is important in order to assess the stability of complex cementitious systems containing, among others, AFm phases at unsaturated conditions, i.e. at < 100% RH. In addition, these data enable the prediction of the mineralogical constitution of cement pastes made from new binder combinations, and will further help to predict phase changes in concrete structures following environmental fluctuations (for example, severe drying at high temperatures, etc.).

Notice that this thesis investigates stoichiometric hydrates formed by the absorption of water molecules in the hydrated crystal structure. There can, however, also be adsorption (on surfaces) and capillary condensation (in pores), but as the specific surfaces and surface/volume-ratios of our samples are comparatively low, we believe that such effects are small except in the high RH region in a few cases.

4.2 Experimental methods

The methodology used to determine the properties of the different hydration states of the AFm phases studied is shown in Chapter 3.

For the sample balance measurements and the sorption calorimetry, the sample masses ranged between 5 to 15 mg, and 50 to 100 mg, respectively.

The salt pair - humidity buffer method was used to study transition RH between two adjacent hydration states as well as the thermodynamic properties associated with these changes on hydroxy-AFm.

In addition, a physisorption analyser ASAP™ 2020 (Micromeritics) (adsorptive gas N_2) was used to measure the surface area and the complete isotherm (adsorption/desorption) of initially degassed (high vacuum at 50 °C) samples. The results can be found in Annex B.

4.3 Results and discussion

The results obtained for the different hydration states and their thermodynamic properties are presented for each of the studied phases. Simplified sorption isotherms and a summary of the derived thermodynamic properties of the different hydration states are shown at the end of this section.

4.3.1 Monocarboaluminate

Figure 4:2 shows the typical hexagonal morphology of monocarboaluminate. The surface area corresponds to 5.1 m^2/g (as measured with ASAP™ 2020). XRD patterns of some samples aged at different conditions are shown in Figure 4:3. Lattice parameters were refined using the crystal structure published by Francois et al. [22] (ICSD# 59327) and the values are presented in Figure 4:4. The refined parameters do not present any significant change in the range 5% - 100% RH at any of the studied temperatures (5 °C, 25 °C and 50 °C). The hydration state at these conditions corresponds to Mc11 as confirmed by TGA. Some hydrogarnet impurities were observed at 50 °C. In order to study the lowest hydration state, a sample consisting of pure Mc11 was vacuum dried for 15 hours at 25°C. The sample dehydrates but still some Mc11 is observed as shown in Figure 4:3, probably due to incomplete dehydration or partial rehydration during XRD sample preparation and/or measurement. The TGA measurement of the vacuum dried sample shows a water content of around 9.3 H_2O. Since the sample was not completely dehydrated it was assumed that this lower hydration state corresponds to Mc9. An in situ measurement using a humidity chamber shows that under nitrogen flow and 80 °C (during 70 min), Mc11 completely dehydrates into Mc9 (Figure 4:3). Attempts to index this lower hydration state were unsuccessful due to the presence of impurities and low quality of the XRD patterns. Thus, it was assumed that Mc9 keeps the same space group as Mc11. Further research is needed to correctly index this lower hydration state.

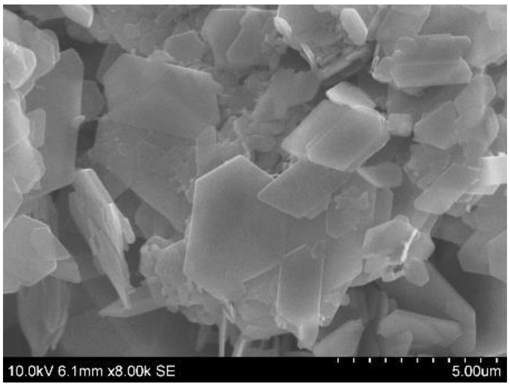

Figure 4:2 SEM pictures of monocarboaluminate.

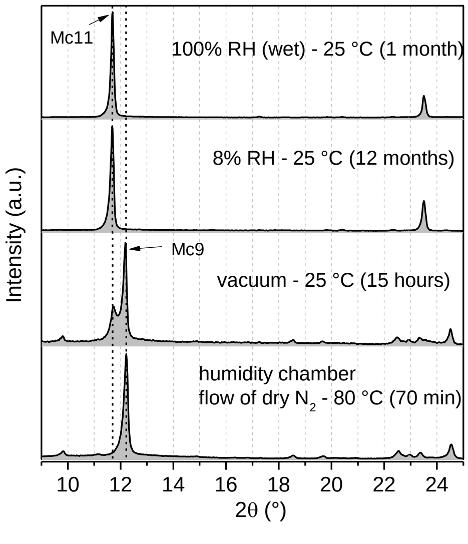

Figure 4:3 XRD patterns of some Mc samples dried at different conditions. Each sample dried at 5°C, 25°C and 50°C down to 5% RH (inside glass bottles with salt solutions) were composed of Mc11, for this reason not every pattern is shown. Under vacuum Mc12 starts to dehydrate into Mc9, which is rapidly formed at high temperatures and low RH as shown in the humidity chamber test. The small peak at around 9.8° may correspond to Mc9.

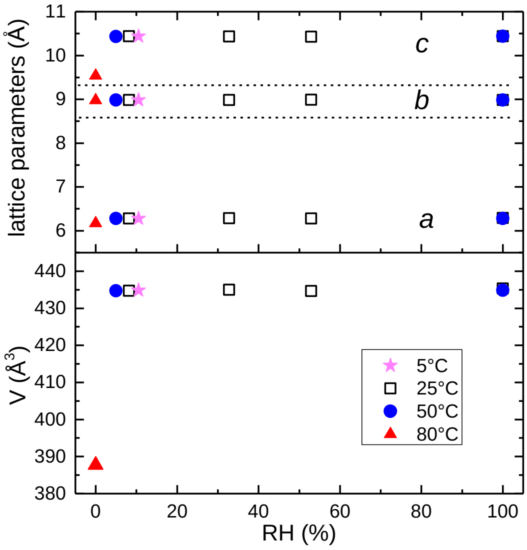

Figure 4:4 Refined lattice parameters of Mc dried at 5, 25 and 50 °C and different RHs during 12-24 months. Sample at 80 °C was dried in the humidity chamber under N_2 flow during 70 min before the measurement.

The sorption balance results are shown in Figure 4:5. The graph was normalized assuming a water content of 11 H_2O (Mc11) at 20% RH (as measured by TGA). The absorption/desorption behaviour was completely reversible. During testing the minimum total water content achieved was approximately 10.45 H_2O i.e. the sample consisted probably of a mix of Mc11 and Mc9, because it did not reach equilibrium after 12 hours under pure N_2 flow, even though the initial sample mass was only 5.6 mg. The desorption kinetics can thus be considered as rather slow.

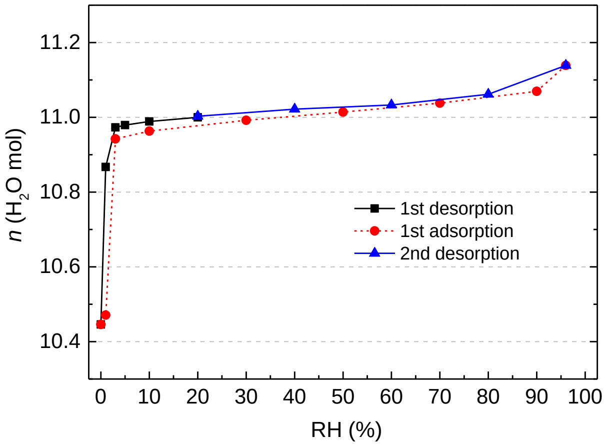

Figure 4:5 Water content of monocarboaluminate as function of RH at 25 °C measured by sorption balance. Water contents larger than 11 H_2O probably correspond to water adsorbed on the surface of the crystals or capillary condensation between the crystals. The lower water content corresponds to 10.45 H_2O due to incomplete dehydration during the test.

The sorption calorimetry results of initially vacuum dried monocarboaluminate (Figure 4:6) shows a single absorption step as previously identified by sorption balance measurements. The initial sample corresponds to Mc9.3, probably due to incomplete dehydration during vacuum drying or partial rehydration before the start of the test. But, since the mixing enthalpy (ΔH_{mix}) is constant for the whole process (-29.4 kJ/mol H_2O), it can be assumed that the rehydration process follows the reaction:

$$\mathrm{Mc9(s)} + 2\mathrm{H_2O(g)} \rightarrow \mathrm{Mc11(s)} \qquad (4.1)$$

The related sorption enthalpy ΔH_{sorp} can be calculated according to Eq. (2.5) and the total enthalpy of reaction ($\Delta H_{\mathrm{r}}°$) with Eq. (2.6). In order to calculate the standard Gibbs free energy of reaction ($\Delta G_{\mathrm{r}}°$) it was assumed that the absorption process takes place at 1%RH at 25 °C as observed by sorption balance and sorption calorimetry. Then $\Delta G_{\mathrm{r}}°$ for reaction (4.1) can be calculated according to Eq. (2.2) and the standard entropy of reaction $\Delta S_r°$ with Eq. (2.4). A summary of the thermodynamic properties determined is given in Table 4:1 and Table 4:2, and a simplified sorption isotherm at 25 °C is shown in Figure 4:27 at the end of this section. For more details about the calculation of the thermodynamic properties of de/rehydration using sorption calorimetry see Chapter 3.

According to our results monocarboaluminate only dehydrates when exposed to very low RH (< 1%) and/or high temperatures. The high stability of Mc is most likely due to the formation of strong hydrogen bonds between the carbonate groups and interlayer water, which seems to contribute to the strong cohesion between layer and interlayer [22].

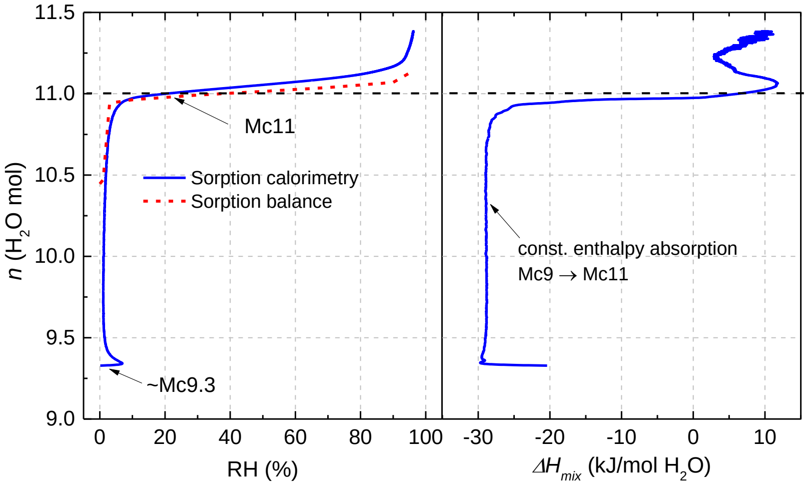

Figure 4:6 Sorption calorimetry results showing the calculated sorption isotherm (left) and mixing enthalpy (right) of dry monocarboaluminate at 25°C (for comparison the isotherm measured by sorption balance is superimposed in the left graph). Graph was normalized assuming a water content of 11 H_2O at 20% RH.

4.3.2 Hemicarboaluminate

Figure 4:7 shows the hexagonal crystal morphology of synthetic hemicarboaluminate; some cubic hydrogarnet (C_3AH_6) impurities can be observed. The surface area measured with ASAP™ 2020 corresponds to 2.7 m^2/g.

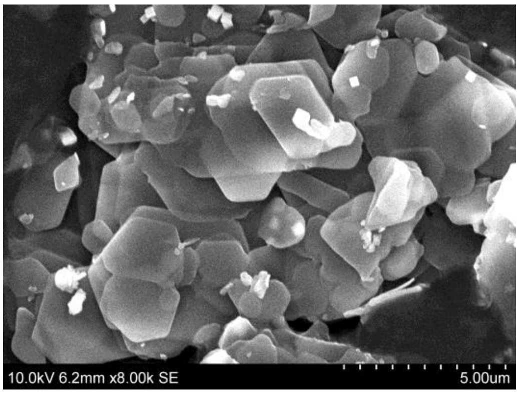

Figure 4:7 SEM pictures of hemicarboaluminate

XRD diffractograms on samples dried at 5, 25 and 50 °C and different RHs during 6 to 30 months and under vacuum for several hours are shown in Figure 4:8). Hydrogarnet was always observed in the samples aged at 25 and 50 °C, in large amounts in the latter, varying from 25 to 45 wt.% (measured by Rietveld analysis). Some portlandite (CH) impurities were also observed at 25 °C, but in very small amounts <1wt.%. In the samples conditioned at 50 °C, portlandite content was significant, varying from 2 to 10 wt.%. Also, calcite was observed in some samples (up to 4%), most likely due to carbonation.

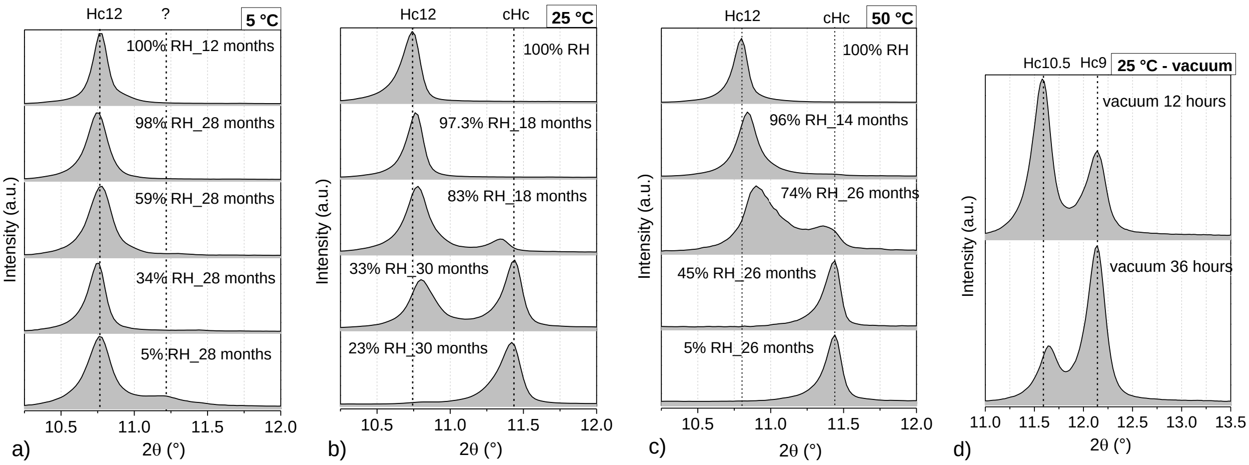

Figure 4:8 XRD patterns of hemicarboaluminate dried at a) 5 °C, b) 25 °C and c) 50 °C at different RHs inside hermetic glass bottles, and d) vacuum dried at 25 °C during 12 h and 36 h.

The lattice parameters were refined using the crystal structure published by Runcevski et al. [26].The results are presented in Figure 4:9. Some samples show a shoulder-type peak together with the (0 0 1) reflections, probably due to disorder in the stacking of the layers, transition between higher to lower hydration states or partial carbonation. For simplicity, these reflections were omitted during refinement.

The stable hydration state at high RHs (> 95% RH) at all temperatures is Hc12, as confirmed by TGA and in agreement with data reported by Fisher and Kuzel [18], although at 100% RH (wet state) and

50 °C up to 10% of hydrogarnet was present in the sample (measured by Rietveld analysis). Hc12 was the stable hydration state at 5 °C at all RHs studied, although some dehydration was observed at 5% RH. A second (0 0 6) reflection at 2θ ~ 11.4° (d ~ 7.75 Å) starts to appear at 25 and 50 °C with decreasing RH, which may correspond to a lower hydration state of Hc or to a solid solution between Hc and Mc. TGA of a sample aged at 25 °C and 23% RH, which contains mostly this secondary phase, confirms a higher CO_2 and lower water content, which agrees with values reported by Runcevski et al. [26] for a phase called carbonated hemicarboaluminate (cHc or $C_4A\hat{C}_{0.8}H_{10.2}$). Since it could not be proved that this phase corresponds to a lower hydration state of hemicarboaluminate, it was assumed that the lower hydration state present at 25 °C and 50 °C is cHc10.2. It seems that the formation of carbonated hemicarboaluminate is promoted with increasing temperature and decreasing RH in the presence of small amounts of CO_2.

The lowest hydration states of hemicarboaluminate were studied using a sample initially aged at 98% RH and 5 °C, composed of almost pure Hc12 as measured by XRD, and then vacuum dried for 12 and 36 hours at 25 °C. As observed in Figure 4:8d, two different hydration states are present in the sample with main reflections at 2θ ~ 11.65° and 12.21° (d ~ 7.59 Å and 7.24 Å, respectively). The lattice parameters of these two lower hydration states were refined assuming that the space group is the same as that reported by Runcevski et al. [26]. After 36 hours there are still 2 hydration states, probably due to incomplete dehydration or to partial rehydration during testing. The water content of the 36 hours vacuum dried sample was 9.5 H_2O, but since the sample was not completely dehydrated it was assumed that this lower hydration state corresponds to 9 H_2O, or Hc9. The other hydration state was assigned as Hc10.5, whose water content was deduced by sorption calorimetry as shown below. No presence of hydrogarnet or portlandite was observed in the samples and the CO_2 weight loss (measured by TGA) corresponds to Hc rather than to cHc, which indicates that the sample did not carbonate during vacuum drying.

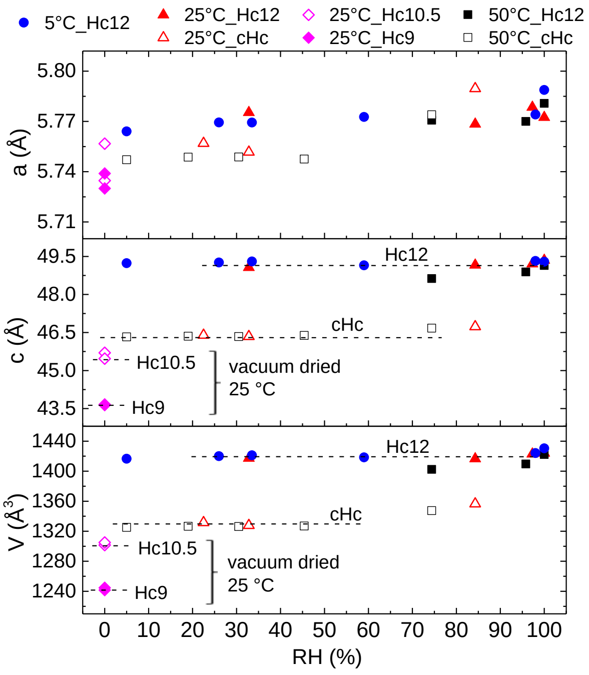

Figure 4:9 Refined lattice parameters of Hc dried at 5, 25 and 50 °C. Under vacuum at 25 °C two lower hydration states Hc10.5 and Hc9 were identified by sorption calorimetry and TGA.

In order to study the stability of cHc10.2, a sample initially dried at 50 °C and 5% RH, composed of cHc, hydrogarnet and portlandite, was exposed to high RH at 5 °C and 25 °C and tested by XRD after 30 days (Figure 4:10). The sample did rehydrate and the refined lattice parameters are close but do not completely fit with Hc12. Whether this rehydration product corresponds to Hc12 or to a higher hydration state of cHc is not clear. The sample rehydrated at 5 °C and 88% RH contained lower quantities of hydrogarnet. Further studies are required to better understand the stability and formation of cHc.

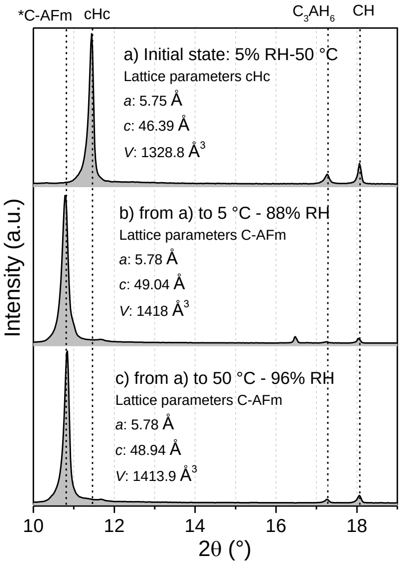

*Figure 4:10 XRD patterns of a sample initially containing cHc, hydrogarnet (C_3AH_6) and portlandite (CH), and subsequently exposed to high RH at 5 and 50 °C. Shift of the main reflection towards lower 2ϑ indicates higher water content. *C-AFm refers to a carbonated AFm phase of unknown composition.*

A sorption balance experiment was carried out on a sample composed of Hc12 as confirmed by XRD and TGA. The resulting sorption isotherm is shown in Figure 4:11. In order to normalize the water content it was assumed (rather arbitrarily) that at 80% RH the sample is composed of pure Hc12 with negligible adsorbed water or capillary condensation. The isotherm presents two stepwise de/re-hydration processes, the first one from 0 to 2% RH, and the second one from 4 to 10% RH approximately. From 12 to 90% RH the sample undergoes a steady absorption/desorption of water, probably due to slow kinetics of de/rehydration. The minimum water content was not reached during the test (sample was still losing water during the first desorption under pure N_2 flow), so the values should be seen as indications of the absorption/desorption behaviour, rather than as quantitative results.

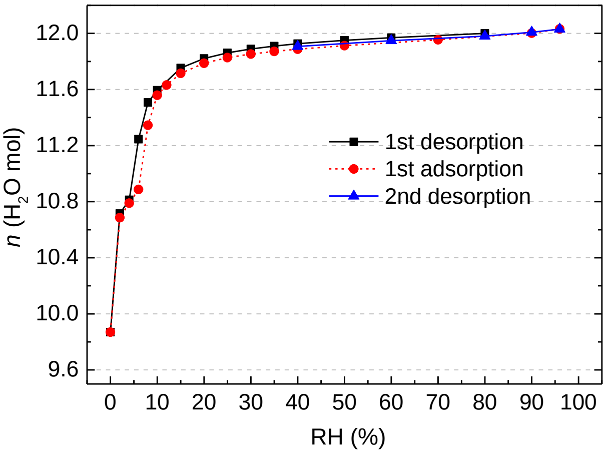

Figure 4:11 Sorption isotherm of hemicarboaluminate at 25 °C measured by the sorption balance method.

Sorption calorimetry was carried out on a hemicarboaluminate sample similar to the one used in the sorption balance test, but vacuum dried overnight. The calculated sorption isotherm and the mixing enthalpy associated with the absorption of water are presented in Figure 4:12. For comparison the isotherm measured by the sorption balance is also shown in Figure 4:12. The graph was also normalized assuming Hc12 as the stable hydration state at 80% RH. The rehydration behaviour is very similar to that observed with the sorption balance except that complete dehydration during the sorption balance test was not achieved. According to the mixing enthalpy plot, none of the absorption processes is at constant enthalpy. It seems that the transition between different hydration states of hemicarboaluminate is a complex process which involves metastable hydrates with slightly different water content, which is confirmed by the scatter in lattice parameters as shown in Figure 4:9. Since the mixing enthalpy values are not constant, they were calculated from the integral of the curve ΔH_{mix} vs. n in the water content regions of interest (as Figure 4:12 right, with axes swapped). The standard Gibbs free energy of reaction $\Delta G_r°$ was calculated according to Eq. (2.2) assuming a change of hydration state taking place at 1% and 7% RH for the transitions Hc9↔Hc10.5 and Hc10.5↔Hc12, respectively. A summary of thermodynamic properties and a simplified sorption isotherm and volume of hemicarboaluminate are given in the next section.

As observed in the experimental results, hemicarboaluminate presents a complex absorption/desorption behaviour, as evidenced by the shoulder-like peak together with the (0 0 1) planes reflections in the XRD patterns, the dehydration and decomposition into cHc with increasing temperature and decreasing RH, and the non-constant enthalpy absorption behaviour. Also the large amount of C_3AH_6 at high temperatures is an indication of the low stability of Hc at such conditions.

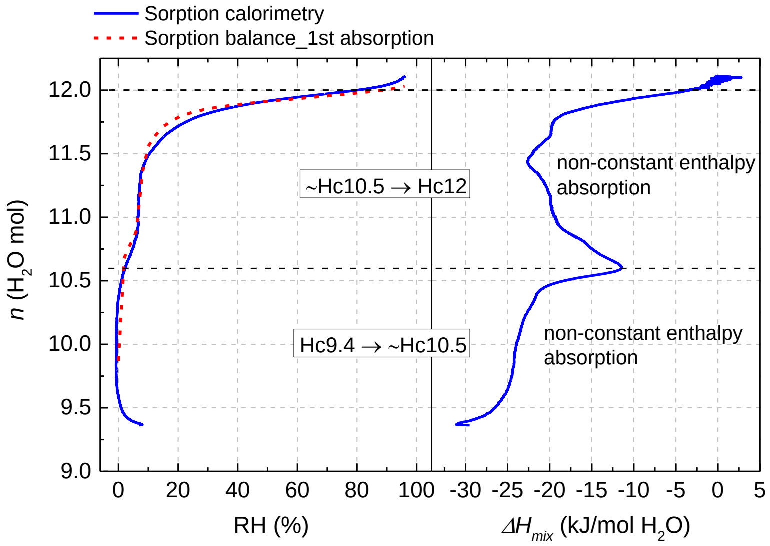

Figure 4:12 Calculated sorption isotherm (left) and mixing enthalpy (right) of initially dry hemicarboaluminate at 25°C from sorption calorimetry testing (for comparison the isotherm measured by sorption balance is superpose in the left graph). Notice the two stepwise water uptakes and the variability of the mixing enthalpy during absorption.

Whether the formation of cHc from Hc12 is time dependent, even in the absence of significant CO_2 impurities, remains unknown. For this reason sorption balance and sorption calorimetry experiments were crucial in order to enable a fast determination of the different hydration states of Hc, because tests were carried out relatively fast (3-5 days), avoiding the formation of cHc. It is surprising that cHc has never been reported in hydrated cement pastes, even when both Hc and Mc are present in the sample. This suggests that it only forms in the presence of gaseous CO_2, which would tend to yield calcite in a paste.

4.3.3 Strätlingite

Figure 4:13a shows the typical hexagonal platelets morphology of synthetic strätlingite, comparable to the one presented by Matschei [21]. The surface area corresponds to 17 m^2/g (as measured with ASAP™ 2020). X-ray diffractograms of strätlingite dried at different conditions are very similar. The main difference can be seen in shifting (0 0 1) reflections. As shown in Figure 4:14, at 25 °C from 100% RH down to 8% RH, a steady and small decrease of the (0 0 1) basal space is observed, followed by a more abrupt shift at 0% RH (vacuum dried). Samples at 5, 25 and 50 °C were conditioned for a minimum of 12 months. The complete XRD patterns of the samples indicate good crystallinity (see Figure 4:13b), as opposed to other reported studies on synthetic strätlingite [21]. Some calcite (Cc) and monocarboaluminate (Mc) impurities are observed in the samples, although Mc was not always detected and, when present, it was in amounts lower than 2 wt.-% according to Rietveld analysis. It has been reported that C-S-H might be present as an impurity when synthesizing strätlingite [21]. We have disregarded its presence in our samples because the N_2 sorption isotherm measurement carried out on one sample (not shown here) presented a sorption/desorption behaviour similar to that observed on other studied AFm phases, with no significant hysteresis, in contrast to what is observed for C-S-H, either synthetic or occurring in Portland cement pastes.

The refined lattice parameters and volume of the lattice are summarized in Figure 4:15. It can be seen that the lattice parameters *a* and *c* decrease with decreasing humidity, and thus the volume of the lattice shrinks slightly during drying.

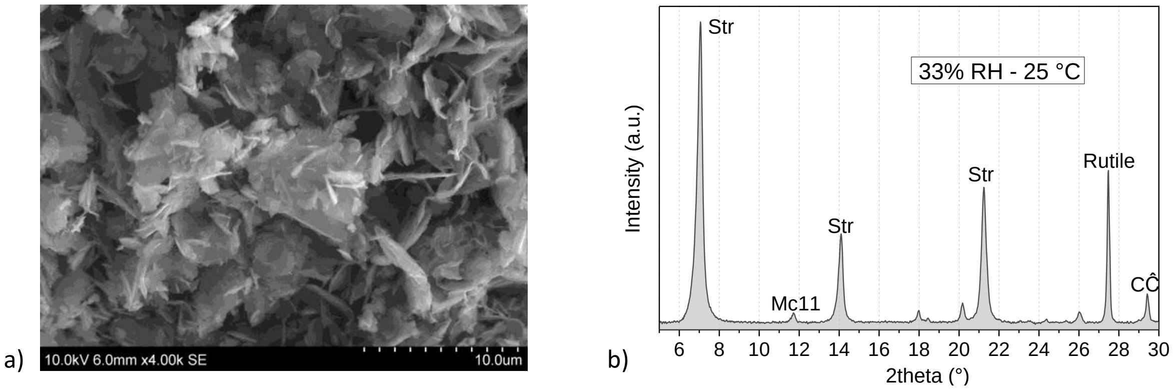

Figure 4:13 a) SEM pictures of strätlingite. b) XRD pattern of a strätlingite sample dried at 33% RH showing good crystallinity

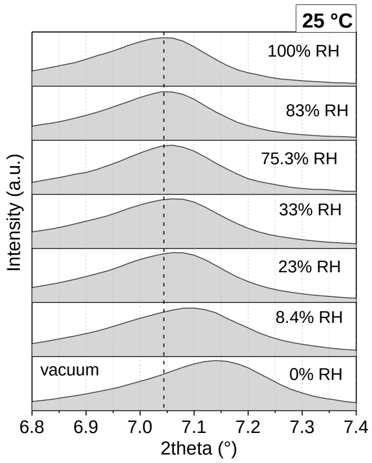

Figure 4:14 XRD patterns of strätlingite dried at 25 °C and different RHs, showing the shift of the (0 0 1) reflection towards higher 2ϑ values (lower d-spacing). A similar trend was observed on samples aged at 5 °C and 50 °C.

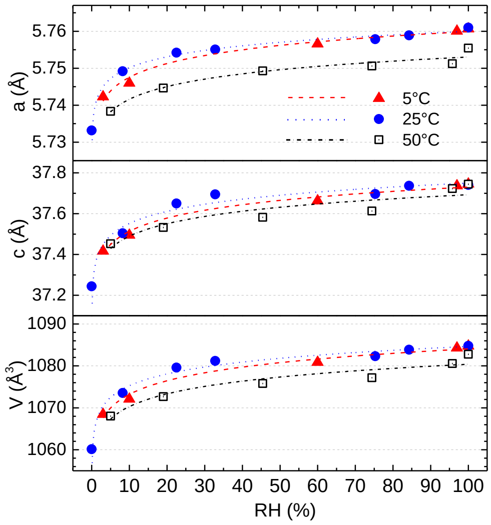

Figure 4:15 Refined lattice parameters at 5 °C, 25 °C and 50 °C (sample at 0% RH was vacuum dried).

A sorption balance measurement was done on a sample which was previously equilibrated at 33% RH for 1 year. The sorption isotherm (Figure 4:16) was normalized assuming a water content of 7.5 H_2O at 30% RH and a purity of 95%, as previously measured by TGA. There was no hysteresis observed in the desorption/absorption cycles. This seems a characteristic of most of the AFm phases and confirms the lack of a porous phase (C-S-H) within the sample. A stepwise uptake/loss of water is observed between 0% and 5% RH and there is a steady absorption of water in the range 10% - 85% RH, which agrees with the volume changes calculated by XRD. The minimum mass at 0% RH was not achieved during 10 hours under pure N_2 flow. Above 85% RH most of the weight increase is probably caused by capillary condensation.

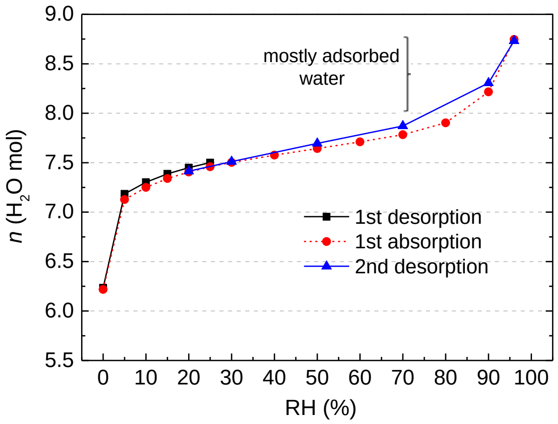

Figure 4:16 Sorption isotherm of strätlingite at 25 °C measured by sorption balance.

Sorption isotherm and mixing enthalpy plots calculated from sorption calorimetry are shown in Figure 4:17. For the analysis it was assumed that the sample contained 5 wt.% calcite (as measured by TGA). Two hydration processes can be differentiated, similar to what is observed by the sorption balance method and XRD:

1) The first absorption process takes place from 0 to about 5% RH, with water content increasing from 5.8 to 7 H_2O. Since TGA measurements in vacuum dried samples give *n* values close to 5.6 H_2O, it was considered that the lowest hydration state corresponds to Str5.5. Then the first absorption process follows the reaction:

$$Str5.5(s) + 1.5H_2O(g) \rightarrow Str7(s) \qquad (4.2)$$

Thermodynamic properties were calculated with Eqs. (2.2)-(2.4). To calculate ΔG_r° it was assumed that reaction (4.2) takes place at 3% RH. A mixing enthalpy of -22.5 kJ/mol H_2O (Figure 4:17) was used to determine ΔH_r°. A summary of the derived thermodynamic properties is given in Table 4:1.

2) During the second rehydration stage the mixing enthalpy varies as function of the RH, from -18 kJ/mol H_2O at ~5% RH to 0 kJ/mol H_2O at ~80% RH. Above 80% RH, ΔH_{mix} values close to zero confirm the adsorption of water on the surface of the sample rather than absorption inside the crystals.

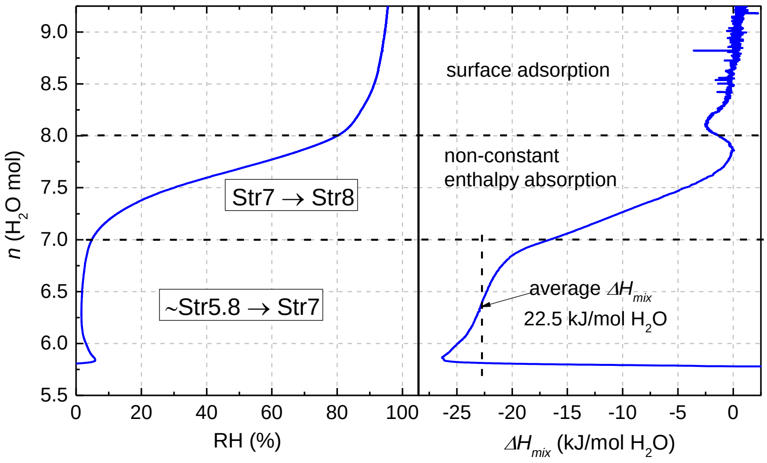

Figure 4:17 Calculated sorption isotherm (left) and measured mixing enthalpy (right) of initially dry strätlingite at 25 °C by sorption calorimetry. The graph was normalized assuming Str7.5 at 30% RH.

A summary graph (Figure 4:18) was plotted using results obtained with the different techniques. Notice that, although the volume of the lattice is not necessarily proportional to the water content, in the case of strätlingite, it seems that these properties are correlated. Above 80% RH no further increase in volume is observed, confirming that the large amounts of water measured by sorption balance measurements, sorption calorimetry, and TGA, are from capillary condensation.

According to our results, the lowest and the highest hydration states of strätlingite corresponds to Str5.5 and Str8, respectively. The chemical composition reported by Rinaldi et al. [29] corresponds to Str7.25, probably due to the lower occupancy (0.25) of a water molecule in the center of the 6-membered rings of the double tetrahedral layers in the interlayer. If one considers full occupancy of this water molecule the water content of strätlingite would correspond to Str8, which is the hydration state we measured at high RH. From 5 to 80% RH there is a rather constant variation of water content, which approximately corresponds to a change of hydration state from Str7 to Str8. We conclude that this change corresponds to an increase in the occupancy of the interlayer water molecules located in between the 6-membered rings of the double tetrahedral layers, which varies from 0 to 1, at 5 and 85% RH, respectively. The stepwise absorption/desorption taking place from 0 to 5% RH (Str5.5 ↔ Str7) is most likely due to the removal or uptake of interlayer water molecules directly bound to the two Ca atoms which are part of the main octahedral layer. This means that close to 0% RH only 0.5 out of 2 H_2O bound to the Ca atoms are still present, which gives a slight shrinkage of the crystal.

According to XRD results, volume changes on strätlingite from 0 to 100% RH at 25 °C were insignificant (~ 2.3%), although water content varies considerably, from 5.5 to 8 H_2O mol as already mentioned. This means that strätlingite may act as a reservoir, losing or absorbing water during drying or rewetting, while keeping its volume almost unchanged. The reason for the nearly constant volume is the large double tetrahedral (Si/Al=1) interlayer, keeping the volume relatively constant while allowing the incorporation of 3 H_2O mol, 2 bonded to the Ca atoms of the interlayer and 1 in the center of the 6-membered rings of the double tetrahedral layers in the interlayer.

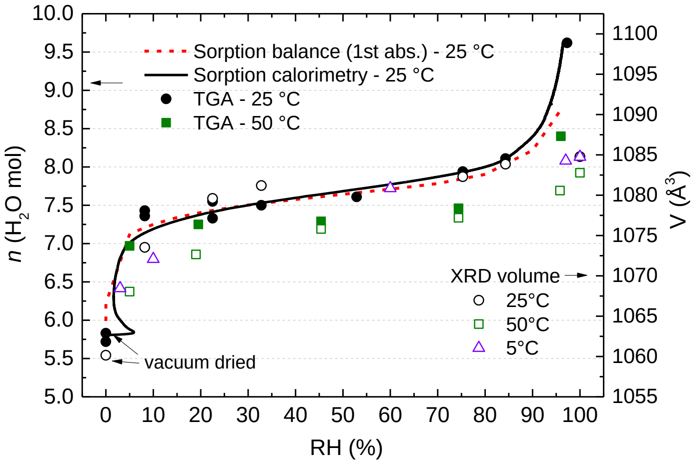

Figure 4:18 Summary graph showing water content and volume of the lattice of strätlingite as a function of RH at different temperatures. TGA tests were carried out in samples aged during 12 to 30 months. Proportionality between water content and volume is observed for strätlingite, but not for other AFm phases.

4.3.4 Hydroxy-AFm

The morphology of synthetic hydroxy-AFm can be observed in Figure 4:19. The particle sizes are rather heterogeneous and seem to be formed by stacking of thin crystals. XRD tests were done on samples dried at 5 and 25 °C and different RHs (Figure 4:20). Samples aged at 5 °C were tested after 24 months using the humidity chamber. Samples conditioned at 25 °C were investigated after 6 months of drying. Due to the metastability of OH-AFm with increasing temperatures the samples aged at 50 °C completely decomposed into hydrogarnet and portlandite and thus they are not included in the analysis.

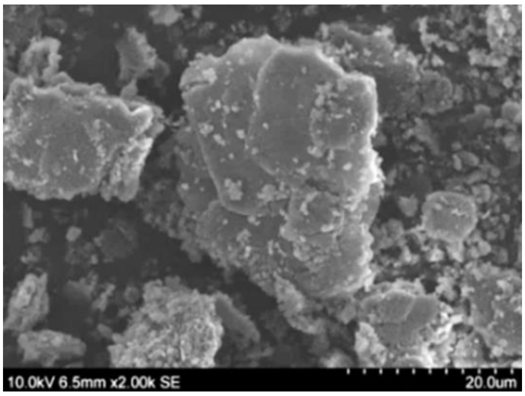

Figure 4:19 SEM pictures of hydroxy-AFm.

As shown in Figure 4:20a and b, at 5 and 25°C three different hydration states were observed in the range from 5% to 100% RH: OH-AFm19, OH-AFm13 and OH-AFm11. The water content of the two latter was confirmed by TGA. The water content of the higher hydration state could not be determined because the sample contained significant amounts of adsorbed water on the surface of the crystals. For this reason its water content was considered to be 19 H_2O (or OH-AFm19), which is the commonly reported hydration state at high RH [3],[10],[18]. A lower hydration state occurring at very low RH (close to 0), OH-AFm7, has been reported by Roberts [14], with a basal space (c') of ca. 5.5 Å. In order to determine the existence of this lower hydration state, a sample consisting of mainly OH-AFm13 was vacuum dried for 48 hours. The XRD pattern shows weak reflections (see Figure 4:20b) and two different basal spaces can be at around 7.23 Å and 6.61 Å, together with a broad hump at approximately 5.35 Å. It seems that the sample undergoes a decomposition process during severe drying rather than dehydrating to a new hydration state. Further research is needed to evaluate the dehydration and/or decomposition of OH-AFm subjected to severe drying.

The refined lattice parameters are presented in Figure 4:20c. It was assumed that all the hydration states belong to the same crystal system and space group, R-3c, as reported by Aruja [30] for the α1 polymorph of OH-AFm19.

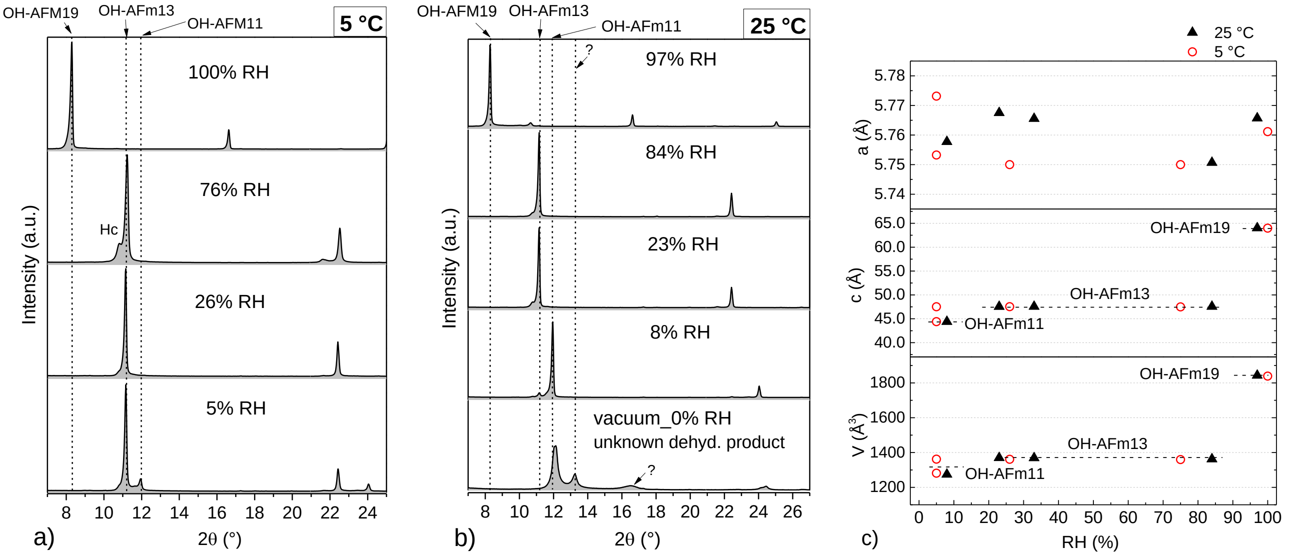

Figure 4:20 XRD patterns of OH-AFm dried at a) 5 °C and b) 25 °C. c) Refined lattice parameter a and c and volume V of samples dried at 5 and 25 °C.

A sorption balance measurement was carried out on a hydroxy-AFm sample initially conditioned for one year at 26% RH and 5°C, corresponding to OH-AFm13 (as confirmed by XRD and TGA) is shown in Figure 4:21 shows the measured sorption isotherm. The water content was normalized assuming OH-AFm13 at 30% RH (as measured by TGA). A step de/re-hydration process is observed between 10-15% RH, corresponding to the change of hydration state OH-AFm13 ↔ OH-AFm11. A further de/re-hydration step is observed below 5% RH (under pure N2 flow) but after 24 hours not much water loss was observed. The transition OH-AFm13 ↔ OH-AFm19 was not observed probably due to slow kinetics of rehydration.

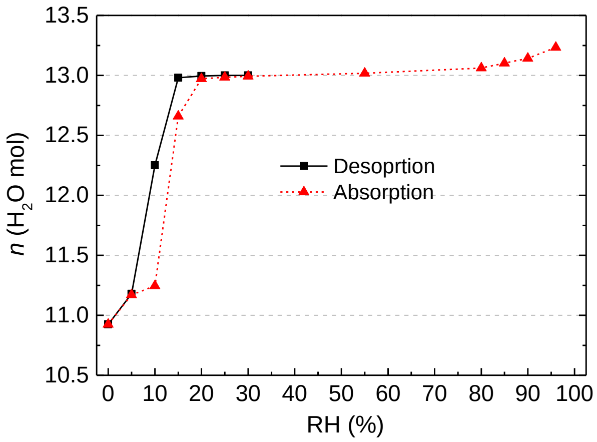

Figure 4:21 Sorption isotherm measured on OH-AFm by sorption balance at 25 °C. The graph was normalized assuming n = 13 H_2O at 30% RH as measured by TGA.

Sorption calorimetry was done on a vacuum dried OH-AFm sample. The calculated sorption isotherm and the mixing enthalpy associated with the absorption of water are shown in Figure 4:22. For comparison, the sorption isotherm measured by the sorption balance is also plotted. Two different rehydration processes are observed. The first absorption step takes place from 0 to 10% RH, showing two distinctive mixing enthalpy values. Since decomposition rather that change of hydration state was observed at very low RH, this rehydration step is shown but not further analyzed. The second rehydration process, from 11.5 to 13 H_2O was considered to be representative of the reaction:

$$\text{OH-AFm11(s)} + 2H_2O(g) \rightarrow \text{OH-AFm13(s)} \quad (4.3)$$

There is a small absorption of water at around 45% RH probably due to delayed rehydration of some of the decomposition products formed during the initial vacuum drying (see Figure 4:22). The enthalpy of mixing of reaction (4.3) was calculated from the integral of the curve ΔH_{mix} vs n from 11.5 H_2O to 13 H_2O. A summary of the thermodynamic properties calculated with Eqs. (2.2) – (2.6) is given in Table 4:1.

There seems to be a further uptake of water taking place above 95% RH, most likely due to the hydrate transition:

$$\text{OH-AFm13(s)} + 6H_2O(g) \rightarrow \text{OH-AFm19(s)} \quad (4.4)$$

During this rehydration step the enthalpy of mixing varies from 0 to 7 kJ/mol H_2O. A bulk absorption process usually has negative values. However, there is a large uncertainty of the enthalpy of mixing measured at water activities over 0.95 (or 95% RH) as mentioned in Chapter 3. In any case the results indicate that the enthalpy of mixing value of this absorption process is small (close to zero).

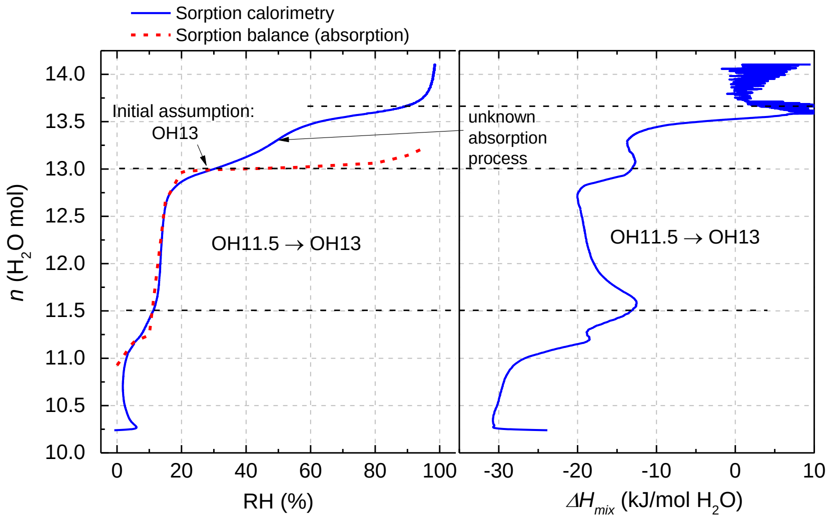

Figure 4:22 Calculated sorption isotherm (left) and mixing enthalpy (right) of initially dry OH-AFm at 25 °C by sorption calorimetry. Water content was normalized assuming n = 13 H2O at 30% RH. During vacuum drying the sample partially decomposed, for this reason different absorption processes (varying enthalpy) are observed.

The hydrate pair – humidity buffer method was used to investigate the critical RH for a temperature dependent hydration state transition. The standard thermodynamic properties $\Delta G_r°$, $\Delta H_r°$ and $\Delta S_r°$ were calculated from the results shown in Figure 4:23 using Eqs. (2.2), (2.3) and (2.4) and are listed in Table 4:1. There is good agreement between the values measured by sorption calorimetry and those calculated using the hydrate pair – humidity buffer method for the hydrate transition OH-AFm13↔OH-AFm11. Although the change of hydration state OH-AFm19↔OH-AFm13 was not well determined by sorption balance measurements and sorption calorimetry, the data shown in Figure 4:23 was used to calculate the thermodynamic properties.

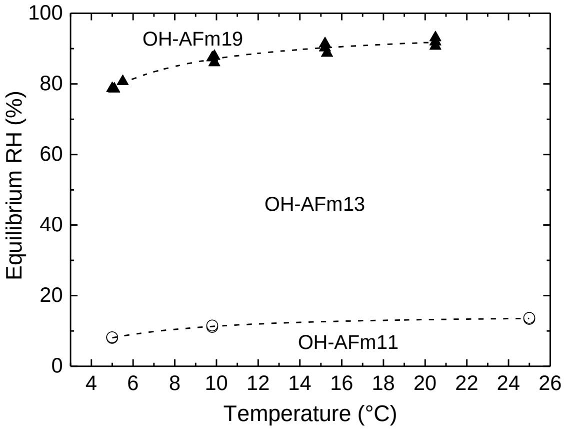

Figure 4:23 OH-AFm10 – OH-AFm13 and OH-AFm13 – OH-AFm11 equilibria at 1 bar measured with the hydrate pair – humidity buffer method.

To summarise, hydroxy-AFm shows well defined sequences of hydration states as function of temperature. Nevertheless, when exposed to very low RH (vacuum drying) OH-AFm11 seems to undergo decomposition into a less structured hydrate rather than a change of hydration state. This was concluded due to the large decrease in peak intensity and occurrence of a hump at lower basal space. At 50 °C, OH-AFm completely decomposes into hydrogarnet and portlandite, and even at 25 °C large amounts of these impurities were observed when dried for long periods. At low temperatures OH-AFm was the main hydrate, together with minor Hc impurities due to carbonation. Although OH-AFm presents the larger crystal volume shrinkage when drying from OH-AFm19 to OH-AFm 13 at 92.5% RH and 25°C (approximately 25.5 vol.%), its formation in hydrated cement is very unlikely due to its metastability with respect to hydrogarnet at normal curing conditions and the presence of sulfate and carbonate in Portland cements which stabilize other AFm phases [19].

4.3.5 Monosulfoaluminate

Different hydration states of monosulfoaluminate were previously reported in Chapter 3, corresponding to Ms14, Ms12, Ms10.5 and Ms9. The existence of a water-rich hydration state, Ms16, was noted but not fully characterised and is therefore further investigated in this chapter.

In the previous chapter we noted that Ms16 is apparently preferably formed at lower temperatures. Therefore, a Ms16 sample stored at 5°C was used for the initial stability (Figure 4:24). The sample was initially conditioned in situ at 97% RH in the XRD humidity chamber for 1 hour and subsequently investigated at lower RHs down to 2.5%. Some Ms12 was still present in the initial sample resulting from incomplete rehydration during the sample equilibration. When the RH is decreased to 85%, the Ms12 reflection at 2θ ~ 9.83° starts to increase in intensity, and at 80% RH this increase is observed for Ms12 and Ms14 reflections (see inset in Figure 4:24). With further decrease of RH, Ms16 completely disappears at 60% RH and Ms14 and Ms12 intensities continue increasing. The results indicate that Ms14 is a transition hydrate between Ms16 and Ms12 and that it is potentially metastable at low temperatures. At 50% RH a hydration state with reflections close to Ms10.5 (a_o 5.74 Å and c_o 24.7 Å) is observed and its (0 0 1) reflection increases in intensity down to 2.5% RH. This hydration state was not observed in the tests carried out at 25 °C and 50 °C reported in Chapter 3. No further investigation was done in this study on the stability of this hydration state. When the sample was dried at 2.5% RH and is re-exposed to 97% RH, the crystals start to rehydrate back into Ms16. However, small amounts of Ms12 and Ms14 remain.

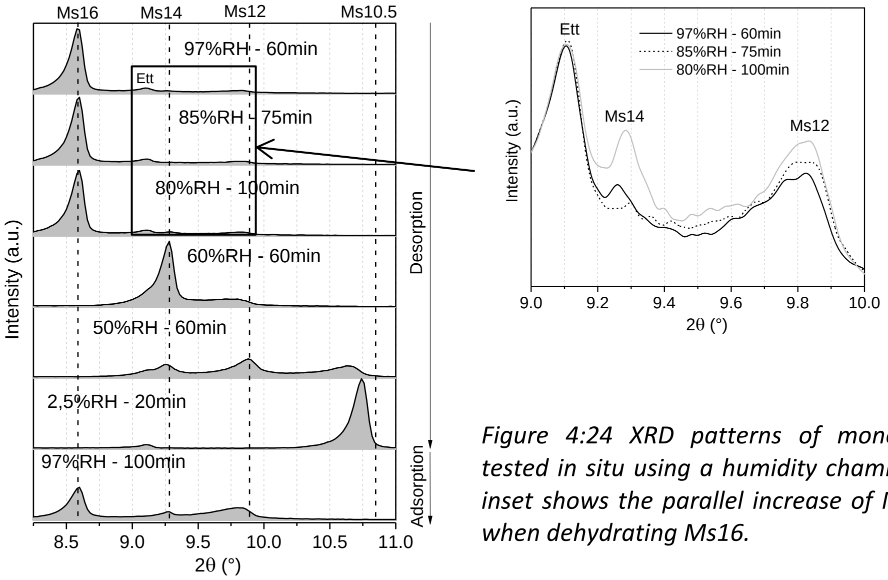

Figure 4:24 XRD patterns of monosulfoaluminate tested in situ using a humidity chamber at 5 °C. The inset shows the parallel increase of Ms14 and Ms12 when dehydrating Ms16.

In order to determine the impact of higher temperatures on the stability of Ms16, a short in situ XRD experiment was done in the humidity chamber. Initially the temperature was stepwise increased from 5 °C to 18 °C at a constant RH of 92% (see Figure 4:25). As mentioned before, small amounts of Ms12 were present at the beginning of the experiment. . From 5 °C to 12 °C Ms16 seems to be a persistent hydration state; this is concluded from similar intensities of the basal reflections in this temperature range. A further temperature increase to 18 °C (at constant RH of 92%) leads to a rapid dehydration of Ms16 first to Ms14 and then to Ms12, indicating again a potential metastability of Ms14 at low temperatures.

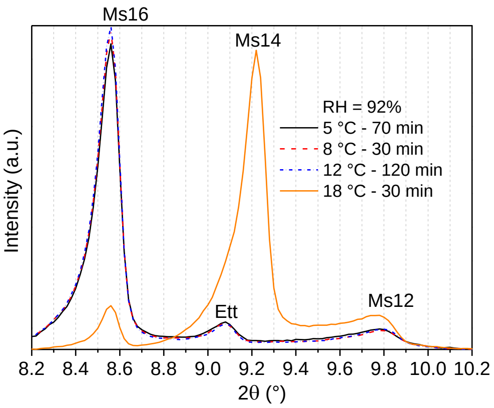

Figure 4:25 XRD patterns of monosulfoaluminate tested in situ using a humidity chamber at 92% RH from 5 °C to 18 °C.

The approximate stability of Ms16 is shown in Figure 4:26. Thermodynamic properties of Ms16 (shown in Table 4:2) were empirically determined to fit experimental results, assuming that this hydration state will dehydrate at 85% and 92% RH, at 5 °C and 14 °C, respectively.

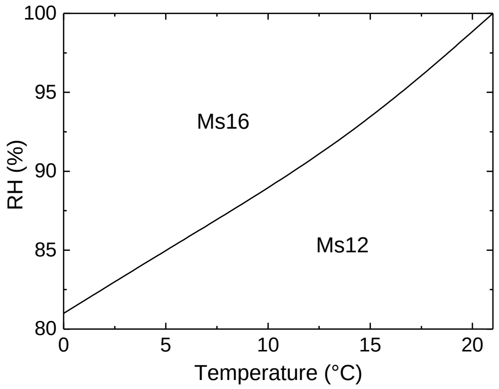

Figure 4:26 Approximate stability regions of Ms16 and Ms12 < 20 °C. Ms14 does not appear in the graph because it was assumed that it is metastable at low temperatures.

4.3.6 Summary of results

In this chapter the impact of relative humidity and temperature on the formation of different hydration states of the most important AFm phases was investigated. To summarise the findings simplified sorption isotherms and volume change plots of the lattice of monocarboaluminate, hemicarboaluminate, hydroxy-AFm, strätlingite and monosulfoaluminate at 25 °C are presented in Figure 4:27.

Based on the results it was possible to derive a thermodynamic dataset which enables a significantly improved prediction of the mineralogical constitution of hydrated cement paste at unsaturated conditions i.e. RH < 100%.Thermodynamic properties of the changes of hydration states of the aforementioned phases are summarized in Table 4:1. Standard molar thermodynamic properties of all the different hydration states, including density values, are presented in Table 4:2.

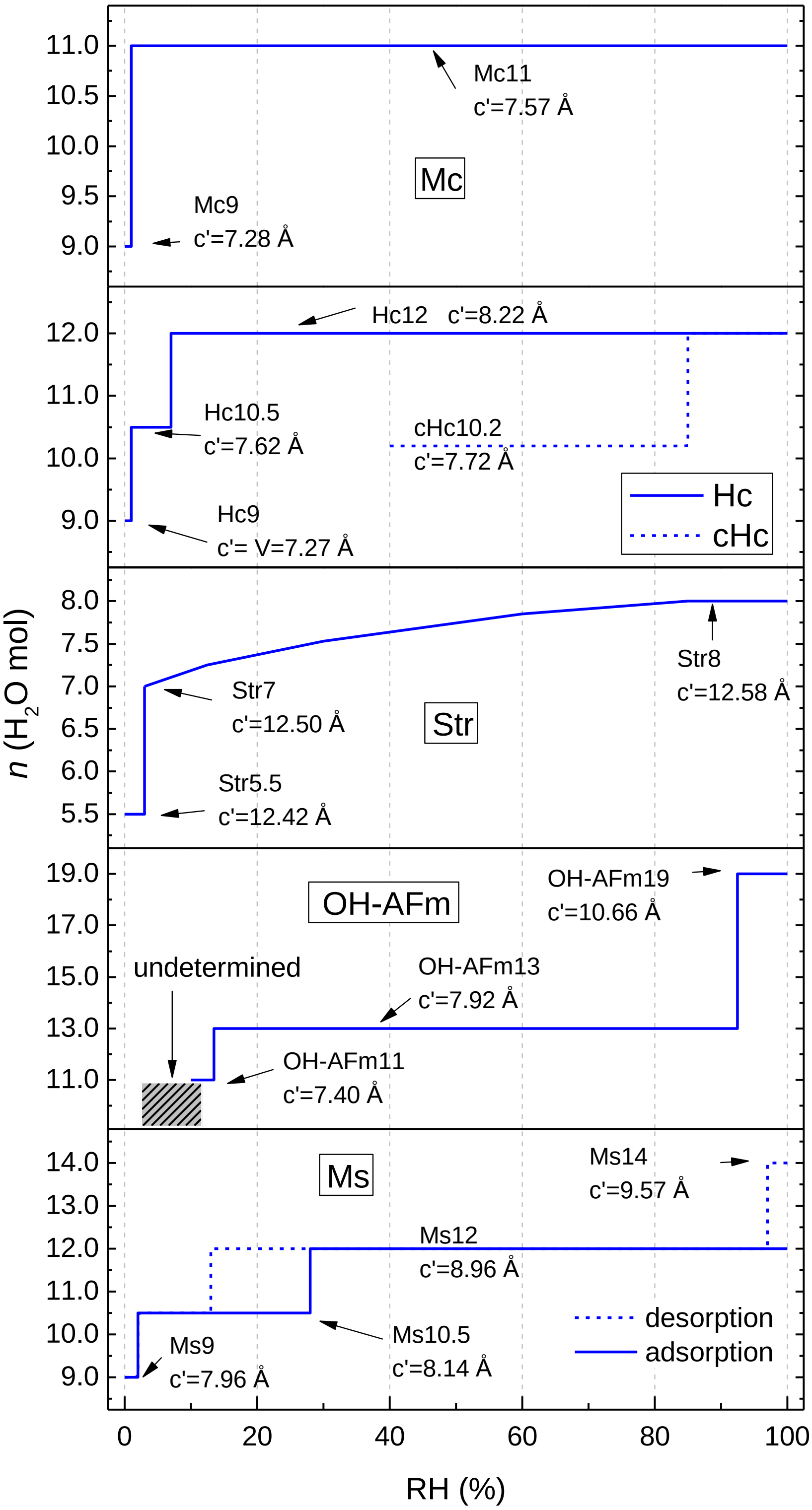

Figure 4:27 Summary graph showing the different hydration states of strätlingite (Str), monocarboaluminate (Mc), hemicarboaluminate (Hc), carbonated hemicarboaluminate (cHc) and hydroxy-AFm (OH-AFm) as function of RH at 25 °C. The sorption isotherm corresponding to cHc is an approximation based on experimental results. The isotherms only consider water that is part of the crystalline samples (structural + interlayer), excluding adsorbed or capillary condensed water, which is negligible on AFm phases due to their low surface area (compared to C-S-H). The interlayer distance c' is the average of several measurements.

Table 4:1 Derived thermodynamic data for the changes of hydration states of AFm phases at 25 °C and 1 bar.

Reaction	RH of change of hyd. state (%)	ΔG_r° (kJ/mol)	[a] ΔH_{mix}° (kJ/mol)	ΔH_r° (kJ/mol)	ΔS_r° (J/mol K)
Monocarboaluminate					
Mc9(s)+2H_2O(g) → Mc11(s)	1.0	-39.8	-58.6	-146.6	-358.2
Hemicarboaluminate					
Hc10.5(s)+1.5H_2O(g) → Hc12(s)	7.0	-22.6	-27.2	-93.2	-236.5
Hc9(s)+1.5H_2O(g) → Hc10.5(s)	1.0	-29.9	-33.2	-99.2	-232.4
Strätlingite					
Str7(s)+H_2O(g) → Str8(s)	20.0 [b]	-12.5	-6.9	-50.9	-128.7
Str5.5(s)+1.5H_2O(g) → Str7(s)	2.0	-25.8	-33.8	-99.8	-351.7
Hydroxy-AFm					
OH-AFm13(s)+6H_2O(g) → OH-AFm19(s)	92.5	-52.2	-37.1	-301.1	-835.0
OH-AFm11(s)+2H_2O(g) → OH-AFm13(s)	13.5	-26.9	-35.4 [c]	-123.4 [c]	-323.7
			-30.6 [d]	-118.6 [d]	-307.6
			-33.0 [e]	-121.0 [e]	-315.6
Monosulfoaluminate					
Ms12(s)+2H_2O(g) → Ms14(s)	97.0	-17.2	9.7	-78.3	-205.2
Ms10.5(s)+1.5H_2O(g) → Ms12(s)	28.5	-17.4	-17.2	-83.2	-220.5
Ms12(s) → Ms10.5(s)+1.5H_2O(g) [f]	12.0	20.5	17.2	83.2	210.2
Ms9(s)+1.5H_2O(g) → Ms10.5(s)	2.0	-27.3	-36.8	-102.8	-253.3

[a] Corresponds to the enthalpy of mixing, excluding the enthalpy associated with the condensation of water

[b] Although the change of hydration state Str8↔Str7 does not take place stepwise, for the calculations it was assumed that it occurs at 20% RH in order to use Str8 and Str7 as end-members of an ideal solid solution Str8-Str7.

[c] From sorption calorimetry

[d] From the hydrate pair – humidity buffer method

[e] Average value

[f] Calculated with the desorption branch of the isotherm

4.4 Discussion and implications on volume stability of cement paste

All the cement hydrates studied in this work existed in different hydration states depending on the external conditions (temperature and RH). From Figure 4:28 the sensitivity of some phases and the high volume stability of others with respect to drying are evident. The most stable hydrate studied was monocarboaluminate, since very low RH (close to zero) and/or high temperatures are required to dehydrate the phase. In absence of CO_2, hemicarboaluminate is also stable, but it tends to decompose at high temperatures and with prolonged times of drying into cHc, hydrogarnet and portlandite. Its stability might be linked to the crystal structure and the bonding of the anion in the interlayer but, since no structural data on atomic positions was obtained in this study, this hypothesis could not be confirmed. Strätlingite shows very good volume stability, although its water content varies considerably. This means that strätlingite may act as a reservoir, losing or absorbing water during drying or rewetting, while keeping its volume almost unchanged due to the large double tetrahedral (Si/Al=1) interlayer. Even though hydroxy-AFm was the hydrate with the larger crystal volume shrinkage when drying, its formation is improbable due to its metastability with respect to hydrogarnet and the presence of other ions in solution which stabilize other AFm phases. A higher hydration state of monosulfoaluminate was observed at low temperatures and its thermodynamic properties determined. Higher hydration states at lower temperatures were not detected in any of the other AFm phases studied.

Table 4:2 Standard molar thermodynamic properties of the studied cement hydrates at 25 °C and 1 bar.

Phase	$\Delta G_f°$ (kJ/mol)	$\Delta H_f°$ (kJ/mol)	$S°$ (J/mol K)	$Cp°$ (J/mol K) [b]	Density (kg/m^3)	$V°$ (cm^3/mol)	Ref.
Monosulfoaluminate							
Ms16 – $C_4A\bar{S}H_{16}$	-8726.8	-9930.5	975.0	1114.8	1981.7	350.5	t.s.
Ms14 – $C_4A\bar{S}H_{14}$	-8252.9	-9321.8	960.9	1028.5	1985.9	331.6	t.s.
Ms12 – $C_4A\bar{S}H_{12}$	-7778.4	-8758.6	791.6	948.4	2007.7	310.1	t.s.
Ms10.5 – $C_4A\bar{S}H_{10.5}$	-7417.9	-8311.9	731.2	888.3	2114.9	281.6	t.s.
Ms10.5 – $C_4A\bar{S}H_{10.5}$ [a]	-7414.9	-8311.9	720.9	888.3	2114.9	281.6	t.s.
Ms9 – $C_4A\bar{S}H_9$	-7047.6	-7845.5	703.6	828.2	2070.2	274.6	t.s.
Monocarboaluminate							
Mc11 – $C_4A\hat{C}H_{11}$	-7337.5	-8250.0	656.9	881.4	2170.0	262.0	[31]
Mc9 – $C_4A\hat{C}H_9$	-6840.3	-7618.6	640.6	801.2	2279.6	233.6	t.s.
Hemicarboaluminate							
Hc12 – $C_4A\hat{C}_{0.5}H_{12}$	-7336.0	-8270.0	712.6	905.8	1984.0	284.5	[31]
Hc10.5 – $C_4A\hat{C}_{0.5}H_{10.5}$	-6970.3	-7813.3	668.3	845.7	2057.1	261.3	t.s.
Hc9 – $C_4A\hat{C}_{0.5}H_9$	-6597.4	-7350.5	619.8	785.6	2047.4	249.3	t.s.
Strätlingite							
Str8 – C_2ASH_8	-5705.1	-6360.0	546.2	602.7	1935.8	216.1	[31]
Str7 – C_2ASH_7 [c]	-5464.0	-6066.8	487.6	562.6	1857.6	215.5	t.s.
Str5.5 – $C_2ASH_{5.5}$	-5095.2	-5603.4	454.8	502.5	1754.2	212.8	t.s.
Hydroxy-AFm							
OH-AFm19 – C_4AH_{19}	-8749.9	-10017.9	1120.0	1382.4	1816.3	368.7	[32]
OH-AFm13 – C_4AH_{13}	-7325.7	-8262.4	831.5	1142.0	2041.8	274.5	t.s.
OH-AFm11 – C_4AH_{11}	-6841.4	-7656.6	772.6	1061.8	2038.2	257.3	t.s.

t.s.: this study

[a] Calculated with the desorption branch of the isotherm.

[b] $C_p°$ was calculated assuming $\Delta Cp = 0$ for the changes of hydration states shown in Table 4:1.

[c] Str7 must be used together with Str8 in an ideal solid solution.

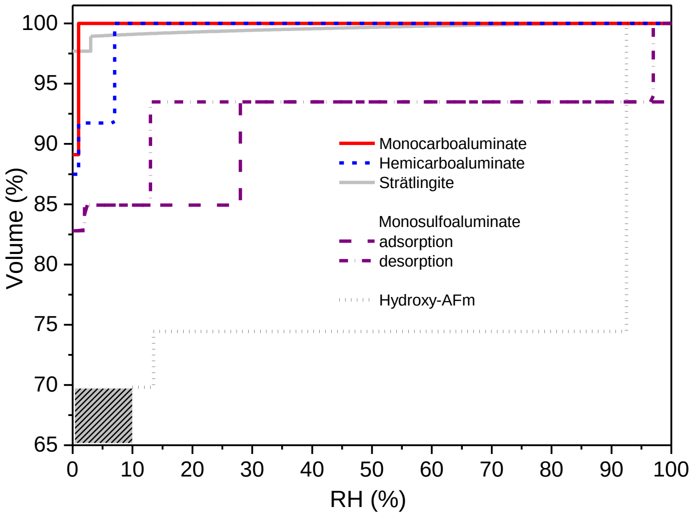

Figure 4:28 Volume changes of the AFm phases studied as function of RH at 25 °C. 100% volume corresponds to the higher hydration state of each phase.

From a practical perspective it is known that concrete expands slightly with a gain in moisture and contracts with a loss in moisture [33], mainly due to absorption/desorption of water from the main cement hydrate present in Portland based binders, C-S-H. Although the impact of AFm phases is rather small in Portland cements, their influence in volume stability might be significant in cementitious systems containing SCM with high alumina content, such as metakaolin, calcined clay, and some types of slag and fly ash, where large amounts of AFm phases can be formed. In this work it was shown that some AFm phases present very good volume stability, which means that cementitious systems containing large amounts of monocarboaluminate and strätlingite, for instance, should be almost insensitive to changes of environmental conditions (temperature and RH), resulting in a potentially improved resistance to drying shrinkage or swelling. Although the volume stability of such systems should be better, their strength might not be as good as typical Portland cement binders because of the absence of C-S-H, which is the responsible of the strength development. This is something that requires further research.

Also an important fact is that every studied AFm phase loses water when exposed to very low RH (close to 0%) and increasing temperature, conditions that can easily be achieved during drying methods such as vacuum drying, P-drying, oven drying, etc. Also different methods to stop hydration of cementitious systems, including solvent exchange with acetone and isopropanol, may impact the water content of some AFm phases due to a decrease in the water activity of the sample. This is something that has to be taken into account when preparing a sample prior characterization, especially by XRD and TGA.

The current study presents, for the first time, a complete picture of the stability of the most important AFm phases present in cement and concrete when exposed to varying external conditions, including critical conditions of de/rehydration and thermodynamic properties related to changes of hydration states. This data will enable the modelling of the volume stability of cementitious systems exposed to different external conditions and opens the possibility to engineer cement mixes less sensitive to changing exposure conditions, which can positively impact the performance and durability of cement based materials.

4.5 References

[1]. L.G. Baquerizo, T. Matschei, K.L. Scrivener, M. Saedipour, L. Wadsö, L. Hydration states of AFm phases, submitted to Cement and Concrete Research.

[2]. B.Z. Dilnesa, E. Wieland, B. Lothenbach, R. Dähn, K.L. Scrivener, Fe-containing phases in hydrated cements, Cem. Concr. Res. 58 (2014) 45-55.

[3]. H.F.W. Taylor, Cement Chemistry, second ed., Thomas Telford, London, 1997.

[4]. H.F.W. Taylor, Crystal structures of some double hydroxide minerals, Mineralogical Magazine 39 (1973) 377-389.

[5]. A. Mesbah, M. Francois, C. Cau-dit-Coumes, F. Frizon, Y. Filinchuk, F. Leroux, J. Ravaux, G. Renaudin, Crystal structure of Kuzel's salt $3CaO{\cdot}Al_2O_3{\cdot}1/2CaSO_4{\cdot}1/2CaCl_2{\cdot}11H_2O$ determined by synchrotron powder diffraction, Cem. Concr. Res. 41 (2011) 504-509.

[6]. H.J. Kuzel, Initial Hydration Reactions and Mechanisms of Delayed Ettringite Formation in Portland Cements, Cem. Concr. Compos. 18 (1996) 195-203.

[7]. R. Allmann, Refinement of the hybrid layer structure $[Ca_2Al(OH)_6]+ \cdot [1/2SO_4{\bullet}3H_2O]-$, Neues Jb. Miner. Monat. (1977) 136-144.

[8]. H.E. Schwiete, U. Ludwig, Crystal structures and properties of cement hydration products (hydrated calcium aluminates and ferrites), 5th ISCC, Vol 2, 1968, pp. 37-67.

[9]. H. Pöllmann, Characterization of Different Water Contents of Ettringite and Kuzelite, Proceeding of the XII Int. Congress on the Chemistry of Cement, Montreal, Canada, 2007.

[10]. W. Dosch, H. Keller, H. Strassen, 5th ISCC, Vol 2, 1968, pp. 72-77.

[11]. D. Damidot, F.P. Glasser, Thermodynamic investigation of the $CaO\text{-}Al_2O_3\text{-}CaSO_4\text{-}H_2O$ at 50°C and 85°C, Cem. Concr. Res. 22 (1992) 1179-1191.

[12]. I. Kaprálik, F. Hanic, Phase relations in the subsystem $C_4A_3\bar{S}\text{-}C\bar{S}H_2\text{-}CH\text{-}H_2O$ of the system $CaO\text{-}Al_2O_3\text{-}C\bar{S}\text{-}H_2O$ referred to hydration of sulphoaluminate cement, Cem. Concr. Res. 19 (1989) 89-102.

[13]. H. Pöllmann, Die Kristallchemie der Neubildungen bei Einwirkung von Schadstoffen auf hydraulische Bindemittel, PhD Dissertation, University of Erlangen-Nuernberg, 1984.

[14]. M.H. Roberts, Calcium Aluminate Hydrates and Related Basic Salt Solid Solutions, 5th ISCC, Vol 2, 1968, pp. 104-117.

[15]. L.G. Baquerizo, T. Matschei, K.L. Scrivener, M. Saedipour, A. Thorell, L. Wadsö, Methods to determine hydration states of minerals and cement hydrates, Cem. Concr. Res. 65 (2014) 85-95.

[16]. S.J. Ahmed, H.F.W. Taylor, Crystal Structures of the Lamellar Calcium Aluminate Hydrates, Nature 215 (1967) 622-623.

[17]. F.G. Buttler, D. Glasser, H.F.W. Taylor, Studies on $4CaO{\cdot}Al_2O_3{\cdot}13H_2O$ and the Related Natural Mineral Hydrocalumite, J. Am. Ceram. Soc. 42 (1959) 121-126.

[18]. R. Fischer, H.J. Kuzel, Reinvestigation of the system $C_4A{\bullet}nH_2O$ - $C_4A{\bullet}CO_2{\bullet}nH_2O$, Cem. Concr. Res. 12 (1982) 517-526.

[19]. T. Matschei, B. Lothenbach, F.P. Glasser, The AFm phase in Portland cement. Cem. Concr. Res. 37 (2007) 118-130.

[20]. D. Damidot, S. Stronach, A. Kindness, M. Atkins, F.P. Glasser, Thermodynamic investigation of the $CaO–Al_2O_3–CaCO_3–H_2O$ closed system at 25 °C and the influence of Na_2O, Cem. Concr. Res. 24 (1994) 563–572.

[21]. T. Matschei, Thermodynamics of Cement Hydration. PhD Dissertation, University of Aberdeen, 2007

[22]. M. Francois, G. Renaudin, O. Evrard, A Cementitious Compound with Composition $3CaO{\bullet}Al_2O_3{\bullet}CaCO_3{\bullet}11H_2O$, Acta Cryst. C54 (1998) 1214-1217.

[23]. G. Renaudin, M. Francois, O. Evrard, Order and disorder in the lamellar hydrated tetracalcium monocarboaluminate compound, Cem. Concr. Res. 29 (1999) 63-69.

[24]. J. Moon, J.E. Oh, M, Balonis, F.P. Glasser, S.M. Clark, P. Monteiro, High pressure study of low compressibility tetracalcium aluminum carbonate hydrates $3CaO{\bullet}Al2O_3{\bullet}CaCO_3{\bullet}11H_2O$, Cem. Concr. Res. 42 (2012) 105-110.

[25]. J. Moon, J.E. Oh, M, Balonis, F.P. Glasser, S.M. Clark, Pressure induced reactions amongst calcium aluminate hydrate phases, Cem. Concr. Res. 41 (2011) 571-578.

[26]. T. Runcevski, R.E. Dinnebier, O.V. Magdysyuk, H. Pöllmann, Crystal structures of calcium hemicarboaluminate and carbonated calcium hemicarboaluminate from synchrotron powder diffraction data, Acta Cryst. B68 (2012) 493-500.

[27]. H.G. Midgley, P. Bhaskara Rao, Formation of stratlingite, 2CaO•SiO2•Al2O3•8H2O, in relation to the hydration of high alumina cement, Cement and Concrete Research, Volume 8, Issue 2, March 1978, Pages 169-172.

[28]. J. Ding, Y. Fu, J.J. Beaudoin, Stratlingite formation in high alumina cement - zeolite systems, Adv. in Cem. Res.7 (1995) 171-178.

[29]. R. Rinaldi, M. Sacerdoti, E. Passaglia, Strätlingite: crystal structure, chemistry, and a reexamination of its polytype vertumnite, Eur. J. Mineral. 2 (1990) 841-849.

[30]. E. Aruja, The Unit Cell and Space Group of $4CaO{\bullet}A1_2O_3{\bullet}19H_2O$ Polymorphs, Acta Cryst. 14 (1961) 1213-1216.

[31]. T. Matschei, B. Lothenbach, F, Glasser, Thermodynamic properties of Portland cement hydrates in the system $CaO–Al_2O_3–SiO_2–CaSO_4–CaCO_3–H_2O$, Cem. Concr. Res. 37 (2007) 1379-1410.

[32]. B. Lothenbach, L. Pelletier-Chaignat, F. Winnefeld, Stability in the system $CaO–Al_2O_3–H_2O$, Cem. Concr. Res. 42 (2012) 1621 – 1634.

[33]. Design and Control of Concrete Mixtures, 15th Edition, Portland Cement Association, 2011.

5 Impact of water activity on the stability of ettringite

5.1 Introduction

Ettringite is a rare mineral in nature, but a common product occurring during the hydration of Portland cements. It is also the main hydration product of special binders such as calcium sulfoaluminate cements and calcium aluminate cements blended with calcium sulphates. The formation of ettringite at early ages is important to avoid flash set but its occurrence at later ages, due to external sulphate attack or delayed ettringite formation, can cause degradation of concrete structures [1]-[3].

The structure of ettringite has been widely studied in the past. Moore and Taylor first reported its crystal structure [4]-[5], and since then, other techniques such as neutron diffraction [6] and time-of-flight neutron diffraction analysis [7] have been used to precisely determine the location of the atoms within the structure, especially the hydrogen atoms. Ettringite has a structure based on columns and channels. The columns, with the empirical formula $[Ca_3Al(OH)_6{\cdot}12H_2O]^{3+}$, run parallel to the c axis and are composed of $Al(OH)_6$ octahedra alternating with triangular groups of edge-sharing CaO_8 polyhedra, with which they share OH^- [8]. Each Ca atom is also coordinated by four H_2O molecules, which form the cylindrical surface of the column. Between the columns are channels containing sulphate and zeolitic water [8]. The structural formula of ettringite is $[Ca_6Al(OH)_{12}{\cdot}24H_2O]^{6+}[3(SO_4){\cdot}2H_2O]^{6-}$, where the first bracket corresponds to the columns and the second to the channels.

The thermal stability of ettringite has also been extensively studied. Hall et al. [9] showed that, in the presence of water, ettringite rapidly decomposes into monosulfoaluminate and bassanite at 114 °C. In unsaturated conditions, i.e. at water vapor pressures below saturation, different dehydration and/or decomposition processes have been reported.

As an individual solid phase, ettringite ideally contains 32 H_2O molecules, from which 30 are fixed in the columns and 2 H_2O of zeolitic water more loosely bound in the channels [10]. There are some reports of ettringite containing up to 6 H_2O of zeolitic water, giving a final water content of $n = 36$ [11], nevertheless most researchers agree on a maximum value of $n = 32$. Renaudin et al. [12] reported that the water content of ettringite in a wet sample and in a sample dried at 35%RH is very similar and that there is no higher water modification of this structure. Removal of the two interchannel H_2O molecules takes place with reducing relative humidity (RH) without significant change of the structure-related properties, such as unit cell size and crystallinity [13]. Nevertheless, part of these 2 water molecules might be adsorbed on the surface of the crystals or in crystal defects, for this reason an accurate quantification of the interchannel water is rather difficult. Below *n* = 30 ettringite is known to undergo a series of structural changes. Skoblinskaya et al. [10],[14] described the decomposition of ettringite from 30 to 6 H_2O in two stages. First the loss of 12 H_2O bound to the Ca atoms until *n* = 18 H_2O, which was said to keep the same structure as crystalline ettringite, but with marked decrease of the *a* lattice parameter (which is related to the inter-columnar distance), although diffraction line broadening during drying may have affected an accurate determination of lattice parameters. The loss of the remaining 12 H_2O, bound to the Ca atoms, was more complex, requiring very low water vapor pressures to reach *n* = 10, and high temperatures (up to 180 °C) to reach *n* = 6. The final decomposition product was said to be amorphous.

Detailed work by Zhou and Glasser [15] described the stability of ettringite as function of water vapour pressure (P_{H2O}) and temperature. At a low P_{H2O} (whose value decreased with decreasing temperature) water content drops below *n* = 30 H_2O to a minimum value of 10 H_2O and the crystallinity decreased progressively. No distinction between different dehydration stages was made, although the decomposition product, termed metaettringite, was said to have a variable water content from 10 to 13 H_2O and to be amorphous, or nearly so, to X-ray diffraction. An important outcome of this study was the determination of the reversibility of the decomposition process, which takes place with a marked hysteresis. The reformation of ettringite occurred at relatively high P_{H2O} at every temperature, which according to the authors might be due to condensation of water on crystal defects and surfaces, which initiate the nucleation of ettringite. Nevertheless no further explanation was given to describe the hysteric behaviour. This reversibility from an amorphous product to a crystalline one was also observed by Clark et al. [16] on ettringite subjected to high pressure. In a subsequent work, Zhou et al. [13] demonstrated that metaettringite shows electron diffraction patterns similar to those of ettringite, with a marked decrease of the *a* lattice parameter and small change in *c*, which suggests that the columns $[Ca_3Al(OH)_6]^{3+}$ are preserved but move closer together.

Hartman et al. [17] reported the decomposition pathway of ettringite to involve simultaneously the loss of water and hydroxyl groups, which contradicts the sequential water loss reported by Skoblinskaya et al. [10],[14] . These results are also in contrast with the suggested structure of metaettringite [13], since a loss of $(OH)^-$ would produce a collapse of the columnar structure with a marked decrease of the *c* parameter.

In the present study, a different approach was used to study the decomposition and recrystallization of ettringite as function of RH (P_{H2O}) and temperature using the multi-method approach described by Baquerizo et al. [18], which includes the use of X-ray diffraction (XRD), thermogravimetric analysis (TGA), sorption calorimetry and sorption balance measurements. Furthermore, differential scanning calorimetry (DSC) and isothermal calorimetry were used to measure the enthalpies of decomposition and reformation, respectively. With this methodology the decomposition and reformation of ettringite can be assessed in detail and the thermodynamic properties associated with these changes can be quantified.

5.2 Experimental procedure

5.2.1 Preparation of ettringite

Ettringite synthesis is described in detail in Chapter 3.2. Once purity has been confirmed by XRD, the solids were vacuum filtered under N2 atmosphere in a glove box and subsequently aged at 5, 25, 50 and 80 °C during different periods of time (from 1 to 30 months, depending on the temperature) inside hermetic glass bottles equilibrated at different RH using saturated salt solutions [20] as shown in Table 3:2.

5.2.2 Experimental methods

The stability of ettringite and its thermodynamic properties were investigated using the methodology described in Chapter 3. In addition DSC, and isothermal calorimetry were also used as described below.

Isothermal calorimetry (Thermometric TAM Air) was used to measure the enthalpy of mixing of rehydration of initially vacuum dried ettringite samples of known water content. The dried sample was equilibrated inside the calorimeter for 1 hour, then water (w/s = 1 - 2) was injected using an Admix Ampoule.

In order to determine the enthalpy associated to the dehydration of ettringite, differential scanning calorimetry (DSC Mettler Toledo 822e) measurements were done on well crystalline ettringite samples of initially known water content under isothermal conditions at 60 and 65 °C under N2 flux. In order to avoid rapid evaporation during testing, a lid with a 2 mm hole was used. The mass of the sample was measured after testing to calculate the final water content.

5.3 Results

5.3.1 XRD and TGA

XRD tests were carried out on samples conditioned at different RHs at 5 °C, 25 °C and 50 °C during 20 months. Samples aged at 80 °C were tested after 50 days of conditioning. Samples at 50 °C were also tested after 6 months in order to compare them with those conditioned during 20 months. Lattice parameters were refined using the Le Bail method [21] and the crystal structure published by Goetz-Neunhoeffer and Neubauer (ICSD# 155395) [6]. Patterns of the samples conditioned at 25 °C, 50 °C and 80 °C, and the refined lattice parameters at every temperature studied are shown in Figure 5:1 and Figure 5:2. At 5 °C no changes were observed down to 10% RH, as also confirmed by TGA (*n* varies from 30 to 32, See Figure 5:3). For this reason those patterns are not shown.

At 50 °C ettringite was preserved down to 19% RH. Nevertheless formation of monosulfoaluminate (Ms) was observed below 31% RH (See Figure 5:1b). Samples tested after 20 months do not show significant differences in the amount of Ms compared to those tested after 6 months, thus precipitation might have taken place during the initial conditioning at 50 °C starting from wet samples or during the release of water from ettringite. The amounts of Ms were in the range of 1 to 3 wt.-%, as quantified by Rietveld analysis and TGA. It can be noted that at 31% and 19% RH the hydration state of monosulfoaluminate corresponds to Ms12, and at 5% RH corresponds to Ms10.5 (the index denote the total water content *n* of the monosulfoaluminate molecule $C_4A\hat{S}H_n$) which is in agreement with previous findings reported in [18]. At 5% RH, diffraction line broadening is observed on the ettringite pattern together with a marked decrease in peak intensities, which might be due to decomposition of ettringite into a less ordered structure [13],[15]. The measured water content of this sample corresponds approximately to n = 25-26 H_2O, which might be due to incomplete decomposition to metaettringite.

At 80 °C no significant changes were observed from 79% down to 26% RH (Figure 5:1c), which was also confirmed by TGA (Figure 5:3). No monosulfoaluminate was observed in any of the samples at this temperature, probably due to the rapid loss of water from the initial wet sample. At 5% RH the long-range order of the ettringite structure is lost, which is confirmed by the absence of reflections. The decomposition product, called metaettringite [13], had a water content of $n \sim 10.3$. In order to study the reversibility of the decomposition reaction, the sample decomposed at 80 °C and 5% RH was equilibrated at the same temperature at 26%, 51% and 79% RH during several days. As observed in Figure 5:1c during absorption, the samples did not reform to ettringite at 26% and 51% RH, although considerable amount of water was absorbed at 51% RH to reach a final water content of $n \sim 14$ H_2O. At 79% RH, complete reformation of crystalline ettringite is achieved, having a water content of $n \sim 31.3$ H_2O as confirmed by TGA. These results agree with Zhou and Glasser [15], who reported the complete reversibility of the decomposition process but with a marked hysteresis.

As observed in Figure 5:2 the refined lattice parameters do not change considerably from 8 to 100% RH, which agrees with the water content measured by TGA and shown in Figure 5:3. Water content of samples conditioned at 80 °C in desorption and absorption show a significant hysteresis, which is further discussed in the coming sections.

In-situ XRD tests were also carried out using the humidity chamber at 25 °C, 60 °C and 80 °C (see Figure 5:4). In the 25 °C and 60 °C tests, an initially crystalline sample was dried in situ and subsequently exposed to increasing RHs in order to determine the approximate reformation RH. As observed in Figure 5:4a and b, the sample seems to slowly reform ettringite at 70% RH and 80% RH at 25 °C and 60 °C, respectively, and the reformation rate increases at higher RHs. At 95% RH at both temperatures the initial peak intensities (before initial drying) were not reached, even though at the end of the test carried out at 60 °C the sample was exposed to 95% RH for 12 hours to promote complete reformation. The reasons for the lower peaks intensities might be incomplete rehydration or lower crystallite size, but none of these hypotheses could be confirmed. In order to determine the approximate decomposition RH at high temperatures, a crystalline ettringite sample was exposed to 80 °C and the RH decreased from 60% to 12 %. As shown in Figure 5:4c, a decrease in peak intensities is already observed at 18% RH, and the decomposition is clearly evident at 12 % RH. The reversibility of the decomposition process with a marked hysteresis is also confirmed in these in-situ tests. With increasing temperature, the RH of decomposition and reformation increased.

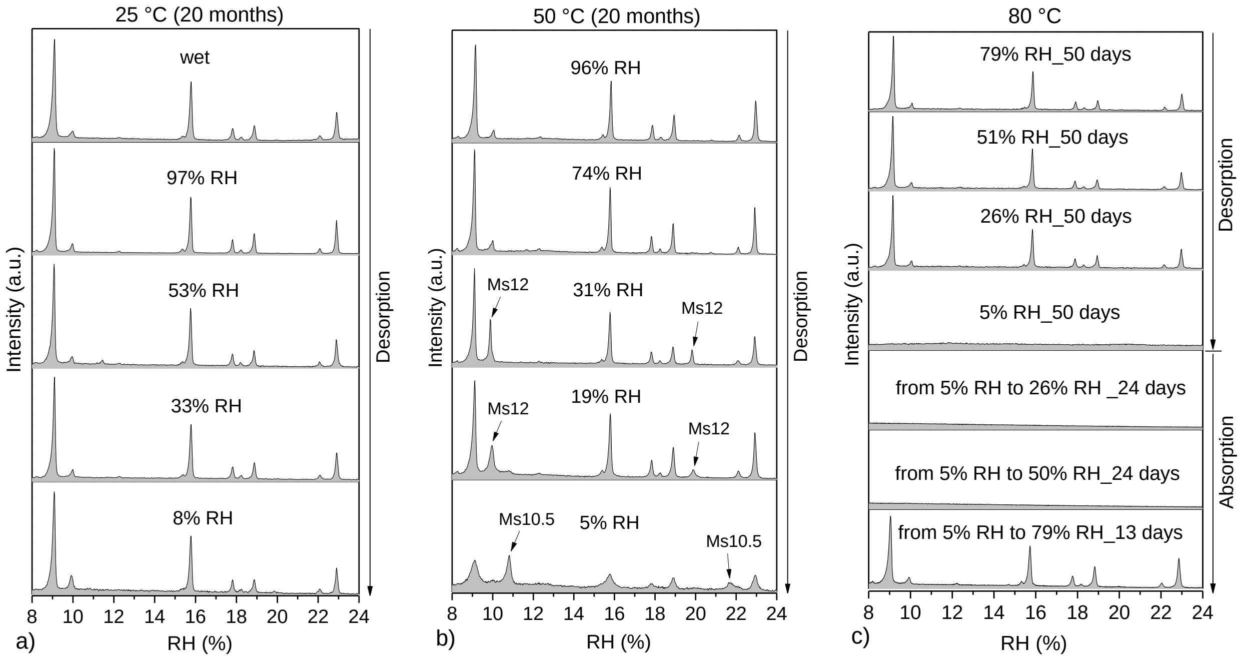

Figure 5:1 XRD patterns of ettringite samples dried at a) 25 °C, b) 50 °C and b) 80 °C.

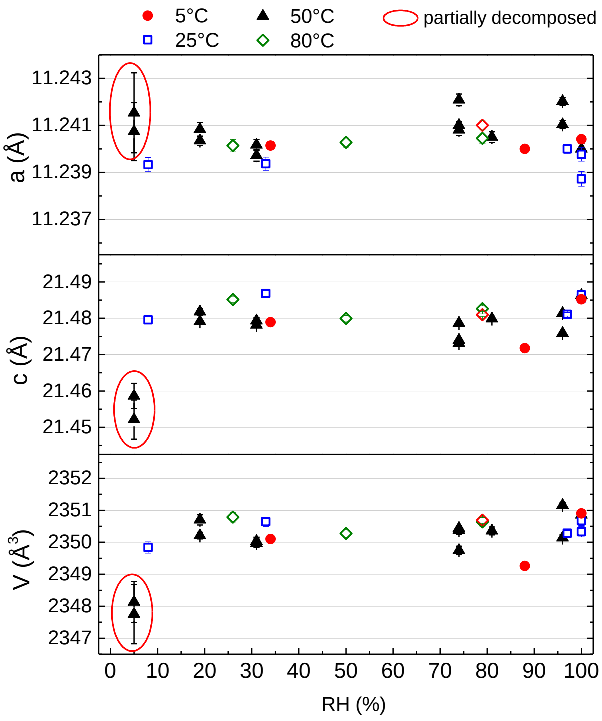

Figure 5:2 Refined lattice parameters of samples aged at all temperatures studied.

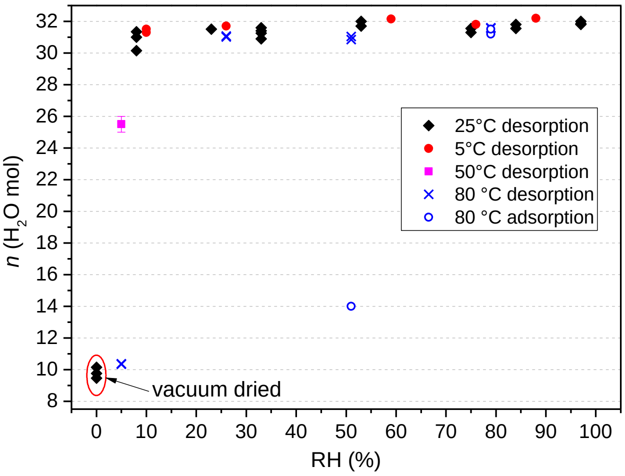

Figure 5:3 TGA water content of samples aged at different temperatures and RHs inside hermetic glass bottles.

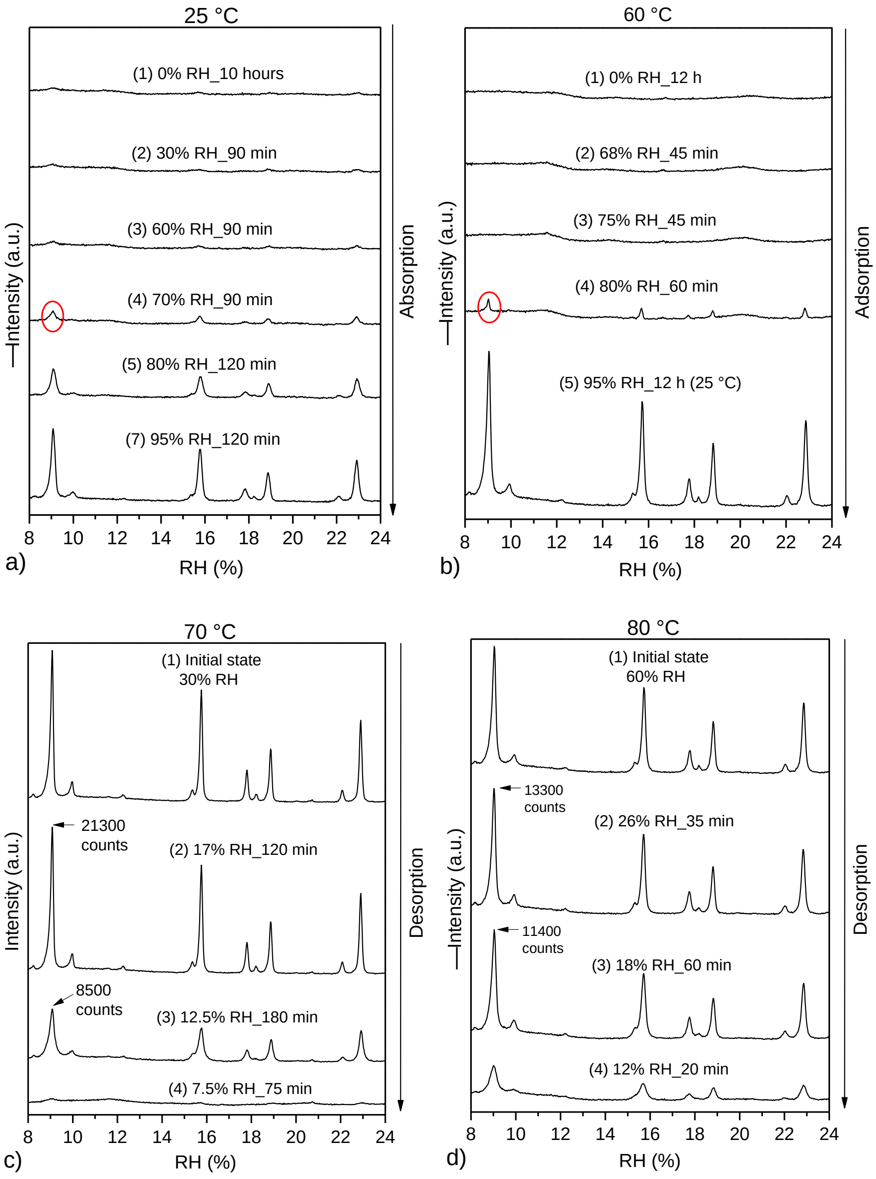

Figure 5:4 XRD patterns of ettringite tested in situ using a humidity chamber in absorption at a) 25 °C, b) 60°C and desorption mode at c) 70 °C and d) 80 °C. At 25 °C and 60 °C reformation is observed at 70% and 80% RH, respectively, while decomposition at 70 °C and 80 °C is already observed at 12.5% and 18% RH, respectively.

5.3.2 Sorption balance

Sorption balance tests were carried out in two ranges of RHs at 25 °C:

- Test 1: 5% → 96% → 5% RH
- Test 2: 10% → 0% → 96% RH

The results are shown in Figure 5:5. During Test 1 the sample did not absorb/release large amounts of water, with values of *n* varying from 30.4 to 31.4 H_2O. The test was completely reversible. Unfortunately it is not possible to differentiate between water adsorbed on the surface of the crystals and absorbed in the interchannel, but since the measured surface area was rather small (6.1 m^2/g as measured using ASAP™ 2020, N_2 BET), it was assumed that all the water absorbed/released in Test 1 corresponds to the incorporation/removal of interchannel water.

In Test 2 during the desorption part from 10% to 0% RH, the sample starts to dehydrate considerably and rapidly below 3% RH and reaches a minimum water content n ~ 8.9 H_2O at 0% RH. Unfortunately, it was not possible to differentiate between different dehydration stages as stated by Skoblinskaya et al. [10]. During rehydration the sample absorbs a small amount of water to reach n ~ 12.5 H_2O at 60% RH. At 70% RH the sample starts to absorb a considerable amount of water to reach a maximum value of n ~ 32 H_2O at 96% RH. If one compares the Test 2: absorption cycle from Figure 5:5 with the in situ XRD test in Figure 5:4 it is clear that from 0 to 60% RH the sample absorbs some water within the structure but remains amorphous to X-rays, and when it is exposed to RH > 60% RH the sample absorbs significant amounts of water, which is accompanied with an increase in crystal ordering (sample starts to be detected by XRD). The points at 70% and 80% RH in Figure 5:5 do not correspond to the real equilibrium because the sample was still absorbing water when the RH was increased (although the exposure time to each of the aforementioned RHs was 6 hours and the initial sample mass was relatively small (7.5 mg)). This illustrates the slow kinetics of rehydration/reformation from 60% to 80% RH.

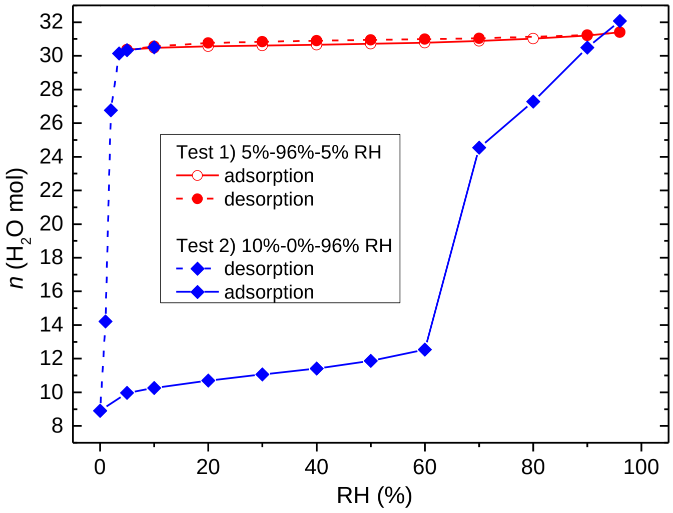

Figure 5:5 Sorption balance test carried out on two ettringite samples. Test 1 shows an absorption cycle from 5% to 96% RH followed by desorption down to 5% RH. Test 2 shows a desorption cycle from 10% to 0% RH followed by absorption up to 96% RH.

5.3.3 Calorimetry tests

5.3.3.1 Sorption calorimetry

Sorption calorimetry results of initially vacuum dried ettringite revealed new information regarding the absorption behaviour of decomposed ettringite (or metaettringite). At the beginning of the test the sample has a water content of $n \sim 9$ H_2O as calculated by the water loss during vacuum drying of that particular sample. The resulting sorption isotherm and enthalpy of mixing as function of water content n are shown in Figure 5:6. For comparison the sorption isotherm measured in the sorption balance is also shown in the same figure. Notice that the enthalpy values presented here correspond to the enthalpy of mixing (ΔH_{mix}), which indicates how much additional heat is obtained from a sorption process compared to the condensation of water. To calculate the enthalpy of sorption (ΔH_{sorp}), i.e. considering water as a gas and thus including the enthalpy of condensation of water, Eq. (2.5) must be used.

As already observed in the results from the sorption balance measurements, there are three main rehydration stages:

1. From points 1 to 2 (Figure 5:6), the sample undergoes a steady absorption of water in the range 0% - 65% RH, going from 9 H_2O up to ~13 H_2O mol, according to the following reaction:

   $$\mathrm{Met9(s)} + 4\mathrm{H_2O(g)} \rightarrow \mathrm{Met13(s)} \qquad (5.1)$$

   where Met stands for metaettringite and the index denotes the total water content. As observed in the XRD tests (Figure 5:1c and Figure 5:4a,b), the sample during this stage remains amorphous to X-rays. Also notice that the enthalpy of mixing values in this stage are not constant, varying from -20.6 kJ/mol H_2O to -13.5 kJ/mol H_2O, from $n = 9$ to 12.1 H_2O. There seems to be a sharp decrease of enthalpy of mixing (more exothermic) from 12 to 13 H_2O, which might be due to conformational/morphological changes before stage 2 (recrystallization) or an artefact of the measurement, thus it was assumed that this step is still part of stage 1. For simplicity an average enthalpy value was calculated from the integral of the plot ΔH_{mix} (kJ/mol H_2O) vs n (H_2O mol), corresponding to -16.5 kJ/mol H_2O or -66.0 kJ/mol for the whole stage 1.

2. During the second absorption stage, from points 2 to 3, the sample undergoes a considerable absorption process at around 62% RH, going from $n \sim 13$ to 30 H_2O, which corresponds to the minimum water content of crystalline ettringite. This process follows the reaction:

   $$\mathrm{Met13(s)} + 17\mathrm{H_2O(g)} \rightarrow \mathrm{Ett30(s)} \qquad (5.2)$$

   This means that in this stage the sample goes from an amorphous to a crystalline state. Although the RH in this process varies from 62% to ~83% RH, it is believed that the whole reformation process would take place at constant RH, since the whole absorption process occurs without significant step changes of enthalpy values as shown in Figure 5:6. The average enthalpy of mixing of this process is -13.3 kJ/mol H_2O or -226.1 kJ/mol for the whole stage.

3. During the third rehydration stage from points 3 to 4, the sample goes from 30 to 32 H_2O according to reaction:

   $$\mathrm{Ett30(s)} + 2\mathrm{H_2O(g)} \rightarrow \mathrm{Ett32(s)} \qquad (5.3)$$

The average enthalpy of mixing value of this reaction is -6 kJ/mol H_2O. This absorption process is continuous and corresponds to the incorporation of 2 H_2O in the interchannel space. It is believed that no structural changes take place during this stage, and the sample is crystalline throughout the process. After point 4 some adsorption of water on the crystals surface is observed and positive enthalpy of mixing values are measured, which may be an artefact due to the accuracy of the technique at high RHs [18].

The enthalpy values during the three aforementioned stages are summarized in Table 5:1. Since stages 1 and 3 show a non-constant enthalpy behaviour, the enthalpy values presented in kJ/mol H_2O are the average. The total $\Delta H_{\text{mix total}}$ is equal to -304.1 kJ/mol for the complete rehydration reaction:

$$\text{Met9(s)} + 23\text{H}_2\text{O(g)} \rightarrow \text{Ett32(s)} \tag{5.4}$$

If one considers the contribution of the condensation of water to reaction (5.4), then the total enthalpy $\Delta H_{\text{sorp total}}$ corresponds to -1316.1 kJ/mol.

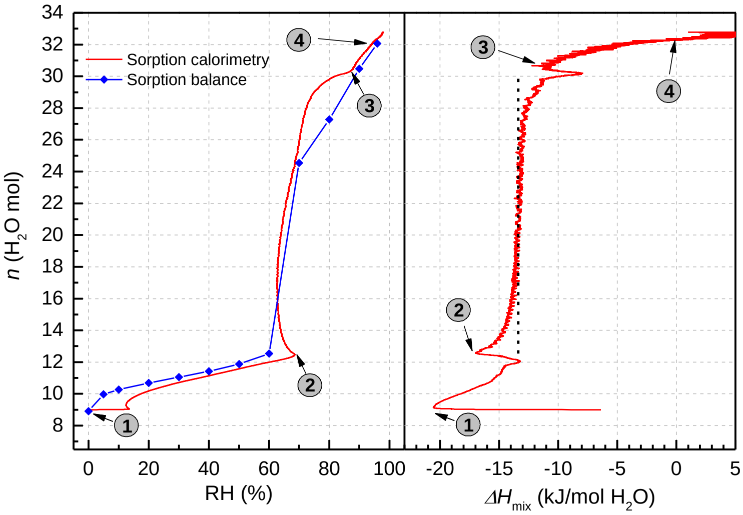

Figure 5:6 Calculated sorption isotherm at 25°C (left) and enthalpy of mixing (right) of vacuum dry ettringite at 25°C during sorption calorimetry testing (for comparison the enthalpy of mixing is plotted in the x axis).

Table 5:1 Molar volume and density of monosulfoaluminate hydration states.

Stage	Reaction	Abs. H_2O (mol)	ΔH_{mix} (kJ/mol H_2O)	ΔH_{sorp} (kJ/mol H_2O) [a]	$\Delta H_{\text{mix stage}}$ (kJ/mol) [b]	$\Delta H_{\text{sorp stage}}$ (kJ/mol) [c]	$\Delta H_{\text{mix total}}$ (kJ/mol) [d]	$\Delta H_{\text{sorp total}}$ (kJ/mol) [e]
1 [f]	$\text{Met9(s)+4H}_2\text{O(g)}\rightarrow\text{Met13(s)}$	4	-16.5	-60.5	-66.0	-242.0	-304.1	-1316.1
2	$\text{Met13(s)+17H}_2\text{O(g)}\rightarrow\text{Ett30(s)}$	17	-13.3	-57.3	-226.1	-974.1		
3 [f]	$\text{Ett30(s)+2H}_2\text{O(g)}\rightarrow\text{Ett32(s)}$	2	-6.0	-50.0	-12.0	-100.0		

[a] Considering the contribution of condensation of water (-44 kJ/mol H_2O), Eq. (2.5).
[b] Equals to ΔH_{mix} × absorbed H_2O per stage.
[c] Equals to ΔH_{sorp} × absorbed H_2O per stage.
[d] Total enthalpy of mixing according to reaction (5.4).
[e] Total enthalpy of sorption according to reaction (5.4).
[f] As enthalpy values are not constant in stages 1 and 3, they were calculated with the integral of the curve ΔH_{mix} (kJ/mol H_2O) vs n (H_2O mol).

5.3.3.2 Isothermal calorimetry

A similar experiment to the one described above was carried out in an isothermal calorimeter (Thermometric TAM Air) on four vacuum dried samples: one large specimen (492 mg) with an initial water content of ~ 9 H_2O and three small samples (50.8 mg, 42.4 mg and38.7 mg) with n ~ 11 H_2O. Liquid water was mixed in situ with the sample with a w/s varying from 1 to 2. The following reactions were assumed to take place during the experiment:

Large sample: $Met9(s) + 23H_2O(l) \rightarrow Ett32(s)$ (5.5)

Small samples: $Met11(s) + 21H_2O(l) \rightarrow Ett32(s)$ (5.6)

As observed in Figure 5:7 the rehydration/reformation of metaettringite to ettringite takes place immediately in the presence of liquid water and is very exothermic. The complete reaction occurs in less than 15 min. The total enthalpy of mixing ΔH_{mix} for reaction (5.5) and reaction (5.6) correspond to -286.8 kJ/mol and -238.5 kJ/mol, respectively. The lower enthalpy measured in the small samples is due to their higher initial water content (Met11). If one adds the enthalpy corresponding to the transition Met9→Met11 (16.5 kJ/mol H_2O × 2 mol H_2O = 33 kJ from Table 5:1), then we get 271.5 kJ/mol, which is relatively close to the enthalpy measured in the large sample. The reasonably small disagreement between the data might be due to partial rehydration of the small samples prior testing (consider that the test does not start immediately, and when dried, metaettringite tends to absorb some water relatively fast). It is interesting to notice that the cumulative heat reached when rehydrating metaettringite after 10 min is very similar in magnitude to the one obtained during hydration of cement paste after 7 days, approximately 300 J/g sample.

Since during these reactions there is no condensation of water involved, the enthalpy values are analogous to the enthalpy of mixing ($\Delta H_{\mathrm{mix\ total}}$) calculated from the sorption calorimetry measurement, which corresponds to -304.1 kJ/mol. The small difference between the enthalpies measured by isothermal calorimetry and those calculated from sorption calorimetry might be the assumption that the condensation of water equals to -44 kJ/mol H_2O, when in reality this enthalpy might be slightly larger due to interaction between the surface and the water molecules. Nevertheless the values obtained with these two calorimetry techniques are consistent and agree relatively well, although the reactions follow different paths.

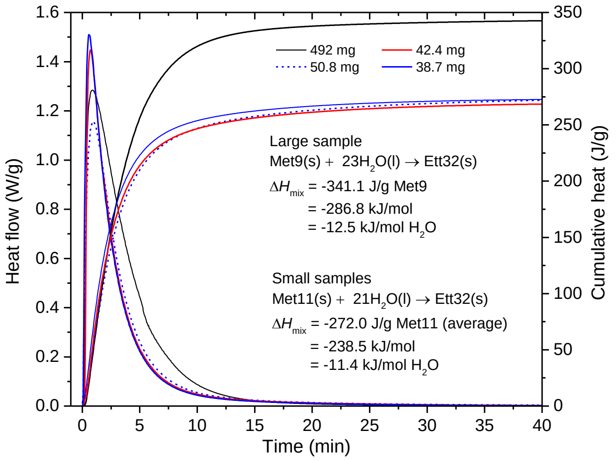

Figure 5:7 Isothermal calorimetry measurements of initially vacuum dried ettringite samples. One large sample corresponding to Met9 and three small specimens corresponding to Met11 were tested.

5.3.3.3 Differential scanning calorimetry (DSC)

In order to determine the enthalpy of decomposition of crystalline ettringite, DSC measurements under isothermal conditions were carried out on samples of known initial water content ($n \sim 31\ H_2O$) at 60 °C and 65 °C. The resulting patterns are presented in Figure 5:8. Samples were weighted at the end of the measurement in order to determine the final water content. Then the total enthalpy of decomposition $\Delta H_{\mathrm{decomp}}$ was calculated from the integral of the curve heat flow vs. time. The larger enthalpy value at 65 °C is due to the slightly larger water loss compared to the sample tested at 60 °C. $\Delta H_{\mathrm{decomp}}$ measured by DSC is analogous (but with opposite sign) to $\Delta H_{\mathrm{sorp\_total}}$ measured by sorption calorimetry.

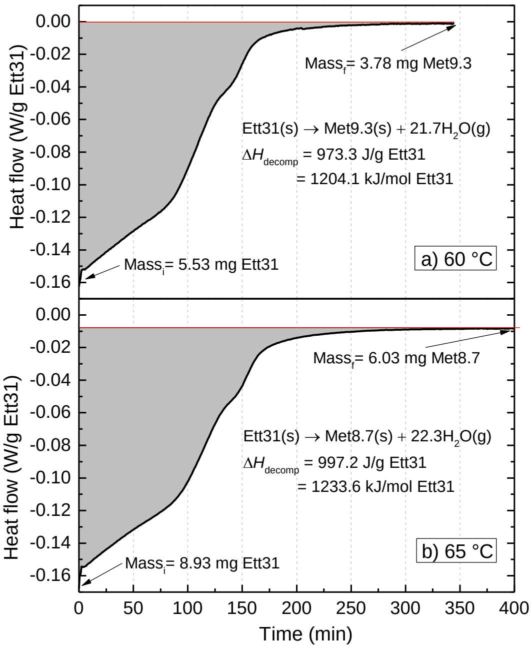

Figure 5:8 DSC measurements on Ett31 at a) 60 °C and b) 65 °C. Samples start losing water from the beginning of the experiment until the curves reach a plateau indicating the end of the dehydration process.

5.3.3.4 Summary of calorimetry results

A summary of the results obtained with the three calorimetry techniques is shown in Table 5:2. Although the reactions taking place during the three experiments follow different paths (sorption balance and isothermal calorimetry measure an absorption process and DSC measures a desorption process), the measured total enthalpy values are consistent and agree reasonably well. The advantage of sorption calorimetry is the possibility to differentiate between different absorption stages taking place during the test, which is not possible with isothermal calorimetry, or during decomposition with DSC. Notice that, although the three techniques were carried out at different temperatures, the similar results also indicate the small temperature dependence of the enthalpy (at least within the range of temperatures studied). One reason for the small differences between the enthalpies measured with the three different techniques might be slight variations of the amorphous product, i.e. the structure of metaettringite might vary depending on the drying conditions (low P_{H2O} or high temperatures).

Table 5:2 Enthalpy of mixing values during absorption.

Technique	Temp. (°C)	Reaction	ΔH_{mix} (kJ/mol)	ΔH_{sorp} [a], ΔH_{decomp} [b] (kJ/mol)
Sorption calorimetry	25	Met9(s) + 23H_2O(g) → Ett32(s)	-304.2	-1316.2
Isothermal calorimetry [c]	20	Met9(s) + 23H_2O(l) → Ett32(s)	-286.8	---
DSC	60	Ett31(s) → Met9.3(s) + 21.7H_2O(g)	---	1204.1
	65	Ett31(s) → Met8.7(s) + 22.3H_2O(g)	---	1233.6

[a] ΔH_{sorp} measured with sorption calorimetry.
[b] ΔH_{decomp} measured with DSC (analogous to ΔH_{sorp} from sorption calorimetry, but with opposite sign).
[c] Value corresponds to the larger sample tested.

5.3.3.5 *Comparison of enthalpy values with other references*

The most accepted data on enthalpies of dehydration and rehydration of ettringite are those reported by Struble and Brown [22]-[23]. The purpose of those studies was the investigation of ettringite for thermal energy storage. The results obtained in this study disagree considerably with those previously reported, most likely due to inconsistencies in the analysis, comparison and collection of the experimental data in [22] and [23]. For example, the authors studied dehydration using a DSC and rehydration using a hydration calorimeter. In the former method the sample is heated and the measured reaction is:

$$\text{Ett(s)} \rightarrow \text{Met(s)} + x\text{H}_2\text{O(g)} \tag{5.7}$$

In the latter, the sample is mixed in situ with liquid water and the measured reaction corresponds to:

$$\text{Met(s)} + x\text{H}_2\text{O(l)} \rightarrow \text{Ett(s)} \tag{5.8}$$

The authors then compared the enthalpies obtained with the two different techniques, although direct comparison cannot be made since H_2O existing in the gaseous and liquid state are part of the reaction during DSC and hydration calorimetry, respectively. In order to be able to compare the results, the enthalpy of evaporation of water should be subtracted from the DSC results [18],[24]. Also the enthalpy values reported for the dehydration and rehydration do not agree with the values reported in this work. Enthalpy of dehydration reported in [22], expressed in kJ/g H_2O is in fact lower than the enthalpy of vaporization of water, which means that the removal of water from ettringite would require less energy than that required to evaporate pure water. All this denotes mistakes in the interpretation of the results and in the measurements. A comparison between results obtained in [22]-[23] and those obtained in this work are presented in Table 5:3. Since in the current study the total enthalpy of decomposition and reformation were similar, the enthalpy values presented in Table 5:1 were used to calculate the reactions shown in Table 5:3.

Table 5:3 Enthalpy of dehydration and rehydration reported by Struble and Brown [22]-[23].

Process	Reaction	ΔH [c]	ΔH (kJ/mol)	Ref.
Dehydration [a]	$\mathrm{Ett32(s)\rightarrow Met12(s)+20H_2O(g)}$	120 cal/g	630	[23]
			1135	t.s.
	$\mathrm{Ett32(s)\rightarrow Met13(s)+19H_2O(g)}$	0.6 kJ/g	753±126	[22]
			1074	t.s.
Rehydration [b]	$\mathrm{Met15.5(s)+16.5H_2O(l)\rightarrow Ett32(s)}$	60 cal/g	241	[23]
			205	t.s.
	$\mathrm{Met10.5(s)+21.5H_2O(l)\rightarrow Ett32(s)}$	106 cal/g	385	[23]
			279	t.s.

t.s.: this study.

[a] Reactions were written considering the loss of water reported in [23] and [22] after the DSC measurement. The initial sample was considered to be Ett32.

[b] Reactions were written considering the loss of water reported in [22] prior the hydration calorimetry measurement.

[c] Exact enthalpy values reported in [23] and [22]. These values are presented per gram of initial sample (either Ett or Met).

5.3.4 Density measurements

The density values of the different hydration states of ettringite, i.e. Ett32 and Ett30, were calculated with Eq. (5.9):

$$D = ZM/N_AV \tag{5.9}$$

where D is the density, Z is the number of formula units per unit cell (which is 2 in our case), M is the molecular weight of the hydration state, V is the unit cell volume obtained from the XRD lattice parameters refinement and N_A is the Avogadro's number. Since no significant volume changes were observed from Ett32 to Ett30, it was assumed that both of them have the same volume (2350 Å^3 as measured by XRD). The density of Met12 was also calculated with Eq. (5.9) using the latticed parameters reported by Zhou et al. [13] (a = 8.5 Å, c ~ 10.6 Å, calculated volume = 663.3 Å^3). The density of a sample composed of Met11 (as measured by TGA) was measured with a Helium pycnometer (AccuPyc™ II 1340). The densities of Ett30, Met12 and Met11 were used to extrapolate the densities of Met13 and Met9 assuming a linear correlation as shown in Figure 5:9. A summary of the densities and molecular volumes is shown in Table 5:4.

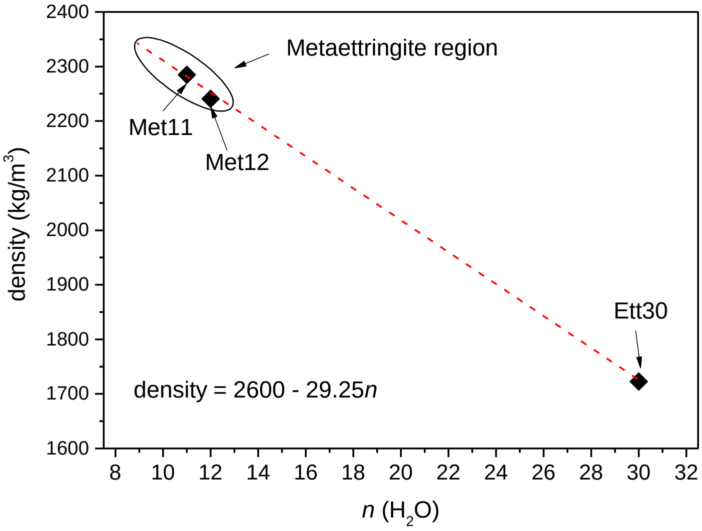

Figure 5:9 Density of the different hydration states of ettringite as function of water content n. The densities of Ett30 and Met12 were calculated from the lattice parameters reported here and in [13], respectively. The density of Met11 was measured with and helium pycnometer.

5.4 Thermodynamic modelling

The experimentally determined thermodynamic properties of the decomposition/dehydration and reformation/rehydration of ettringite were used to model its behaviour during drying and rewetting as function of temperature. GEM-Selektor [25]-[26] including its built-in thermodynamic database [27] complemented with the cemdata14 database [28]-[30], was used for the thermodynamic simulations (see Chapter 2).

5.4.1 Thermodynamic modelling of hysteresis loops

As observed in the DVS measurements (Figure 5:5) there is a considerable hysteresis between the critical RH to decompose ettringite to metaettringite and the critical RH needed to reverse this reaction, i.e. to reform ettringite from metaettringite at isothermal conditions. Thermodynamically this is difficult to handle as in a perfectly reversible reaction, decomposition and reformation should take place at the point where the free energies of the two adjacent hydrates (ettringite and metaettringite) are equal, i.e. at the same RH at every temperature.

Similar issues with the calculation of thermodynamic properties in systems with hysteresis have been reported in the past. Van Olphen [31] reported the interlayer adsorption/desorption of water in sodium vermiculite clays with a marked hysteresis, and used the desorption branch of the isotherms at two different temperatures to calculate the thermodynamic constants. The desorption branch has also been used by other authors to determine variations of thermodynamic properties [32]. Other authors have stated that the adsorption branch may represents the true equilibrium in a certain region of the isotherm, and that desorption never represents equilibrium conditions [33]. Nevertheless, La Mer [34] questioned the validity of these assumptions, saying that any thermal result must be incorrect for at least one branch of the isotherm, and perhaps both branches. In order to use experimental isotherms showing hysteresis, an extended Clausius-Clapeyron equation was proposed in [35] considering an uncompensated heat, which is related to an entropy production [34]. Nevertheless, this uncompensated heat should be measurable by calorimetric means, and in the current work no significant variation between the enthalpy of decomposition and enthalpy of reformation was observed. Furthermore, similar differential heats of absorption and desorption have been measured in the past in different types on montmorillonites, which are known to present a marked hysteresis [24], which agrees with our experimental results.

The reason for the hysteresis in hydrated phases such as clays was explained by Tambach et al. [36] using molecular simulations. In their work it was demonstrated that hysteresis in clays has a thermodynamic origin, i.e. a free-energy barrier separating the transition between two adjacent hydration states. Then the RH has to be increased or decreased significantly beyond the real point of equal free energies in order to overcome these barriers. It seems that a similar mechanism is observed in ettringite.

Finally, it is commonly agreed when treating phases showing a hysteretic behaviour during desorption and adsorption that the true equilibrium lies within the hysteresis loop. Although some assumptions such as irreversible loss of entropy during adsorption and uncompensated heat could explain small regions of hysteresis, in the case of ettringite none of these hypotheses can account for the large hysteresis during decomposition and reformation (2.5% RH and 62% RH at 25 °C).

5.4.2 Decomposition and reformation modelling of ettringite vs metaettringite

As observed in our experimental results and in other works [10],[14]-[15], there is a critical RH at which decomposition (during desorption) and reformation (during absorption) takes place spontaneously. In order to model this desorption/absorption behaviour, the following considerations were done:

- Reformation takes place according to reaction (5.2): $Met13(s)+17H_2O(g)\rightarrow Ett30(s)$, at 62% RH at 25 °C as observed during the sorption calorimetry test.
- Since during decomposition different stages could not be determined, for simplicity it was assumed that during this process the sample undergoes a similar reaction path as during reformation, i.e. ettringite decomposes first into Met13 and subsequently into Met9. Although this assumption is not completely correct, it is a good approximation. Then decomposition is considered to take place in one single step at 2.5% RH at 25 °C as follows:

$$Ett30(s) \rightarrow Met13(s) + 17H_2O(g) \qquad (5.10)$$

Since in the presence of hysteresis thermodynamic modelling is not a simple task (as mentioned in the previous section), the reformation and decomposition behaviour were modelled with two different approaches:

1. *Thermodynamic modelling using ΔH_r determined by calorimetry, ΔG_r calculated with the transition RH according to Eq. (2.2) and ΔS_r from Eq. (2.4).*

   Since experimental results obtained with the three calorimetry techniques were consistent, the enthalpy values used for the modelling were those obtained by sorption calorimetry. It was assumed that the enthalpy of decomposition (for reaction (5.10)) has the same magnitude as the enthalpy of reformation (for reaction (5.2)), i.e. 974.1 kJ/mol (see Table 5:1). Then the molar thermodynamic properties were calculated and the data used to model with this first approach is shown in Table 5:4 (lines 1, 2, 3 and 6). The simulated RH and P_{H2O} of decomposition and reformation as function of temperature are shown in Figure 5:10 and Figure 5:11, respectively. The modelled curve (solid line) disagrees significantly with experimental data reported by Zhou and Glasser [15] and with our experimental values of decomposition and reformation.

2. *Thermodynamic modelling using ΔH_r calculated with the van't Hoff equation (Eq. (2.3)), using the approximate reformation and decomposition RHs as function of temperature obtained experimentally.*

   These experimental points are shown in Figure 5:10 and Figure 5:11. ΔG_r and ΔS_r were calculated according to Eq. (2.2) and Eq. (2.4), respectively. The ΔH_r values calculated for decomposition (reaction (5.10)) and reformation (reaction (5.2)) correspond to 1300 kJ/mol and -788.8 kJ/mol, respectively. The final molar thermodynamic properties used are shown in Table 5:4 (lines 1, 2, 4 and 7). The simulated RH and P_{H2O} of decomposition and reformation as function of temperature are shown in Figure 5:10 and Figure 5:11 (dashed lines), respectively. Although the modelled curves agree with the experimental reformation and decomposition results, the enthalpies of reaction required to model it disagree largely with the enthalpy measured by sorption calorimetry (ΔH_r = -974.1 kJ/mol). The equations of best fit proposed by Zhou and Glasser [15] (dot lines in Figure 5:10 and Figure 5:11) agrees with our modelled decomposition curve. However the reformation behaviour proposed by them presents an atypical behaviour below 60 °C and does not represent real observations.

To summarize, in order to model the decomposition and reformation behaviour, the modelling approach 2 must be used, but it has to be noted that the $\Delta H_r°$ (and thus the $\Delta S_r°$) do not represent the real values, since the conventional thermodynamic relations do not work when dealing with hysteretic systems, especially considering the large hysteresis observed on the transition ettringite – metaettringite. On the other hand in applications where the real exothermic and endothermic enthalpies are required, the values shown in Table 5:1 should be used.

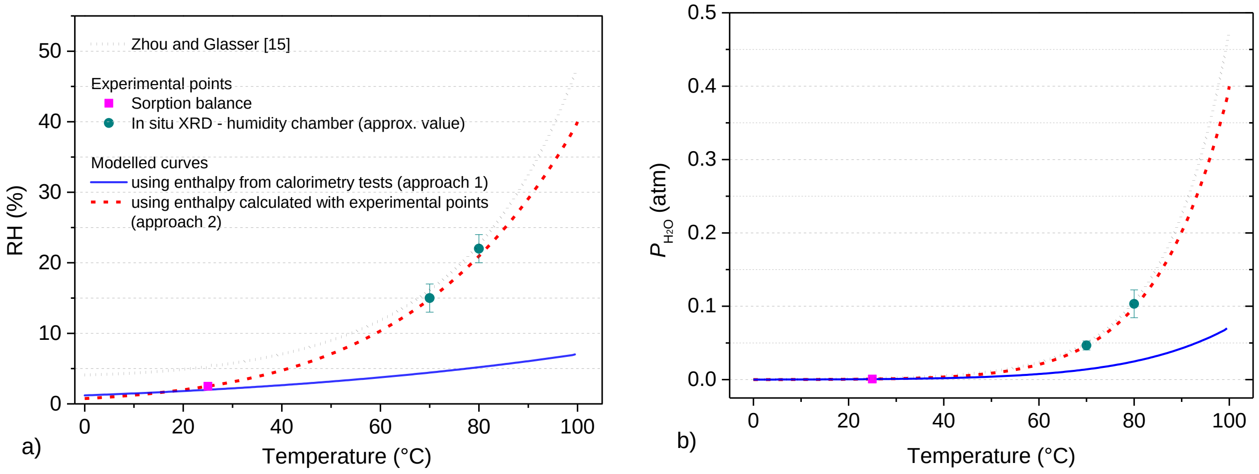

Figure 5:10 Decomposition a) RH and b) PH2O as function of temperature modelled using enthalpy values obtained from calorimetry and enthalpy calculated with the van't Hoff equation using the decomposition experimental points. The curve from Zhou and Glasser corresponds to the equation of best fit lnP=-1.61+0.075T given in [15].

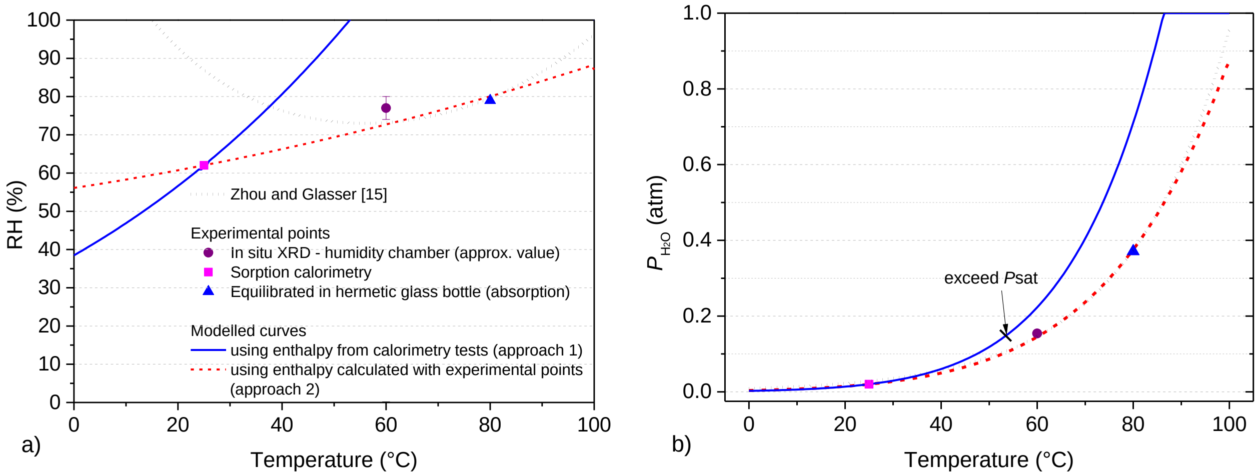

Figure 5:11 Reformation a) RH and b) PH2O as function of temperature modelled using enthalpy values obtained from calorimetry and enthalpy calculated with the van't Hoff equation using the reformation experimental points. The curve from Zhou and Glasser corresponds to the equation of best fit lnP=1.89+0.047T given in [15].

Table 5:4 Standard molar thermodynamic properties of the ettringite and metaettringite hydrates at 25 °C and 1 bar calculated according to the two approaches detailed in Section 5.4.2 and according to the zero hysteresis analysis shown in Section 5.4.3.

Line	Phase	$\Delta G_f°$ (kJ/mol)	$\Delta H_f°$ (kJ/mol)	$S°$ (J/mol K)	$Cp°$ (J/mol K) [a]	Density (kg/m^3)	$V°$ (cm^3/mol)	Ref.
Desorption								
1	Ett32	-15205.9	-17535.0	1900	2174.4	1773.4	707.8 [b]	[29]
2	Ett30 [c]	-14728.1	-16950.2	1792.4	2094.2	1722.5	707.8	t.s.
3	Met13$_{des}$ [d]	-10540.6	-11855.3	870.4	1412.9	2223.0	410.6	t.s.
4	Met13$_{des}$ [e]	-10540.6	-11530.3	1960.4	1412.9	2223.0	410.6	t.s.
5	Met9 [f]	-9540.4	-10643.7	646.6	1252.6	2329.0	361.0	t.s.
Absorption [g]								
6	Met13$_{abs}$ [d]	-10678.2	-11855.3	1332.1	1412.9	2223.0	410.6	t.s.
7	Met13$_{abs}$ [e]	-10678.2	-12040.6	710.6	1412.9	2223.0	410.6	t.s.
Zero hysteresis								
8	Ett32	-15205.9	-17535.0	1900	2174.4	1773.4	707.8 [b]	[29]
9	Ett30 [c]	-14728.1	-16950.2	1792.4	2094.2	1722.5	707.8	t.s.
10	Met13	-10618.7	-11855.3	1132.5	1412.9	2223.0	410.6	t.s.

[a] $Cp°$ was calculated assuming $\Delta Cp = 0$ for the changes of hydration states.

[b] Calculated using the average volume of the lattice from this study.

[c] Thermodynamic properties of Ett30 should be used in an ideal solid solution with Ett32.

[d] Calculated using the enthalpy of reaction measured by calorimetry.

[e] Calculated using the enthalpy of reaction calculated using the van’t Hoff equation and the experimental reformation and decomposition points.

[f] Thermodynamic properties of Met9 were calculated assuming a transition Met13→Met9 at 1% RH at 25 °C. $\Delta H_f°$ was calculated with the enthalpy changes measured by calorimetry.

[g] Calculated using the enthalpy of reaction measured by calorimetry.

5.4.3 Determination of the theoretical decomposition/reformation behaviour with no hysteresis

Due to the good agreement between the measured enthalpy of decomposition and reformation by the used calorimetric measurements, we believe that this value is correct and that the hysteresis loop of ettringite de- and rehydration shown in Figure 5:5 is caused by free energy barriers, similarly as in transition state theory laws which need to be overcome in order to initiate ettringite decomposition and metaettringite formation or vice versa. In order to estimate the “true” free energy of formation of metaettringite – under the assumption that the calorimetrically determined enthalpy values are correct- we first need to determine the critical temperature, at which, theoretically, no hysteresis takes place.

This will be graphically elaborated as shown in Figure 5:12. First, the reformation and decomposition processes were plotted as dashed lines with the thermodynamic data of Met 13 that were previously derived to fit the experimental decomposition and reformation data obtained in this study (approach 2: using enthalpies calculated with the van't Hoff equation) as well as by Zhou and Glasser. As one can see the lines cross at ~135°C – which represents the estimated theoretical point of zero hysteresis. This point is in reasonable agreement with the experimental findings of Zhou and Glasser (~ 115 °C).

This point was used to plot a line using the enthalpy value determined by calorimetry, which corresponds to the theoretical ln *K* vs 1/T if no hysteresis takes place. The extrapolated RH at 25 °C corresponds to 18% RH. Consider that the zero hysteresis plot represents a theoretical behaviour that in fact is not observed experimentally, but gives an idea of how far the equilibrium RH might be from the experimental decomposition and reformation RHs as function of temperature if no hysteresis is observed.

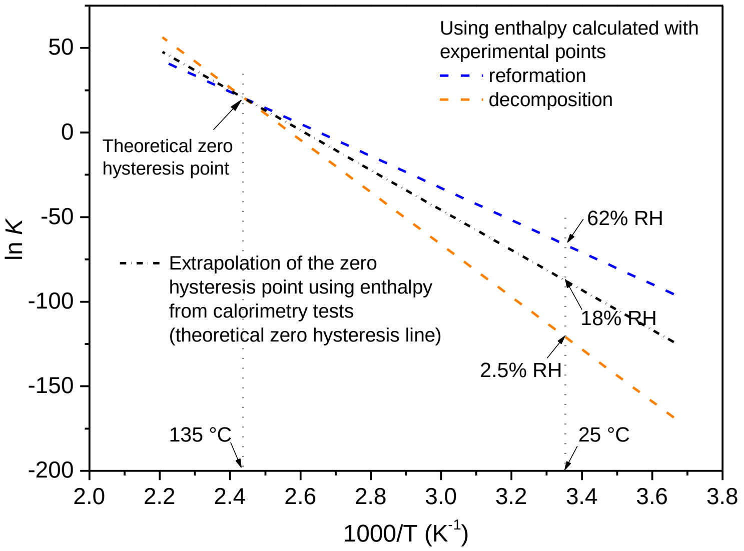

Figure 5:12 Van't Hoff plots of the decomposition and reformation processes calculated using the enthalpies measured by calorimetry and those calculated with the experimental transition points. The theoretical zero hysteresis point was used to plot a line using the enthalpy determined by calorimetry, which corresponds to the theoretical van't Hoff plot if no hysteresis takes place. The RHs shown at 25 °C were calculated according to Eq. (2.2) for reaction (5.2) (reformation) and reaction (5.10) (decomposition).

5.4.4 The impact of water activity on the stability of ettringite

In order to model the practical stability of ettringite calculated based on the experimentally observed transition RHs at different temperatures the thermodynamic data for Ett32, Ett30 and Met13 were used (see Table 5:4, lines 1, 2 and 4). Although the so fitted enthalpy values do not agree with those obtained by calorimetry, the modelled behaviour using them fits the experimental observations. The modelled reformation, decomposition and hysteresis zones are summarized in Figure 5:13. Above 60 °C the curves presented here agree well with Zhou and Glasser [15], but differ below 60 °C, especially during reformation. In the hysteresis loop zone, when starting from saturated water vapour pressures, crystalline ettringite will not undergo decomposition unless the zone of decomposition is reached. On the other hand, once decomposed, amorphous metaettringite will not reform to ettringite unless the zone of reformation is reached. A theoretical stability limit of ettringite based on the assumptions derived in Section 5.3 is also plotted using the data shown in Figure 5:12. Hence the dashed lines in Figure 5:13 represent the theoretical thermodynamic stability limits of ettringite and metaettringite without consideration of the experimentally observed hysteresis behaviour. Based on these assumptions we estimate that at 25°C ettringite would be stable at RH's >18%, at 50°C the theoretical stability limit is ~30%RH, whereas at 80°C it would theoretically not be stable at < 45% RH. Note that in Figure 5:13 it was assumed that ettringite would only decompose to metaettringite and vice versa. This assumption seems reasonable since it is supposed that at low humidities the nucleation of secondary phases, i.e. structurally different phases e.g. monosulfoaluminate, is hindered due to the absence of an aqueous phase.

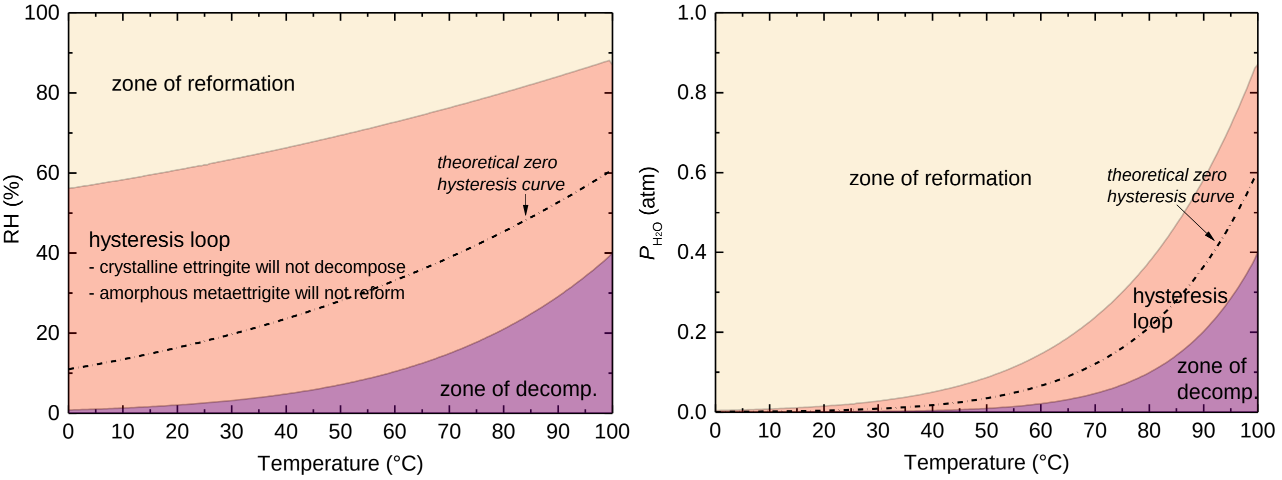

Figure 5:13 a) RH and b) PH_2O as function of temperature showing the zones of reformation and decomposition of ettringite. Equations of best fit for decomposition and reformation corresponds to $RH=0.327+0.108T-0.002T^2+4.8E\text{-}5T^3$ and $RH=56.608+0.186T+0.001T^2$, respectively. The theoretical ettringite stability limit was plotted as dashed line using the data shown in Figure 5:12.

On the other hand, thermodynamically the formation of new phase assemblages is possible, due to the strong impact of changing water activities on the free energy relations within an isochemical system. Figure 5:14 shows the results of the calculation, considering the formation of other cement hydrates (as listed in the thermodynamic database Table 5:4). According to the model at decreasing water vapour pressures, ettringite becomes first metastable with respect to monosulfoaluminate (Ms) and calcium sulfate ($C\hat{S}$). Depending on temperature and relative humidity different hydration states of monosulfoaluminate, as previously reported in Chapter 3, are predicted. Further drying leads to a decomposition of monosulfoaluminate into hydrogarnet (C_3AH_6) and calcium sulfate. The favoured stability of monosulfoaluminate over ettringite at lower RHs was also predicted by Albert et al. [37]. Interestingly a partial decomposition of ettringite into monosulfoaluminate with different hydration states was experimentally confirmed in ettringite samples exposed from saturated conditions to lower humidities at 50 °C (Figure 5:1b). At 80°C however a rapid conversion of ettringite into metaettringite was observed as described in Figure 5:1c. As assumed above it seems that the lack of a reaction medium, such as liquid water, diminishes the likelihood of predicted decomposition. Whether decomposition might be observed after long drying exposure times remains unknown, as in the current study no other major phases were observed, even after 36 months of drying. Note also that metaettringite would never occur as thermodynamically stable phase in the calculations. In experiments however its formation was observed by several authors including results of this study. This emphasizes the need of considering metastability restrictions as applied in Figure 5:13 in order to predict a realistic drying and wetting behaviour of ettringite and metaettringite.

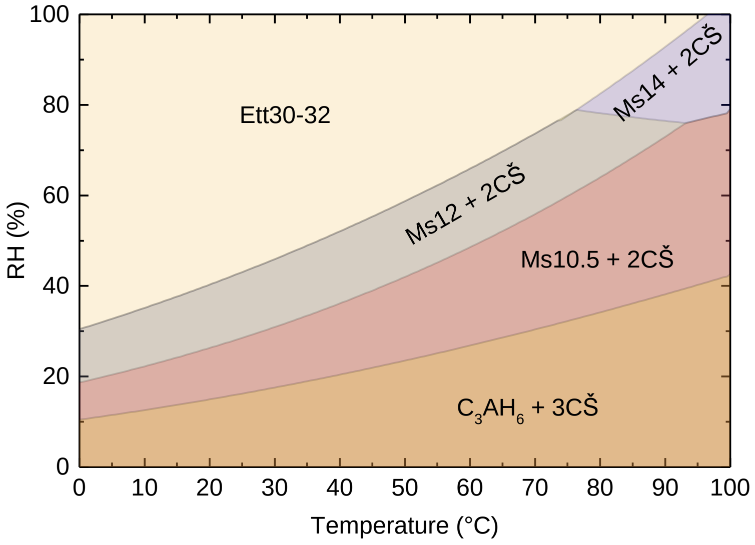

Figure 5:14 Predicted RH vs temperature phase diagram during drying of ettringite in equilibrium with other cement hydrates. According to the model ettringite should decompose into monosulfoaluminate (Ms) and calcium sulfate (CŜ). Index next to Ms corresponds to the total water content of monosulfoaluminate.

5.5 Discussion

The multi-method approach proposed earlier [18], complemented with isothermal calorimetry and DSC were used to determine the stability, hydration states and thermodynamic properties of synthetic ettringite. Ettringite as a crystalline phase has a water content *n* which varies from 30 to 32 H_2O. The decomposition product, called metaettringite, has values of *n* varying from 9 to 13 H_2O. These results are in good agreement with previously published data [13],[15]. Since decomposition takes place at very low RHs, it is difficult to identify different dehydration stages, as reported by Skoblinskaya et al. [14]. Nevertheless, since the complete decomposition takes place from 3% to 0% RH at 25 °C, the assumption that it occurs in one step is acceptable. In order to reform ettringite from metaettringite, high RHs (P_{H2O}) must be reached. For example, at 25°C metaettringite only reforms to ettringite at RH > ~62%. Thus decomposition and reformation of ettringite takes place reversibly but with a marked hysteresis, whose occurrence can be explained by a free-energy barrier separating the transition between ettringite and metaettringite, similar to that reported by Tambach et al. [36] on clays. With the approach explained in section 5.4.3 we can derive a numerical value of the critical energy barrier of the transition as difference between the free energy plot of reformation or decomposition (dashed lines) to the theoretical stability limit (solid line).The zone of decomposition reported here is similar to that reported in [15], however it does not agree with the reported zone of reformation below 60 °C.

According to the thermodynamic model used, ettringite is predicted to decompose to monosulfoaluminate and calcium sulfate (also predicted in other models [37]) below a certain critical vapour pressure as function of temperature. This was partially observed in our experiments at 50°C but not at 80°C. Whether decomposition at 80°C is not observed due to kinetic constraints remains unknown. Therefore, we introduced some metastability constraints for the decomposition to monosulfoaluminate and for most practical purposes Figure 5:13 represents a more realistic behaviour of ettringite/metaettringite stability than Figure 5:14.

Although Zhou and Glasser suggested that the “area of performance” should be limited, we find no reason for not extending this area down at least to the region of Ett30-32 stability in Figure 5:14 if not to the estimated thermodynamic stability limit as shown by the dashed line in Figure 5:13 since no significant dehydration was observed until the zone of decomposition was reached

5.6 References

[1]. M. Collepardi, A state-of-the-art review on delayed ettringite attack on concrete, Cem. Concr. Compos. 25 (2003) 401-407.

[2]. H.F.W. Taylor, C. Famy, K.L. Scrivener, Delayed ettringite formation, Cem. Concr. Res. 31 (2001) 683-693.

[3]. Kuzel, H.J., Initial Hydration Reactions and Mechanisms of Delayed Ettringite Formation in Portland Cements, Cement and Concrete Composites 18, 1996, 195-203.

[4]. A.E. Moore, H.F.W. Taylor, Crystal Structure of Ettringite, Nature 218 (1968) 1048-1049.

[5]. A.E. Moore, H.F.W. Taylor, Crystal Structure of Ettringite, Acta Cryst. B26 (1970) 386-393.

[6]. F. Goetz-Neunhoeffer, J. Neubauer, Refined ettringite ($Ca_6Al_2(SO_4)_3(OH)_{12}\cdot 26H_2O$) structure for quantitative X-ray diffraction analysis, Powder Diffr. 21 (2006) 4-11.

[7]. M.R. Hartman, R. Berliner, Investigation of the structure of ettringite by time-of-flight neutron powder diffraction techniques, Cem. Concr. Res. 36 (2006) 364-370.

[8]. H.F.W. Taylor, Cement Chemistry, second ed., Thomas Telford, London, 1997.

[9]. C. Hall, P. Barnes, A.D. Billimore, A.C. Jupe, X. Turrillas, Thermal decomposition of ettringite $Ca_6[Al(OH)_6]_2(SO_4)_3\cdot 26H_2O$, J. Chem. Soc. Faraday Trans. 92(12) (1996) 2125-2129.

[10]. N.N. Skoblinskaya, K.G. Krasilnikov, Changes in crystal structure of ettringite on dehydration. 1, Cem. Concr. Res. 5 (1975) 381-394.

[11]. H. Pöllmann, Characterization of Different Water Contents of Ettringite and Kuzelite, in: Proceeding of the XII Int. Congress on the Chemistry of Cement, Montreal, Canada, 2007.

[12]. G. Reanudin, Y. Filinchuk, J. Neubauer, F. Goetz-Neunhoeffer, A comparative structural study of wet and dried ettringite, Cem. Concr. Res. 40 (2010) 370-375.

[13]. Q. Zhou, E.E. Lachowski, F.P. Glasser, Metaettringite, a decomposition product of ettringite, Cem. Concr. Res. 34 (2004) 703-710.

[14]. N.N. Skoblinskaya, K.G. Krasilnikov, L.V. Nikitina, V.P. Varlamov, Changes in crystal structure of ettringite on dehydration. 2, Cem. Concr. Res. 5 (1975) 419-432.

[15]. Q. Zhou, F.P. Glasser, Thermal stability and decomposition mechanisms of ettringite at <120°C, Cem. Concr. Res. 31 (2001) 1333-1339.

[16]. S.M. Clark, B. Colas, M. Kunz, S. Speziale, P.J.M. Monteiro, Effect of pressure on the crystal structure of ettringite, Cem. Concr. Res. 38 (2008) 19-26.

[17]. M.R. Hartman, S.K. Brady, R. Berliner, M.S. Conradi, The evolution of structural changes in ettringite during thermal decomposition, J. Solid State Chem. 179 (2006) 1259-1272.

[18]. L.G. Baquerizo, T. Matschei, K.L. Scrivener, M. Saedipour, A. Thorell, L. Wadsö, Methods to determine hydration states of minerals and cement hydrates, Cem. Concr. Res. 65 (2014) 85-95.

[19]. L.G. Baquerizo, T. Matschei, K.L. Scrivener, M. Saedipour, L. Wadsö, Hydration states of AFm phases, submitted to Cement and Concrete Research.

[20]. L. Greenspan, Humidity fixed points of binary saturated aqueous solutions, J. Res. Nat. Bur. Standards Sect. A 81 (1977) 89–96.

[21]. A. Le Bail, H. Duroy, J.L. Fourquet, Ab-initio structure determination of $LiSbWO_6$ by X-ray powder diffraction, Mat. Res. Bull. 23 (1988) 447-452.

[22]. L.J. Struble, P.W. Brown, Heats of dehydration and specific heats of compounds found in concrete and their potential for thermal energy storage, Solar Energy Materials 4 (1986) 1-12.

[23]. L.J. Struble, P.W. Brown, An Evaluation of Ettringite and Related Compounds for Use in Solar Energy Storage: Progress Report, Volume 84, Issue 2942 of NBSIR, United States National Bureau of Standards, 1984.

[24]. G. Dios Cancela, F.J. Huertas, E. Romero Taboada, F. Sánchez-Rasero, A. Hernández Laguna, Adsorption of Water Vapor by Homoionic Montmorillonites. Heats of Adsorption and Desorption, J. Colloid. Interf. Sci. 185 (1997) 343-354.

[25]. D. Kulik, T. Wagner, S.V. Dmytrieva, G. Kosakowski, F.F. Hingerl., K.V. Chudnenko, U. Berner, GEM-Selektor geochemical modeling package: revised algorithm and GEMS3K numerical kernel for coupled simulation codes, Comput. Geochem 17 (2013) 1-24. http://gems.web.psi.ch

[26]. T. Wagner, D.A. Kulik, F.F. Hingerl, S.V. Dmytrieva, GEM-Selektor geochemical modeling package: TSolMod library and data interface for multicomponent phase models, Canadian Mineralogist 50 (2012) 1173-1195.

[27]. Hummel W, Berner U, Curti E, Pearson F J, Thönen T. Nagra/PSI Chemical Thermodynamic Data Base 01/01.Universal Publishers, Parkland, Florida, USA, 2002.

[28]. T. Matschei, B. Lothenbach, F. Glasser, Thermodynamic properties of Portland cement hydrates in the system CaO-Al_2O_3-SiO_2-$CaSO_4$-$CaCO_3$-H_2O, Cem. Concr. Res. 37 (2007) 1379-1410.

[29]. B. Lothenbach, T. Matschei, G. Möschner, F. Glasser, Thermodynamic modelling of the effect of temperature on the hydration and porosity of Portland cement, Cem. Concr. Res. 38 (2008) 1-18.

[30]. B. Lothenbach, L. Pelletier-Chaignat, F. Winnefeld, Stability in the system CaO–Al_2O_3–H_2O, Cem. Concr. Res. 42 (2012) 1621 – 1634.

[31]. H. van Olphen, Thermodynamics of interlayer adsorption of water in clays. I – Sodium vermiculite, Journal of colloid science 20 (1965) 822-837.

[32]. A. Khalfi, P. Blanchart, Desorption of water during the drying of clay minerals. Enthalpy and entropy variation, Ceramics International 25 (1999) 409-414.

[33]. T.K. Hill, Statistical mechanics of adsorption. V. Thermodynamics and heat of adsorption. J. Chem. Phys. 17 (1949) 520–535.

[34]. V.K. La Mer, The calculation of thermodynamic quantities from hysteresis data, Journal of Colloid and Interface Science 23 (1967) 297-301

[35]. D.H. Everett, D.I. Whitton, Proc. Royal Soc. (London) A230, 91-110, 1955.

[36]. T. Tambach, P.G. Bolhuis, B. Smit, A Molecular Mechanism of Hysteresis in Clay Swelling, Angew. Chem. 116 (2004) 2704 –2706.

[37]. B. Albert, B. Guy, D. Damidot, Water chemical potential: A key parameter to determine the thermodynamic stability of some hydrated cement phases in concrete?, Cem. Concr. Res. 36 (2006) 783-790.

6 Thermodynamic modelling of the water content of cementitious systems

6.1 Introduction

In the past 25 years big advances have been made in the development and use of thermodynamic models to predict hydrate phase assemblages and pore solutions of cementitious systems. Thermodynamics has been demonstrated to be a trustworthy approach, due to the consistent basis and the ability to deal with complex systems. The reliability of thermodynamic models depends on the quality of the database used. Some of the databases developed focussing on cements phases include those by Atkins et al. [1], Bennet et al. [2] Damidot et al. [3], Reardon [4]-[5], Lothenbach and Winnefeld [6]-[7], Matschei et al. [8] and Blanc et al. [9]. In order to model the hydration behaviour using a consistent database, a computer-based code is needed. Codes based on the Gibbs free energy minimisation (such as GEM-Selektor [10]-[11]) have been demonstrated to be a reliable approach. In this method the total Gibbs energy of the system studied is minimised; for this the Gibbs free energy per mole of each component at the temperature and pressure of interest must be provided. This method has successfully been used to model the hydration behaviour of Portland cements (PC) [6]-[8], PC blended with supplementary cementitious materials [12]-[13], and alternative cementitious systems containing calcium sulfoaluminate [14]-[17] and calcium aluminate cements [17]-[18].

A common factor in the thermodynamic models developed for cementitious systems so far is the fact that almost all of them consider saturated conditions, i.e. in excess of water. Nevertheless, this condition is not fulfilled in many cases, since for some applications less water than that required to obtain complete hydration is used e.g. for ultra-high performance concretes and most of the concrete structures are exposed to a service environment which is not saturated (RH < 100%). This becomes important considering that cement hydrates are very sensitive to changing water vapor pressure. In addition modern concretes are often specified to fulfil certain durability requirements; one of them is carbonation resistance, which is very much dependent on the relative humidity of the service environment. In order to be able to better describe parameters relevant to carbonation, it is necessary to have a thermodynamic model that predicts phase changes as function of relative humidity, temperature and CO_2 vapor pressure.

Several thermodynamic models have been previously developed to predict the hydration and dehydration behaviour of hydrated phases such as clays [19]-[23] and sulfate salts [24]-[27]. However, at present, there is no thermodynamic model capable of predicting the influence of water activity on the hydrate constitution of cementitious systems.

This chapter makes use of the database of thermodynamic properties of the different hydration states of AFm phases and ettringite reported in Chapter 4 and 5 (also reported in [28]-[29]) to model the impact of water activity in the hydrate phase assemblage of various cementitious systems. The results presented in this chapter include:

1) The thermodynamic stability of the most important AFm phases as function of RH and temperature.

2) The hydration behaviour of systems containing C_3A and CA in the presence of $Ca(OH)_2$, $CaSO_4$, $CaCO_3$, in water saturated and non-saturated conditions (shown in ternary diagrams). A new approach was developed to assess the reaction rate limiting thermodynamic properties of C_3A and CA in presence of water vapor.

3) The phase evolution on drying of an already hydrated cementitious system.

6.2 Materials and methods

C_3A and CA were synthesized as shown in Chapter 3.

XRD and TGA on selected samples were carried out following the procedures described in Chapter 3.

The hydrate pair - humidity buffer method described in chapter 3 was used to study the critical humidity at a steady state between C_3A or CA and their hydration products at which further hydration of the clinker phases is limited. For this, 4 to 7 grams of the clinker phases were introduced in a small glass container (20 ml), then mixed with small amounts of water (w/s ~ 0.05) and subsequently the RH at a specific temperature was measured until no significant variations were noticeable. Then the temperature was slightly increased and the RH was recorded until a new steady state was reached again. This methodology was also used to validate some points from the modelled ternary diagrams shown in Section 6.5.

An important point to be considered is that in order to model the behaviour of cementitious systems in water-unsaturated conditions, steam has to be introduced into the project database. For more information about the implementation of GEM-Selektor please refer to Chapter 2.

6.3 Experimental results on C_3A and CA

The equilibrium internal RH of cementitious systems due to self-desiccation have been reported for several systems under varying conditions [30]-[32], which also depends on the ambient temperature. It is also known that each clinker phase starts hydrating when a critical RH is reached [33]-[35], which causes it to prehydrate.

During modelling the hydration of cementitious materials, clinker phases react with water to form hydrated products. When low w/c ratios are used, i.e. the water content is lower than that required to get 100% degree of hydration, the final phase assemblage is composed of cement hydrates plus unreacted clinker phases. If clinker phases remain in the final assemblage and we take the published thermodynamic data from Babushkin [36] into the model, then the predicted water activity of the gaseous phase, i.e. the RH of the system, will be close to zero due to the instability of clinker phases in the presence of any source of water, either liquid or gas. In most reported practical cases the internal RH due to self-desiccation is usually > 50% RH despite the presence of unreacted clinker phases. This means that there is a strong contradiction between experimental values and predictions from thermodynamic approaches considering bulk chemical information only. Jensen et al. [33] suggested that the limited hydration of clinker phases at low RH is most likely a consequence of thermodynamically hampered nucleation and results in very long induction times to initiate hydration at low water vapour pressures. Berodier [37] found that there is a critical pore size which thermodynamically limits further growth of C-S-H and therefore reactions come to a standstill independently of water activity. Others [38]-[39] suggest decoupling the bulk thermodynamic properties of unhydrated clinker phases from the surface thermodynamic properties of hydroxylated layers around the clinker grains. Bellmann et al. [40] suggested the presence of a passivation-type layer that physically hinders hydration.

In order to enable a calculation of phase relations involving the presence of anhydrous clinker phases, e.g. relevant to estimate safe storage conditions for cement clinker to avoid pre-hydration, the critical humidities at which clinker phases started to interact with water have to be estimated. For practicality in this work the approach suggested by Nicoleau et al. [38] was used. We separated the thermodynamic bulk properties of C_3A and CA from those of an assumed hydroxylated surface layer, which were thermodynamically treated as separate phases with the same stoichiometry as the anhydrous clinker phases. The hydrate pair - humidity buffer method (introduced in Chapter 3) was used to determine the critical self-buffered RH inside the recipient after C_3A or CA was mixed with very low amounts of water. For this, 4 to 7 g of C_3A or CA were mixed with water (w/c ~ 0.05). In order to achieve a high interaction volume between clinker surface and water vapour small glass bottles (20 ml) were used. After the addition of water RH will drop and according to the phase rule constraints explained in Chapter 3 the final RH corresponds to a steady state between the unreacted clinker phase and the hydrated phases formed, which we treat here as a lower practical limit of hydration continuation.

As shown in Figure 6:1 in the case of C_3A the addition of some water drops led to an increase of the RH to 100% RH for up to two hours, followed by a sudden drop to a minimum of ~ 47% RH in tests 1 and 2, then a slight increase was observed and finally the RH stabilizes at ~ 55% at 25 °C. The fluctuation of RH might be caused by the initial formation of C_4AH_x and C_2AH_8 which was later converted to the more stable C_3AH_6. After reaching a steady state at 25 °C the temperature was increased and a slight increase of the steady state RH was observed. Although, as already mentioned before, the hydration of C_3A may produce different hydrated phases, it was assumed that the RH measured corresponds to the reaction (6.1), as confirmed by the TGA shown Figure 6:3:

$$C_3A(s) + 6H_2O(l) \text{ or } (g) \rightarrow C_3AH_6(s) \tag{6.1}$$

In the case of CA (Figure 6:2), when it is mixed with water (w/c ~ 0.05) the RH remains at 100% for several hours (~ 6 h), then the RH decreased until a minimum steady state was reached at approximately 60% RH at 22 °C after ~7d (see Figure 6:2 Test 4). No significant changes were observed between 7 and 15 days. When increasing the temperature to 35°C the corresponding RH did also slightly increase. In another experiment (test 5 in Figure 6:2) CA was pre-hydrated at 90% RH for

6 days and then left to equilibrate at 22 °C for several days. The resulting steady state RH (~60% RH) was similar to the one obtained when directly mixed with water. Although the TGA of test 4 (Figure 6:3) confirmed the presence of some AFm phases (probably C_2AH_8), for simplicity it was assumed that the RH measured corresponds to the equilibrium reaction (6.2):

$$3CA(s) + 12H_2O(l) \text{ or } (g) \rightarrow C_3AH_6(s) + 2AH_3 \qquad (6.2)$$

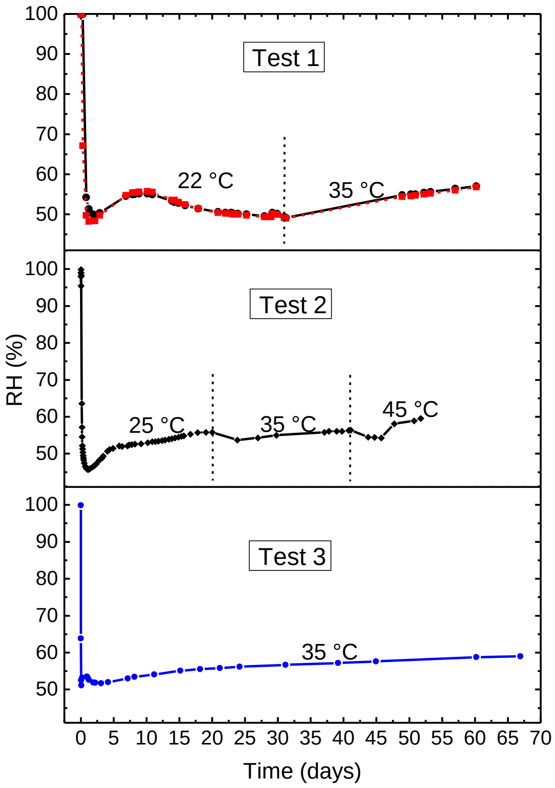

Figure 6:1 Measured RH using the hydrate pair-humidity buffer method on C_3A mixed with small amounts of water (w/s ~ 0.05). The RH remains at 100% for a couple of hours, followed by a sudden drop down to 45-50% RH, and a slight increment up to 50-55% RH. The temperature was increased in Test 1 and Test 2 in order to determine the equilibrium RH at higher temperatures. During Test 3 the temperature was kept constant at 35 °C. With increasing temperature the equilibrium RH shows a slight increase.

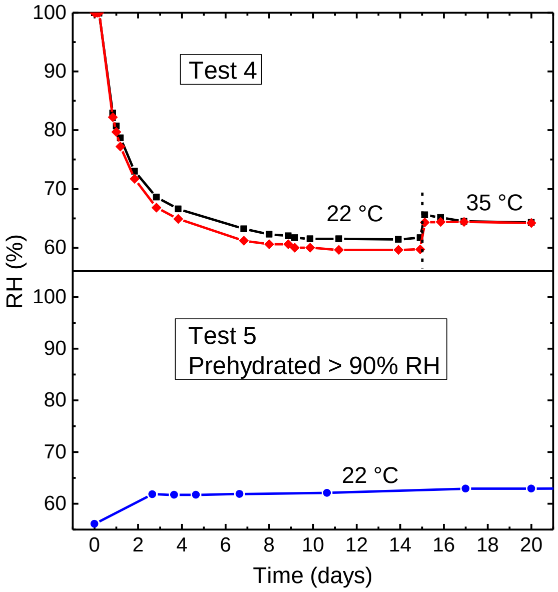

Figure 6:2 Test4: Measured RH using the hydrate pair-humidity buffer method on CA mixed with small amounts of water (w/s ~ 0.05). The RH remains at 100% for ~ 6 h, followed by a steady decrease of RH down to ~ 60% RH. With increasing temperature the equilibrium RH shows a slight increase. Test 5: Measured RH of CA initially prehydrated at 90% RH and 22 °C for 6 days. The equilibrium RH is similar to the one observed when CA was directly mixed with water.

Subsequently, the thermodynamic properties of the studied clinker phases were empirically modified to fit the experimentally obtained steady state RHs (shown as filled dots in Figure 6:4). With the relation given in Eq. (2.2) and the known relative humidity the free energy of reactions (6.1) and (6.2) were estimated. As the thermodynamic properties of water steam and of the hydrates are known it is straightforward to estimate free energy of formation of the surface properties of the clinker phases. With the obtained experimental data points at higher temperatures it was possible to estimate the enthalpy of reaction using a van't Hoff approach (Eq. (2.3)). The resulting thermodynamic data are summarised in Table 6:1. Although these data do not correspond to the real thermodynamic properties of C_3A and CA, they may have a physical explanation, such as the properties of a hydroxylated layer [40]-[41] covering the unreacted clinker phases, which prevent further reaction and are therefore called C_3A_hyd and CA_{hyd}. The modelled reaction behaviour is also shown in Figure 6:4 for the hydration of CA and C_3A according to reactions (6.1) and (6.2) and indicate two possible scenarios: i) in the presence of water vapour hydration will take place at or above the RH indicated in the modelled curve, and ii) if the studied clinker phases are mixed with water in such a way that unreacted anhydrous phases remain, then the predicted RH will be given by the modelled curve and the anhydrous clinker phases would act as buffer of the limiting RH.

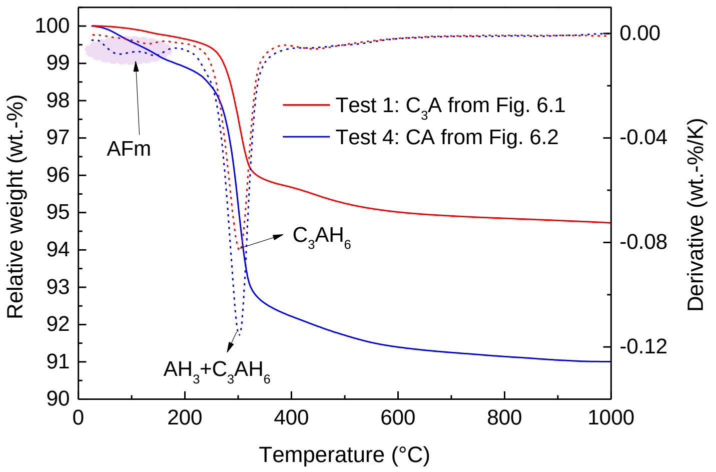

Figure 6:3 TGA patterns of the C_3A and CA experiments (test 1 and 4 from Figure 6:1 and Figure 6:2).

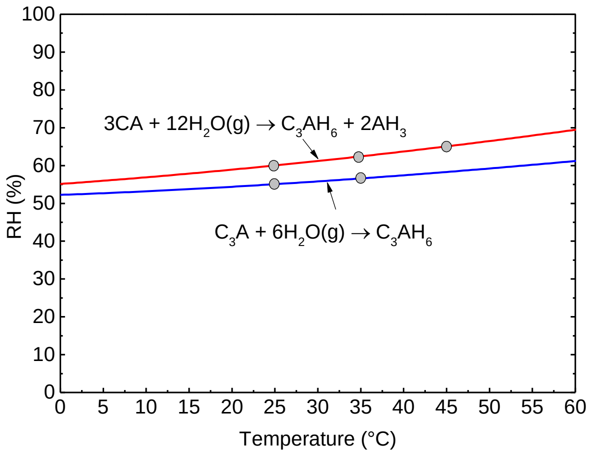

Figure 6:4 Experimental points (filled dots) used to calculate the thermodynamic properties of C_3A_hyd and CA_hyd shown in Table 6:1. The graph shows the curves fitted to these data which indicate the RH at which hydration will take place as function of temperature. The curves also indicate the equilibrium RH of a hydrated system due to self-desiccation, i.e. anhydrous clinker phases remain at the end of the hydration process.

Table 6:1 Empirical standard molar thermodynamic properties of bulk and hydroxylated C_3A and CA at 25 °C and 1 bar.

Phase	ΔG_f° (kJ/mol)	ΔH_f° (kJ/mol)	S° (J/mol K)	Cp° (J/mol K)	V° (cm^3/mol)	Ref.
C_3A_{hyd} [b]	-3576.2	-3810.6	10.6	209.4	89.2 [a]	t.s.
C_3A	-3382.3	-3560.6	205.4	209.4	89.2	[36]
CA_{hyd} [b]	-2246.8	-2378.1	68.2	125.7	---	t.s.
CA	-2207.9	-2327.1	114.2	125.7	---	[36]

[a] From [47].
[b] hyd stands for hydroxylated.

6.4 Stability of AFm phases as function of RH and temperature

The behaviour of pure AFm phases as function of temperature and RH was modelled using the thermodynamic properties of the hydration states of monosulfoaluminate, monocarboaluminate, hemicarboaluminate, strätlingite and hydroxy-AFm reported in Chapter 4. The GEM-Selektor code [10]-[11] was used to model the stability of AFm phases. For more details about the modelling please refer to Chapter 2. The phase diagrams shown for each of these phases were modelled assuming two different scenarios: i) only one mineral with different hydration states was considered (referred as modelling in metastable conditions) and ii) other phases are allowed to form during drying and/or change of temperature (referred as modelling in equilibrium conditions but under isochemical compositions). In order to compare the volume changes during drying, the volumes of the different phases were normalized considering the higher hydration state of each AFm phase as 100 vol.%. Since only the stability of already formed AFm hydrates was of interest in this section, clinker phases were not considered during modelling.

6.4.1 Monosulfoaluminate

The modelled phase diagram of the system monosulfoaluminate – H_2O is shown in Figure 6:5. The predicted stability of Ms16 is based on thermodynamic properties determined from experimental observations, as described in Chapter 3. The atypical behaviour observed in the modelled stability of Ms14, i.e. lower transition RH with increasing temperature, is due to the positive enthalpy of mixing (ΔH_{mix}) for the rehydration $Ms12+2H_2O \rightarrow Ms14$ reported in Chapter 3. Usually rehydration processes have negative (exothermic) ΔH_{mix} values. One possible reason for this unusual behaviour is the hysteresis reported in Chapter 3 for the transition Ms12↔Ms14. When dealing with hysteresis sometimes the enthalpies calculated using the van't Hoff equation (either from the desorption or absorption branch of the isotherm) do not agree with the measured enthalpies (by calorimetry). Another reason for the atypical behaviour might be the high stability of Ms12, meaning that in order to incorporate water within the structure of Ms12 (usually an exothermic process), probably some bonds must be broken (typically an endothermic process). If the second process dominates, that may be an indication of the positive energy of mixing. Typically processes with positive enthalpies of mixing are leading often to phase immiscibility at changing temperatures. This may be an explanation why Ms14 is only experimentally observed at higher temperatures >20°C in the phase diagram.

In any case, the phase diagrams shown in Figure 6:5 predict reasonably well the experimental observations. For the transition Ms12↔Ms10.5, a marked hysteresis was also reported between desorption and absorption. In Chapter 4 the thermodynamic properties were reported for both, absorption and desorption, assuming that the enthalpy of reaction was equal in both processes. The stability of Ms10.5 shown in Figure 6:5a was modelled using both values (for absorption and desorption) (see Annex Table C:2), resulting in a shaded area representing the impact of the hysteresis loop in Figure 6:5a. The exact boundaries of the hysteresis loop were not determined experimentally and are based on calculations. To be on the safe side it is advised to assume that dehydration will take place when crossing the absorption curve of the hysteresis loop. Ms9 is predicted at low RH. Its stability increases with rising temperatures.

Figure 6:5a was calculated assuming iso-mineral phase assemblages, considering only the different hydration states of monosulfoaluminate and water. In order to model the impact of water activity and temperature on phase assemblages relevant to the system $CaO-Al_2O_3-SO_3-H_2O$ at isochemical composition (i.e. reflecting the stoichiometry of monosulfoaluminate but with variable water content) at equilibrium conditions Figure 6:5b was constructed. As advised above it was assumed that the adsorption curve for the transition Ms12↔Ms10.5 corresponds to equilibrium. According to the model, Ms10.5 should decompose into C_3AH_6 and $CaSO_4$, although this was not observed in any of the experimental results previously reported. To conclude, it is assumed that the dehydration behaviour of monosulfoaluminate is best explained by using Figure 6:5a under consideration of the metastability constraints imposed on hydrogrossular and anhydrite.

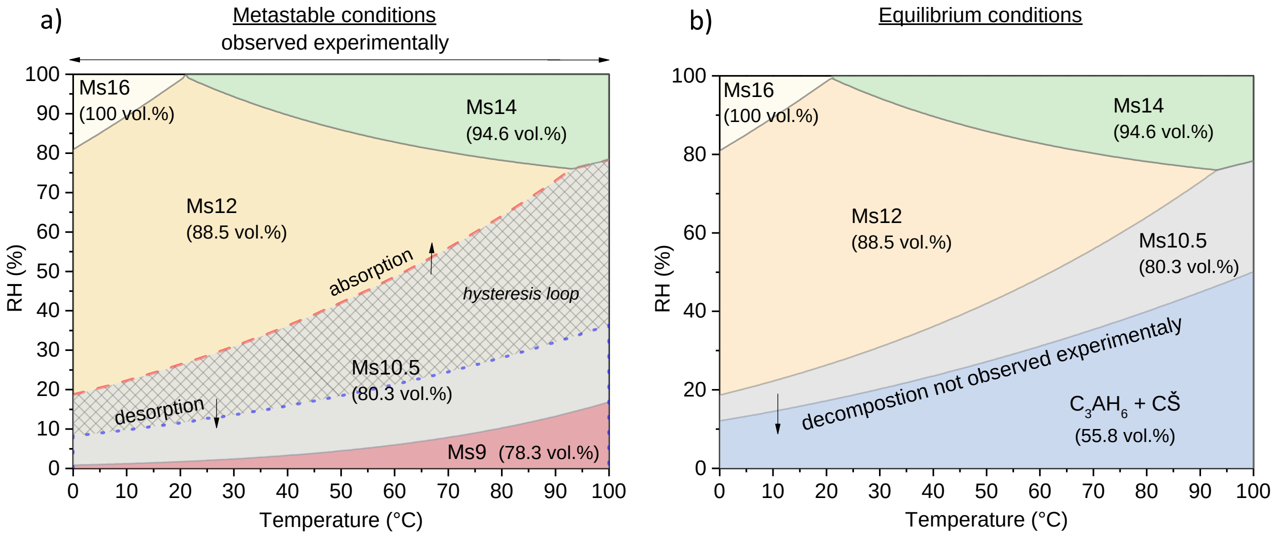

Figure 6:5 Predicted stability of monosulfoaluminate as function of RH and temperature at 1 bar under a) metastable and b) equilibrium conditions. The graph at metastable conditions agrees better with the experimental results.

6.4.2 Monocarboaluminate

The phase diagrams of monocarboaluminate as function of RH and temperature are presented in Figure 6:6. At metastable (iso-mineralogical) conditions, very low RHs are required in order to decompose Mc11. On the other hand, in equilibrium conditions considering the formation of other hydrates, the model predicts decomposition of Mc11 into hydrogarnet (C_3AH_6) and calcite ($C\hat{C}$) during drying. This has not been observed experimentally to a large extent. Nevertheless small amounts of hydrogarnet (up to 3%) were observed in the samples at 50 °C (see Chapter 4). Whether the absence of decomposition during drying is due to kinetic constraints or due to lack of a favourable media (liquid) for nucleation remains unknown. The predicted decomposition in saturated conditions above 93 °C (Figure 6:6b) was also predicted by Matschei et al. [8] but this was not confirmed in this study.

The experimentally observed persistence of monocarboaluminate agrees better with the phase diagram modelled under metastable conditions.

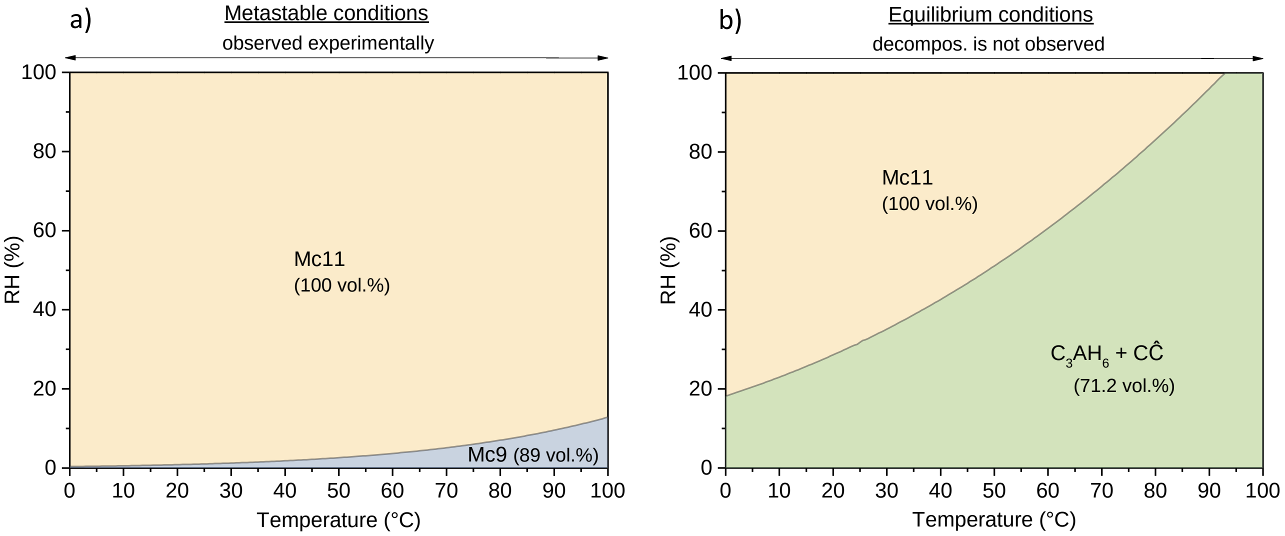

Figure 6:6 Predicted stability of monocarboaluminate as function of RH and temperature at 1 bar under a) metastable and b) equilibrium conditions. The graph at metastable conditions agrees with the experimental observations.

6.4.3 Hemicarboaluminate

Hemicarboaluminate was one of the most complex AFm phases studied experimentally in this thesis (see Chapter 4) and this is reflected in the phase diagrams shown in Figure 6:7. The complexity might be due to the occurrence of partial solid solutions, disorder in the stacking of the layers, transition between higher to lower hydration states, and/or lower stability compared to other phases.

In metastable conditions (Figure 6:7a), Hc12 is predicted to be present over a wide range of RHs. Then Hc12 dehydrates to Hc10.5 and later to Hc9. The first dehydration step (Hc12→Hc10.5) was experimentally confirmed at 5 °C. At 25 °C this reversible transition was confirmed by sorption balance measurements and sorption calorimetry. Nevertheless, after long drying periods at 25 °C a second phase called carbonated hemicarboaluminate ($C_4AC_{0.8}H_{10.2}$ or cHc, see Chapter 4) was observed in significant amounts with decreasing RH, together with C_3AH_6 and CH impurities. At 50 °C the decomposition into cHc, C_3AH_6 and CH was faster and completed < 50% RH. Due to the lack of sufficient experimental and thermodynamic data for cHc it was assumed that the metastable phase diagram represents realistically the experimental observations from 0 °C to 20 °C (non-shadow area in Figure 6:7a).

On the other hand under equilibrium conditions the model predicts the decomposition of Hc12 into Mc11, C_3AH_6 and CH with decreasing RH or increasing temperature. As outlined in Chapter 4 at high temperatures the formation of cHc (instead of Mc), C_3AH_6 and CH was experimentally observed. As cH_c is compositionally close to Mc, it is recommended to consider that the equilibrium phase diagram Figure 6:7b) represents experimental observations at temperatures > 20 °C, but assuming cHc instead of Mc as the decomposition product.

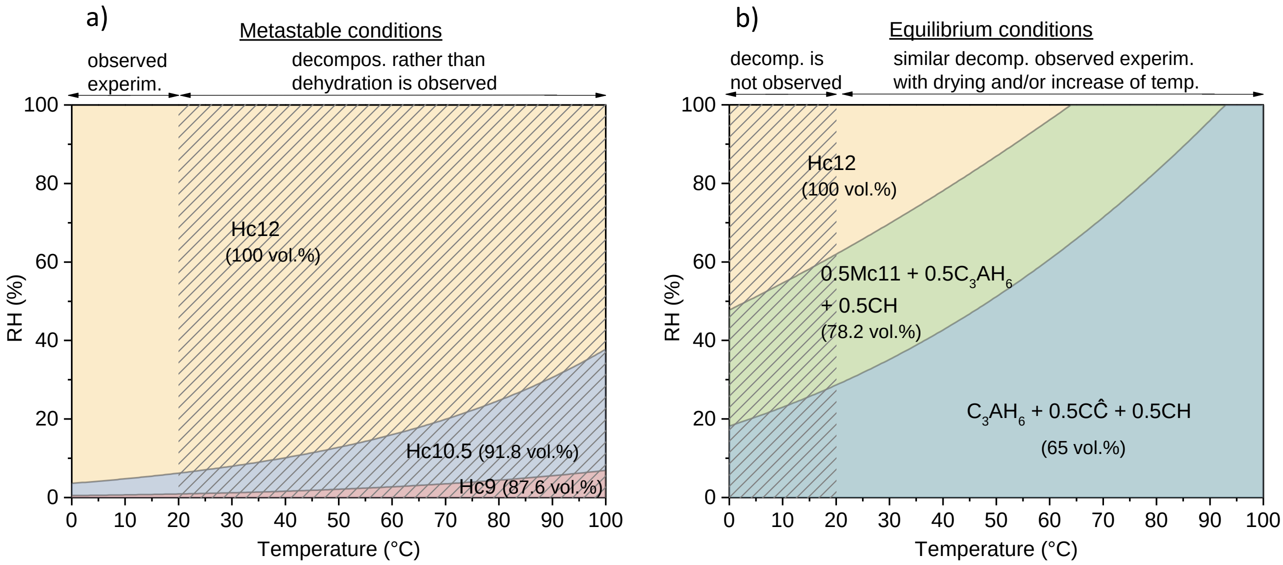

Figure 6:7 Predicted stability of hemicarboaluminate as function of RH and temperature at 1 bar under a) metastable and b) equilibrium conditions.

6.4.4 Hydroxy-AFm

Hydroxy-AFm is probably one of the least stable cement hydrates. Samples aged above 25 °C tend to decompose quickly into C_3AH_6 and CH, and Hc12 is usually observed due to the presence of small amounts of CO_2 in the experiments. Therefore, although the phase diagram shown in Figure 6:8a (under metastable conditions) presents different hydration states of OH-AFm up to 100 °C, this phase will tend to decompose at temperatures > 25 °C.

On the other hand under equilibrium conditions (Figure 6:8b), OH-AFm19 is predicted to be stable below 19 °C and with further increase of temperature or during drying it should decompose into C_3AH_6 and CH. This decomposition behaviour has been observed when drying at temperatures > 25 °C.

The dehydration behaviour observed experimentally agrees with the unshaded sides of the metastable phase diagram and the equilibrium phase diagram. Since no specific limiting temperature was determined experimentally, it was assumed that 19 °C corresponds to the maximum stability limit as predicted in equilibrium in saturated conditions.

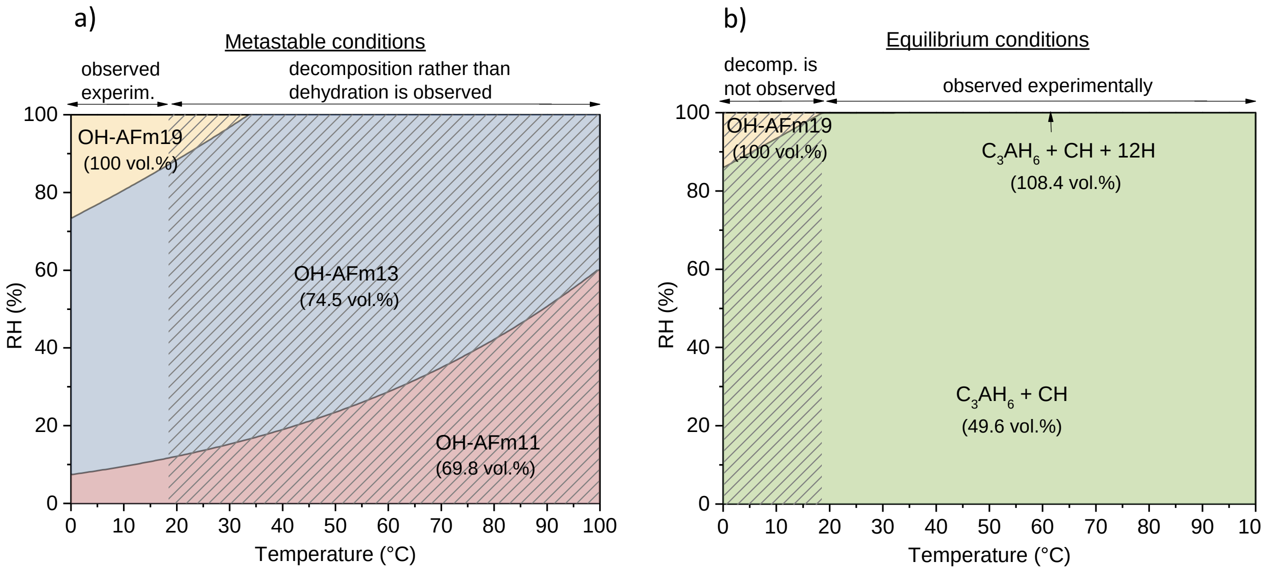

Figure 6:8 Predicted stability of hydroxy-AFm as function of RH and temperature at 1 bar under a) metastable and b) equilibrium conditions. The graph in metastable conditions agrees with the experimental observations below 19 °C. At temperatures > 19 °C refer to the graph in equilibrium conditions.

6.4.5 Strätlingite

The phase diagram of strätlingite is shown in Figure 6:9. Since the transition Str8↔Str7 does not take place stepwise, an ideal solid solution model (see Chapter 2) was used to model the response during drying. The stability modelled in metastable and equilibrium conditions are equal and agree with experimental observations. The Str8-Str7 solid solution is predicted along a wide range of temperatures and RHs, and when exposed to very low RHs it dehydrates into Str5.5. According to the modelled behaviour, strätlingite appears to be a very stable phase during drying. Although the water content varies significantly (from 8 to 5.5 H_2O) the volume remains almost unchanged.

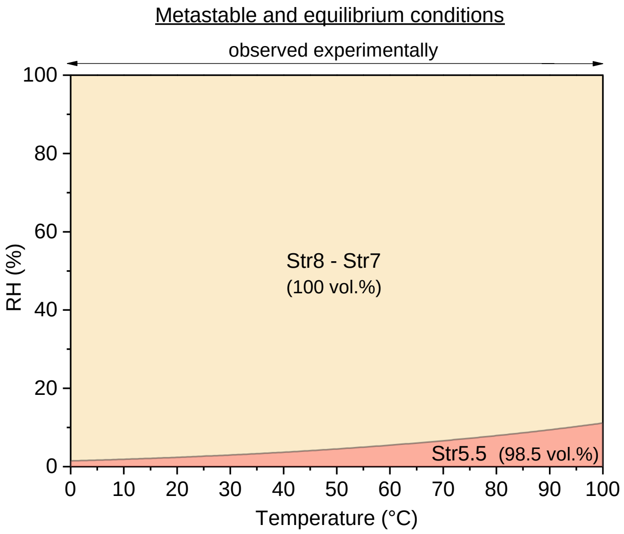

Figure 6:9 Predicted stability of strätlingite as function of RH and temperature at 1 bar. Modelling under metastable and equilibrium conditions results in the same phase diagram.

6.4.6 Remarks on AFm phases

During modelling it was found that the experimental behaviour of some AFm phases agrees better with the modelling in metastable conditions and others with both metastable and equilibrium conditions. When modelling in equilibrium conditions decomposition into more stable phases rather than dehydration is predicted for every AFm phase, except strätlingite. The modelled results for hemicarboaluminate and hydroxy-AFm agree with the metastable phase diagrams at lower temperatures (< ~20 °C) but with the equilibrium conditions at higher temperatures (> ~20 °C). The reason why the predicted decomposition to some phases like C_3AH_6 and anhydrite from monosulfoaluminate under equilibrium conditions is not observed experimentally might be the absence of a liquid aqueous phase that allows the dissolution and precipitation needed for decomposition. On the other hand phases like hydroxy AFm and hemicarboaluminate do decompose to C_3AH_6 and portlandite also at unsaturated conditions (RH < 100%), although a complete decomposition can take several days (depending on the temperature and amount of sample).

6.5 Thermodynamic modelling of the hydration of C_3A and CA in the presence of calcium hydroxide, calcium carbonate and calcium sulfate

The hydration of two clinker phases relevant to Portland based cements and calcium aluminate cements, C_3A and CA, respectively, were modelled in the presence of $Ca(OH)_2$, $CaCO_3$ and $CaSO_4$. For practical applicability the scales on the axes of the calculated ternary phase diagrams were chosen in wt.%. When less water than that required to achieve 100% hydration is used, the final phase assemblage contains anhydrous phases, and thus the predicted RH is < 100%. On the other hand when excess of water is present in the modelled phase assemblages the predicted RH is close to 100%. This might not be the case in solutions with high ionic strength, such as cementitious systems with high alkali content, but since in this work the Debye–Hückel equations (included in GEM-Selektor [10]-[11]) rather than the Pitzer equations [42] were used to model the hydration behaviour, we restricted the final RH in presence of water to 100%. Nevertheless the general relations shown in the phase diagrams are also valid for solutions with lower water activity.

In case ettringite is present in a predicted phase diagram, it will be represented as Ett, indicating a water content from 30 to 32 H_2O, i.e. an ideal solid solution Ett32-Ett30.

6.5.1 The C_3A subsystem

In this section the hydration behaviour of C_3A in the presence of CH, $CaCO_3$ and $CaSO_4$ is modelled. This subsystem is relevant to Portland-based cementitious systems, were C_3A is present. The newly derived thermodynamic properties of the hydroxylated C_3Awere used in the modelling.

6.5.1.1 Hydration of C_3A in the presence of CH

The hydration of C_3A in the presence of CH was modelled at 25 °C and 5 °C. The results are shown in Figure 6:10.

At 25 °C there is no influence of the CH additions in the final modelled phase assemblage, since C_3AH_6 is the most stable phase at temperatures > 19 °C (as also shown in Figure 6:8b). The predicted RH in unsaturated conditions corresponds to 55%, which agrees with the experimental curve shown in Figure 6:4 for the C_3A reaction according to Eq. (6.1). In this case the presence of C_3A and C_3AH_6 buffers the RH to 55% and CH does not affect the predicted value.

At 5 °C the modelled phase assemblage differs considerably from the one at 25 °C. With increasing amounts of water OH-AFm19 becomes the predominant phase, together with C_3AH_6 in some regions. Due to the appearance of OH-AFm19 in the phase diagram the chemical water binding capacity increases significantly compared to 25°C. The optimum water binding is achieved along the C4AH19 boundary in Figure 6:10b. In water deficient regions and in presence of high amounts of C_3A, C_3AH_6 rather than OH-AFm19 is predicted. This agrees with the calculations shown in Figure 6:8b whereas C_4AH_{19} becomes metastable with respect to C_3AH_6 at <90% RH.

For a careful interpretation of the phase diagrams kinetics of hydration should be taken into account, especially at low water contents. For example during the initial hydration of C_3A in presence of water the first hydrates to precipitate are C_4AH_{19} and C_2AH_8 [43] which later will decompose to C_3AH_6 and CH in the course of drying or self-desiccation.

From the calculations it becomes obvious that temperature as well as water activity have a big impact on the predicted phase assemblages of cementitious systems.

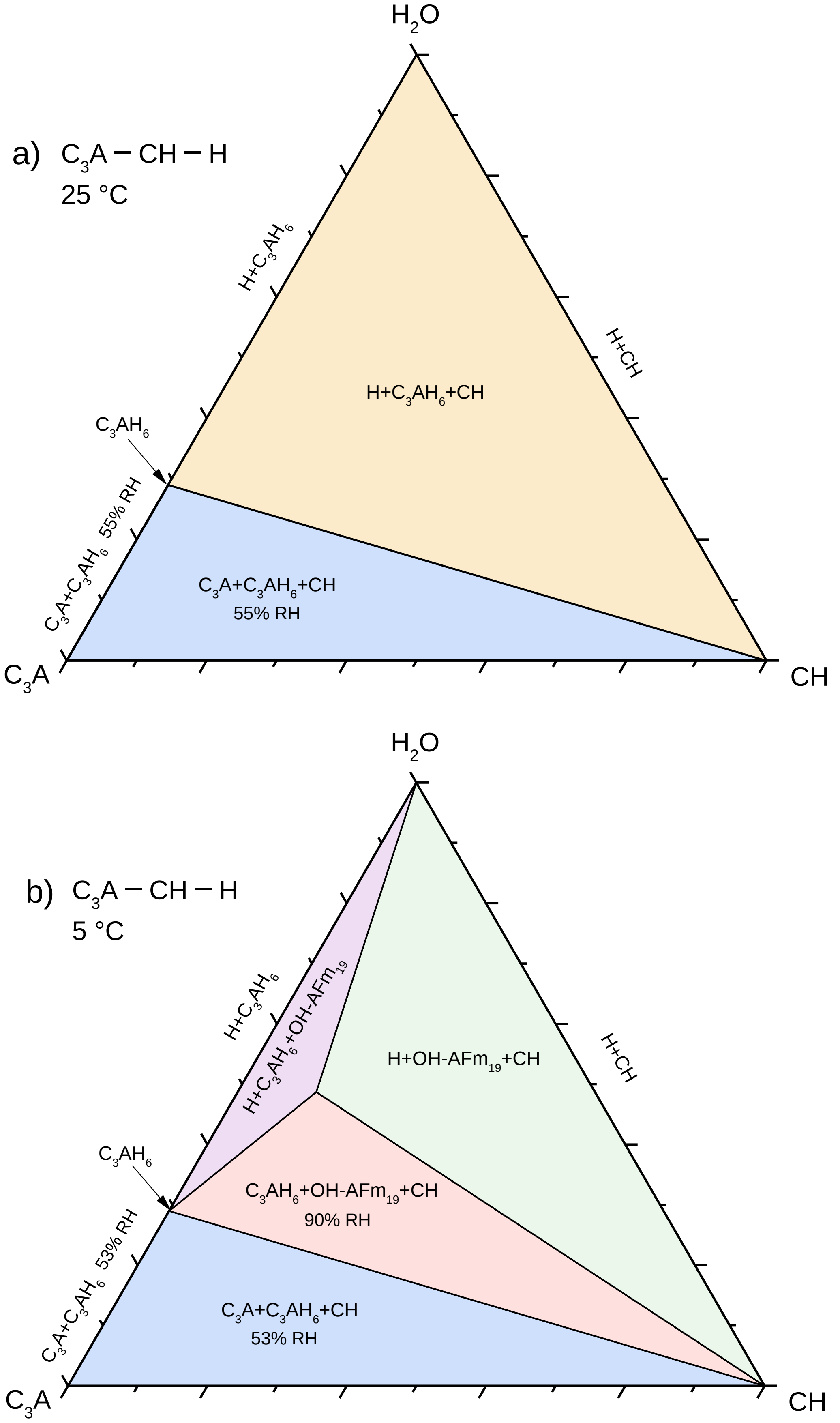
a)
C_3A – CH – H
25 °C
H_2O
$H+C_3AH_6$
H+CH
$H+C_3AH_6+CH$
C_3AH_6
55% RH
$C_3A+C_3AH_6$
$C_3A+C_3AH_6+CH$
55% RH
C_3A
CH
b)
C_3A – CH – H
5 °C
H_2O
$H+C_3AH_6$
$H+C_3AH_6+OH\text{-}AFm_{19}$
$H+OH\text{-}AFm_{19}+CH$
H+CH
C_3AH_6
$C_3AH_6+OH\text{-}AFm_{19}+CH$
90% RH
53% RH
$C_3A+C_3AH_6$
$C_3A+C_3AH_6+CH$
53% RH
C_3A
CH

Figure 6:10 Calculated ternary phase diagram C_3A-CH-H_2O at a) 25 °C and b) 5 °C. Axes units in wt.%.

6.5.1.2 Hydration of C_3A in the presence of $CaCO_3$

The modelled hydration behaviour of C_3A in presence of $CaCO_3$ is shown in Figure 6:11. The stable cement hydrate in every region is monocarboaluminate (Mc11). In low calcite systems C_3AH_6 will be formed additionally together with Mc11. It is important to note that theoretically small shifts of the water content of the system may have a big impact on the resulting water activity e.g. along the boundary Mc11 and $CaCO_3$ in presence of unreacted $C3A_{hyd}$ the theoretical RH would be predicted to be 43%, whereas in presence of water the RH would naturally be close to 100%. Due to kinetics of hydration as well as due to the impact of microstructural features, e.g. porosity and the formation of local equilibria, these abrupt hydration steps are unlikely to occur in real systems. Furthermore, it is interesting to note that in presence of calcite C_3A would theoretically start to react at RH > 43% whereas in absence of calcite this critical humidity would be increased to 55%.

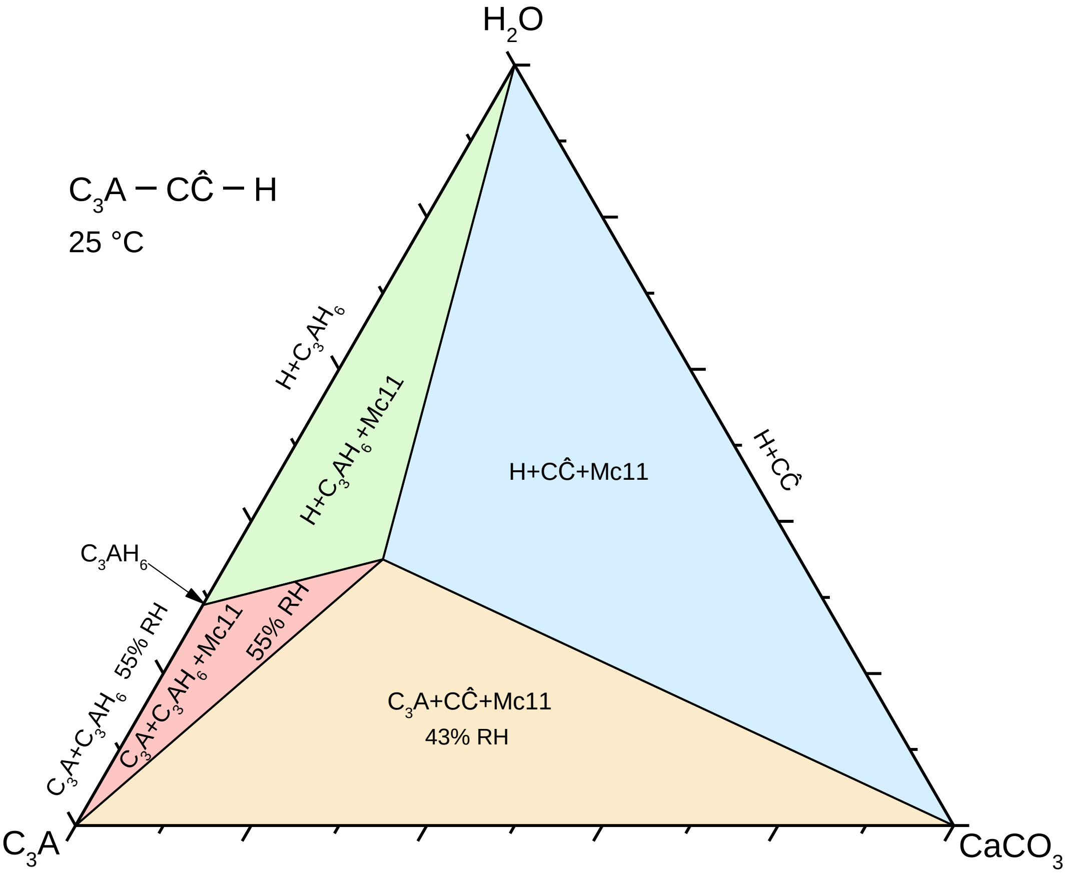

Figure 6:11 Calculated ternary phase diagram C_3A-$CaCO_3$-H_2O at 25 °C and 1 bar. Axes units in wt.%.

Figure 6:12 shows the same phase diagram in presence of CH. In the regions with a molar CO_2/Al_2O_3 ratio < 1, hemicarboaluminate Hc12 is predicted to occur as additional phase. This has an impact on the total water binding capacity of the system, which is optimum along the Hc12-Mc11 boundary of the phase diagram.

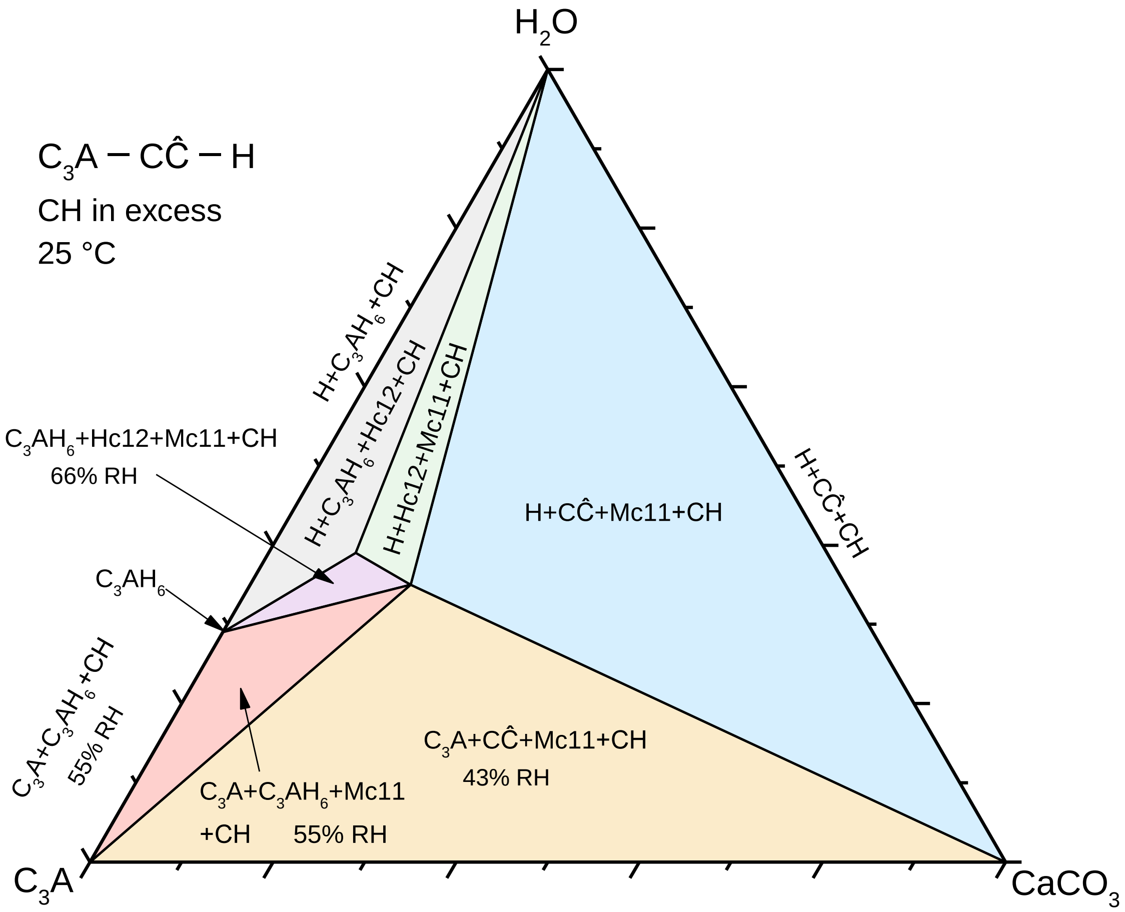

Figure 6:12 Calculated ternary phase diagram C_3A-$CaCO_3$-H_2O at 25 °C and 1 bar in portlandite (CH) saturated conditions. Axes units in wt.%.

6.5.1.3 Hydration of C_3A in the presence of $CaSO_4$

The modelled hydration behaviour of C_3A in the presence of $CaSO_4$ at equilibrium conditions is shown in Figure 6:13. The regions with liquid water present in the final phase assemblage agree very well with experimental observations. Not surprisingly the point of the highest theoretical water binding capacity coincides with the stoichiometry of ettringite. This explains why ettringite based hydrated cementitious systems are also preferably used for application where fast drying and/or high water binding, e.g. for flooring or repair systems, is of high interest. Care has to be taken to optimise a cementitious system to obtain maximum ettringite contents as due to kinetic restrictions dimensional stability problems as consequence of a late ettringite formation may occur.

According to the validation experiments subsequently described, in some areas at unsaturated conditions the model does not agree with experimentation due to the kinetic and/or metastability constraints: experimentally, during hydration of C_3A in the presence of sulfates, the first hydration product formed is ettringite; once the system is depleted of sulfates ettringite will react with the remaining C_3A to form Ms14, all this in the presence of water. If all the water is consumed, for instance, before all the C_3A and sulfates react, then hydration will not proceed and the final phase assemblage will be composed of Ett plus unreacted C_3A and $CaSO_4$.

Two validation experiments were carried out (indicated as V1 and V2 in Figure 6:13) using the hydrate pair – humidity buffer method, and the measured RH as function of time is shown in Figure 6:14. The predicted and experimental phase composition and RHs are shown in Figure 6:15 for the two points. Some remarks follow:

- V1 (C_3A: 32.4 wt.%, $C\hat{S}$: 32.4 wt.%, H: 35.2 wt.%): This test was carried out with enough water to produce a paste, which was then poured in the small glass recipients for the hydrate pair – humidity buffer test. The experimental observations are best explained following the reaction path shown by the red arrow of V2 in Figure 6:13. Pore solution analysis of OPC showed that in presence of calcium sulphate equilibrium with gypsum/anhydrite is reached within a couple of seconds after mixing. For simplicity we assume that at the beginning of the test an equilibrium close to gypsum or anhydrite saturation will be reached very fast, the RH reaches 100% and then the C3A starts to react to form ettringite. As shown in Figure 6:14 due to a high w/s ratio used the phase assemblage ettringite-gypsum/anhydrite-water is buffering the RH for up to 5 days. After 5 days all water was consumed and consequently a transition to a new equilibrium should be observed. This is the case as the RH rapidly decreased. In order to enhance equilibration the sample was crushed after 9 days. As shown in Figure 6:14 after ~40d the RH still decreases slowly and has reached 52% when the test was stopped. According to the phase diagram (Figure 6:13), in equilibrium we would expect that C_3A should have completely reacted to form ettringite, anhydrite and monosulfoaluminate at a RH of 43% as described on the left-hand side of Figure 6:15a. Nevertheless an XRD-Rietveld quantification showed the presence of unreacted C_3A, anhydrite and ettringite in the experimental sample, which means that the conversion of ettringite to monosulfoaluminate was not observed. If we now model the phase assemblage again and we do not consider a transformation to monosulfoaluminate our modelled metastable phase assemblage (C_3A, ettringite and anhydrite) agrees qualitatively and quantitatively very well with the experimental one. Nevertheless the experimental RH of (52%) is still higher than the predicted (38% RH) as shown in Figure 6:15a.

- V2 (C_3A: 29.4 wt.%, $C\hat{S}$: 63.6 wt.%, H: 7 wt.%): The setup of experiment V2 is similar to the test we used to obtain the thermodynamic properties of C_3A_{hyd}. Here we wanted i) to force the systems to reach equilibrium very fast and ii) to check the impact of calcium sulphate on the equilibrium RH. If we look closer to the expected reaction path according to the phase diagram, we would assume a reaction of the used anhydrite to gypsum which would already be sufficient to decrease RH to 77%. Nevertheless the RH remained at 100% for 7h which is an indication that a formation of gypsum did not occur but the phase assemblage water, ettringite and anhydrite buffers the RH at initial stages of reaction. After 7h a sudden drop of humidity occurs, which means that the phase assemblage shifts from water saturation to undersaturation. Within 5 days the RH reached 38% and remained unchanged until the end of the test after 35 days (Figure 6:14). According to the phase diagram (Figure 6:13) at equilibrium conditions monosulfoaluminate, anhydrite and C_3A would have been expected as phase assemblage (RH = 32%). Similarly as in test V1 the XRD Rietveld analysis showed the persistence of ettringite and no monosulfoaluminate was detected. Therefore the calculations were repeated taking the metastability of ettringite into account. As before the predictions agree qualitatively and quantitatively very well with the measured phase assemblage (Figure 6:15b). It is also important to note that the measured RH agrees well with the predictions, which shows that the presence of calcium sulphate impacts the critical RH at which C_3A starts to react.

The consideration of known metastability criteria is a valid approach in thermodynamics in order to account for kinetics, as mentioned by Matschei [45] in PC systems, where the stable phases tobermorite and jennite have been suppressed in favour of metastable C-S-H. Therefore experimental knowledge of phase relations needs to be taken into account when modelling these systems, especially when liquid water is not present in the final phase assemblage.

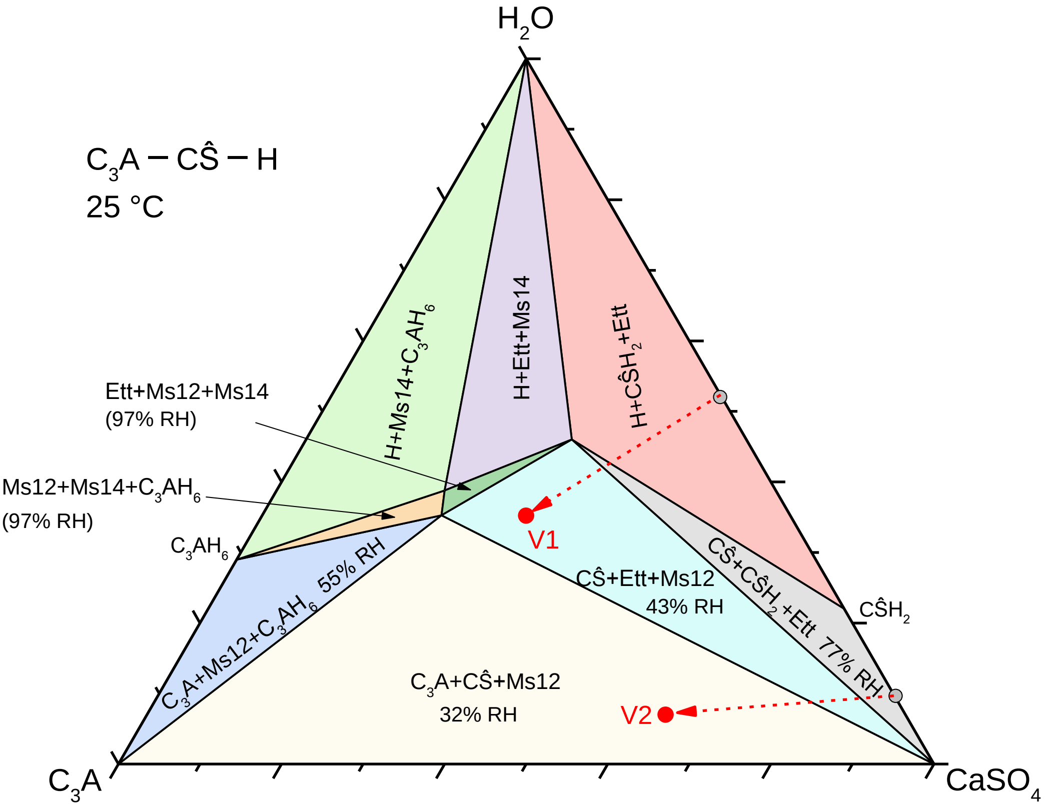
H_2O
$C_3A - C\hat{S} - H$
25 °C
$H+Ms14+C_3AH_6$
H+Ett+Ms14
$H+C\hat{S}H_2+Ett$
Ett+Ms12+Ms14
(97% RH)
$Ms12+Ms14+C_3AH_6$
(97% RH)
C_3AH_6
V1
$C\hat{S}$+Ett+Ms12
43% RH
$C\hat{S}+C\hat{S}H_2$+Ett 77% RH
$C\hat{S}H_2$
$C_3A+Ms12+C_3AH_6$ 55% RH
$C_3A+C\hat{S}$+Ms12
32% RH
V2
C_3A
$CaSO_4$

Figure 6:13 Calculated ternary phase diagram C_3A-$CaSO_4$-H_2O at 25 °C and 1 bar. Points V1 and V2 are two validation tests. Axes units in wt.%.

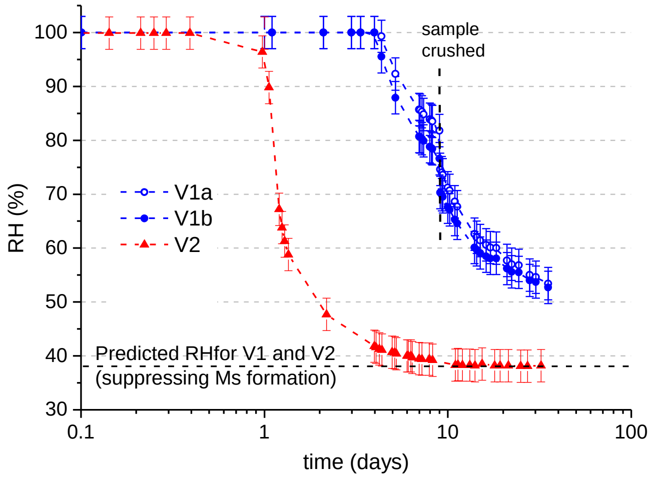

Figure 6:14 Measured RH using the hydrate pair – humidity buffer method on two validation tests, denoted as V1 and V2 in Figure 6:13 (the former was done twice).

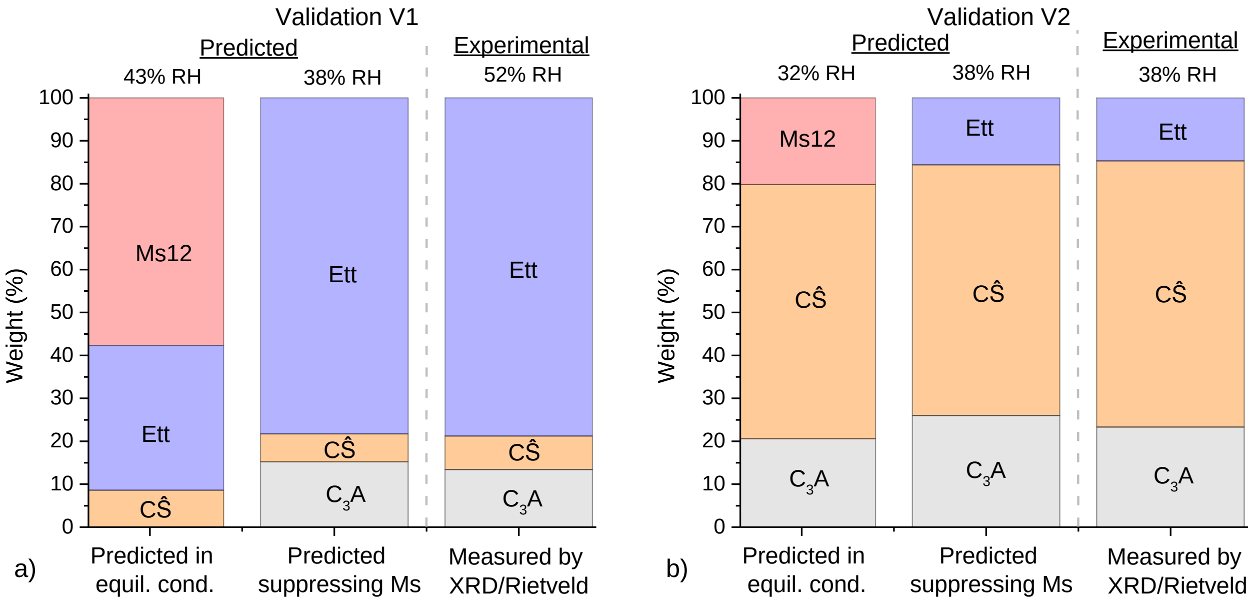

Figure 6:15 Predicted and measured phase assemblage and RH of the validation points a) V1 and b) V2 shown in Figure 6:13. The predicted values were modelled also suppressing the formation of Ms to account for kinetics constraints.

In portlandite saturated conditions the modelled phase diagram of this system is very similar to the one shown in Figure 6:13.

6.5.1.4 Hydration of C_3A in the presence of $CaSO_4$ and saturated with respect to $CaCO_3$

Figure 6:16 shows the phase diagrams of the C_3A-$CaSO_4$-H_2O subsystem and saturated with respect to $CaCO_3$, i.e. calcite was always present in every predicted region of the ternary phase diagram. In contrast to a normal ternary diagram, we allow here the presence of calcite as an excess phase, which means that the sum of C_3A, $CaSO_4$ and H_2O was kept at 100% but excess calcite was considered in the calculations. Therefore this diagram is useful to study the final phase assemblage relevant to limestone blended systems. Since experimentally in this system monocarboaluminate is formed instead of monosulfoaluminate, the formation of the latter was suppressed during modelling due to inconsistencies in unsaturated conditions, i.e. monosulfoaluminate was predicted although it is not observed experimentally.

The dashed line represents a typical PC composition (considering only C_3A and $CaSO_4$) [46]. In order to consume $CaCO_3$ all the sulfates must react and the remaining C_3A will produce Mc11. Point 1 (P1) shows the mix composition required to react all the sulfates considering the PC composition. On the other hand, in order to react the maximum possible amount of $CaCO_3$, point 2 (P2) must be reached, i.e. monocarboaluminate formation is favoured at high water contents.

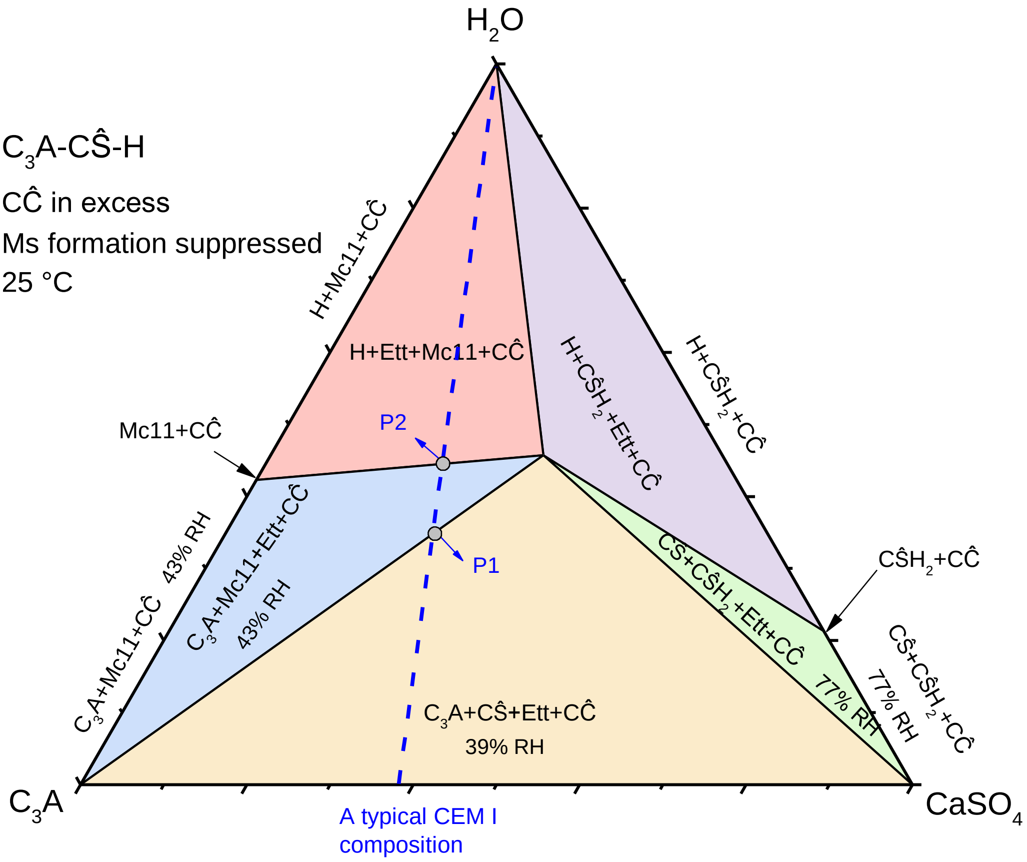
H2O
C3A-CŜ-H
CĈ in excess
Ms formation suppressed
25 °C
H+Mc11+CĈ
H+Ett+Mc11+CĈ
H+CŜH2+Ett+CĈ
H+CŜH2+CĈ
Mc11+CĈ
P2
P1
43% RH
C3A+Mc11+CĈ
C3A+Mc11+Ett+CĈ
43% RH
CŜ+CŜH2+Ett+CĈ
CŜH2+CĈ
CŜ+CŜH2+CĈ
77% RH
77% RH
C3A+CŜ+Ett+CĈ
39% RH
C3A
CaSO4
A typical CEM I composition

Figure 6:16 Calculated ternary phase diagram C_3A-$CaSO_4$-H_2O, saturated with respect to $CaCO_3$, at 25 °C and 1 bar. Axes units in wt.%.

6.5.2 The CA subsystem

In this section the hydration behaviour of CA in the presence of CH, $CaCO_3$ and $CaSO_4$ is modelled. This subsystem is relevant for binders based on calcium aluminate cements

6.5.2.1 Hydration of CA in the presence of CH

The ternary phase relations in the subsystem CA-CH-H_2O were modelled at 25 °C and 5 °C (see Figure 6:17).

At 25 °C the hydration of CA should give the stable phases C_3AH_6 and AH_3, and the latter should react with the added CH to form more C_3AH_6 (see Figure 6:17a). Experimentally, other hydrates, such as CAH_{10} and C_2AH_8, were temporarily reported during the hydration of CA at room temperature. Nevertheless these hydrates are metastable with respect to C_3AH_6, especially with increasing temperature, and for this reason are not predicted in the ternary phase diagram. The predicted RH in the region composed of CA, C_3AH_6 and AH_3 corresponds to 60%, which agrees with the experimental curve shown in Figure 6:4 for reaction (6.2). It is very interesting to note that the presence of CH lowers the stability of CA_{hyd} significantly. Theoretically and by only considering the bulk thermodynamic approach, CA should react to form C_3AH_6 at humidities ~15% RH. In practice in presence of CH the formation of AFm phases is often reported as a precursor to C_3AH_6 formation, which may lead to higher critical RH's than theoretically predicted to initiate CA hydration.

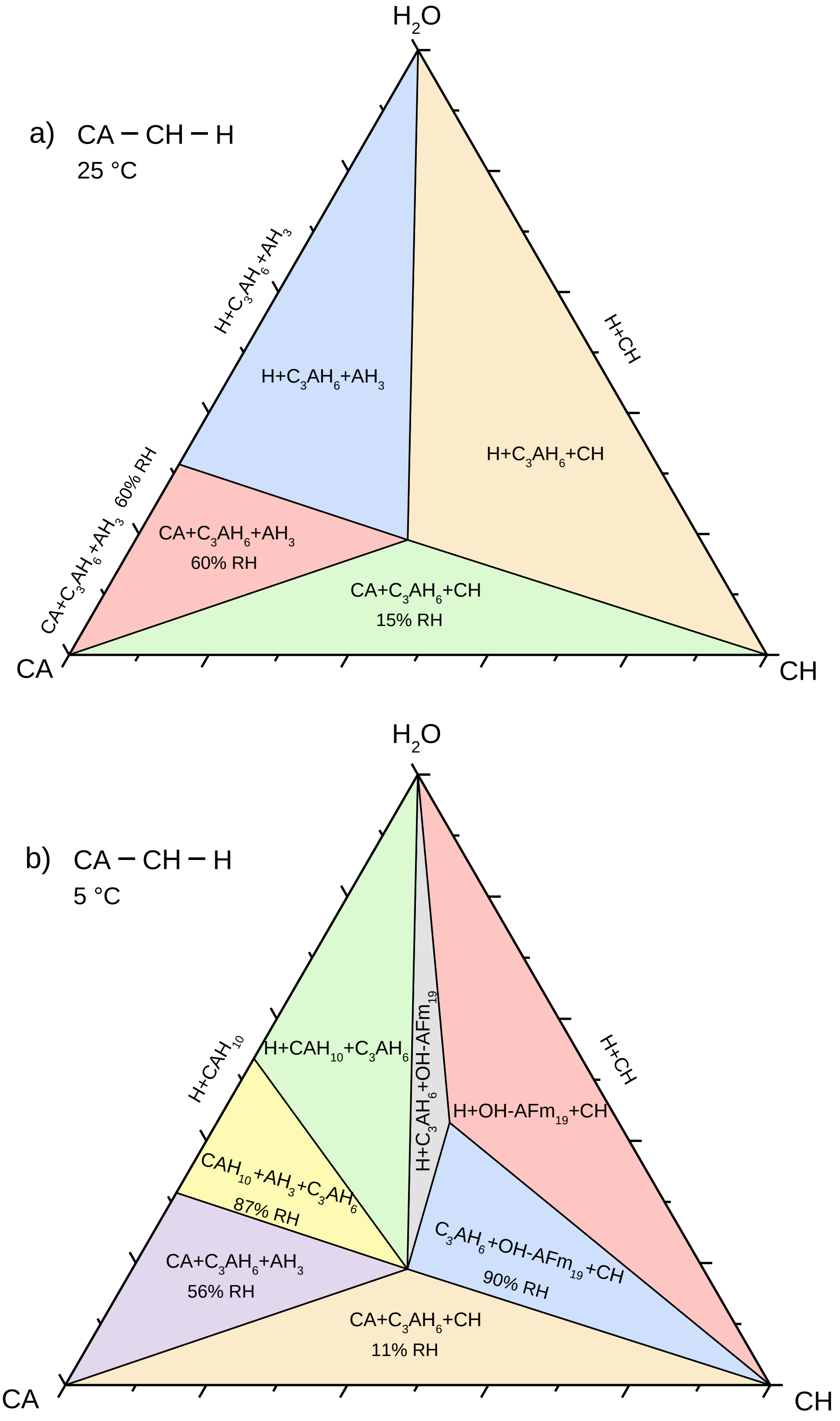
H2O
a) CA – CH – H
25 °C
H+C3AH6+AH3
H+C3AH6+AH3
H+CH
H+C3AH6+CH
60% RH
CA+C3AH6+AH3
CA+C3AH6+AH3
60% RH
CA+C3AH6+CH
15% RH
CA
CH
H2O
b) CA – CH – H
5 °C
H+CAH10
H+CAH10+C3AH6
H+C3AH6+OH-AFm19
H+CH
H+OH-AFm19+CH
CAH10+AH3+C3AH6
87% RH
CA+C3AH6+AH3
56% RH
C3AH6+OH-AFm19+CH
90% RH
CA+C3AH6+CH
11% RH
CA
CH

Figure 6:17 Calculated ternary phase diagram CA-CH-H_2O at a) 25 °C and b) 5 °C. Axes units in wt.%.

The ternary diagram modelled at 5 °C (Figure 6:17b) shows that CA hydration is very sensitive to temperature. At 5°C OH-AFm19 and CAH_{10} were predicted in some regions of the phase diagram, depending on the CaO/Al_2O_3. This strongly impacts the chemical water binding capacity of the cementitious system. Whereas at 25°C maximum water binding is achieved via formation of C_3AH_6 and AH_3 at low temperatures due to the stability of CAH_{10} and OH-AFm19 more water can be chemically bound. On the other hand if OH-AFm19 and CAH_{10} are formed in the initial stages of hydration and do later decompose due to drying and/or exposure to higher temperatures the porosity of the hydrated system will increase significantly as reported in [47].

The phase diagrams shown in Figure 6:17 (in the water saturated regions) agree with the stable hydrate phase assemblage reported by Lothenbach et al. [48].

Since the formation of C_3AH_6 at low temperatures is known to be slow the ternary phase diagram at 5 °C shown in Figure 6:17b was modelled supressing the formation of C_3AH_6 (see Figure 6:18). The predicted phase assemblage differs considerably from the one at 25 °C. Other hydrates such as OH-AFm13, OH-AFm19, C_2AH_8 and CAH_{10} are predicted in some regions. At low water contents OH-AFm13 is predicted instead of OH-AFm19.

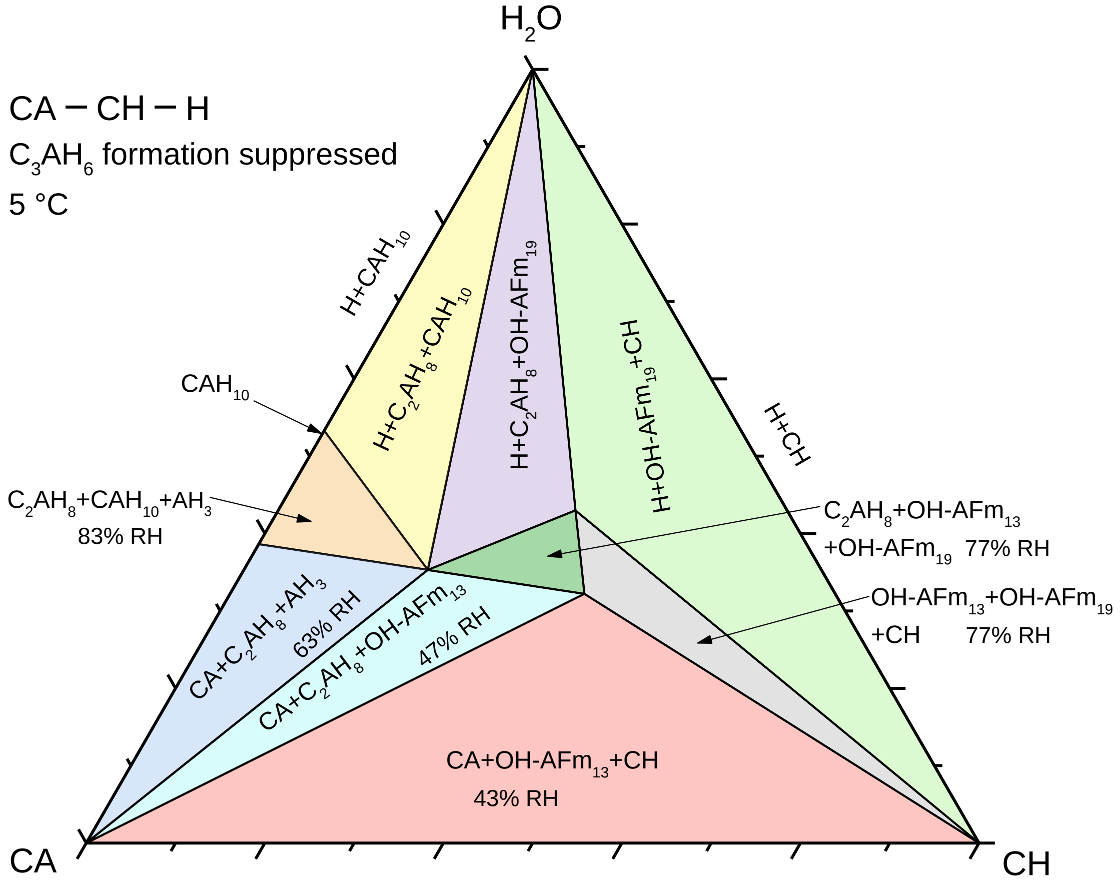
H_2O
CA – CH – H
C_3AH_6 formation suppressed
5 °C
$H+CAH_{10}$
$H+C_2AH_8+CAH_{10}$
$H+C_2AH_8+OH\text{-}AFm_{19}$
$H+OH\text{-}AFm_{19}+CH$
H+CH
CAH_{10}
$C_2AH_8+CAH_{10}+AH_3$ 83% RH
$C_2AH_8+OH\text{-}AFm_{13}$ $+OH\text{-}AFm_{19}$ 77% RH
$OH\text{-}AFm_{13}+OH\text{-}AFm_{19}$ +CH 77% RH
$CA+C_2AH_8+AH_3$ 63% RH
$CA+C_2AH_8+OH\text{-}AFm_{13}$ 47% RH
$CA+OH\text{-}AFm_{13}+CH$ 43% RH
CA
CH

Figure 6:18 Calculated ternary phase diagram CA-CH-H_2O at 5 °C and 1 bar, suppressing the formation of C_3AH_6. Axes units in wt.%.

6.5.2.2 Hydration of CA in the presence of $CaCO_3$

The modelled hydration behaviour of CA with additions of $CaCO_3$ is very similar to its C_3A counterpart, but with the addition of AH_3 in each region (see Figure 6:19). Monocarboaluminate (Mc11) is also the stable carboaluminate hydrate. The addition of small amounts of calcite to CA is advantageous as the additional formation of monocarboaluminate leads to a further increase of water binding and improves the space filling of CA cements. Thermodynamically, in presence of calcite the critical humidity to initiate CA hydration is slightly lower than in carbonate free systems.

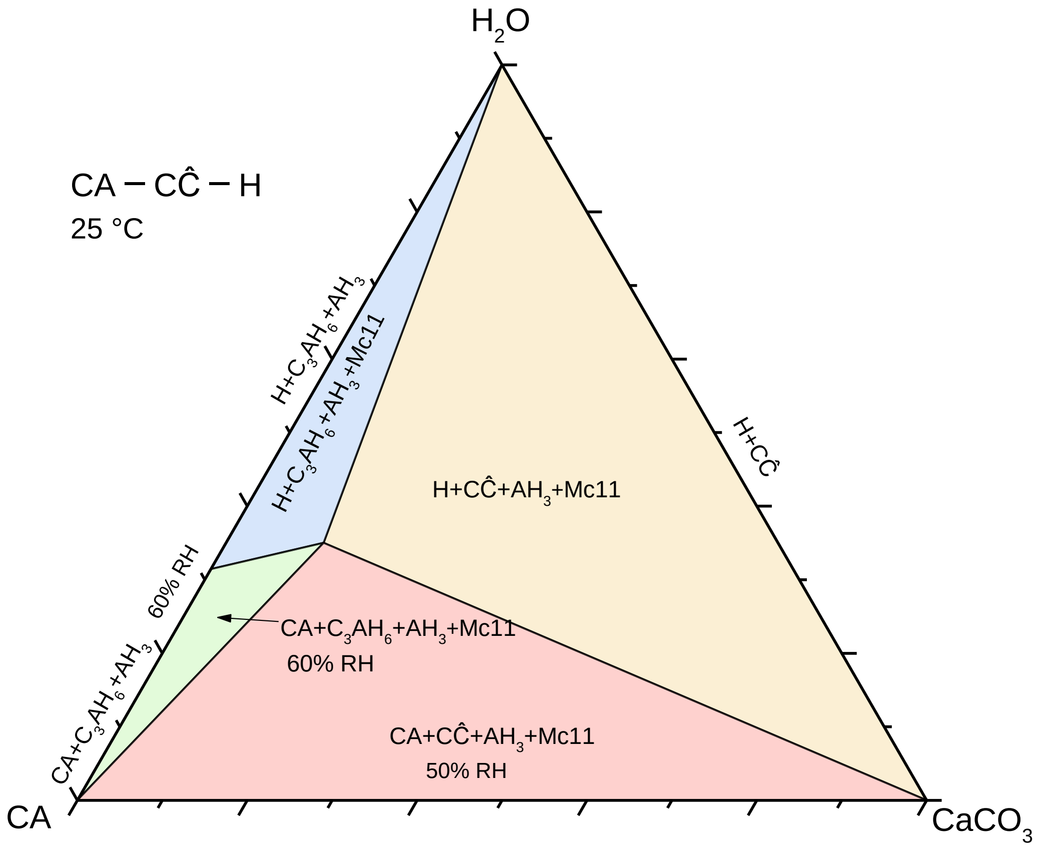

Figure 6:19 Calculated ternary phase diagram CA-$CaCO_3$-H_2O at 25 °C and 1 bar. Axes units in wt.%.

6.5.2.3 Hydration of CA in the presence of CaSO4

The predicted phase relations of CA in the presence of $CaSO_4$ and H_2O in equilibrium conditions are presented in Figure 6:20. It is shown that the addition of calcium sulphate leads to the formation of ettringite which increases the amounts of chemical bound water significantly. At water saturated conditions the predictions agree very well with experimental observations; monosulfoaluminate (Ms14) is stable at molar SO_3/Al2O3 < 1, ettringite and monosulfate (Ms14) at molar SO_3/Al_2O_3 ratios between 1 and 3 and finally ettringite and gypsum will be present at $SO_3/Al_2O_3 > 3$. Due to the absence of portlandite and the high alumina contents in this system, AH_3 will be present as additional hydrate phase. Apart from the formation of AH_3 the phase diagram is very similar to the hydration of C_3A in presence of CŜ (Figure 6:13). As experimentally a conversion of ettringite into monosulfoaluminate during drying was not observed we think that the phase relations in the regions CA+CŜ+AH_3+Ms12 and CŜ+Ett+AH_3+Ms12 are most likely not observed and ettringite, anhydrite, AH_3 will coexist with CA_{hyd}.

Thus, similar to what was mentioned for the hydration of C_3A in the presence of CŜ, metastability and kinetics should be taken into account when modelling the hydration behaviour of this subsystem, especially in the two regions mentioned in the previous paragraph, where Ms can be supressed in order to model what is observed experimentally.

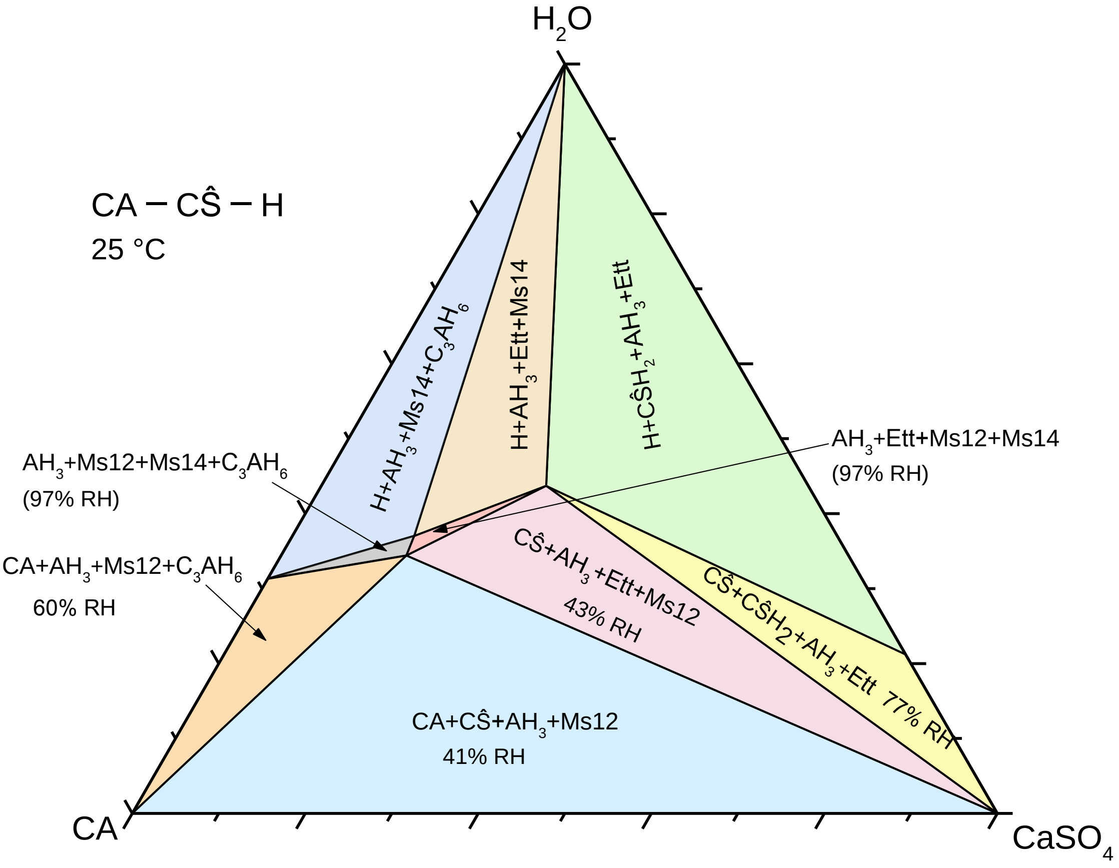
H2O
CA – CŜ – H
25 °C
H+AH3+Ms14+C3AH6
H+AH3+Ett+Ms14
H+CŜH2+AH3+Ett
AH3+Ett+Ms12+Ms14
(97% RH)
AH3+Ms12+Ms14+C3AH6
(97% RH)
CA+AH3+Ms12+C3AH6
60% RH
CŜ+AH3+Ett+Ms12
43% RH
CŜ+CŜH2+AH3+Ett 77% RH
CA+CŜ+AH3+Ms12
41% RH
CA
CaSO4

Figure 6:20 Calculated ternary phase diagram CA-$CaSO_4$-H_2O at 25 °C and 1 bar. Axes units in wt.%.

6.5.2.4 Hydration of CA in the presence of $CaSO_4$ and saturated with respect to $CaCO_3$

The modelled hydration behaviour of CA with additions of $CaSO_4$ and saturated with respect to $CaCO_3$ is shown in Figure 6:21. Similar to the approach used to model the hydration of C_3A, the formation of monosulfoaluminate was suppressed since experimentally in these systems monocarboaluminate is formed.

The dashed line represents the limit between partially reactive and non-reactive inert calcite. The more to the left of the dashed line the larger will be the amount of monocarboaluminate formed (and thus of calcite reacted). On the other hand, at the right of this line no calcite reacts and behaves as inert filler. Also, as described in Figure 6:21, the fraction of reactive calcite increases strongly with increasing humidity and is the most at water saturated conditions.

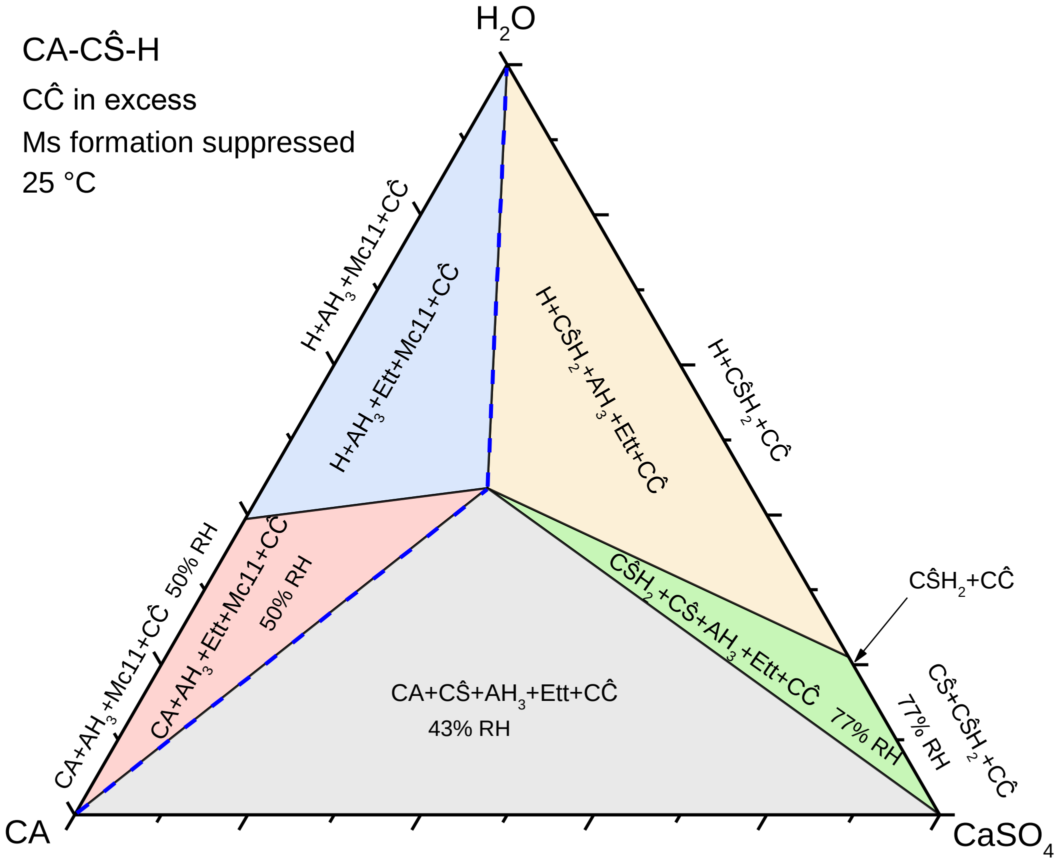
CA-CŜ-H
CĈ in excess
Ms formation suppressed
25 °C
H_2O
$H+AH_3+Mc11+CĈ$
$H+AH_3+Ett+Mc11+CĈ$
$H+CŜH_2+AH_3+Ett+CĈ$
$H+CŜH_2+CĈ$
$CŜH_2+CĈ$
$CŜH_2+CŜ+AH_3+Ett+CĈ$
77% RH
$CŜ+CŜH_2+CĈ$
77% RH
$CA+CŜ+AH_3+Ett+CĈ$
43% RH
$CA+AH_3+Ett+Mc11+CĈ$
50% RH
$CA+AH_3+Mc11+CĈ$
50% RH
CA
$CaSO_4$

Figure 6:21 Calculated ternary phase diagram CA-$CaSO_4$-H_2O, saturated with respect to $CaCO_3$, at 25 °C and 1 bar. Axes units in wt.%.

6.6 Applied thermodynamic modelling to assess the drying behaviour of hydrated cementitious systems

6.6.1 Subsystem relevant to OPC and limestone blended cements

To simulate drying the system CaO-Al_2O_3-SO_3-CO_2-H_2O, which is relevant to OPC and limestone blended cements, was chosen. The initial model mixture contained C_3A, portlandite (CH), calcium sulfate (SO_3/Al_2O_3=1 molar bulk ratio), and varying amounts of calcite at 25°C. The amount of solids was kept constant (100 g) and reacted with 90 g water. A diagram of the specific volume changes of the hydrated mixture with respect to calcite content is based on previous calculations by Matschei [45] and can be found in Figure 6:22.

Due to their differing AFm - AFt mineralogy, hydrate phase assemblages A and B, with 0%, and 13% of calcite respectively, were selected as initial hydrated systems for the drying modelling. Drying was simulated by continuously removing water from the assemblages until a RH close to zero was reached.

The calculated volume changes during drying of the systems A and B are shown in Figure 6:23. Since C_3AH_6 is not observed during drying, its formation was suppressed. Dehydration takes place stepwise at critical RHs, representing invariant points where the RH is fixed due to phase rule restrictions. At this critical RH two hydration states of the same cement hydrate coexist and buffer the humidity similar to salt solutions. It is interesting to note that the volume changes in system B are much less than in system A under drying conditions, indicating a potential benefit of limestone blended cements exposed to drying conditions.

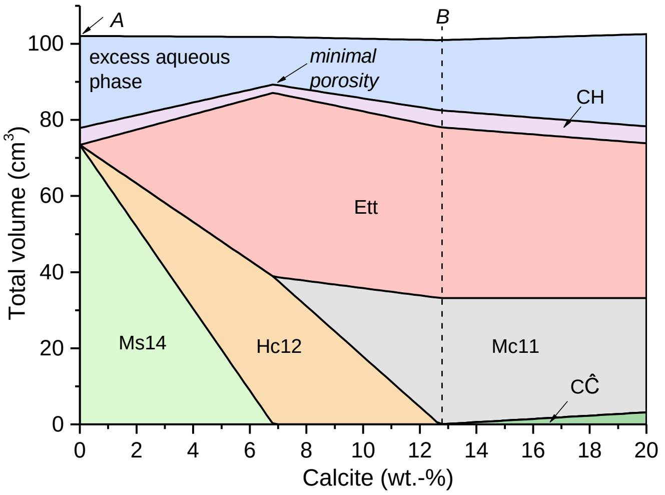

Figure 6:22 Calculated specific volume changes of a hydrated model mixture consisting of C_3A, portlandite and with fixed sulfate ratio (SO_3/Al_2O_3=1, molar bulk ratio) in dependence of changing calcite content at 25°C.

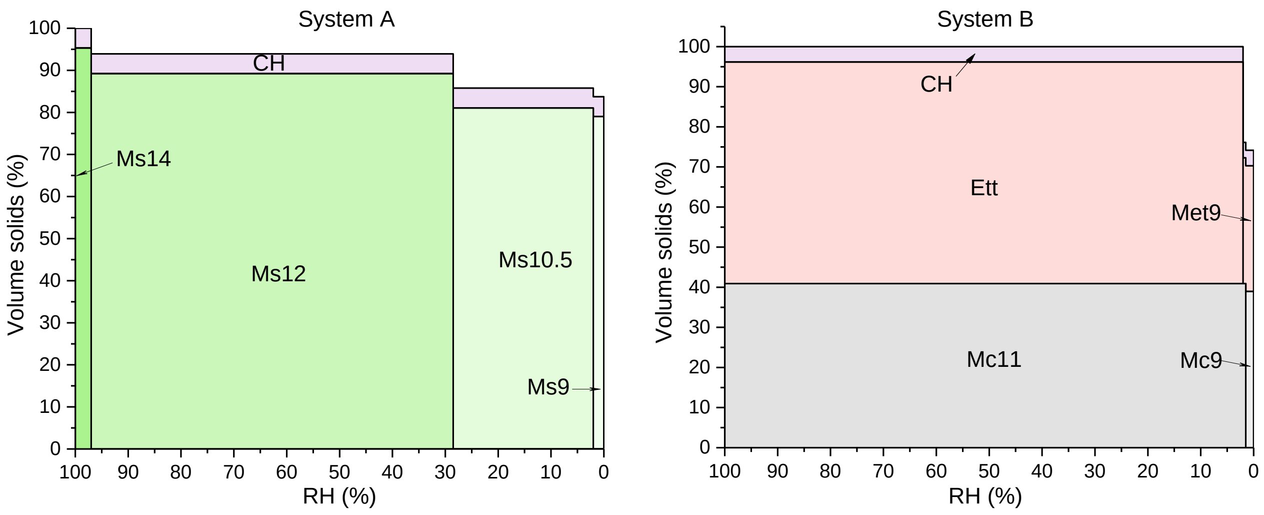

Figure 6:23 Calculated volume phase assemblages with respect to changes in RH at 25°C in the Systems A and B shown in Figure 6:22.

6.6.2 Subsystem relevant to calcium aluminate cements

The initial model mixture contained CA, CŜ (SO_3/Al_2O_3 = 0.546 molar bulk ratio), and varying amounts of calcite at 25°C. As above the amount of solids was kept constant (100 g) and reacted with 80 g water. A diagram of the resulting specific volume changes of the hydrate assemblages as function of calcite content is shown in Figure 6:24. During hydration of CA a poorly crystalline AH_3 is formed, however different hydration states of this phase could not be considered in this study due to lack of available data.

Hydrate phase assemblages A and B from Figure 6:24, with 0% and 6.2% of calcite respectively, were selected as initial hydrated systems for the drying modelling. Since C_3AH_6 is not observed during drying, its formation was suppressed. Changes of specific solid volume as function of RH are presented in Figure 6:25. Dehydration happens stepwise at specific RHs, similar to what was observed in the previous subsystem (relevant to PC). It has to be noticed that the addition of calcite and the formation of monocarboaluminate and ettringite may enhance the dimensional stability of a hydrated cement paste, making it less sensitive to humidity variations as shown in the calculations for System *B*.

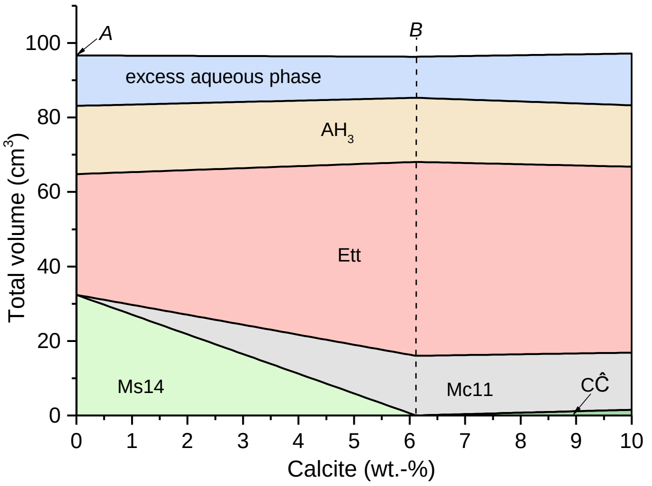

Figure 6:24 Calculated specific volume changes of a hydrated model mixture consisting of CA, $CaSO_4$ (SO_3/Al_2O_3=0.546 molar bulk ratio) in dependence of changing calcite content at 25°C.

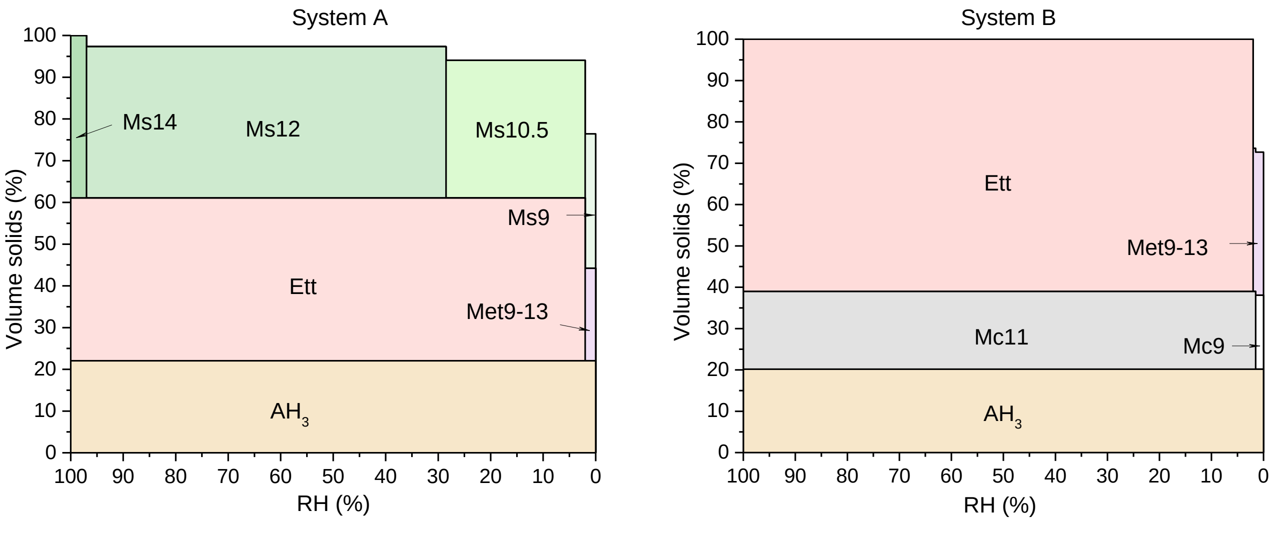

Figure 6:25 Calculated volume phase assemblages with respect to changes in RH at 25°C in the Systems A and B shown in Figure 6:24.

6.6.3 Remarks on the drying behaviour of hydrated systems

This study showed that, as a consequence of their varying hydration states, AFm phases can act as *humidity buffers* in hydrating cement paste. It was further shown that *calcite rich systems are the most stable* upon drying due to the persistence of monocarboaluminate and ettringite with respect to dehydration. Thus hydrated limestone blended cements are likely to have *slightly improved volume* stability compared to pure OPC systems.

6.7 Discussions

From the ternary diagrams for several subsystems containing C_3A and CA a number of observations were made. The predicted phase assemblages containing liquid water, i.e. regions where complete hydration was achieved, agree very well with experimental observations.

In water deficient regions, i.e. at RH's < 100%, it was shown that water activity can be a very strong thermodynamic driving force to initiate phase changes. For example the formation of monosulfoaluminate in the system $CaO\text{-}Al_2O_3\text{-}CaSO_4\text{-}H_2O$ is thermodynamically favoured at low humidities even in presence of calcium sulphate where at water-saturated conditions ettringite would be modelled. This agrees well with the findings of Albert et al. [49]. Therefore, if there are systems in which monosulfoaluminate is formed at high humidities it will get stabilised if this cement paste is exposed to drying conditions. The opposite is happening for ettringite. Ettringite is thermodynamically favoured to form at saturated conditions in presence of anhydrite or gypsum. If an ettringite-based system is exposed to drying in presence of unreacted C_3A then at RH < 43 % at 25°C it should start to react with C_3A to form monosulfoaluminate independently of the presence of gypsum or anhydrite. Nevertheless, our validation experiments showed that ettringite, once formed at high humidities, is persistent also until very low humidities (see Chapter 5) and a conversion to monosulfoaluminate was never observed. This shows that in order to apply the thermodynamic phase relations in a practical way it is important to have additional experimental knowledge of regions of metastability, which can then be considered in the subsequent modelling attempt. As a consequence, in order to better consider real hydration behaviour, some regions of certain diagrams or complete diagrams were calculated suppressing the formation of some hydrates that were experimentally not observed.

The experimental results obtained for the subsystem $C_3A\text{-}CaSO_4\text{-}H_2O$ demonstrate nicely the combined power of thermodynamic calculations and focussed experiments to assess metastability constraints. From the paste experiments shown in Figure 6:14 and Figure 6:15 we knew that ettringite will remain as persistent phase even at humidities < 40%. By applying a metastability criterion and supressing monosulfoaluminate formation in the phase assemblages we were able to quantitatively predict the experimentally observed phase assemblage and by omitting microstructural features, e.g. moisture gradients due to diffusion in porous systems, we could predict very well the experimentally measured RH value.

Another important point to consider is that this work has shown that there is most likely no single critical humidity value per clinker phase at which it starts to react with water. Based on the assumptions we took at the onset of this chapter we estimated the thermodynamic properties of hydroxylated clinker phase surfaces, which were considered in the construction of the phase diagrams. According to our simulations the theoretical critical humidity at which C_3A or CA reacts with water can change significantly as function of the accompanying phases. For example C_3A would start to form C_3AH_6 above 55% whereas in presence of sulphate C_3A hydration continues until 38% RH. This could be validated experimentally. Although of course this work is just a first attempt to assess rate-limiting thermodynamic properties of clinker phases, the chosen practical approach requires more attention in future work.

This work has shown that it is also necessary to examine the impact of water activity on phase assemblages as function of temperature. The phase diagrams presented in this chapter were mainly given for 25°C and 5°C. From the phase relations relevant to CA it can be seen that temperature may significantly change the predicted phase assemblages due to changing phase stability relations. In combination with severe drying/wetting cycles, thermodynamic driving forces to decompose initially formed metastable phase assemblages can be considerably higher at changing temperatures and they can lead to the formation of different phase assemblages as in the case of CA hydration.

Salt hydrate pair buffering is a well-known principle in physical chemistry. But so far no associations of this principle were done with respect to cementitious systems. Our study has shown that in the absence of water the present phase assemblage impacts the relative humidity. The phase diagrams show that crossing a critical phase boundary may impact the resulting water vapour pressure above the phase assemblage significantly and even stepwise changes may occur. It is therefore possible that, within a cross-section of concrete which is exposed to lower humidities, a stepwise moisture gradient may takes place, caused by different buffering phase assemblages instead of a Fickian type diffusion behaviour of water vapour. It is currently of course a hypothesis which needs a further follow-up as microstructural features, amorphous or gel –like hydrates (e.g. C-S-H) and intrinsic porosity, may dominate the impact of RH of cementitious systems.

6.8 References

[1]. M. Atkins, D.G. Bennet, A.C. Dawes, F.P. Glasser, A. Kindness, D. Read, A thermodynamic model for blended cements, Cem. Concr. Res. 22 (1992) 497–502.

[2]. D.G. Bennet, D. Read, M. Atkins, F.P. Glasser, A thermodynamic model for blended cements II: Cement hydrate phases; thermodynamic values and modelling studies, J. Nucl. Mater. 190 (1992) 315–325.

[3]. D. Damidot, S.J. Barnett, F.P. Glasser, D. Macphee, Investigation of the CaO–Al2O3–SiO2–CaSO4–CaCO3–H2O system at 25 °C by thermodynamic calculations, Adv. Cem. Res. 16 (2004) 69–76.

[4]. E.J. Reardon, An ion interaction model for the determination of chemical equilibria in cement/water systems, Cem. Concr. Res. 20 (1990) 175–192.

[5]. E.J. Reardon, Problems and approaches to the prediction of the chemical composition in cement/water systems, Waste Manage. 12 (1992) 221–239.

[6]. B. Lothenbach, F. Winnefeld, Thermodynamic modelling of the hydration of Portland cement, Cem. Concr. Res. 36 (2006) 209–226.

[7]. B. Lothenbach, T. Matschei, G. Möschner, F. Glasser, Thermodynamic modelling of the effect of temperature on the hydration and porosity of Portland cement, Cem. Concr. Res. 38 (2008) 1-18.

[8]. T. Matschei, B. Lothenbach, F.P. Glasser, Thermodynamic properties of Portland cement hydrates in the system CaO–Al2O3–SiO2–CaSO4–CaCO3–H2O, Cem. Concr. Res. 37 (2007) 1379-1410.

[9]. Ph. Blanc, X. Bourbon, A. Lassin, E.C. Gaucher, Chemical model for cement-based materials: Thermodynamic data assessment for phases other than C–S–H, Cem. Concr. Res 40 (2010) 1360-1374.

[10]. D. Kulik, T. Wagner, S.V. Dmytrieva, G. Kosakowski, F.F. Hingerl., K.V. Chudnenko, U. Berner, GEM-Selektor geochemical modeling package: revised algorithm and GEMS3K numerical kernel for coupled simulation codes, Comput. Geosci. 17 (2013) 1-24. http://gems.web.psi.ch

[11]. T. Wagner, D.A. Kulik, F.F. Hingerl, S.V. Dmytrieva, GEM-Selektor geochemical modeling package: TSolMod library and data interface for multicomponent phase models, Canadian Mineralogist 50 (2012) 1173-1195.

[12]. B. Lothenbach, D. Rentsch, E. Wieland, Hydration of a silica fume blended low-alkali shotcrete cement, Phys. Chem. Earth Pt A/B/C 70–71 (2014) 3-16.

[13]. F. Deschner, B. Lothenbach, F. Winnefeld, J. Neubauer, Effect of temperature on the hydration of Portland cement blended with siliceous fly ash, Cem. Concr. Res. 52, (2013) 169-181.

[14]. G. Le Saoût, B. Lothenbach, A. Hori, T. Higuchi, F. Winnefeld, Hydration of Portland cement with additions of calcium sulfoaluminates, Cem. Concr. Res. 43 (2013) 81-94.

[15]. L. Pelletier, F. Winnefeld, B. Lothenbach, The ternary system Portland cement–calcium sulphoaluminate clinker–anhydrite: Hydration mechanism and mortar properties, Cem. Concr. Comp. 32 (2010) 497-507.

[16]. F. Winnefeld, B. Lothenbach, Hydration of calcium sulfoaluminate cements — Experimental findings and thermodynamic modelling, Cem. Concr. Res. 40 (2010) 1239-1247.

[17]. J. Bizzozero, C. Gosselin, K.L. Scrivener, Expansion mechanisms in calcium aluminate and sulfoaluminate systems with calcium sulfate, Cem. Concr. Res. 56, (2014) 190-202.

[18]. L. Baquerizo, T. Matschei and K. Scrivener, Volume stability of CAC-$CaSO_4$-$CaCO_3$-H_2O systems during drying, International Conference on Calcium Aluminates, Avignon - France, May. 18 – 21, 2014, pp. 274-283.

[19]. O. Vidal, B. Dubacq, Thermodynamic modelling of clay dehydration, stability and compositional evolution with temperature, pressure and H2O activity, Geochim. Cosmochim. Ac. 73 (2009) 6544-6564.

[20]. B. Dubacq, O. Vidal, V. De Andrade, Dehydration of dioctahedral aluminous phyllosilicates: thermodynamic modelling and implications for thermobarometric estimates, Contrib. Mineral. Petr. 159 (2010) 159-174.

[21]. R. Keren, I. Shainberg, Water vapor isotherms and heat of immersion of Na/Ca-montmorillonite systems-I: homoionic clay, Clay. Clay. Miner. 23 (1975) 193-200.

[22]. P. Vieillard, P. Blanc, C. I. Fialips, H. Gailhanou, S. Gaboreau, Hydration thermodynamics of the SWy-1 montmorillonite saturated with alkali and alkaline-earth cations: A predictive model, Geochim. Cosmochim. Acta 75 (2011) 5664-5685.

[23]. H. Gailhanou, P. Blanc, J. Rogez, G. Mikaelian, H. Kawaji, J. Olives, M. Amouric, R. Denoyel, S. Bourrelly, V. Montouillout, P. Vieillard, C.I. Fialips, N. Michau, E.C. Gaucher, Thermodynamic properties of illite, smectite and beidellite by calorimetric methods: Enthalpies of formation, heat capacities, entropies and Gibbs free energies of formation, Geochim. Cosmochim. Acta 89 (2012) 279-301.

[24]. I.M. Chou, R.R. Seal II, B.S. Hemingway, Determination of melanterite-rozenite and chalcanthite-bonattite equilibria by humidity measurements at 0.1MPa, Am. Mineral. 87 (2002) 108-114.

[25]. I.M. Chou, R.R. Seal II, Determination of epsomite-hexahydrite equilibria by the humidity-buffer technique at 0.1MPa with implications for phase equilibria in the system $MgSO_4$-H_2O, Astrobiology 3 (2003) 619-630.

[26]. I.M. Chou, R.R. Seal II, Determination of goslarite-bianchite equilibria by the humidity-buffer technique at 0.1MPa, Chem. Geol. 215 (2005) 517-523.

[27]. I.M. Chou, R.R. Seal II, Acquisition and Evaluation of Thermodynamic Data for Morenosite-Retgersite Equilibria at 0.1 MPa, Am. Mineral. 88 (2003) 1943-1948

[28]. L.G. Baquerizo, T. Matschei, K.L. Scrivener, M. Saedipour, A. Thorell, L. Wadsö, Methods to determine hydration states of minerals and cement hydrates, Cem. Concr. Res. 65 (2014) 85-95.

[29]. L.G. Baquerizo, T. Matschei, K.L. Scrivener, M. Saedipour, L. Wadsö, Hydration states of AFm phases, submitted to Cem. Concr. Res.

[30]. A. Loukili, A. Khelidj, P. Richard, Hydration kinetics, change of relative humidity, and autogenous shrinkage of ultra-high-strength concrete, Cem. Concr. Res. 29 (1999) 577-584.

[31]. O.M. Jensen, P.F. Hansen, Influence of temperature on autogenous deformation and relative humidity change in hardening cement paste, Cem. Concr. Res. 29 (1999) 567-575.

[32]. C. Andrade, J. Sarría, C. Alonso, Relative humidity in the interior of concrete exposed to natural and artificial weathering, Cem. Concr. Res. 29 (1999) 1249-1259.

[33]. O. M. Jensen, P. F. Hansen, E.E. Lachowski, F.P. Glasser, Clinker mineral hydration at reduced relative humidities, Cem. Concr. Res. 29 (1999) 1505-1512.

[34]. E. Breval, Gas-phase and liquid-phase hydration of C_3A, Cem. Concr. Res. 7 (1977) 297-303.

[35]. E. Dubina, L. Wadsö, J. Plank, A sorption balance study of water vapour sorption on anhydrous cement minerals and cement constituents, Cem. Concr. Res. 41 (2011) 1196-1204.

[36]. V.I. Babushkin, G.M. Matveyev, O.P. Mchedlov-Petrossyan, Thermodynamics of Silicates, Springer-Verlag, Berlin, 1985.

[37]. E. Berodier, Impact of the Supplementary cementitious Materials on the kinetics and microstructural development of cement hydration, Ph.D dissertation, EPFL, 2015.

[38]. L. Nicoleau, A. Nonat, D. Perrey, The di-and tricalcium silicate dissolutions, Cem. Concr. Res. 47 (2013) 14-30.

[39]. P. Barret, D. Ménétrier, D. Bertrandie, Mechanism of C3S dissolution and problem of the congruency in the very initial period and later on, Cem. Concr. Res. 13 (1983) 728-738.

[40]. F. Bellmann, T. Sowoidnich, H.-M. Ludwig, D. Damidot, Analysis of the surface of tricalcium silicate during the induction period by X-ray photoelectron spectroscopy, Cem. Concr. Res. 42 (2012) 1189-1198.

[41]. P. Barret, D. Ménétrier, D. Bertrandie, Mechanism of C_3S dissolution and problem of the congruency in the very initial period and later on, Cem. Concr. Res. 13 (1983) 728–738.

[42]. K.S. Pitzer, Activity coefficients in electrolyte solutions, 2nd ed,. C.R,C. Press, 1991.

[43]. P. Barnes, A.C. Lewis, X. Turillas, C. Hall, M. Hanfland, D. Hausermann, Experiment: Use of energy-dispersive diffraction conical slit geometry to study fast hydration reactions, 1995, ESRF.

[44]. T. Matschei, F.P. Glasser, Buffering in cementitious systems based on OPC, Proceedings of the 13th ICCC, Madrid, 2011.

[45]. T. Matschei, Thermodynamics of Cement Hydration. PhD Dissertation, University of Aberdeen, 2007.

[46]. Design and Control of Concrete Mixtures, 15th Edition, Portland Cement Association, 2011.

[47]. H.F.W. Taylor, Cement Chemistry, second ed., Thomas Telford, London, 1997.

[48]. B. Lothenbach, L. Pelletier-Chaignat, F. Winnefeld, Stability in the system $CaO–Al_2O_3–H_2O$, Cem. Concr. Res. 42 (2012) 1621 – 1634.

[49]. B. Albert, B. Guy, D. Damidot, Water chemical potential: A key parameter to determine the thermodynamic stability of some hydrated cement phases in concrete?, Cem. Concr. Res. 36 (2006) 783-790.

7 Conclusions

7.1 Main results obtained

A summary of the main achievements of this thesis are shown below:

- A powerful multi-method approach was developed to investigate the impact of relative humidity (RH) and temperature on structural and thermodynamic properties of crystalline minerals and cement hydrates with different hydration states (i.e. varying molar water contents). This methodology includes the use of XRD, TGA, sorption balance, sorption calorimetry and the hydrate-pair humidity buffer method. Sorption calorimetry can give an almost complete thermodynamic description of a sorption process, although part of a measurement or a whole measurement may take place at metastable conditions. The hydrate pair – humidity buffer method was demonstrated to be a simple and rapid technique to find out the transition RHs between adjacent hydrates. Furthermore, this method can be used to follow a hydration process in water deficient systems. Additionally, DSC and isothermal calorimetry measurements were applied to complement results obtained by sorption calorimetry.
- This thesis presents novel experimental results on the different hydration states of the most important AFm phases: monocarboaluminate, hemicarboaluminate, strätlingite, hydroxy-AFm and monosulfoaluminate, and the thermodynamic properties associated with changes in their water content during adsorption/desorption. In AFm phases water molecules are incorporated in the interlayer. With a combined use of sorption calorimetry and sorption balance measurements we were able to characterise different types of interlayer water. “Space filling” water molecules with thermodynamic properties close to liquid water are loosely integrated and can be easily removed from the structure upon increase of temperature or at an initial small decrease of RH. Furthermore the removal of “structural water” molecules, strongly bound to the calcium cations of the main layer, is only possible at low water activities and/or high temperatures, typically accompanied by high mixing enthalpies values as shown by sorption calorimetry measurements.
- A new study on the stability of ettringite as function of temperature and water vapor pressure was presented. Thermodynamic properties associated to the decomposition of ettringite into metaettringite and to the reformation of metaettringite into ettringite were determined and a model to predict its stability as function of temperature proposed. Empirical enthalpies based on experimental transition RHs were used to model the observed hysteretic behaviour of ettringite-metaettringite conversions. Based on the calculations we were able to propose a thermodynamic dataset for metaettringite that is fully capable to reproduce the hysteresis loop as well as to estimate the “true” stability limits of ettringite and metaettringite as function of temperature and water vapour pressure. Stable and metastable hydrate phase assemblages as function of water

activity were derived. Application- relevant recommendations concerning the performance of ettringite based cementitious systems at RH≤ 100% were deduced.

- The hydrate pair – humidity buffer method was used to determine the equilibrium RH of slightly hydrated clinker phases. Empirical thermodynamic properties of the studied phases were calculated in order to pragmatically model cement clinker - water vapour interactions. The reported properties may have a physical explanation, such as the properties of a hydroxylated surface layer phase covering the unreacted clinker phases in presence of water vapor.
- This thesis enabled the derivation of a thermodynamic database capable to describe the constitution of hydrated cement paste at RH ≤ 100% in the temperature range 1 – 99 °C. A novel thermodynamic model capable of assessing the impact of water activity on the hydrate constitution of cement paste upon hydration and during drying was developed. The model was used to construct phase diagrams showing the stability regions of the different hydration states of the most important AFm and AFt phases as function of temperature and relative humidity. Furthermore, the model was used to predict the hydration of the system $CaO–Al_2O_3–SO_3–CO_2–H_2O$ (including the equilibrium RH) and the drying behaviour of an already hydrated cementitious system. A series of ternary diagrams was developed that enables qualitative and quantitative assessment of phase assemblages relevant to hydrated cement systems. The thermodynamic model presented in this thesis opens the possibility to predict the mineralogy and internal relative humidity of binders at low water/solid ratios and the response of hydrated systems exposed to varying drying conditions.

7.2 Remarks and future development

During this work we have started the study of what was, until recently, an unexplored field: the stability of cement phases in water unsaturated conditions and the real water content of cement hydrates as function of water activity, external RH and temperature. Although a good basis has been laid with the current work, there are still several points that should be assessed in the future.

- **C-S-H**

  This thesis focussed on the study of AFm and AFt phases. The multi-method approach proposed here could also be used to assess the water content, stability and thermodynamic properties of C-S-H as function of water activity and temperature. Although the molar volume of amorphous or semi-crystalline phases cannot be straightforwardly studied with the proposed methodology, other techniques such as ^{1}H NMR can be extremely useful in doing so. In order to cover most of the real applications involving PC, the study of C-S-H, its water content as function of temperature and RH and its impact on the predicted thermodynamic equilibria is a *must* and should be considered for future studies.

- **Microcrystalline AH_3**

  The aluminium hydroxide (AH_3) phase occurring during the hydration of CA is poorly crystalline and is frequently called "alumina gel". At high temperatures crystalline AH_3 (gibbsite) is formed. Although the water content is assumed to be constant, due to the gel-like nature of the amorphous AH_3 it is possible that it is variable. All these aspects can therefore impact the predicted phase assemblages and RH of systems containing AH_3. Further research is required in order to determine the influence of crystallinity and whether variable water contents are possible in this phase.

- **Stability of clinker phases in the presence of water vapour**

  In this project the equilibrium RH measured in partially hydrated clinker phases was used to estimate the thermodynamic properties of an assumed hydroxylated surface layer phase covering the mentioned phases. Nevertheless a more precise and systematic study is needed in order to assess the complete nature and properties of these layers, and whether it is influenced by the presence of other ions (SO_4^{2-}, CO_3^{2-}) and temperature. The hydrate pair – humidity buffer method, complemented with XRD and TGA can be used in order to determine more accurate data. The validity of the chosen pragmatic approach needs further evaluation.

- **Metastability of several hydration states**

  It was found that, when modelling in equilibrium conditions, several phases such as C_3AH_6, $C\hat{S}$ and CH, were more stable than certain assemblages seen experimentally at lower RH. The absence of decomposition products in the experimental tests might be due to the lack of a reactive media, such as liquid water, that facilitates nucleation of structurally different phases during drying or wetting. This hypothesis can be studied using a solution with low water activity, but this alternative was not followed thoroughly in the current work.

  A phase called carbonated hemicarboaluminate, or cHc, was reported in the literature, but its complete stability could not be assessed. Further research is needed to determine the formation conditions of this phase, if present.

- **Hysteresis**

  The presence of hysteresis between dehydration and rehydration revealed the metastability of some hydration states, especially in ettringite and monosulfoaluminate. The desorption and the absorption branches of the isotherms do not represent the real equilibrium in systems showing hysteresis. The hysteretic behaviour that is described here has most likely its origin in a free energy barrier that needs to be overcome in order to get an absorption or desorption process going. This was confirmed by the disagreement between the modelled and experimental phase assemblages, especially when working with ettringite. Although some calculations were done to determine the theoretical decomposition/reformation RH if no hysteresis takes place, this approach has not been crosschecked due to the lack of references. In the clay literature similar observations exist but contradicting explanations were given. If the approach introduced in this work is confirmed with other materials then it can be used in other fields where hysteresis is a common issue, such as clays, minerals, food science, etc. Further work is required to assess the hysteretic behaviour of cement hydrates and to validate some of the methods used in this work.

- **Validation of the ternary diagrams**

  Although several points of some of the ternary diagrams modelled were tested, a more in-depth validation is still required. When doing so, kinetics and metastability constraints of some phases need to be considered.

- **Solid solutions**

  Several of the cement hydrates studied are known to form solid solutions, especially between SO_4 and OH-AFm and SO_4- and CO_3-AFt. During this thesis the stability of the solid solutions with respect to water activity and temperature was not studied. This is something that should be addressed in future works.

Annexes

A. TGA measurements

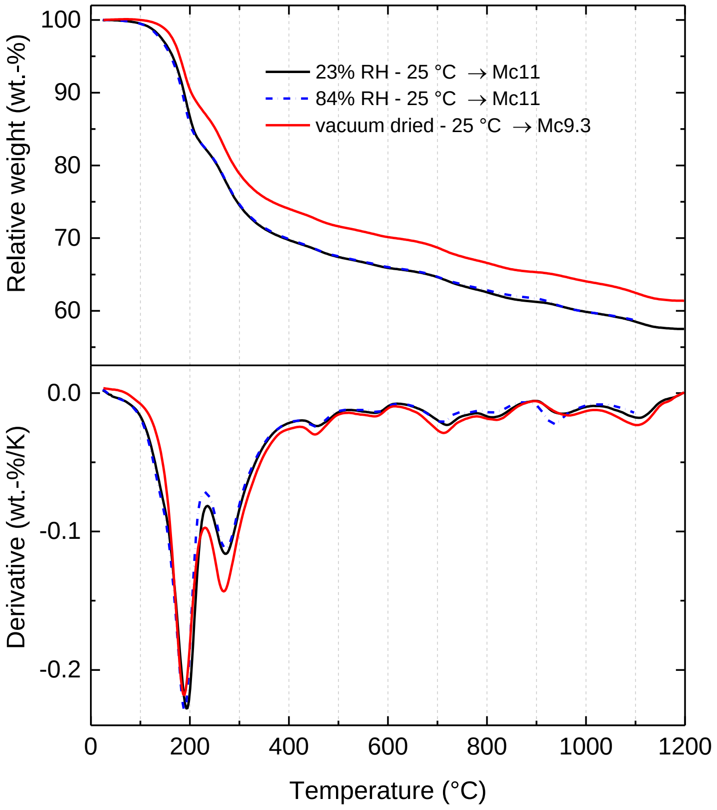

Figure A:1 TGA and DTG patters of ***monocarboaluminate*** *dried at different conditions at 25 °C . Every sample dried at 5 °C, 25 °C and 50 °C showed very similar patterns as they were composed of Mc11, for this reason not every pattern is shown. The sample dried under vacuum was not completely dehydrated. If complete dehydration is achieved the hydration state would correspond to Mc9.*

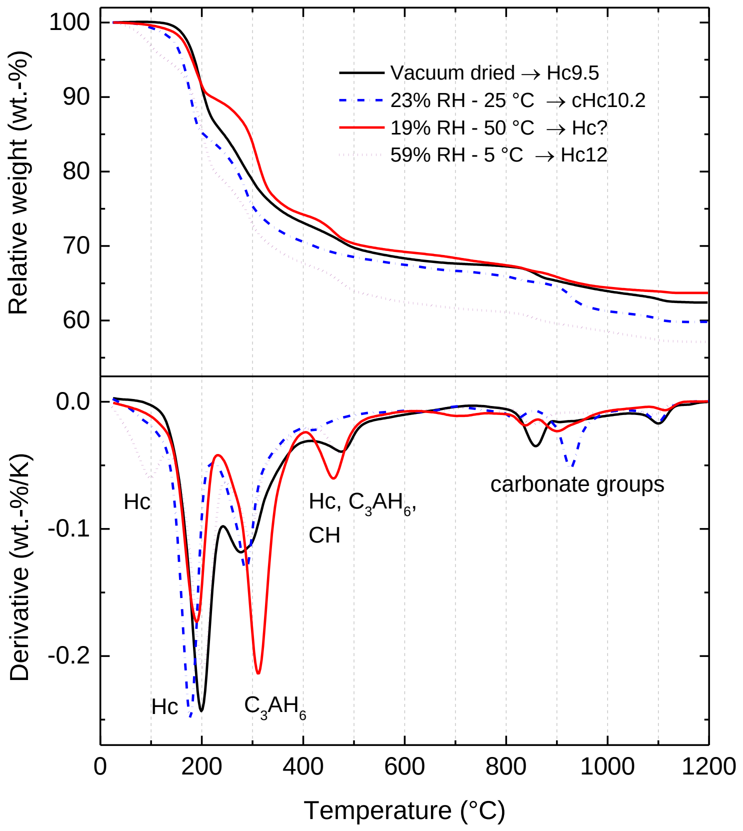

Figure A:2 TGA and DTG patters of ***hemicarboaluminate*** *dried at different conditions. The sample dried under vacuum was not completely dehydrated, thus its water content was 9.5 H_2O instead of 9 H_2O as reported in Chapter 5. The sample dried at 23% RH and 25 °C was composed of cHc as confirmed by XRD and by the larger CO_2 content of the sample. The sample dried at 50 °C presents large amounts of C_3AH_6 and CH due to decomposition, which was observed in every sample dried at this temperature. The sample dried at 5 °C corresponds to Hc12 and did not present any decomposition or carbonation. Every sample dried at this temperature down to 10% RH showed similar behavior.*

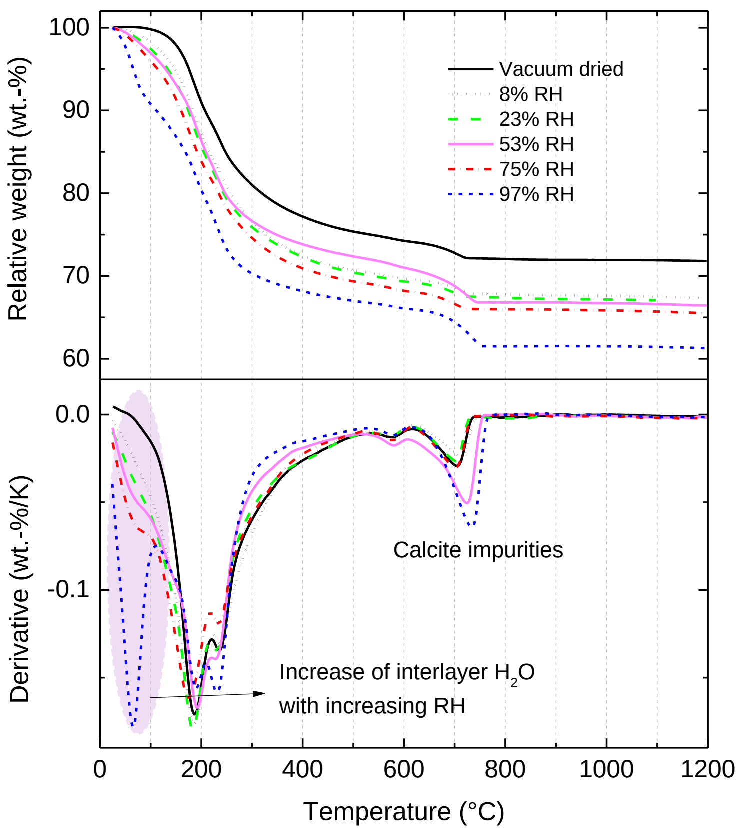

Figure A:3 TGA and DTG patters of ***strätlingite*** *dried at 25 °C. Notice the larger content of interlayer water with increasing RH. Large amounts of calcite impurities were present in the samples.*

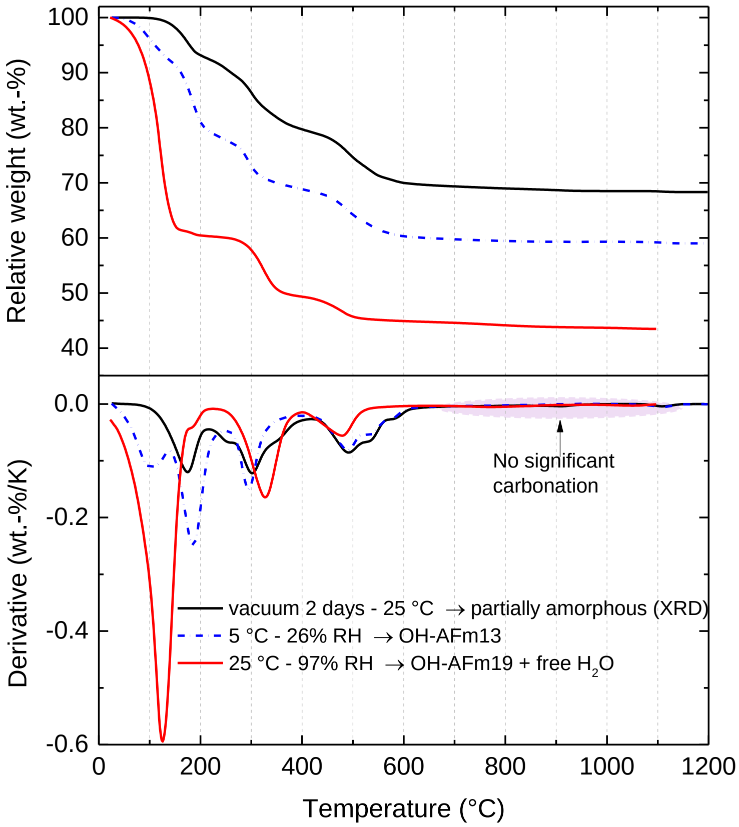

Figure A:4 TGA and DTG patters of ***hydroxy-AFm*** *dried at different conditions. The sample stored at 97% RH contained large amounts of free water. The sample dried under vacuum had lower content its crystallinity decreased significantly as shown in Capter 4.3.4.*

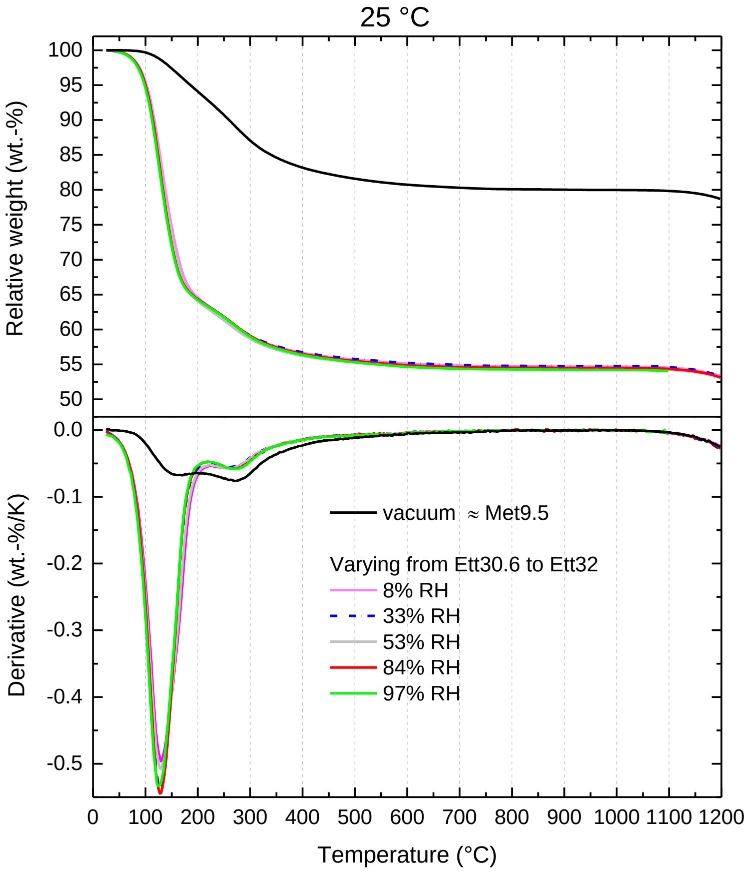

Figure A:5 TGA and DTG patters of ***ettringite*** *dried at 25 °C. The sample dried under vacuum for 12 hours present a water content of 9.5 H_2O; a minimum of n = 8.5 – 9 H_2O can be reached with longer drying times longer drying times. All the samples dried from 97% to 8% RH had a water content varying from 30.6 to 32 H_2O.*

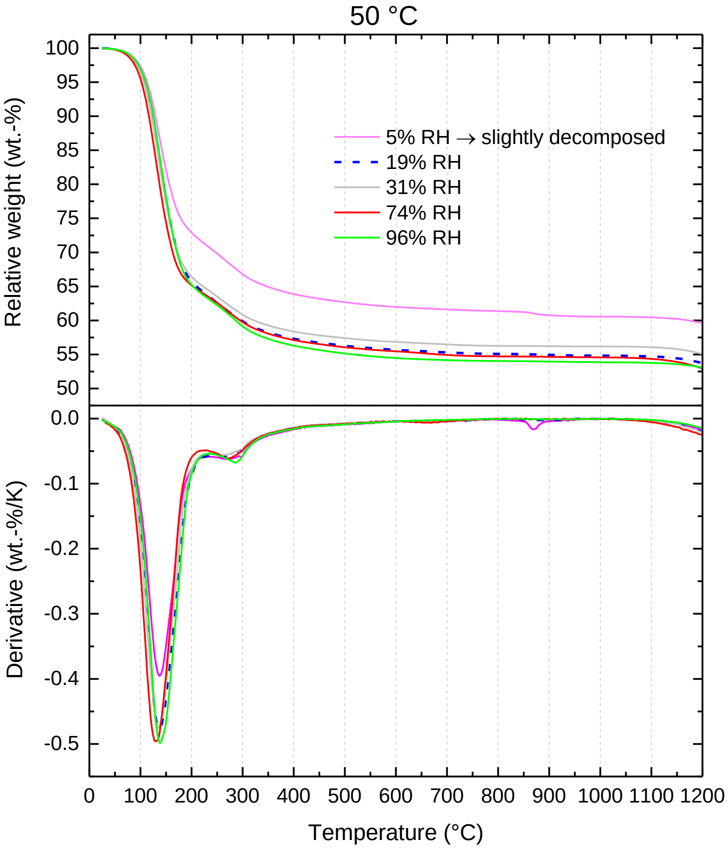

Figure A:6 TGA and DTG patters of ***ettringite*** *dried at 50 °C. The sample dried at 5% RH showed slight decomposition (see Figure 5:1b).*

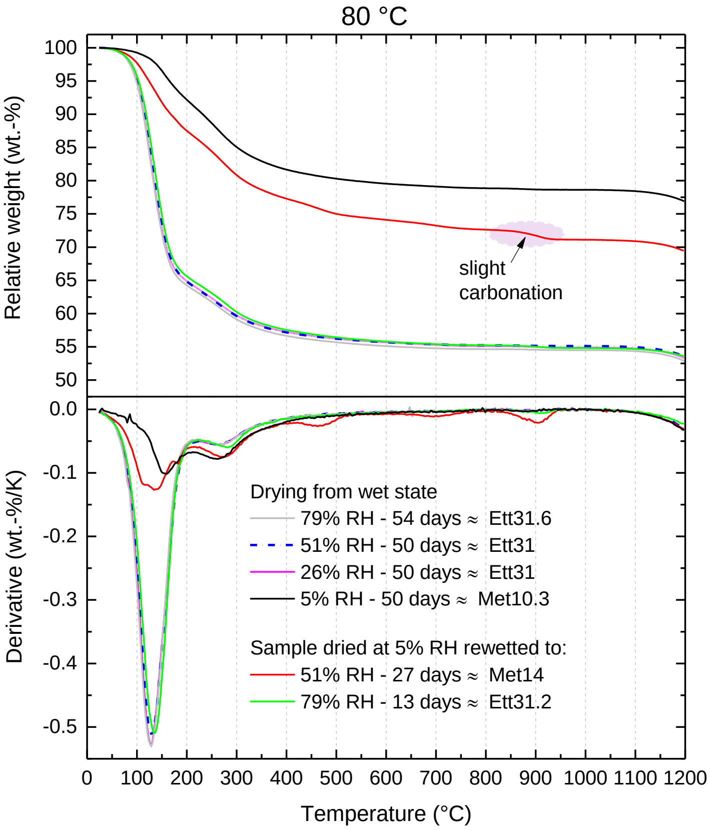

Figure A:7 TGA and DTG patters of ***ettringite*** *stored at 80 °C under drying and rewetting conditions. During drying decomposition could be observed at 5% RH. During rewetting the decomposed sample reformed when conditioned at 79% RH.*

B. N_2 – sorption isotherms

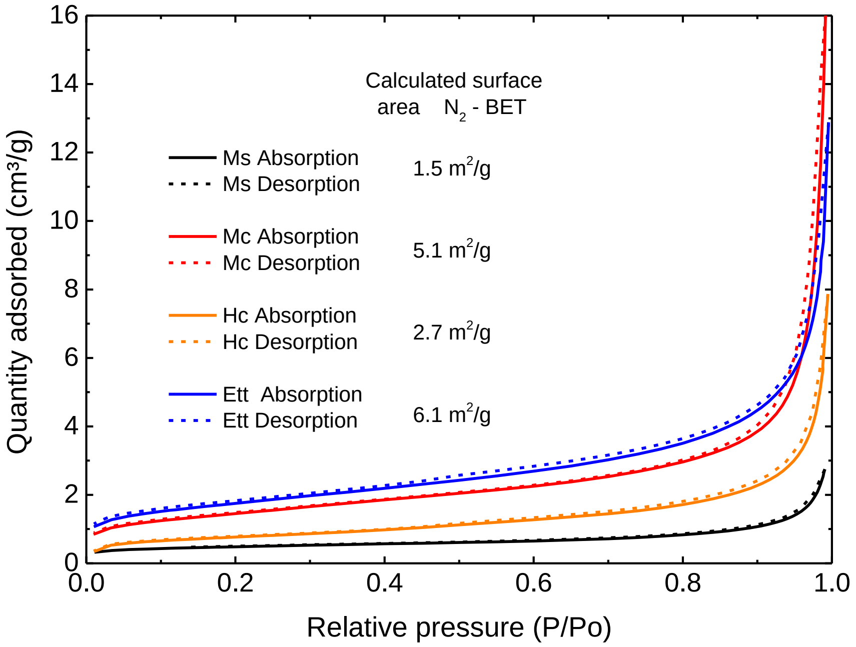

Figure B:1 N_2 – isotherm measured using ASAP^{TM} 2020 (Micromeritics) on Ms, Mc, Hc and Ett. Note the lack of hysteresis and the relatively small surface area. The BET equation was used to calculate the surface area using the points from 0 to 0.3 P/P_0 (calculated with the ASAP 2020 software)

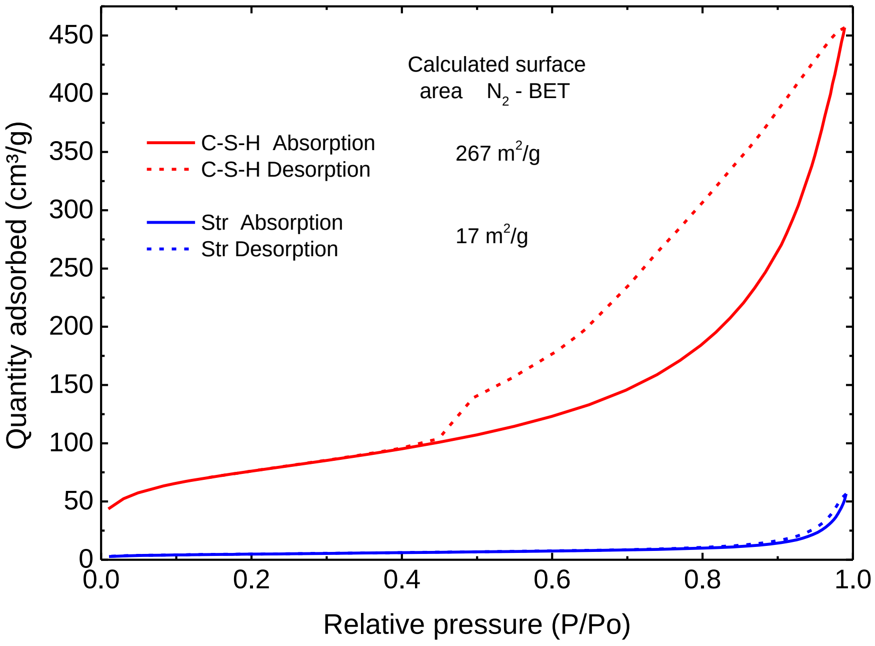

Figure B:2 N_2 – isotherm measured using ASAP^{TM} 2020 (Micromeritics) on Str and synthetic C-S-H (Ca/Si = 0.66). Although C-S-H was not studied in this work, a measurement was carried out in order to show the difference between this phase and the other AFm phases. C-S-H has a large surface area and presents a marked hysteresis due to its intrinsic porosity.

C. Thermodynamic properties

Table C:1 Standard molar thermodynamic properties of clinker phases and other cement phases at 25 °C and 1 bar.

Phase	ΔG_f° (kJ/mol)	ΔH_f° (kJ/mol)	S° (J/mol K)	Cp° (J/mol K) [a]	V° (cm^3/mol)	Ref.
Clinker phases						
C_3S	-2784.3	-2930.6	168.6	171.6	73.2	[1],[2]
β-C_2S	-2193.2	-2308.5	127.6	128.6	51.8	[1],[2]
C_3A	-3382.3	-3560.6	205.4	209.4	89.2	[1],[2]
CA	-2207.9	-2327.1	114.2	125.7	---	[1]
C_4AF	-4786.5	-5080	326	396.1	130.2	[1],[2]
Hydroxylated clinker phases [a]						
C_3A_{hyd}	-3576.2	-3810.6	10.6	209.4	89.2	t.s.
CA_{hyd}	-2246.8	-2378.1	68.2	125.7	---	t.s.
C-S-H						
TobH ($C_{0.66}SH_{1.5}$)	-1668.6	−1841.5	89.9	141.6	55.3	[3]
TobD ($C_{0.83}S_{0.66}H_{1.83}$)	-1570.9	−1742.4	121.8	166.9	48.0	[3]
JenH ($C_{1.33}SH_{2.16}$)	-2274.0	−2506.3	142.5	207.9	75.6	[3]
JenD ($C_{1.5}S_{0.66}H_{2.5}$)	-2169.6	−2400.7	173.4	232.8	80.6	[3]
Other hydrates						
C_3AH_6	-5008.2	-5537.3	421.7	445.6	149.7	[4]
C_2AH_8 [b]	-4814.1	-5420.5	485.0	558.6	184.0 [c]	t.s.
CAH_{10}	−4623.0	−5288.2	610.0	667.8	194.0	[4]
AH_3 (microcrystalline)	−1148.4	−1265.3	140	93.1	32	[4]
Supplementary data						
H_2O (liquid)	−237.2	−285.9	69.9	75.4	18.1	[5]
H_2O (steam)	-228.7	-242.4	187.3	40.1	2479.0	[6]
lime (CaO)	-604.0	-635.1	39.7	42.8	16.8	[5]
calcite ($CaCO_3$	-1129.2	-1207.4	92.7	81.9	36.9	[5]
$Ca(OH)_2$	−897.0	−984.7	83.4	87.5	33.0	[5]
$CaSO_4$	-1322.1	-1434.6	106.7	99.6	45.9	[5]
$CaSO_4 \cdot 2H_2O$	-1797.8	-2023.4	193.8	186.2	74.7	[5]

[a] Notice that the properties reported for the hydroxylated clinker phases are empirical. For more details on the calculation please refer to Chapter 6.

[b] Calculated from $C_2AH_{7.5}$ reported in [4], adding the contribution of 0.5 H_2O.

[c] Taken from [2].

Table C:2 Standard molar thermodynamic properties of the studied cement hydrates at 25 °C and 1 bar.

Phase	ΔG_f° (kJ/mol)	ΔH_f° (kJ/mol)	S° (J/mol K)	Cp° (J/mol K) [a]	Density (kg/m^3)	V° (cm^3/mol)	Ref.
Monosulfoaluminate							
Ms16 – $C_4A\bar{S}H_{16}$	-8726.8	-9930.5	975.0	1114.8	1981.7	350.5	t.s.
Ms14 – $C_4A\bar{S}H_{14}$	-8252.9	-9321.8	960.9	1028.5	1985.9	331.6	t.s.
Ms12 – $C_4A\bar{S}H_{12}$	-7778.4	-8758.6	791.6	948.4	2007.7	310.1	t.s.
Ms10.5 – $C_4A\bar{S}H_{10.5}$ [b]	-7417.9	-8311.9	731.2	888.3	2114.9	281.6	t.s.
Ms10.5 – $C_4A\bar{S}H_{10.5}$ [c]	-7414.9	-8311.9	720.9	888.3	2114.9	281.6	t.s.
Ms9 – $C_4A\bar{S}H_9$	-7047.6	-7845.5	703.6	828.2	2070.2	274.6	t.s.
Monocarboaluminate							
Mc11 – $C_4A\hat{C}H_{11}$	-7337.5	-8250.0	656.9	881.4	2170.0	262.0	[2]
Mc9 – $C_4A\hat{C}H_9$	-6840.3	-7618.6	640.6	801.2	2279.6	233.6	t.s.
Hemicarboaluminate							
Hc12 – $C_4A\hat{C}_{0.5}H_{12}$	-7336.0	-8270	712.6	905.8	1984.0	284.5	[2]
Hc10.5 – $C_4A\hat{C}_{0.5}H_{10.5}$	-6970.3	-7813.3	668.3	845.7	2057.1	261.3	t.s.
Hc9 – $C_4A\hat{C}_{0.5}H_9$	-6597.4	-7349.7	622.46	785.6	2047.4	249.3	t.s.
Strätlingite							
Str8 – C_2ASH_8	-5705.1	-6360	546.2	602.7	1935.8	216.1	[2]
Str7 – C_2ASH_7 [d]	-5464.0	-6066.8	487.6	562.6	1857.6	215.5	t.s.
Str5.5 – $C_2ASH_{5.5}$	-5095.2	-5603.4	454.8	502.5	1754.2	212.8	t.s.
Hydroxy-AFm							
OH-AFm19 – C_4AH_{19}	-8749.9	-10017.9	1120	1382.4	1816.3	368.7	[4]
OH-AFm13 – C_4AH_{13}	-7325.7	-8262.4	831.5	1142.0	2041.8	274.5	t.s.
OH-AFm11 – C_4AH_{11}	-6841.4	-7656.6	772.6	1061.8	2038.2	257.3	t.s.
Ettringite [e]							
Ett32	-15205.9	-17535.0	1900	2174.4	1773.4	707.8 [f]	[2]
Ett30 [g]	-14728.1	-16950.2	1792.4	2094.2	1722.5	707.8	t.s.
Met13_desorption	-10540.6	-11530.3	1960.4	1412.9	2223.0	410.6	t.s.
Met13_absorption	-10678.2	-12040.6	710.6	1412.9	2223.0	410.6	t.s.
Met9	-9540.4	-10643.7	646.6	1252.6	2329.0	361.0	t.s.

[a] Cp° was calculated assuming $\Delta Cp = 0$ for the changes of hydration states. Ms16 and Ms14 were calculated according to Eq. (2.7)

[b] Calculated with the absorption branch of the isotherm.

[c] Calculated with the desorption branch of the isotherm.

[d] Str7 must be used together with Str8 in an ideal solid solution.

[e] The properties reported in this table for ettringite correspond to those required to model the experimentally observed behaviour. In case experimental enthalpies and empirical zero-hysteresis properties are required please refer to Chapter 5.

[f] Calculated using the average volume of the lattice from this study.

[g] Thermodynamic properties of Ett30 should be used in an ideal solid solution with Ett32.

D. References Annexes

[1]. V.I. Babushkin, G.M. Matveyev, O.P. Mchedlov-Petrossyan, Thermodynamics of Silicates, Springer-Verlag, Berlin, 1985.

[2]. B. Lothenbach, T. Matschei, G. Möschner, F. Glasser, Thermodynamic modelling of the effect of temperature on the hydration and porosity of Portland cement, Cem. Concr. Res. 38 (2008) 1-18.

[3]. D.A. Kulik, Improving the structural consistency of C-S-H solid solution thermodynamic models, Cem. Conc. Res. 41 (2011) 477-495.

[4]. B. Lothenbach, L. Pelletier-Chaignat, F. Winnefeld, Stability in the system $CaO–Al_2O_3–H_2O$, Cem. Concr. Res. 42 (2012) 1621 – 1634.

[5]. W. Hummel, U. Berner, E. Curti, F.J. Pearson, T. Thönen, Nagra/PSI Chemical Thermodynamic Data Base 01/01.Universal Publishers, Parkland, Florida, USA, 2002.

[6]. J.W. Johnson, E.H. Oelkers, H.C. Helgeson, SUPCRT92 – A software package for calculating the standard molal thermodynamic properties of minerals, gases, aqueous species, and reactions from 1 bar to 5000 bar and 0 to 1000 degrees C, Computers & Geosciences 18 (1992) 899-947.

Curriculum Vitae

Name: Luis G. Baquerizo Ibarra
Gender: Male
Date of Birth: 06/12/1983
Nationality: Ecuadorian
Marital status: married
Current address: Trieschweg 43, 5033 Buchs, Switzerland
Telephone: +41-62 822 1912
Email: luis.baquerizo.ibarra@gmail.com, luis.baquerizoibarra@holcim.com

EDUCATION

Ecole Polytechnique Fédérale de Lausanne (EPFL). Lausanne, Switzerland (2011 – 2015)

- PhD in Cement and Concrete Science, Materials Engineering
- PhD program carried out in Holcim Technology Ltd. (Holderbank, Switzerland) together with the Ecole Polytechnique Fédérale de Lausanne
- Thesis director: Prof. Karen Scrivener, EPFL
- Thesis co-director: PhD. Thomas Mastchei, Holcim Technology Ltd.

Universitat Politècnica de Catalunya (UPC). Barcelona, Spain (2009 – 2010)

- Master in Advanced Materials Science and Engineering

Luleå tekniska universitet (LTU). Luleå, Sweden (2008 – 2009)

- Master in Advanced Materials Science and Engineering

Escuela Superior Politécnica del Litoral (ESPOL). Guayaquil, Ecuador (2002 – 2008)

- Bachelor in Mechanical Engineering

WORK EXPERIENCE

Holcim Technology Ltd. Holderbank, Switzerland (2011-2015)

- Industrial PhD carried out in the headquarters of Holcim Technology Ltd in Switzerland together with the Ecole Polytechnique Fédérale de Lausanne.
- Main topic of the project is the study of the behaviour of cementitious systems during drying, i.e. volume stability and performance in dependence on the environmental conditions.

IIASA Caterpillar. Guayaquil, Ecuador (2008)

- Instructor (trainer) of maintenance, operation and safety of heavy machines and diesel engines.

La Llave S.A. Guayaquil, Ecuador (2007)

- Sales, installation and implementation of Chesterton products: ARC composites, mechanical seals and packing, technical products.

PUBLICATIONS

Journal papers

- L.G. Baquerizo, T. Matschei, K.L. Scrivener, M. Saeidpour, A. Thorell, L. Wadsö, *Methods to determine hydration states of minerals and cement hydrates,* Cem. Concr. Res. 65 (2014) 85-95.
- L.G. Baquerizo, T. Matschei, K.L. Scrivener, M. Saeidpour, L. Wadsö, *Hydration states of AFm phases*, submitted Cement and Concrete Research.
- L.G. Baquerizo, T. Matschei, K.L. Scrivener, *Impact of water activity on the stability of Ettringite*, to be submitted Cement and Concrete Research.
- L.G. Baquerizo, T. Matschei, K.L. Scrivener, *Thermodynamic modelling of the water content of cementitious systems*, to be submitted to Cement and Concrete Research.

Conference papers

- L. Baquerizo, T. Matschei, K. Scrivener, *Volume stability of* $CAC\text{-}CaSO_4\text{-}CaCO_3\text{-}H_2O$ *systems during drying*, International Conference on Calcium Aluminates, Avignon - France, May. 18 – 21, 2014.
- L. Baquerizo, T. Matschei, K. Scrivener, *Impact of water activity on volume stability of cement hydrates*, Transcend Conference, Guildford - UK, Nov. 3 – 6, 2013.
- L. Baquerizo, T. Matschei, K. Scrivener, *Impact of water activity on the water content of cement hydrates*, 18th Ibausil Conference, Weimar - Germany, Sept. 12 – 15, 2012.
- L. Baquerizo, T. Matschei, K. Scrivener, *The impact of water chemical potential on the hydration states of Monosulfoaluminate*, 31st Cement and Concrete Science Conference, London, 2011.

SKILLS RELATED TO CEMENT AND CONCRETE SCIENCE

- Analysis of supplementary cementitious materials (SCMs): slag, fly ash, natural pozzolans, metakaolin, silica fume, etc.
- Synthesis of clinker phases.
- Hydration analysis of cement blended with different SCMs and limestone.
- Hydration quantification using XRD-Rietveld analysis (internal and external standard) and thermal analysis.
- Thermodynamic modelling of cement hydration and drying.
- Volume and thermal stability of cement hydrates in dependence of environmental conditions.
- Use of analytical characterization techniques such as X-Ray diffraction, thermal analysis, infrared spectroscopy, calorimetry, optical microscopy, scanning electron microscopy, porosity analysis, sorption balance, etc.

LANGUAGES

- Spanish: mother tongue
- English: advanced
- French: Basic

AWARDS AND PRIZES

- Marie Curie Scholarship, PhD studies, 2011 - 2013
- AMASE Erasmus mundus scholarship, 2009 – 2010
- Best graduate student, secondary school, 2002

HOBBIES

- Football, ping-pong, padel, table football.
- Travelling, hiking and camping.
- Movies.
- IT and technology developments.